PhD Dissertation

International Doctorate School in Information and Communication Technologies

DISI - University of Trento

Advanced Methods For Building Information Extraction From Very High Resolution SAR Data To Support Emergency Response

Dominik Brunner

Advisor:
Prof. Lorenzo Bruzzone
University of Trento

Co-Advisor:
Guido Lemoine
Joint Research Centre
European Commission

December 2009

Abstract

Rapid damage assessment after natural disasters (e.g. earthquakes, floods) and violent conflicts (e.g. war-related destruction) is crucial for initiating effective emergency response actions. Remote sensing satellites equipped with multispectral and Synthetic Aperture Radar (SAR) imaging sensors can provide vital information due to their ability to map affected areas of interest with high geometric precision and in an uncensored manner.

The new spaceborne Very High Resolution (VHR) SAR sensors onboard the TerraSAR-X and COSMO-SkyMed satellites can achieve spatial resolutions in the order of 1 m. In VHR SAR data, features from individual urban structures (like buildings) can be identified in their characteristic settings in urban settlement patterns.

This thesis presents novel techniques to support emergency response after catastrophic events using latest generation earth observation imagery. In this context, the potential and limits of VHR SAR imagery for extracting information about individual buildings in an (semi-) automatic manner is investigated.

The following main novel contributions are presented. First, we investigate the potential of the characteristic double bounce of a building in VHR SAR imagery to be exploited in automatic damage assessment techniques. In particular, we analyze empirically the relation between the double bounce effect and the aspect angle. Then, we propose a radar imaging simulator for urban structures, which is based on an adapted ray tracing procedure and a Lambertian-specular mixture model, emphasizing the geometrical effects of the scattering. Furthermore, we propose an approach to the height estimation of buildings from single detected SAR data. It is based on a "hypothesis generation - rendering - matching" procedure, where a series of hypotheses are generated and rendered by the previously introduced radar imaging simulator in order to compare the simulations with the actual VHR SAR data. Moreover, we present a method that detects buildings destroyed in an earthquake using pre-event VHR optical and post-event detected VHR SAR imagery. This technique evaluates the similarity between the predicted signature of the intact building in the post-event SAR scene and the actual scene to distinguish between damaged and undamaged buildings. Finally, we address the practical requirements of rapid emergency response scenarios by proposing an IT system infrastructure that enables collaborative and distributed geospatial data processing and on-demand map visualization.

The effectiveness of all proposed techniques is confirmed by quantitative and qualitative experimental results obtained on airborne and spaceborne VHR SAR imagery.

Keywords

Very High Spatial Resolution Images, Synthetic Aperture Radar, Radar Imaging Simulation, Building Analysis, Multisensor Change Detection, Emergency Response, Damage Assessment, Natural Disasters, Remote Sensing, Pattern Recognition, Image Processing.

Acknowledgments

The research presented in this thesis stems from an active collaboration between the Joint Research Centre of the European Commission and the Information Engineering and Computer Science Department of the University of Trento. In the following I would like to express my profound gratitude to numerous persons who made a *difference* during the development of this project.

I am deeply grateful to Guido Lemoine, not only for his excellent on-site supervision during my three years at the JRC, but also for his good sense of humor which made work a real pleasure. I would like to thank Dr. Delilah Al-Khudhairy, Dr. Daniele Ehrlich, and Martino Pesaresi, for giving me the opportunity to carry out the research work at the JRC. Furthermore, I am thankful to Dr. Joaquim Fortuny, Marco Basso, and Jorge Figueiredo-Morgado for their support during the EMSL measurements. I am grateful to my colleagues at the Institute for the Protection and Security of the Citizen for the inspiring and constructive working atmosphere. In this respect, Dr. Conrad Bielski, Dirk Buda, Clementine Burnley, Dr. Tom De Groeve, Milosz Dziembowski, Dr. Sandra Eckert, Dr. Thomas Kemper, Lauren Rizzo, Marco Scavazzon, Dr. Pierre Soille, and Dr. Ralf Steinberger, deserve special mentioning. I want to thank Dr. Harm Greidanus for fruitful discussions on SAR and the "field trips" we did together around the globe. I would like to especially thank Gunter Zeug for keeping my mind off work and for reminding me that there is life besides the PhD.

I want to express my sincere gratitude to Prof. Lorenzo Bruzzone for his outstanding scientific guidance throughout this thesis and for giving me the opportunity to finish my PhD at the University of Trento. I would like to thank Adamo Ferro for his dedication in his master thesis, reviewing parts of my thesis, and the passionate discussions we had on SAR and Bavarian beer. I have not forgotten my team members at the Remote Sensing Laboratory at the University of Trento. Without them I would not have enjoyed my time in Trentino as much as I did. In this regard I want to especially mention Dr. Francesca Bovolo, Michele Dalponte, Silvia Marchesi, Mauro Dalla Mura, and Claudio Persello.

I would like to thank the thesis committee members Prof. Uwe Stilla, TU Munich, and Prof. Florence Tupin, Telecom ParisTech, for reviewing and evaluating the thesis.

Dr. Daniel Eriksson, Prof. Richard Goebel, and Dr. Fritz Brunner deserve special thanks for encouraging me to seek to obtain a research degree. Without this, I probably never had started this thesis.

I would like to thank my parents for their motivation, support, and confidence throughout my life, which are the basis for my personal and professional development.

Most importantly, I am profoundly grateful to my wife Anja. To agree to the life of uncertainty which came along with this project is not a matter of course. Her understanding, support, and encouragements were invaluable for finishing this thesis.

Contents

List of Figures

List of Tables

List of Abbreviations

ASI	Italian Space Agency
CCC	Co-polarized Correlation Coefficient
CPU	Central Processing Unit
DBMS	Database Management System
DEM	Digital Elevation Model
DLR	German Aerospace Center
DSM	Digital Surface Model
EC	European Commission
EM	Expectation Maximization
EMSL	European Microwave Signature Laboratory
EU	European Union
FDTD	Finite-Difference Time-Domain
GDAL	Geospatial Data Abstraction Library
GIS	Geographic Information System
GO	Geometrical Optics
GPS	Global Positioning System
GPU	Graphical Processing Unit
HS	High-resolution SpotLight
HTTP	Hypertext Transfer Protocol
IEM	Integral Equation Method
InSAR	Interferometric Synthetic Aperture Radar
JRC	Joint Research Center
KML	Keyhole Markup Language
LIDAR	Light Detection And Ranging
MAP	Maximum A-Posteriori Probability
MI	Mutual Information
NMI	Normalized Mutual Information
NRCS	Normalized Radar Cross Section
OGC	OpenGIS Consortium
PO	Physical Optics
PV	Partial Volume
Q-Q-Plot	Quantile-Quantile-Plot
RADAR	Radio Detection And Ranging
RAR	Real Aperture Radar
RCS	Radar Cross Section

RGB	Red-Green-Blue
RMA	Rendering/Matching Analysis
RMS	Root Mean Square
ROI	Region Of Interest
SAR	Synthetic Aperture Radar
SC	ScanSAR
SL	SpotLight
SM	StripMap
SNR	Signal-to-Noise Ratio
UML	Unified Modeling Language
URL	Uniform Resource Locator
UTM	Universal Transverse Mercator
VHR	Very High Resolution
WMS	Web Map Service

List of Symbols

P_T	Transmitted power
P_R	Power returned by target
P_E	Power recorded at the receiving antenna
S_N	Non-directional power density at target
r	Distance between transmitter and target
G	Antenna gain
A_A	Geometric antenna area
K_a	Efficiency of antenna
λ	Wavelength
S_D	Directional power density at target
σ	Radar cross section
P_I	Incident power at target
L	System losses
$k \approx 1.38 \cdot 10^{-23}$ Ws/K	Boltzmann constant
K	Noise temperature
τ	Pulse duration
θ	Incidence angle
W_x, W_y	Axes parallel and orthogonal to flight trajectory
L_a, L_e	Antenna dimensions
h_S	Sensor flight height
δ_{ra}	RAR azimuth resolution
$c \approx 3 \cdot 10^8$ m/s	Speed of light
δ_{slr}	Slant range resolution
δ_{gr}	Ground range resolution
B	Frequency bandwidth
L_{sa}	Synthetic antenna length
θ_{sa}	Angular aperture in azimuth direction of SAR
δ_a	SAR azimuth resolution
σ_s	Surface roughness
ϵ_r	Relative dielectric constant
μ_r	Relative permeability
A	Amplitude of SAR signal
φ	Phase of SAR signal
$\vec{E}^i$	Incident field
$\vec{E}^s$	Scattered field

$[S]$	Scattering matrix
HH, HV, VH, VV	Polarization of transmitted and received fields; H = horizontal; V = vertical
P	Total power received by polarimetric radar
Ψ_P	Pauli basis
$[\sigma]_0$, $[\sigma]_1$, $[\sigma]_2$, $[\sigma]_3$	Pauli spin matrices
α_p, β_p, γ_p	Weighting factors related to odd-bounce, even-bounce and volume scattering (derived from Pauli decomposition)
$[C]$, $\langle[C]\rangle$	Covariance matrix, average covariance matrix
$[T]$, $\langle[T]\rangle$	Coherency matrix, average coherency matrix
$\vec{u}$, λ_e	Eigenvector, eigenvalue
α, β	Angles related to the scattering mechanism and the orientation of the target (derived from the $H/A/\alpha$ decomposition)
p_e	Eigenvalue probabilities
H	Entropy
A	Anisotropy
w, l, h	Width, length, height of building
l_s, l_l	Length of shadow area, length of layover area
α_r	Roof inclination angle of gable roof building
ϕ	Aspect angle
$\vec{S}$	Sensor position in Cartesian coordinate system
$\vec{r}$	Ray
$\Delta\theta$	Variation of incidence angle
$\vec{n}$	Surface normal
θ_l	Local incidence angle
ζ	Angle between reflected ray and specular direction
σ°	Normalized radar cross section
A_e	Effective area
q	Specularity of surface
$\vec{H}$	Vector containing the parameters for a simulation
$f(h)$	Similarity function
F	Similarity measure
Δ_{min}, Δ_{act}	Minimum and actual distances between two buildings
ω_u, ω_d	Undamaged and damaged building classes
m_{max}	Maximum match value between simulation and actual scene
$P(\omega_u)$, $P(\omega_d)$	Prior probabilities of classes ω_u, ω_d
$p(Y\|\omega_u)$, $p(Y\|\omega_d)$	Conditional probability density functions for classes ω_u, ω_d
Y	Random variable for match values
μ_u, σ_u, μ_d, σ_d,	Mean values and standard deviations of classes ω_u and ω_d
T_0	Threshold value

Chapter 1

Introduction

In this chapter, we give an introduction to this dissertation. In particular, we define and present the framework of this thesis by providing an overview to remote sensing data assisted damage assessment after natural disasters. Furthermore, we highlight the main objectives and novel contributions of this work. Finally, the structure and organization of this document is described.

1.1 Motivation

The reported occurrence of natural disasters, such as earthquakes, floods and cyclones, is on the rise [1], [2], leading to an increased public awareness of the impact of catastrophic events. In the short term, the occurrence of such events cannot be reduced by immediate human actions, whereas long term trends may be influenced for events that are tentatively linked to climate change. To understand and possibly mitigate the impact of such catastrophic events on human beings and their environment, research is being carried out for each of the characteristic phases of such events, i.e. before the event (early warning systems, risk assessment, preparedness) [3], [4], [5], the moment the event occurs (disaster alerting systems) [6], and after the event (emergency response) [7].

Emergency response is generally understood as supporting the organized intervention of civil security entities after a catastrophic event, either caused by a natural disaster or resulting from human conflict. Geospatial processing activities in support of emergency response range from the provision of relevant archived map products to dedicated data processing to provide thematic inputs into the various phases of emergency response, e.g. situation assessment, logistical planning, detailed damage assessment, and post-disaster reconstruction. The dynamics of the typical emergency response cycle and the institutional structures that are in place to trigger geospatial support actions, especially in the case of natural disasters, are detailed in [8].

Rapid damage assessment after a catastrophic event is crucial for initiating effective emergency response actions. Remote sensing satellites equipped with optical and SAR imaging sensors can provide important information about the affected areas since they can map the regions of interest quickly, with a high geometric precision, and in an uncensored manner. In [9] some of the operational aspects of using earth observation data for rapid

damage assessment and the integration of their derived information into the information flow for emergency response are highlighted. The authors propose novel automatic change detection methods, using the Indian Ocean tsunami 2004 disaster as a demonstration case. Other examples of the application of remote sensing data to rapid damage detection are given in [10] for the 2003 Bam earthquake in Iran, and in [11] and [12] for the 2004 Central Indian Ocean tsunami, the 1999 Izmir earthquake in Turkey, and the 2006 Java earthquake in Indonesia, respectively. Technical papers proposing novel methodologies for earth observation data processing increasingly address topics relevant for emergency response [13], [14], [15], [16], [17].

Current spaceborne VHR optical sensors, such as IKONOS, QuickBird, EROS-B, WorldView-1, and the recently launched GeoEye, have meter and submeter spatial resolutions. These sensors fall into the passive optical systems category and depend on sun illumination and cloud free weather conditions to acquire useful imagery. In contrast, active SAR sensors can acquire imagery independently of illumination conditions and with a relative insensitivity to weather conditions. Until recently, spaceborne commercial SAR sensors were only capable of imaging the earth surface with a spatial resolution no better than 9 m. This changed after the new VHR SAR sensors onboard the TerraSAR-X [18], and COSMO-SkyMed [19] satellites were launched in 2007 and 2008, providing SAR imagery with spatial resolutions down to 1 m. Current experimental airborne SAR systems even reach spatial resolutions of about 0.1 m [20]. In such imagery, features from individual urban structures, such as buildings, can be identified in their characteristic settings in urban settlement patterns (e.g. residential areas, city centers, industrial parks). Therefore, VHR SAR revolutionizes the perspective and the goal of the analysis of radar data: from a global study of the main scattering mechanisms and texture properties of extended groups of buildings, to the analysis of the scattering properties of individual buildings. Due to the meter resolution and the intrinsic reliability of the acquisition of SAR data, it is expected that VHR SAR becomes an important source of information to support emergency response actions after catastrophic events in urban areas.

1.2 Objectives and novel contributions of the thesis

In this thesis we present novel techniques to support emergency response after catastrophic events using latest generation earth observation imagery. In this context, the potential and limits of VHR SAR for extracting, in an (semi-) automatic manner, information about individual buildings in urban areas are investigated. The focus is on the usage of publicly available VHR SAR imagery from operational spaceborne sensors, i.e. TerraSAR-X and COSMO-SkyMed.

In this framework we introduce five main novel contributions:

1. an empirical analysis of the properties of the double bounce scattering mechanism of buildings;
2. a radar imaging simulator for buildings based on an adapted ray tracing procedure and a Lambertian-specular mixture model;
3. a method to estimate the heights of buildings from single detected SAR data;

4. a method that detects buildings destroyed in an earthquake using pre-event VHR optical and post-event detected VHR SAR imagery;
5. an approach to integrate earth observation imagery into the operational workflow of geospatial information processing to support emergency response actions.

In the next sub-sections the main objectives and novelties of this research work will be briefly described.

Analysis of the properties of the double bounce scattering mechanism of buildings

The double bounce effect of buildings is an important characteristic in VHR SAR images. It typically appears as a strong scattering mechanism caused by a corner reflector, which is made by the front wall of the building and its surrounding ground area. It indicates the presence of an intact building and is used as feature for the automatic detection and reconstruction of buildings from SAR data. In order to exploit this feature effectively for automatic damage assessment techniques its stability with respect to changes in the viewing configuration and material properties needs to be understood in detail. Until now, the double bounce mechanism was only studied using electromagnetic scattering models, and medium resolution SAR images. No detailed empirical analysis using VHR SAR data has been proposed in literature at the time of the development of this work.

In this thesis, we present an empirical analysis of the behavior of the double bounce effect of buildings in VHR SAR data with respect to the aspect angle of buildings and their surrounding ground material. First, we conduct polarimetric scaled building model measurements under well-controlled conditions with a variety of viewing configurations in the European Microwave Signature Laboratory (EMSL) of the European Commission (EC) - Joint Research Center (JRC) [21]. Since the laboratory experiment is subject to a number of simplifying assumptions which limit their generalization capabilities, we validate and refine in a second phase the results from the EMSL by analyzing a set of industrial and residential buildings with two different ground materials (grass and asphalt) in actual VHR spaceborne SAR data.

Radar imaging simulation for buildings

Radar imaging simulators can be used to support the analysis of radar scattering effects, assist in scene interpretation, and for training and teaching. Moreover, they can be used for information extraction, by generating simulated images based on hypotheses and comparing them with measured images, as proposed in this thesis for estimating building heights from single detected VHR SAR imagery, and for detecting damaged buildings using VHR optical pre-event and VHR SAR post-event imagery. Especially in the latter use cases, surface roughness parameters and dielectric properties of the materials in the scene are generally not known a priori, so that electromagnetic models such as the Physical Optics (PO) and Geometrical Optics (GO) approximations [22], the Finite-Difference Time-Domain method (FDTD) [23], or the Integral Equation method (IEM) [24] cannot be used to calculate the backscattering from the surfaces.

Therefore, we propose in this thesis as radar imaging simulator that is relatively simple to implement and that finds a balance between accuracy and efficiency. The main goal

of the proposed method is to obtain a precise simulation of the geometry of objects in SAR imagery, rather than a detailed simulation of the radiometry. The simulator is based on an adapted ray tracing procedure to determine which surfaces of a generic object are visible. The backscatter contributions are calculated by means of a novel Lambertian-specular mixture model. We illustrate its efficiency on two rather different structures, a rectangular gable roof building and an Egyptian pyramid.

Building height estimation from single detected VHR SAR imagery

Building volume is the product of the spatial extent of a built-up structure and its height. It is an indirect measure for population density, which is an essential parameter in impact assessment for emergency response. Furthermore, the height of a building is a structural indicator about the status of a building after a catastrophic event, i.e. whether it is still structurally intact. Hence, height determination of buildings is a key issue for post-emergency event information extraction in urban areas.

Currently reported methods for height extraction from SAR data rely on multidimensional data, where the same area is imaged from different flight paths, such as Interferometric SAR (InSAR), multistatic SAR, multiaspect SAR, or circular SAR. Operational spaceborne VHR SAR sensors have revisit times of several days (e.g. 11 days for TerraSAR-X), limiting the usefulness of multidimensional data to support fast emergency response.

In this thesis, we present a novel concept for the height estimation of buildings from single detected SAR data. The proposed approach is based on the definition of a hypothesis on the height of the building and on the simulation of a SAR image for testing that hypothesis. A matching procedure is applied between the estimated and the actual SAR image in order to test the height hypothesis. The process is iterated for different height assumptions until the matching function is optimized and thus the building height is estimated.

Earthquake damage assessment of buildings using VHR optical and SAR imagery

Information on the impact of a catastrophic event can be derived from suitable satellite imagery by comparing reference data before the event (pre-event) to imagery acquired shortly after the event (post-event). The advantage of SAR imagery is being independent of cloud conditions and not requiring the sun illumination. Suitable SAR data availability directly after an event is thus, in principle, only based on the SAR sensor's orbiting characteristics. Spaceborne VHR SAR only became available recently, so that their data archives have limited pre-event imagery. Consequently, VHR SAR is not yet a reliable source of pre-event reference data. In contrary, optical VHR sensors have existed for almost a decade and have already imaged large parts of the earth. The increased availability of this type of sensors and their growing image archives (which are frequently updated), make VHR optical data well suited as the pre-event reference data source.

Considering the above mentioned practical difficulties, the best combination of imagery for rapid damage assessment is spaceborne VHR optical for the pre-event imagery and spaceborne VHR SAR for post-event imagery. However, they cannot be compared

directly in a change detection approach because both types of data have entirely different radiometric and physical image formation characteristics.

In this thesis, we present a novel method that detects buildings destroyed in an earthquake using pre-event VHR optical and post-event detected VHR SAR imagery. In the first step, the 3-D parameters of a building are estimated from the pre-event optical imagery. Second, the building information and the acquisition parameters of the VHR SAR scene are used to predict the expected signature of the building in the post-event SAR scene assuming that it would not be affected by the event. Third, the similarity between the predicted image and the actual SAR image is analyzed. If the similarity is high, the building is likely to be still intact, whereas a low similarity indicates that the building is destroyed. A similarity threshold is used to classify the individual buildings.

Distributed geospatial data processing functionality to support collaborative and rapid emergency response

Emergency response actions are at local or regional scales, thematically specific (e.g. classification of individual urban structures), and have stringent timing requirements for the delivery of the relevant data layers. The main requirements for geospatial support activities when responding to a call for emergency response support can be summarized as: 1) the collection of data from different archives and acquisition capabilities; 2) the need for customized rapid visualization for each of the actors in the emergency response community; and 3) the need to trigger, in near real-time, geospatial processing tasks, organize collaborative analysis (e.g. manual feature capturing by photo-interpreters), and inform decision makers with tailored output. Often, these requirements are only met in an ad hoc manner, whereas the success and effectiveness of using geospatial data to support emergency response strongly depends on the personal experience of each team member, as well as the overall experience of the team.

In this thesis, we propose common steps for using geospatial data to support emergency response actions. This effort aims at increasing the efficiency of analyzing the data and the overall effectiveness of using geospatial data for supporting the relief effort. In particular, we propose a novel approach, based on an IT system infrastructure, to collate geospatial feature data from distributed sources and integrate them in image processing and visualization. The IT system infrastructure enables rapid collaborative mapping, support for in-situ data collection, customized on-demand image processing, geospatial data queries, and near instantaneous map visualization.

1.3 Structure of the thesis

This thesis is organized in 9 chapters.

The present chapter pointed out the motivation for this thesis, and highlighted the objectives as well as the main novel contributions.

Chapter 2 describes the principles of real and synthetic aperture radar. The geometric effects of the side looking geometry of SAR are highlighted, which are especially important for analyzing buildings in VHR SAR data. Furthermore, the polarimetric parameters and decompositions used to analyze the EMSL data are explained. Finally, different

SAR acquisition modes are presented together with the characteristics of operational spaceborne VHR SAR sensors.

Chapter 3 investigates the appearance of buildings in VHR SAR imagery. In particular, the main characteristics of idealized rectangular flat and gable roof buildings are presented. Using actual VHR SAR imagery, specific scattering phenomena are discussed, which often limit the robustness of automatic building detection and reconstruction techniques.

Chapter 4 presents the empirical analysis of the relation between the double bounce effect and the aspect angle of a building in VHR SAR data. First, we focus the attention on the laboratory experiment. Then, in a second stage, we conduct the analysis of the actual spaceborne VHR SAR data.

Chapter 5 presents the radar imaging simulator. First, the enhanced ray tracing procedure is explained in detail. Then the Lambertian-specular mixture model is introduced before its main characteristics are discussed. The simulator is one of the core components for the methods introduced in Chapter 6 and Chapter 7.

Chapter 6 presents the method for building height estimation from single detected VHR SAR imagery. The characteristics of the method are highlighted using a large set of buildings imaged by airborne and spaceborne VHR SAR sensors with varying viewing configurations from the city of Dorsten, Germany.

Chapter 7 introduces the method for detecting buildings destroyed in an earthquake using pre-event VHR optical and post-event detected VHR SAR imagery. It relies on concepts presented in Chapter 6. As test case we use a subset of the town of Yingxiu, China, which was heavily damaged in the Sichuan earthquake of May 12, 2008.

Chapter 8 presents an IT system enabling distributed geospatial data processing to support collaborative and rapid emergency response. First, we discuss the typical sequence of geospatial support activities carried out for emergency response. Then the IT system architecture is described in detail. In this context we also highlight the integration of the method introduced in Chapter 7 into the proposed infrastructure. The usage of the system is explained for a damage assessment scenario for the Lebanon armed conflict between Lebanese and Israeli forces in July 2006 using VHR optical imagery. Furthermore, using the Sichuan earthquake 2008 as test case, we demonstrate the system for a damage assessment scenario using VHR SAR imagery.

Finally, Chapter 9 draws the conclusions of this thesis. Furthermore, future developments of the research activity are discussed.

Chapter 2

Fundamentals

In this chapter we review the basic principles of radar and radar imaging systems. First, we introduce the radar equation before we highlight the fundamentals of Real Aperture Radar (RAR) and SAR. Then we discuss some important characteristics of SAR imagery, which are relevant for the understanding of the appearance of buildings in VHR SAR data. Furthermore, we describe the basics of polarimetry and highlight some important polarimetric parameters and decompositions used to analyze the EMSL data. Finally, we explain some common acquisition modes implemented in state of the art VHR SAR sensors, before we outline the main characteristics of the TerraSAR-X and COSMO-SkyMed sensors.

2.1 Radar equation

Radio detection and ranging (radar) systems are active systems which measure the scattering of a transmitted pulse in a narrow microwave frequency band (see Table 2.1). The scattering of the transmitted microwave pulse is primarily determined by the geometry and dielectric properties of the target and the transmit/receive configuration of the SAR sensor. In the following we will only consider monostatic systems, i.e. transmitter and receiver antenna are the same, or their relative distance is negligible. In this context, the scattering recorded at the receiving antenna is also termed backscattering.

Table 2.1: Microwave frequency bands.

Band	Frequency (GHz)	Wavelength (cm)
UHF	0.3 - 1.0	100.0 - 30.0
L	1.0 - 2.0	30.0 - 15.0
S	2.0 - 4.0	15.0 - 7.5
C	4.0 - 8.0	7.5 - 3.8
X	8.0 - 12.0	3.8 - 2.5
Ku	12.0 - 18.0	2.5 - 1.7
K	18.0 - 27.0	1.7 - 1.1
Ka	27.0 - 40.0	1.1 - 0.75
V	40.0 - 75.0	0.75 - 0.40
W	75.0 - 100.0	0.40 - 0.27

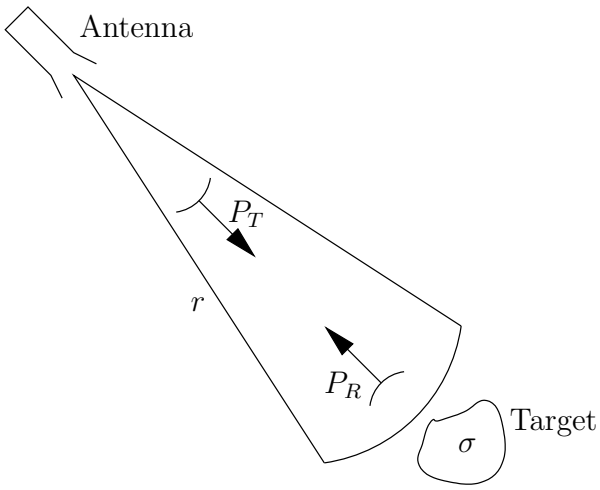

Figure 2.1: Geometry of scattering from target.

The relation between the transmitted power P_T , the power returned by the target P_R, and the power recorded at the receiving antenna P_E is described by the radar equation (see Figure 2.1) [25]. Considering an isotropic radiator, the emitted energy propagates uniformly in all directions. The non-directional power density S_N at the target with distance r is given by:

$$S_N = \frac{P_T}{4 \cdot \pi \cdot r^2}. \tag{2.1}$$

Radar systems typically use directional antennas to form a small beam. These antennas have an increase of the power density in the direction of the beam, which is called antenna gain G:

$$G = \frac{4 \cdot \pi \cdot A_A \cdot K_a}{\lambda^2}, \tag{2.2}$$

with A_A being the geometric antenna area, K_a a factor expressing the efficiency of the antenna, and λ the wavelength. Then, the directional power density S_D at the target is given by:

$$S_D = S_N \cdot G. \tag{2.3}$$

The power returned from the target does not only depend on the power density at the target itself, but also on the Radar Cross Section (RCS) σ, which is a measure of the reflective strength of a target. Assuming that the target is small with respect to the radar beam, it is defined as:

$$\sigma = 4 \cdot \pi \cdot r^2 \cdot \frac{P_R}{P_I}, \tag{2.4}$$

with P_I being the incident power. The power returned from the target can be written as:

$$P_R = S_D \cdot \sigma. \tag{2.5}$$

Since we consider here the monostatic case the transmitter→target and target→receiver distances are the same. Furthermore we can assume that the antenna gains of the transmitting and receiving antennas are equal, and thus the power received at the sensor is

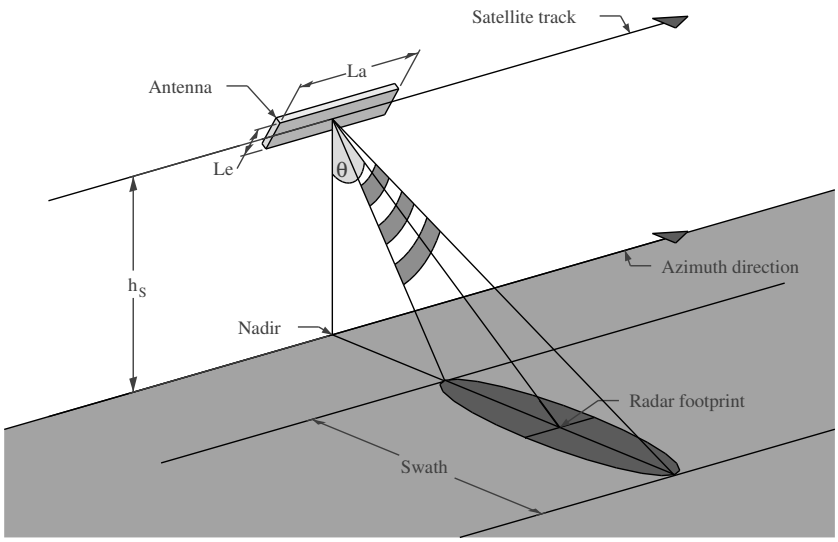

Figure 2.2: Side looking geometry of imaging radar systems.

given by:

$$P_E = \frac{P_R \cdot A_A \cdot K_a}{4 \cdot \pi \cdot r^2 \cdot L} = \frac{P_T \cdot G^2 \cdot \lambda^2 \cdot \sigma}{(4 \cdot \pi)^3 \cdot r^4 \cdot L}, \tag{2.6}$$

with L being a factor for the system losses.

An important factor for the assessment of the quality of radar measurements is the Signal-to-Noise Ratio (SNR) :

$$SNR = \frac{P_E \cdot \tau}{k \cdot K} = \frac{P_T \cdot G^2 \cdot \lambda^2 \cdot \sigma \cdot \tau}{(4 \cdot \pi)^3 \cdot r^4 \cdot L \cdot k \cdot K}, \tag{2.7}$$

with k denoting the Boltzmann constant, K the noise temperature and τ the microwave pulse duration. The higher the SNR is, the less disruptive the noise is, and hence the better it is to detect also weak signals in the recorded data.

2.2 Real aperture radar

Airborne and spaceborne imaging radar systems, such as RAR and SAR, illuminate the scene in side looking geometry (see Figure 2.2). The antenna of the radar system is mounted on a platform in such a way that the horizontal and vertical axes of the antenna are parallel and orthogonal to the azimuth direction, respectively. The angle between Nadir and the radar beam direction is called the incidence angle θ.

The footprint of the main lobe of the radar beam on the ground can be approximated by an ellipse with the principal axis:

$$W_x = r \cdot \theta_a = \frac{h_S \cdot \theta_a}{\cos(\theta)}, \tag{2.8}$$

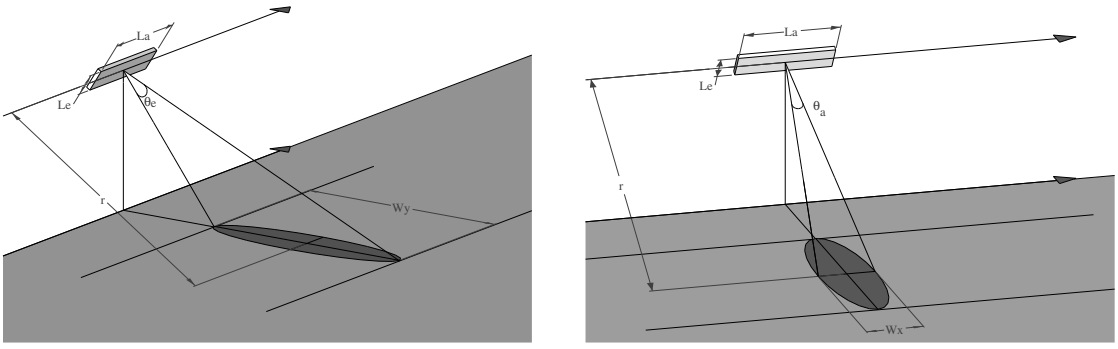

(a) (b)

Figure 2.3: Angles and footprint dimensions of imaging radars. (a) Range direction. (b) Azimuth direction.

$$W_y = \frac{r \cdot \theta_e}{\cos(\theta)} = \frac{h_S \cdot \theta_e}{\cos^2(\theta)}, \tag{2.9}$$

$$\theta_a = \frac{\lambda}{L_a}, \tag{2.10}$$

$$\theta_e = \frac{\lambda}{L_e}, \tag{2.11}$$

where W_x and W_y refer to the axes parallel and orthogonal to the flight trajectory, respectively, L_a and L_e to the antenna dimensions (see Figure 2.3), and h_S to the sensor flight height.

For a RAR system, the azimuth resolution δ_{ra} is determined by (2.8) and hence is given by the size of the antenna, the wavelength, and the distance between sensor and target $[h_S/\cos(\theta)]$. Indeed, a spaceborne platform with an antenna with 5 m length in azimuth, which is flying with a low altitude of 300 km and measuring with a wavelength of 0.1 m (3 GHz) with an incidence angle of 50° only achieves an azimuth resolution of about 9.3 km.

Two objects located in the same azimuth resolution cell can only be resolved by the sensor if their distance in range direction is greater than the spatial extent of an individual microwave pulse. Otherwise, the echoes of the objects will overlap. The microwaves propagate at light velocity c and travel the distance between the radar sensor and the target twice: from the transmitter to the target and vice versa. Thus, the slant range resolution δ_{slr} is given by:

$$\delta_{slr} = \frac{c \cdot \tau}{2}, \tag{2.12}$$

highlighting that it is only a function of the pulse duration. The ground range resolution δ_{gr} depends on the incidence angle and is calculated by projecting δ_{slr} geometrically on the ground plane (see Figure 2.4):

$$\delta_{gr} = \frac{c \cdot \tau}{2 \cdot \sin(\theta)}. \tag{2.13}$$

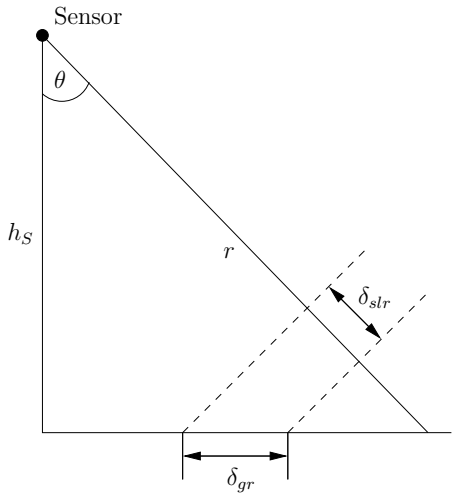

Figure 2.4: Geometry in slant- and ground range projection.

It is not possible to reduce the pulse duration arbitrarily in order to achieve a good range resolution, since this would imply a low emitted/return power and consequently a low SNR. Instead, pulse compression techniques with matched filter processing are used, achieving sufficient range resolutions and high SNR at the same time. With these techniques δ_{slr} and δ_{gr} are related to the frequency bandwidth B of the transmitted radar pulse by:

$$\delta_{slr} = \frac{c}{2 \cdot B}, \tag{2.14}$$

$$\delta_{gr} = \frac{c}{2 \cdot B \cdot \sin(\theta)}. \tag{2.15}$$

The used waveform is known as linear frequency modulated chirp. In Figure 2.5 we show the schematic view of the real part (Figure 2.5a) and the time-frequency relation (Figure 2.5b) of chirp signals. The instant frequency follows a raising linear ramp with duration T and bandwidth B.

2.3 Synthetic aperture radar

We highlighted in the previous section that due to practical limitations RAR systems have a poor azimuth resolution. This is especially valid for spaceborne sensors, where the distance between sensor and target is very large. Instead, SAR systems can considerably improve the azimuth resolution by processing the phase information of the complex signals.

Figure 2.6 shows the principle of SAR. A point target is illuminated by the SAR beam during a time span depending on W_x, in which the platform is moving. During this time, which is called integration time, a SAR system records the phase history of the signal. By exploiting the Doppler shifts of the complex signals, different objects can be resolved, even if they are located in azimuth direction closer than the real azimuth aperture of the

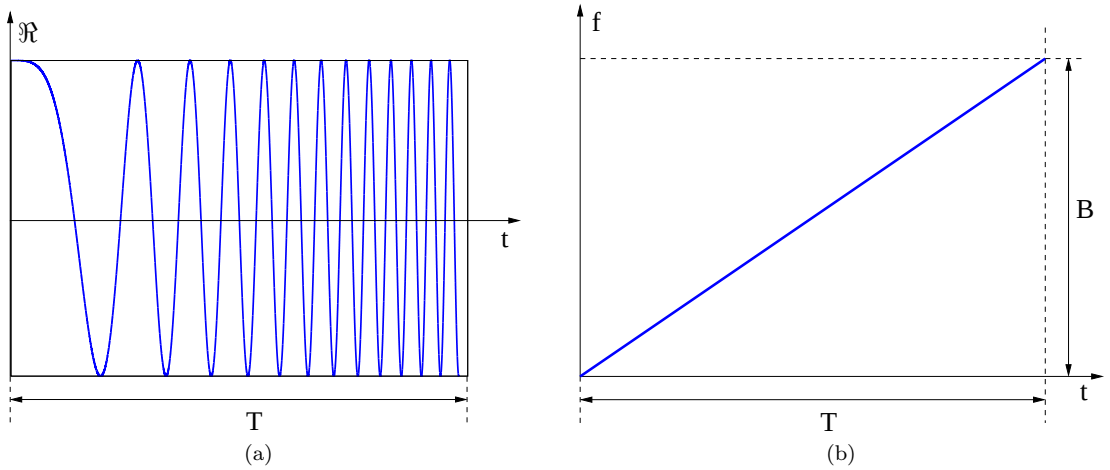

Figure 2.5: Schematic view of chirp signal. (a) Real part of a chirp pulse. (b) Time-frequency relation.

antenna. The synthetic aperture corresponds to a synthetic antenna length L_{sa} which is equal to the distance travelled by the sensor in which a target is illuminated by the beam:

$$L_{sa} = W_x = \frac{h_S \cdot \lambda}{L_a \cdot \cos(\theta)}. \tag{2.16}$$

The achieved angular aperture in azimuth direction of SAR is half of the one of RAR:

$$\theta_{sa} = \frac{\lambda}{2 \cdot L_{sa}}. \tag{2.17}$$

The azimuth resolution δ_a of SAR is given by:

$$\delta_a \approx r \cdot \theta_{sa} = \frac{\lambda \cdot h_S}{2 \cdot L_{sa} \cdot \cos(\theta)} = \frac{L_a}{2}, \tag{2.18}$$

demonstrating that it is only dependent on the length of the actual antenna, but not on the distance between sensor and target.

2.4 Characteristics of SAR imagery

2.4.1 Geometric distortions

The side looking geometry of SAR together with non-flat terrain causes geometric distortions, such as foreshortening, and relief displacement. Furthermore, it is source for layover- and shadow effects, which are visible as relatively bright and dark regions in SAR imagery, respectively.

Foreshortening: In Figure 2.7a we show the foreshortening phenomena, which is a dominant effect in mountainous areas. Inclined surfaces, which are oriented towards the sensor, appear shortened in SAR imagery. For instance distance $\overline{AB}$ is much longer then its projection $\overline{A'B'}$ on SAR slant range image space. The slant range compression results

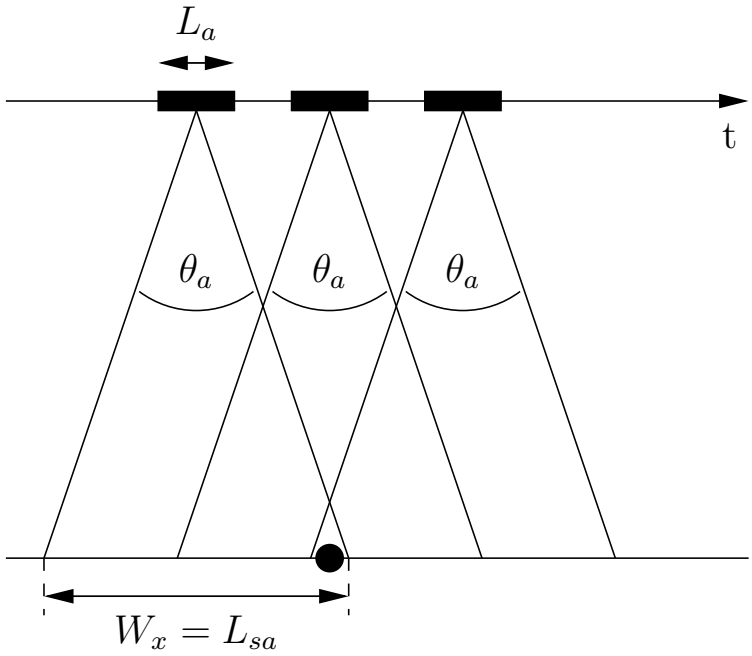

Figure 2.6: Principle of SAR. The point target is illuminated for the duration the sensor travels distance W_x that is the length of the synthetic antenna.

in a brighter area $\overline{A'B'}$, since it contains the entire energy scattered by the longer $\overline{AB}$ area.

Relief displacement: SAR measures the distances between an object and the sensor. Hence, if the inclination of the surface is larger than the incidence angle, the top of the elevated structure is shifted in the image towards the sensor, as shown in Figure 2.7b. Even so that A is located on the ground in front of the elevated point B, the projection on the SAR slant range space results in a reversed order, i.e. B' is closer to the sensor than A'.

Layover: The layover effect is related to the relief displacement. If a slope is steeper than the radar beam, parts of the ground surface, the slope facing the sensor, and parts of the slope turned away from the sensor are equidistant to the SAR antenna. Therefore, their backscattering return to the sensor at the same time, causing the layover effect, whereas the different signals cannot be separated anymore. For instance, in Figure 2.7c, the slope $\overline{BC}$ is steeper than the incidence angle of the radar beam so that $\overline{AB}$, $\overline{BC}$, and $\overline{CD}$ are located within the same distance to the sensor. Hence, their backscattering overlays in the area $\overline{C'B'} + \overline{A'B'} + \overline{C'D'}$.

Shadow: Shadows are areas where no backscattering is recorded at the sensor, because they are occluded from the radar beam. This occurs when surfaces which are turned away from the sensor are steeper than the SAR illumination, as shown in Figure 2.7d. The area between $\overline{BD}$ can not be illuminated by the radar beam, since $\overline{BC}$ is steeper than the radar beam, causing the shadow area $\overline{B'D'}$.

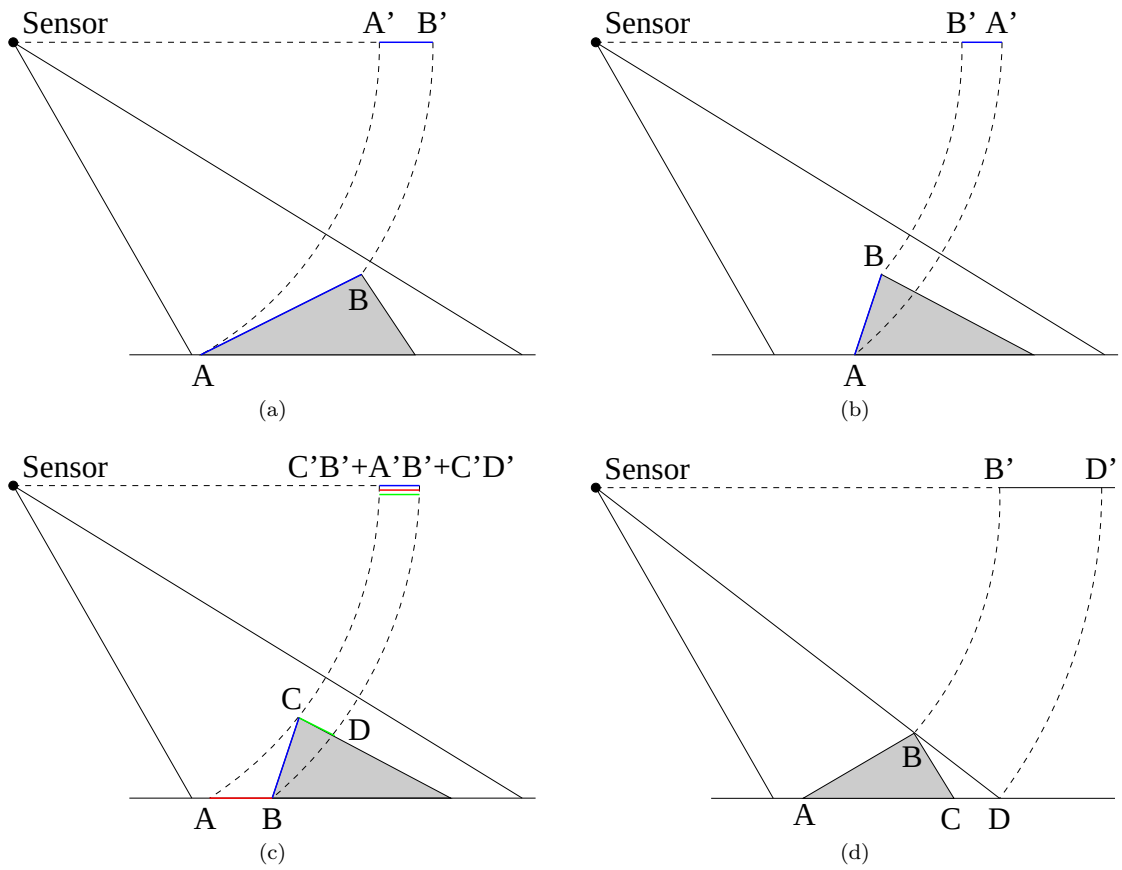

Figure 2.7: Geometric effects of SAR. (a) Foreshortening. (b) Relief displacement. (c) Layover. (d) Shadow.

.

2.4.2 Surface scattering

The scattering of microwaves from a surface is composed by a mix of specular and Lambertian scattering, depending on the surface roughness σ_s with respect to the wavelength [22]. For a perfectly smooth ($\sigma_s \ll \lambda$) and infinitely large (size $\gg \lambda$) surface, the field is entirely scattered in specular direction (see Figure 2.8a). Hence, no backscattering is recorded by the sensor. A perfectly rough surface ($\sigma_s \gg \lambda$) instead scatters according to the Lambertian cosine law (see Figure 2.8c). For a slightly rough surface ($\sigma_s < \lambda$) the scattering is characterized by a large specular component, and a Lambertian component with less power scattered in all directions (see Figure 2.8b). The rougher the surface, the weaker are the specular and the stronger are the Lambertian components.

Besides being dependent on the surface roughness, the scattering is also influenced by the relative dielectric constant ϵ_r and the relative permeability μ_r of the surface material. For SAR imaging the influence of μ_r is negligible and therefore $\mu_r = 1$. ϵ_r is a complex number that depends on the dielectric properties of the material and varies with respect to the material moisture content and the SAR frequency. Materials with low ϵ_r have less reflectivity and hence a higher penetration into the medium.

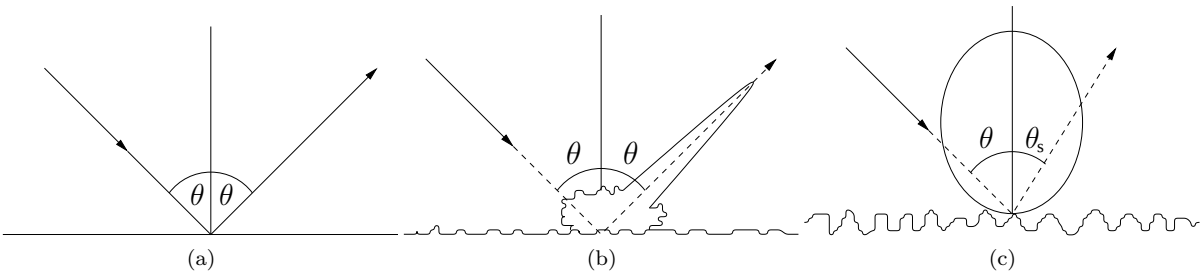

Figure 2.8: Specular and Lambertian scattering from surfaces (adopted from [22]). (a) Scattering from smooth surface. (b) Scattering from slightly rough surface. (c) Scattering from rough surface.

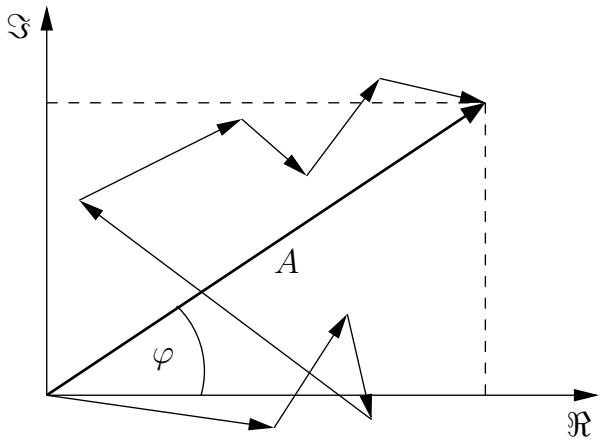

Figure 2.9: Coherent sum of individual scatterers.

2.4.3 Speckle noise

SAR data are affected by a characteristic noise called "speckle", which causes the granular appearance of SAR imagery. In reality it is not a noise effect but the result of constructive and destructive interferences between the complex returns from the scatterers in a resolution cell. Since the resolution cell is large compared to the wavelength, N targets are present in one cell. Their individual scattering contributions sum up coherently resulting in a single complex value measured at the sensor (see Figure 2.9):

$$A \cdot e^{i\varphi} = \sum_{n=0}^{N} A_n \cdot e^{i\varphi_n}, \tag{2.19}$$

with A being the modulus and φ the phase. Even so that the speckle effect is not random as it depends on the scatterers present in the scene, it is often modeled as random multiplicative noise effect. It can be reduced by averaging correlated samples implying a reduction of the spatial resolution. Multilooking techniques average samples directly during the processing of the SAR signals (image formation), while speckle filters are applied to the processed SAR image [26].

2.5 Radar polarimetry

The characteristics of a scatterer influence the polarimetric parameters of the scattered electromagnetic wave. Consequently, using radar polarimetry [27], the polarimetric characteristics of a scatterer can be derived. With this information it is possible to distinguish between different scattering mechanisms and to calculate physical parameters from the investigated scene.

2.5.1 Scattering matrix

To determine the scattering behavior of a target, the relationship between the polarization characteristics of the incident and scattered waves is investigated. The polarization states of both waves can be described as a vector, so that the polarization behavior of the target can be represented by:

$$\begin{bmatrix} \vec{E}_H^s \\ \vec{E}_V^s \end{bmatrix} = [S] \cdot \begin{bmatrix} \vec{E}_H^i \\ \vec{E}_V^i \end{bmatrix}, \tag{2.20}$$

$$[S] = \begin{bmatrix} S_{HH} & S_{HV} \\ S_{VH} & S_{VV} \end{bmatrix}, \tag{2.21}$$

with $\vec{E}^i$ denoting the incident field and $\vec{E}^s$ the scattered field. The scattering matrix $[S]$ is obtained from the magnitudes and phases measured by the four channels of a polarimetric radar. H and V denote the horizontal linear and vertical linear polarizations, respectively. The first index refers to the polarization of the transmit antenna, and the second to the one of the receive antenna, so that HV refers to the combination of a H polarized transmit and V polarized receive antenna. HH, and VV, are referred to as co-polarized channels, while HV and VH are called cross-polarized channels. In the monostatic case, which we will consider in the remainder of this thesis, $[S]$ is symmetric, as the reciprocity property holds for most targets and $S_{HV} = S_{VH}$. Note that also other polarizations with orthogonal states can be used, such as left and right circular.

2.5.2 Polarimetric parameters

Total power

The total power P received by a polarimetric radar is the sum of the squared modulus of all the elements of the scattering matrix.

$$P = |S_{HH}|^2 + 2 \cdot |S_{HV}|^2 + |S_{VV}|^2. \tag{2.22}$$

Co-polarized correlation coefficient

The Co-polarized Correlation Coefficient (CCC), permits separating even and odd bounce contributions by analyzing its phase information. It is given by:

$$CCC = \frac{\langle S_{HH} \cdot S_{VV}^* \rangle}{\sqrt{\langle |S_{HH}|^2 \rangle \cdot \langle |S_{VV}|^2 \rangle}} \qquad \begin{matrix} 0 \leq |CCC| \leq 1 \\ 0^\circ \leq \angle CCC \leq 180^\circ \end{matrix} \tag{2.23}$$

where S_{pp} indicates the pp-coefficient (p=$\{H, V\}$) of the scattering matrix, * is the complex conjugate operator, and $\langle . \rangle$ is the average operator.

If the magnitude of CCC is unity, the received signals from the two channels are linearly related. If it is less than one it may mean that the backscattering at the two channels is not directly related, that noise is present, or that the received waves are only partially polarized.

The CCC phase angle is the phase difference between the two co-polarized channels. This value can assist in classifying a pixel, as it depends on the number of bounces that the wave experiences. An ideal single bounce (or odd-bounce) scatterer has a CCC phase of 0°, while an ideal double bounce (or even-bounce) scatterer has a CCC phase of 180°. In practice, this parameter shows some variations, so that odd or even-bounce scattering mechanisms are characterized by a CCC phase range near the ideal values.

2.5.3 Polarimetric decompositions

Coherent decompositions

Coherent decompositions express the measured scattering matrix as a combination of the scattering returns of simpler objects:

$$[S] = \sum_{i=1}^{I} c_{s,i} \cdot [S]_i, \tag{2.24}$$

with $[S]_i$ denoting the response of each of the I canonical objects, and $c_{s,i}$ denoting the respective weight with which $[S]_i$ contributes to $[S]$. An large number of sets $[S]_i; i = 1, \ldots, I$ can be used to decompose the scattering matrix, but only some of them are actually useful to interpret the information contained in $[S]$. Note that coherent decompositions can only be employed effectively if the incident and the scattered waves are entirely polarized, which is only valid for coherent targets, i.e. point/pure scatterers.

A widely used coherent decomposition is the Pauli decomposition [28], which uses the Pauli basis Ψ_P to decompose the scattering matrix:

$$\Psi_P : \frac{1}{\sqrt{2}} \cdot \{[\sigma]_i\}, \quad i = 0, 1, 2, 3 \tag{2.25}$$

where

$$[\sigma]_0 = \begin{bmatrix} 1 & 0 \\ 0 & 1 \end{bmatrix}, \quad [\sigma]_1 = \begin{bmatrix} 1 & 0 \\ 0 & -1 \end{bmatrix}, \quad [\sigma]_2 = \begin{bmatrix} 0 & 1 \\ 1 & 0 \end{bmatrix}, \quad [\sigma]_3 = \begin{bmatrix} 0 & -1 \\ 1 & 0 \end{bmatrix}, \tag{2.26}$$

are the Pauli spin matrices. The Pauli decomposition is given by:

$$[S] = \begin{bmatrix} S_{HH} & S_{HV} \\ S_{VH} & S_{VV} \end{bmatrix} = \frac{\alpha_p}{\sqrt{2}} \cdot [\sigma]_0 + \frac{\beta_p}{\sqrt{2}} \cdot [\sigma]_1 + \frac{\gamma_p}{\sqrt{2}} \cdot [\sigma]_2, \tag{2.27}$$

with

$$\alpha_p = \frac{S_{HH} + S_{VV}}{\sqrt{2}}, \quad \beta_p = \frac{S_{HH} - S_{VV}}{\sqrt{2}}, \quad \gamma_p = \sqrt{2} \cdot S_{HV}. \tag{2.28}$$

The first summand in (2.27) refers to the scattering from a general odd-bounce scattering target, like a sphere, a plate or a trihedral. The second term represents the contributions from a dihedral, or, in general, scattering characterized by even-bounce. The third term represents those scatterers which return the orthogonal polarization of the incidence wave, such as the volume scattering produced by forest canopy.

The coefficients α_p, β_p and γ_p are the factors by which the associated matrices need to be weighted to obtain the original scattering matrix. The total power (2.22) is given by:

$$P = |\alpha_p|^2 + |\beta_p|^2 + |\gamma_p|^2, \tag{2.29}$$

so that the values $|\alpha_p|^2$, $|\beta_p|^2$, and $|\gamma_p|^2$ denote the scattered power by odd-bounce, even-bounce, and volume scattering, respectively.

Incoherent decompositions

In the previous section we pointed out that coherent decompositions can only characterize pure scattering mechanisms. However, in reality, scatterers are typically not ideal so that the returned waves are only partially polarized. In order to extract the polarimetric information of these returns, a statistical analysis of the average covariance $\langle[C]\rangle$ and coherency $\langle[T]\rangle$ matrix can be performed with:

$$[C] = \begin{bmatrix} |S_{HH}|^2 & \sqrt{2}\cdot S_{HH}\cdot S_{HV}^* & S_{HH}\cdot S_{VV}^* \\ \sqrt{2}\cdot S_{HV}\cdot S_{HH}^* & 2\cdot|S_{HV}|^2 & \sqrt{2}\cdot S_{HV}\cdot S_{VV}^* \\ S_{VV}\cdot S_{HH}^* & \sqrt{2}\cdot S_{VV}\cdot S_{HV}^* & |S_{VV}|^2 \end{bmatrix}, \tag{2.30}$$

and

$$[T] = \frac{1}{2}\cdot \begin{bmatrix} |S_{HH}+S_{VV}|^2 & (S_{HH}+S_{VV})(S_{HH}-S_{VV})^* & 2(S_{HH}+S_{VV})S_{HV}^* \\ (S_{HH}-S_{VV})(S_{HH}+S_{VV})^* & |S_{HH}-S_{VV}|^2 & 2(S_{HH}-S_{VV})S_{HV}^* \\ 2\cdot S_{HV}\cdot(S_{HH}+S_{VV}) & 2\cdot S_{HV}\cdot(S_{HH}-S_{VV})^* & 4\cdot|S_{HV}|^2 \end{bmatrix}. \tag{2.31}$$

The $\langle . \rangle$ matrices are computed by averaging separately each of its elements, which can be achieved either by multilooking the SAR image, or by means of a sliding window.

The objective of the incoherent decompositions is to separate $\langle[C]\rangle$ and $\langle[T]\rangle$ as the combination of second order descriptors, corresponding to simpler or canonical objects:

$$\langle[C]\rangle = \sum_{i=1}^{I} c_{c,i}\cdot[C]_i, \tag{2.32}$$

$$\langle[T]\rangle = \sum_{i=1}^{I} c_{t,i}\cdot[T]_i, \tag{2.33}$$

with $[C]_i$ and $[T]_i$ denoting the canonical responses, and c_c and c_t the respective coefficients.

A commonly used incoherent decomposition is the $H/A/\bar{\alpha}$ decomposition [29], which is based on an eigenvalue decomposition. It can be shown that:

$$\langle [T] \rangle = \sum_{i=1}^{3} \lambda_{e,i} \cdot \vec{u}_i \cdot \vec{u}_i^{+}, \tag{2.34}$$

with $^{+}$ denoting the conjugate transpose operator, and $\lambda_{e,i}$ the eigenvalues. $\vec{u}_i$ are the eigenvectors:

$$\vec{u}_i = \begin{bmatrix} \cos\alpha_i & \sin\alpha_i \cdot \cos\beta_i \cdot e^{j\varphi_{e,i}} & \sin\alpha_i \cdot \cos\beta_i \cdot e^{j\upsilon_{e,i}} \end{bmatrix}^T. \tag{2.35}$$

υ_e and φ_e are phase terms without direct interpretation. Instead, the α angle is related to the scattering mechanism:

- $\alpha \approx 0$: single bounce scattering;
- $\alpha \approx \pi/4$: volume scattering;
- $\alpha \approx \pi/2$: double bounce scattering.

The β angle is the orientation of the target corresponding to the scattering mechanism determined by α. A more advanced analysis of the physical information can be achieved by the calculation of the following parameters:

- Total power:
$$P = \lambda_{e,1} + \lambda_{e,2} + \lambda_{e,3} \tag{2.36}$$
- Eigenvalue probabilities:
$$p_{e,i} = \frac{\lambda_{e,i}}{\sum_{i=1}^{3} \lambda_{e,i}} \tag{2.37}$$
- Entropy:
$$H = -\sum_{i=1}^{3} p_{e,i} \cdot log_3(p_{e,i}) \tag{2.38}$$
- Anisotropy:
$$A = \frac{\lambda_{e,2} - \lambda_{e,3}}{\lambda_{e,2} + \lambda_{e,3}} \tag{2.39}$$
- Mean α angle:
$$\bar{\alpha} = \sum_{i=1}^{3} p_{e,i} \cdot \alpha_i \tag{2.40}$$

The eigenvalues express the significance of the corresponding eigenvector (or scattering mechanism). The composition of scattering mechanisms is analyzed by means of the entropy and the anisotropy. The entropy and anisotropy determine the degree of randomness of the scattering process. From a practical point of view, the anisotropy can only be employed as a source of information when H > 0.7, since for lower entropies the second and third eigenvalues are highly affected by noise.

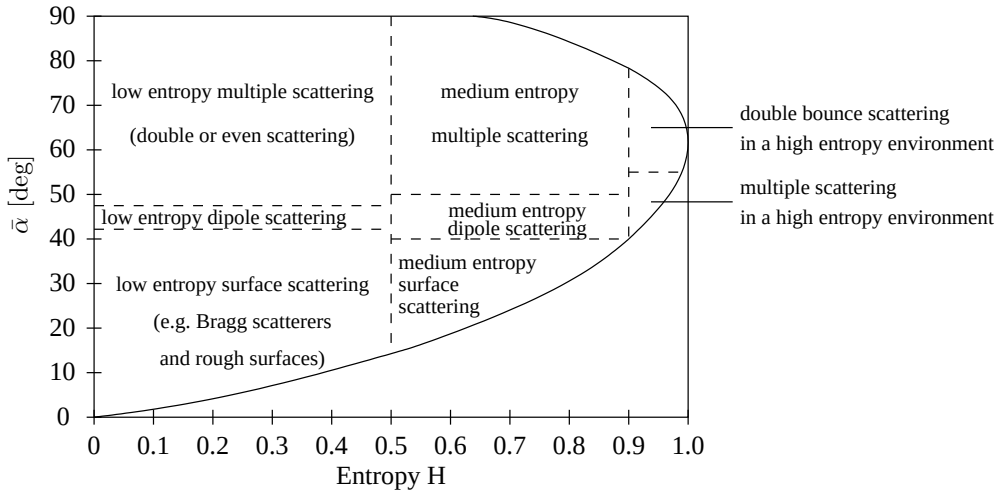

Figure 2.10: The H/α plane and the clustering zones (adopted from [29]).

Considering H, A, and $\bar{\alpha}$, an unsupervised classification scheme (see Figure 2.10) is defined, which is based on the projection of the pixels on the H/α plane. The plane is bound by a curve taking into account that for high entropies the scattering mechanisms cannot be classified reliably anymore.

2.6 SAR operation modes

Several sensor operation modes for acquiring SAR data were developed in the past. The most common modes which are implemented in spaceborne SAR missions are StripMap (SM), SpotLight (SL), and ScanSAR (SC).

The SM mode (see Figure 2.11a), which is in fact the mode presented in detail in Section 2.3, is a standard mode in SAR. The radar antenna has a fixed viewing angle with respect to the platform flight path. The antenna records, while the platform is moving along the azimuth direction, the return from the footprint, which covers a theoretically unlimited strip on the ground.

The SL mode (see Figure 2.11b) aims at improving the azimuth resolution. The radar antenna steers the beam direction to illuminate the required scene for a longer period compared to the standard SM mode. A larger synthetic aperture is created by dedicated processing, resulting in a better azimuth resolution. Due to the antenna steering, the use of the SL mode decreases the ground coverage of the acquisition. The hybrid SM/SL mode offers a compromise between better azimuth resolution than in SM mode, and increased ground coverage with respect to the SL mode [30].

The SC mode (see Figure 2.11c) provides a larger swath. The larger coverage is obtained by scanning several adjacent sub-swaths with quasi-simultaneous beams, each with a different incidence angle. This results in a worse azimuth resolution compared to the SM mode because the same azimuth bandwidth is used for the sub-swaths. Note that the SC mode is not of interest for VHR SAR.

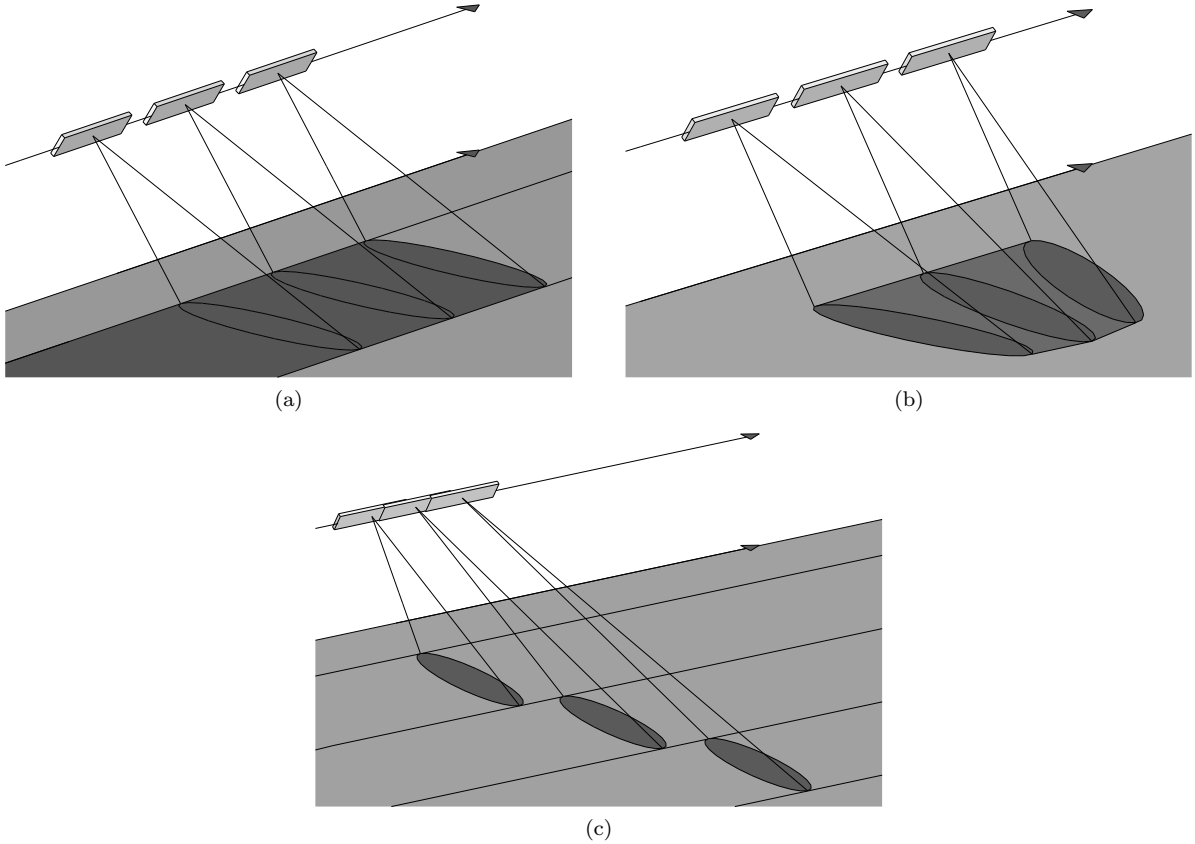

Figure 2.11: SAR operation modes. (a) StripMap mode. (b) SpotLight mode. (c) ScanSAR mode.

2.7 VHR SAR sensors

Until recently, SAR images with resolutions in the order of 1 m could only be obtained by airborne sensors. The first spaceborne VHR SAR sensors became available with the launch of the German TerraSAR-X satellite (Figure 2.12a) and the Italian COSMO-SkyMed constellation (Figure 2.12b). TerraSAR-X is fully operational and will be complemented by the TanDEM-X mission [31], which supports the acquisition of single pass InSAR data to produce a global Digital Elevation Model (DEM) according to the HRTI-3 specification [32]. Instead, the COSMO-SkyMed program consists in a constellation of four satellites whereas three were launched successfully so far.

The TerraSAR-X satellite is equipped with a high resolution polarimetric SAR that operates in X-band (9.65 GHz) [33]. It acquires data with single or dual polarization in four acquisition modes: High-resolution SpotLight (HS), SL, SM and SC. Furthermore, it can acquire fully polarimetric data using an experimental high resolution mode. An overview of the main acquisition parameters of TerraSAR-X is given in Table 2.2.

Similar to TerraSAR-X, the COSMO-SkyMed satellite constellation is equipped with X-band sensors which support the SL, SM and SC modes [34]. Another fine SL acquisition mode is dedicated to defense applications. It supports the HH, HV, VH and VV polarization in single and dual polarization modes (the latter only in a special SM mode).

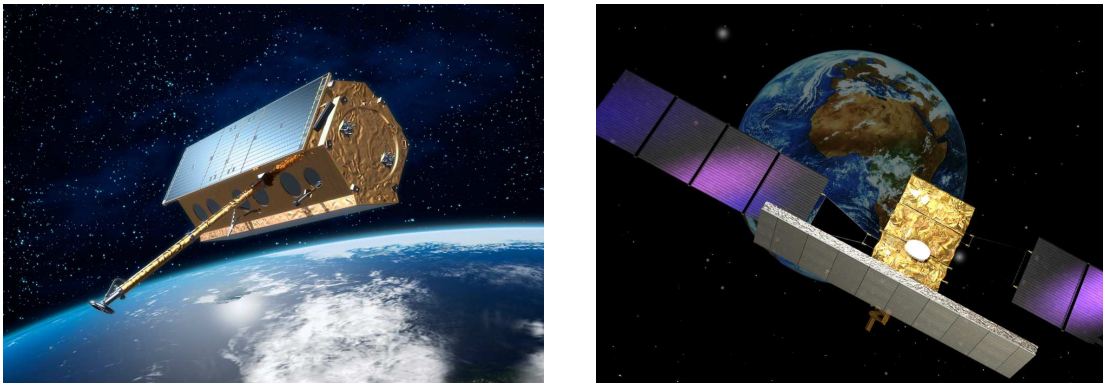

(a) (b)

Figure 2.12: VHR SAR satellites. (a) TerraSAR-X. (b) COSMO-SkyMed. (TerraSAR-X image: © German Aerospace Center (DLR), 2009; COSMO-SkyMed image: © Telespazio, 2009.)

Since COSMO-SkyMed will consist of four satellites it will provide images from the same region with a worst case response time of three days and a short worst case revisit time of 12 hours. The main characteristics of COSMO-SkyMed are summarized in Table 2.3.

Table 2.2: Main acquisition characteristics of TerraSAR-X.

Parameter	HS	SL	SM	SC
Coverage (azimuth x ground range)	5 km x 10 km	10 km x 10 km	$<$ 1500 km x 30 km	$<$ 1500 km x 100 km
θ	20° - 55°	20° - 55°	20° - 45°	20° - 45°
δ_a	1 m	2 m	3 m	16 m
δ_{gr}	1.5 m - 3.5 m	1.5 m - 3.5 m	1.7 m - 3.5 m	1.7 m - 3.5 m

Table 2.3: Main acquisition characteristics of COSMO-SkyMed.

Parameter	SL	SM	SC
Coverage (azimuth x ground range)	10 km x 10 km	30 km - 40 km x 30 km - 40 km	100 km - 200 km x 100 km - 200 km
θ	25° - 50°	25° - 50°	25° - 50°
δ_a	1 m	3 m - 5 m	30 m - 100 m
δ_{gr}	1 m	3 m - 5 m	30 m - 100 m

Chapter 3

Properties of buildings in VHR SAR imagery

In this chapter, we review the fundamentals of microwave backscattering of buildings, which form the basis for the methods and analyzes presented in this thesis. In Section 3.1, we describe the theoretic appearance of flat and gable roof rectangular buildings under a variety of viewing configurations. Then, in Section 3.2, we show some examples in actual SAR data, based on which we discuss common effects often limiting the performance of automatic building detection and reconstruction methods.

3.1 Theoretic properties of buildings

In SAR imagery, typical urban structures are affected by layover, double bounce and shadowing effects, which relate to the ranging geometry of radar sensors. To highlight these effects, Figure 3.1 shows examples of the backscattering range profiles of a simple flat roof building model, which is a rectangular box with uniformed surfaces and flat surroundings, with a common width w, and different heights h viewed by a SAR sensor with incidence angle θ: a shows the return from the ground, b highlights the double bounce caused by the dihedral corner reflector that arises from the intersection of the building vertical wall and the surrounding ground, c indicates single backscattering from the front wall, while d depicts the returns from the building roof, and e represents the shadow area from which there is no return from the building or the ground. The symbols l_l [$l_l = h \cdot cot(\theta)$] and l_s [$l_s = h \cdot tan(\theta)$] denote the lengths of the areas affected by layover and shadow in the ground projected image space, respectively. For the backscattering of flat roof buildings, three different situations can be observed according to the boundary condition $h < w \cdot tan(\theta)$ [35], [36]. If this condition is fulfilled (Figure 3.1a), part of the roof scattering d is superimposed on the scattering from the ground a and the front wall c in the region a+c+d, while there is a region d which is only characterized by returns from the roof. In the case of $h = w \cdot tan(\theta)$ (Figure 3.1b), the entire roof contribution d is sensed before the double bounce area in such a way that there is a homogeneous layover area a+c+d, which has contributions from the ground, the building front wall and the roof. If $h > w \cdot tan(\theta)$ (Figure 3.1c), all roof contributions are sensed before the double

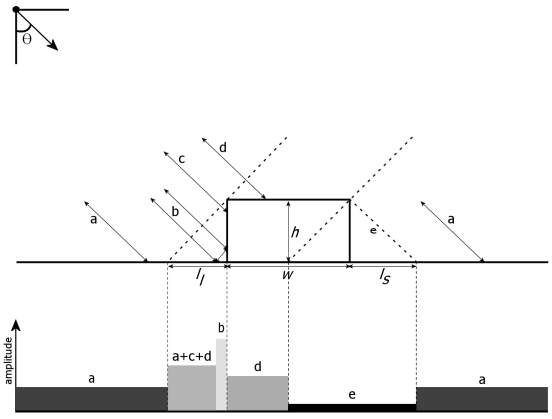

(a)

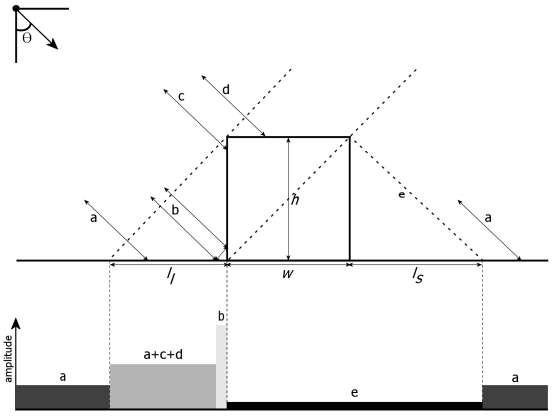

(b)

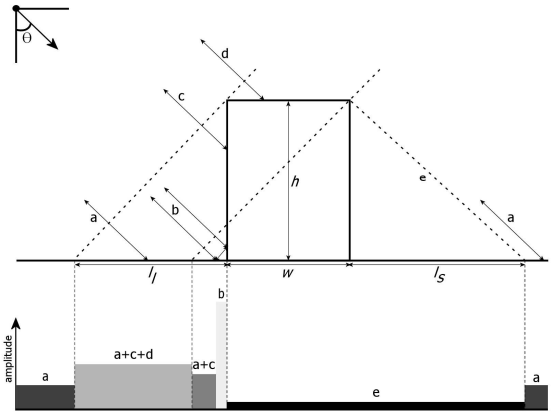

(c)

Figure 3.1: Scattering from a simple flat roof building model with width w and different heights h: ground scattering a; double bounce b; scattering from vertical wall c; backscattering from roof d; shadow area e; length of layover area in ground projected image space l_l; length of shadow area in ground projected image space l_s. The gray values in the backscattering profiles correspond to the relative amplitudes. (a) $h < w \cdot tan(\theta)$. (b) $h = w \cdot tan(\theta)$. (c) $h > w \cdot tan(\theta)$.

bounce area again, with the difference that the layover area is split in an area *a+c+d*, which has contributions from the ground, the front wall and the roof, and an area *a+c*, which only has backscatter from the ground and the front wall of the building.

An interferogram is a phase difference image, which is calculated from the phases of two complex images acquired from the same region with the same flight path orientation, but which were separated by a baseline, so that their respective viewing configurations are slightly different. Taking into account the geometry of SAR interferometry, the height of individual objects can be calculated from the interferogram. However, if $h \geq w \cdot tan(\theta)$ (Figure 3.1b and Figure 3.1c), the calculation of a meaningful Digital Surface Model (DSM) fails due to the signal mixture from different altitudes (ground and roof), which is also known as the "front porch" effect [37]. To tackle this problem, [38] proposes two models, one for interferometric and one for polarimetric data.

The scattering effects of a gable roof building are different from what is observed for a flat roof building [35], [39]. Figure 3.2 shows three examples of backscattering profiles from a gable roof building with roof inclination angle α_r for different incidence angles. The major difference with respect to flat roof buildings is the presence of a second bright scattering feature, which is closer to the sensor than the double bounce, resulting from direct backscattering *d1* from the part of the roof which is oriented towards the sensor. For incidence angles which are not equal to the inclination angle of the roof (Figure 3.2a and Figure 3.2c), this feature is extended to an area, while in case of $\theta = \alpha_r$ (Figure 3.2b) these contributions return to the sensor at the same instance of time and are therefore integrated into a bright line similar to the double bounce of a building. In case that $\theta > \alpha_r$ there is no backscattering *d2* from the part of the roof which faces away from the sensor, since this part is occluded by the front side of the building.

The viewing configuration of a sensor with respect to the building is not only defined by the incidence angle of the sensor, but also by the orientation of the building with reference to the azimuth direction, known as aspect angle ϕ. This is the angle between the sensor facing wall and the azimuth direction of the sensor (see Figure 3.3). If the front wall of the building is parallel to the azimuth direction then $\phi = 0°$. The width w and length l of a building are the dimensions of the short side and long side of the building, respectively. For spaceborne acquisitions, the possible aspect angles of a building are fixed by ascending and descending passes, while for airborne measurements the aspect angle is defined by the flight track of the airplane and the squint angle of the antenna. Therefore, airborne acquisitions permit more flexibility for varying ϕ than spaceborne measurements, which can be an advantage for missions where buildings need to be investigated from a predefined viewing configuration.

As highlighted in Figure 3.1 and Figure 3.2, the double bounce effect is a significant characteristic of buildings in VHR SAR signals [40]. It indicates the presence of a building and appears in correspondence with its front wall. It can be used as a feature for the automatic detection and reconstruction of buildings from SAR data [41], [42]. However, the strength of the double bounce effect depends on both, the height of the building (i.e. the higher the building the stronger the double bounce) and the aspect angle. Theoretical models for the double bounce of a building show a quadratic dependence of its RCS on the building height [40], [43].

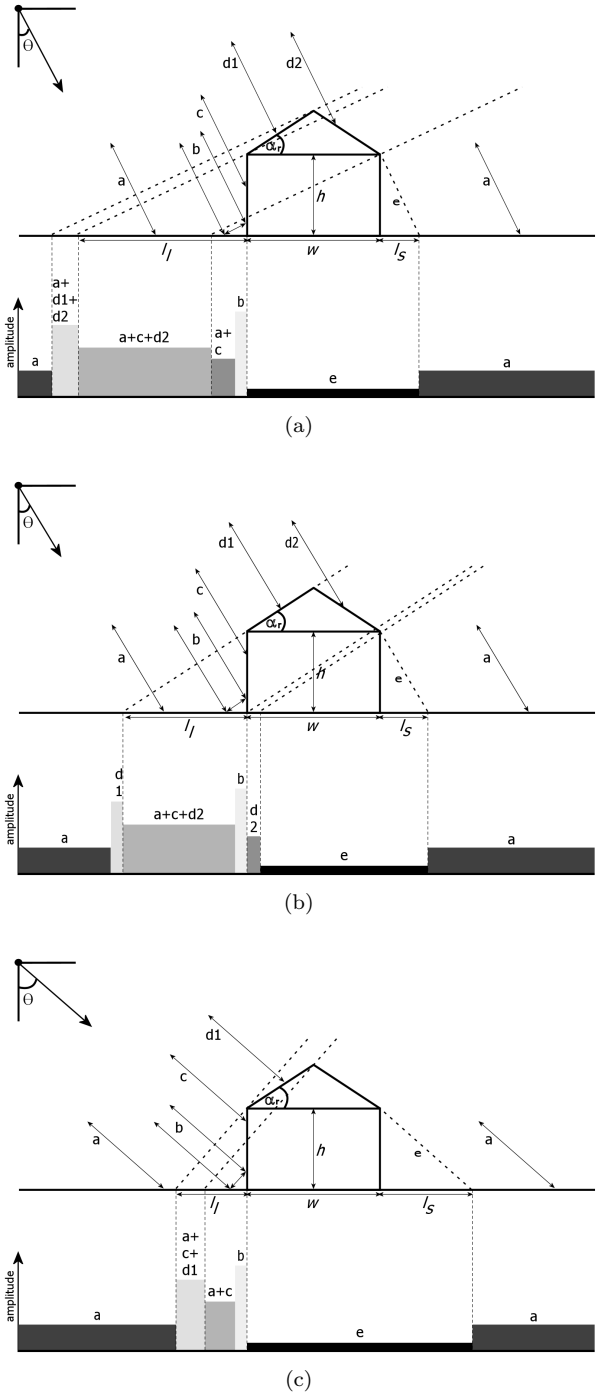

Figure 3.2: Examples of backscattering profiles from a gable roof building with roof inclination angle α_r at various incidence angles. The legend is similar to the one for flat roof buildings in Figure 3.1. *d1* denotes the scattering from the side of the roof which is oriented towards the sensor, while *d2* represents the scattering from the part of the roof which faces away from the sensor. The gray values in the backscattering profiles correspond to the relative amplitudes. (a) $\theta < \alpha_r$. (b) $\theta = \alpha_r$. (c) $\theta > \alpha_r$.

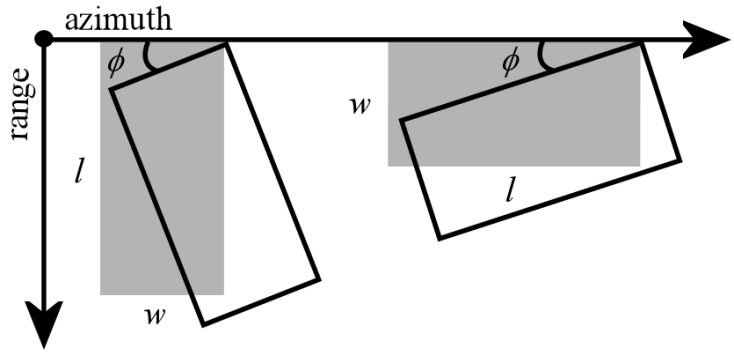

Figure 3.3: Definition of width w, length l, and aspect angle ϕ of a building. The buildings in gray are oriented parallel to the azimuth direction with $\phi = 0°$, while the buildings with the solid black lines were rotated by ϕ with respect to the azimuth direction.

The aspect angle mainly influences the appearance of the layover and shadow areas. In Figure 3.4, we present the results of simulations (for more details on the simulator see Chapter 5) of a flat roof building model with dimensions 50 m × 100 m × 30 m (width × length × height) at $\phi = 0°$ (Figure 3.4a), $\phi = 22.5°$ (Figure 3.4b), and $\phi = 45°$ (Figure 3.4c), which reflects the situation depicted in the right part of Figure 3.3. From this point on dimensions will always be presented in the format "width × length × height". The simulations were performed with $\theta = 50°$ and 1.0 m azimuth and slant range resolution corresponding to a configuration supported by current spaceborne sensors like TerraSAR-X or COSMO-SkyMed. The images on the left side show the simulation results with viewing direction from the bottom, while the images in the right column display the corresponding 3-D views of the building, as it would appear visually. Since we want to highlight the major scattering effects of buildings in SAR, we suppressed the calculation of speckle. In the situation of $\phi = 0°$, the shadow and layover areas have a rectangular shape, which changes with increasing aspect angle to L-shape. The area at which there is only backscattering from the roof also has a rectangular shape at $\phi = 0°$, but it changes for $\phi > 0°$ to a parallelogram. Note that in these simulations the relative strength of the double bounce may be overestimated for the cases of larger aspect angles ($\phi = 22.5°$, and $\phi = 45.0°$) (see Chapter 4).

3.2 Properties of buildings in actual VHR SAR imagery

In Figure 3.5a we show a flat roof industrial building, which is approximately 11.8 m high[1], in the panchromatic channel of QuickBird imagery. The corresponding subset in meter resolution TerraSAR-X imagery is shown in Figure 3.5b, with viewing direction from the left. The building was measured with incidence angle $\theta = 49.1°$, and aspect angle $\phi = 8.2°$. The shadow area is visible as the large dark almost rectangular area in the middle of the scene. The SAR signature shows two bright stripes, and some other

[1]The height was estimated from the length of the shadow in the optical image.

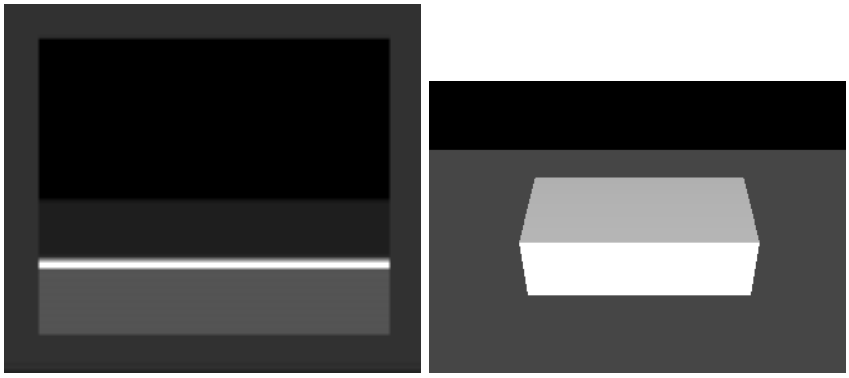

(a)

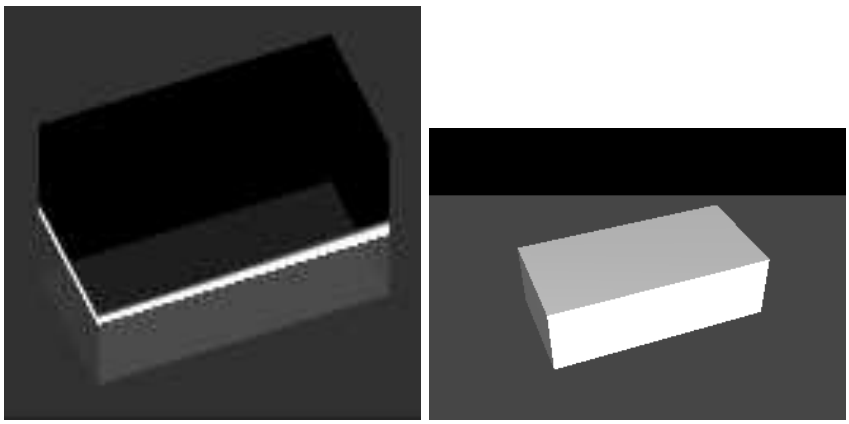

(b)

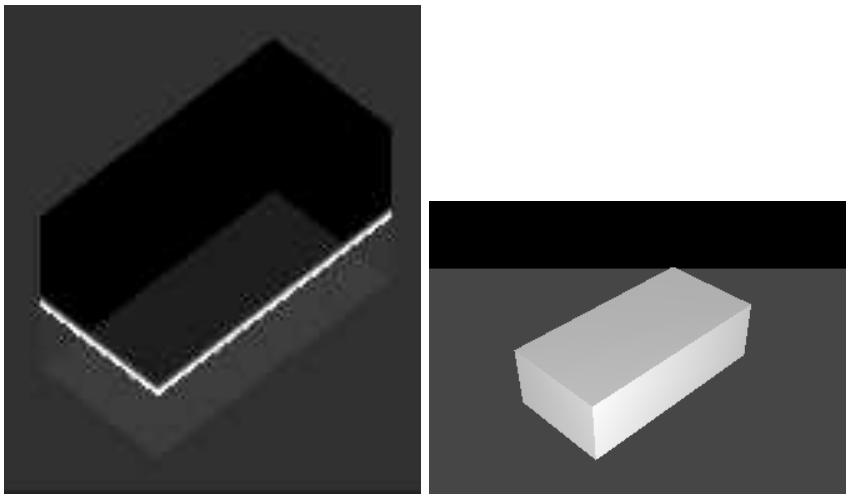

(c)

Figure 3.4: Simulations (without speckle) of a flat roof building model (corresponding to Figure 3.1a) with dimensions 50 m × 100 m × 30 m (width × length × height) with $\theta = 50°$ and 1.0 m azimuth- and slant range resolution. The images in the left column show the simulations with viewing direction from the bottom, while the images in the right column show the corresponding 3-D models as they would appear visually. (a) $\phi = 0°$. (b) $\phi = 22.5°$. (c) $\phi = 45°$.

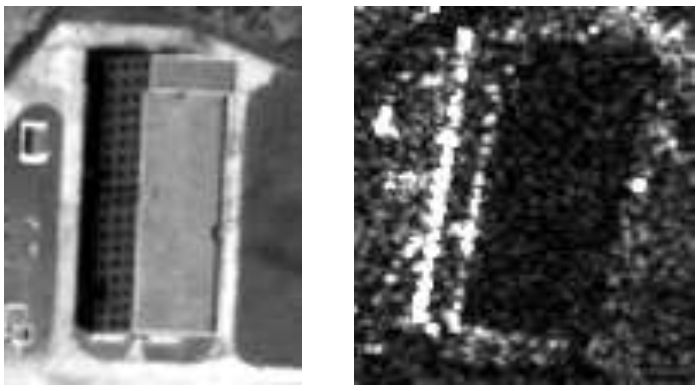

(a) (b)

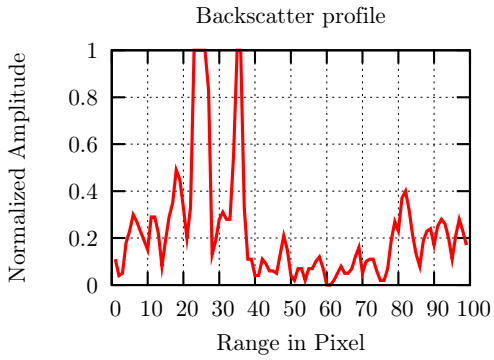

(c)

Figure 3.5: Example of an industrial flat roof building. (a) Building in QuickBird image. (b) Building in slant range TerraSAR-X image with 1 m resolution with viewing direction from the left. (c) Normalized backscatter range profile of row 59 of TerraSAR-X subset. (QuickBird image: © DigitalGlobe distributed by Eurimage S.p.A, 2005; SAR image: © Infoterra GmbH/DLR, 2008.)

random bright spots at the sensor close side (left) of the shadow area. The stronger bright stripe corresponds to the double bounce. Since the aspect angle is small and hence the front wall is almost parallel to the azimuth direction, this scattering effect is pronounced.

The weaker bright stripe corresponds to a smaller corner reflector at the roof, which is visible at the right side of the top of the building in Figure 3.5a. Buildings usually do not have a very smooth front wall with one homogeneous material. For instance, the walls have window frames with small corner reflectors, the windows have a material different to the walls, the walls have metal rain drains attached to it, which are the reasons for the random bright scattering spots. In Figure 3.5c we show the normalized backscatter range profile of row 59 of the TerraSAR-X subset. The two bright peaks are very distinct, as well as the shadow area in the pixel range [40,75]. Due to the speckle, no distinct roof scattering or layover area is visible.

In many cases, the shadow regions of buildings in urban areas are superimposed by the scattering of other objects, such as trees and neighboring buildings, which are located in its immediate surrounding, influencing the actual shape and size of the shadow area. In Figure 3.6 we show for instance a flat roof apartment building, which has some trees in the immediate surrounding. The meter resolution TerraSAR-X subset shown in Figure 3.6b

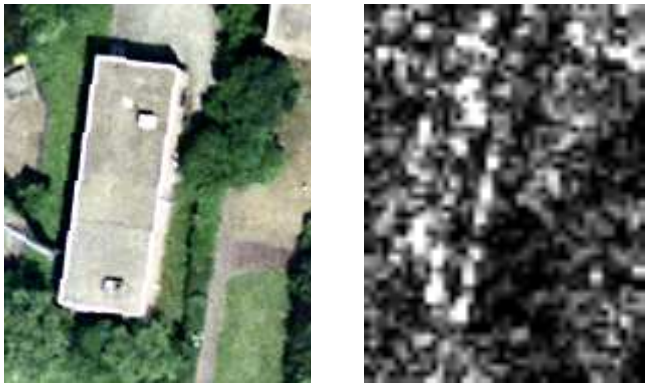

(a) (b)

Figure 3.6: Example of a flat roof building which has trees in its immediate surrounding. (a) Building in orthophoto. (b) Building in slant range TerraSAR-X image with 1 m resolution with viewing direction from the left. Half of the potential shadow area of the building is affected by trees, which are as high as the building itself. (Orthophoto: © Landesvermessungsamt NRW, Bonn, 2007; SAR image: © Infoterra GmbH/DLR, 2008.)

was imaged with $\phi = 7.0°$ and $\theta = 50.7°$ from the left side. The trees in the top right quadrant of the orthophoto in Figure 3.6a are located from the sensor point of view behind the building and therefore in its potential shadow area. Since their height is similar to the height of the building itself, they are not excluded from the radar beam and cause backscattering, diminishing the shadow area of the building to about half of its theoretic full size. Instead, trees in front of the building occlude (part of) the corner reflector of the building and hence lead to an (partial) absence of the double bounce.

In summary, we have seen that the appearance of buildings in SAR depends on many different parameters. First, the characteristics of the object itself (e.g. materials of the walls, shape of footprint, dimensions of building, roof structure, objects attached to the walls) influence the backscattering. Furthermore, the viewing configuration (incidence and aspect angle) with which the building was sensed has a significant impact. Finally, due to the ranging geometry of SAR sensors, also the scattering of objects in the immediate surrounding can interfere with the backscattering of the building. This large variety of parameters is the main limiting factor for the performance of existing building information extraction algorithms and challenges the development of novel robust methods.

Chapter 4

Analysis of the properties of the double bounce scattering mechanism of buildings

The double bounce effect is a significant characteristic of buildings in VHR SAR signals. It indicates the presence of a building and appears in correspondence with its front wall. Double bounce is already used as feature for the automatic detection and reconstruction of buildings from SAR data. In order to exploit this feature effectively for automatic damage assessment techniques, its stability with respect to changes in the viewing configuration and the material properties need to be understood in detail. Thus, this chapter[1] addresses the empirical analysis of the relation between the double bounce effect and the aspect angle of a building for different ground materials. The study is carried out in two phases: 1) development of a laboratory experimental setup on a scaled building model under well-controlled conditions with a variety of viewing configurations; 2) validation and refinement of the results obtained from the laboratory measurements by analyzing a set of industrial and residential buildings with two different ground materials (grass and asphalt) in actual VHR spaceborne SAR data.

4.1 Introduction to the analysis of the double bounce mechanism

Among the different scattering contributions present in urban areas, the double bounce effect of buildings is an important scattering characteristic. It can be exploited for the

[1] This chapter appears in:

[44] D. Brunner, G. Lemoine, J. Fortuny, and L. Bruzzone, "Building characterization in VHR SAR data acquired under controlled EMSL conditions," in *Proceedings of IEEE International Geoscience and Remote Sensing Symposium (IGARSS)*, Barcelona, Spain, July 2007, pp. 2694-2697.

[45] D. Brunner, L. Bruzzone, A. Ferro, J. Fortuny, and G. Lemoine, "Analysis of the double bounce scattering mechanism of buildings in VHR SAR data," in *Proceedings of SPIE Conference on Image and Signal Processing for Remote Sensing XIV*, vol. 7109, Cardiff, Wales, UK, September 2008, pp. 71090Q-1-71090Q-12.

[46] D. Brunner, L. Bruzzone, A. Ferro, and G. Lemoine, "Analysis of the reliability of the double bounce scattering mechanism for detecting buildings in VHR SAR images," in *Proceedings of IEEE Radar Conference (RadarCon09)*, Pasadena, CA, USA, May 2009.

development of automatic methods for the detection and reconstruction of buildings from VHR SAR data [47], [42]. At first glance, the usage of this feature for the development of an automatic method for the detection of destroyed buildings in damage assessment scenarios seems promising. However, the relation between the double bounce effect and the SAR illumination conditions has not yet been investigated to a sufficient extent in real VHR SAR images. In particular, the effect of the aspect angle of a building on the power signature of the double bounce is important. As buildings are imaged with different aspect angles, its behavior implies the limits of detection techniques which are solely based on the double bounce effect.

In order to model the double bounce effect of a building, the theory of dihedral corner reflectors has been extended to simplified building models, which are generally constituted by rectangular parallelepipeds with smooth walls surrounded by a homogeneous ground surface [40], [43]. These models are considered isolated in the electromagnetic sense, i.e. no interactions with other structures in the scene are taken into account. In particular, [40] presents a fully analytical electromagnetic model for urban environments that also includes a study on the double bounce contribution from buildings based on GO and PO, according to the surface roughness.

The choice of the adequate roughness and dielectric parameters of a surface (and thus of the theoretical model that has to be used) is non-trivial. In the literature typical parameters for different types of soils have been reported [48], [49], [50], [51], [52]. However, RCS measurements made directly on SAR images can differ considerably with theoretical predictions using material parameters reported in literature, e.g. due to the effect of the moisture content or the temperature of the material. Furthermore, surfaces in urban areas are not homogeneous, which is even true within one resolution cell. For instance, a paved street in a city is characterized by manhole covers causing bumps, which affect the effective surface roughness. Moreover, they also have a different material since they are made from metal. Hence, using only the dielectric constant and surface roughness parameters of asphalt to calculate the RCS of a street in urban areas is a significant simplification. In addition, in dense urban environments, scattering effects coming from adjacent objects can interfere and therefore invalidate the assumption of isolated buildings. As a result, the theoretical models currently reported in literature can only be considered as a tool for making preliminary predictions of the scattering behavior of buildings in urban environments imposing the need for empirical studies.

Some empirical studies have been conducted so far. In [53], the preliminary results of an experiment performed by means of an outdoor inverse SAR facility on corner reflector models made of different real world materials are presented. This study indicates that the double bounce effect gives a strong power signature to buildings with walls almost parallel to the SAR azimuth direction, but decays rapidly in a narrow range of aspect angles. Using actual medium resolution SAR data, [54] demonstrated the influence of polarization and incidence angle on the double bounce effect, which showed that the corner reflector has generally a higher return in HH polarization. Instead, VV polarization is more sensitive to variations of the incidence angle, as the neighborhood of the Brewster angles for the surfaces might significantly affect the return signal. The analysis was conducted on buildings parallel or perpendicular to the azimuth direction. In [43] the authors discuss

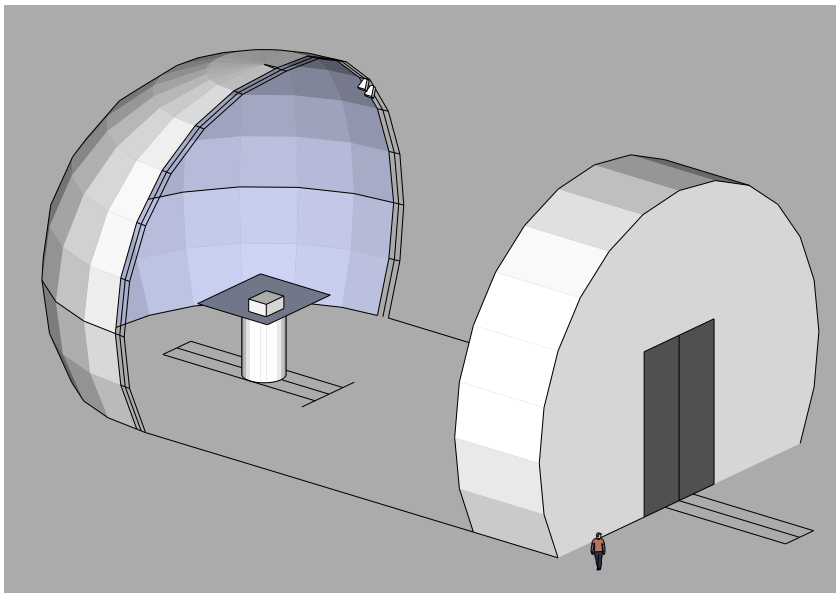

Figure 4.1: 3-D sketch of EMSL.

the influence of both incidence and aspect angle in the scattering from urban environments using actual SAR airborne data. They observed that buildings which are parallel to the azimuth direction have a stronger double bounce contribution than buildings facing away from the radar. Their study was conducted on a small set of residential and commercial buildings. Nonetheless, in real world settings only few buildings can be acquired with 0° aspect angle. For instance in spaceborne acquisitions, the aspect angle of a building is fixed by the combination of descending and ascending passes.

In this chapter, we present a detailed experimental study on the behavior of the double bounce effect from the building front wall with respect to: 1) the aspect angle of buildings; and 2) their surrounding ground material, using polarimetric and non-polarimetric VHR SAR images under different conditions. Firstly, we perform and analyze scaled building model measurements in the EMSL under varying viewing configurations. Due to the practical limitations of the laboratory facility, simplifying assumptions were necessary for the design of the experiments, which limit the generalization capabilities of the results. Therefore, we validate and refine in the second step the laboratory results by analyzing a set of industrial and residential buildings with two different ground materials (grass and asphalt) in actual VHR spaceborne data.

The remainder of this chapter is organized as follows. Section 4.2 provides a detailed description of the laboratory experimental setup, while Section 4.3 presents the analysis of the obtained data carried out according to different and complementary techniques. Section 4.4 reports the steps and the results of the second phase of this work, i.e. the analysis of actual VHR SAR spaceborne images. Finally, Section 4.5 summarizes the results of the analyzes and draws some conclusions.

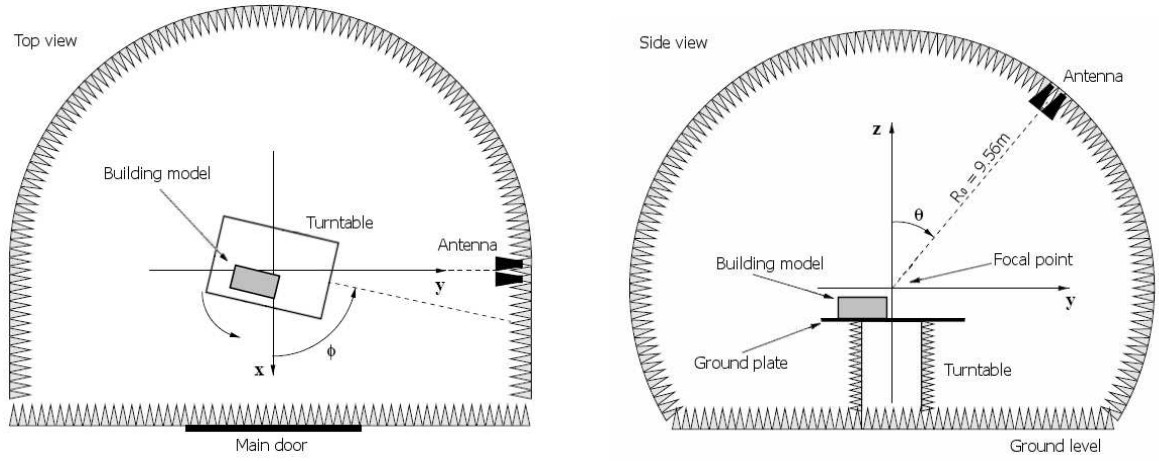

Figure 4.2: Schematic view of the EMSL and measurement setup of the experiment.

4.2 Description of the EMSL experiment

4.2.1 The European Microwave Signature Laboratory

The EMSL of the EC-JRC located in Ispra, Italy, is a fully controlled laboratory facility. It was designed in 1993 to permit a wide range of measurement setups (wide frequency range, possibility to vary viewing configuration, monostatic or bistatic measurements, etc.) and to provide operational modes similar to those used by airborne and spaceborne sensors. Its dimensions allow to study both, small objects and real natural targets, e.g. trees [55].

The EMSL anechoic chamber is formed by the conjunction of a hemispheric and a cylindrical part, both with a diameter of 10 m (see Figure 4.1). Two antennas are mounted on two sleds located between the two parts. They can move independently on a rail in a range between $\pm 115^{\circ}$ around the zenith. Targets are mounted on a carrier that can move on a rail to enter/remove the measurement targets through a 5 m wide door. This target support allows precise linear and rotational (360°) positioning of the target, also during the measurements.

The EMSL supports wideband polarimetric radar measurements in the scatterometric and imaging mode. In the scatterometric mode the resolution is determined by the antenna footprint which is used to characterize the return of the whole target or to obtain independent samples varying the setup parameters, e.g. the aspect angle. In the imaging mode the angular and frequency diversity is exploited to create one-, two- or three-dimensional images of the target scattering properties. The frequencies supported by the laboratory range from 300 MHz to 26.5 GHz, with an overall dynamic range of 100 dB.

4.2.2 Experiment setup

In order to simulate in the EMSL a flat roof normal sized building in real world, a cuboid with dimensions 90 cm $\times$120 cm $\times$ 60 cm was used (scaling factor 1:10). It was a glued

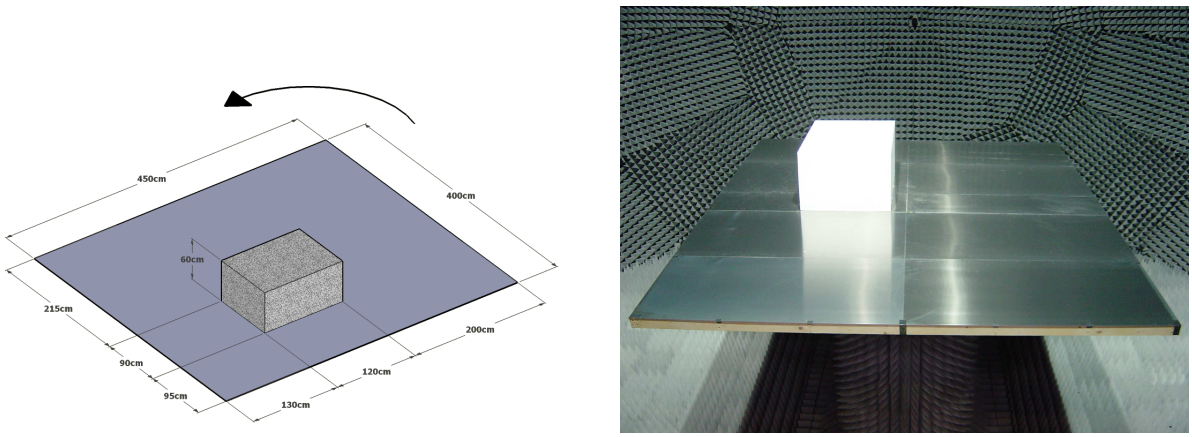

(a) (b)

Figure 4.3: (a) Position of the building model on the ground plane. The arrow indicates the direction of rotation. (b) A photo of the experiment setup (without aluminum foil).

wooden frame with 2.6 cm thick gypsum plates attached to it. Some problems occurred due to the inside-model multiple reflections and the low roughness of the building walls and ground plate. This induced to cover the plate and the model with aluminum foil, which was crumpled and flattened again in order to simulate random surface roughness (authentic ground materials could not be used due to the weight limitations of the carrier). The frequency used to illuminate the building model was 10 GHz, with a bandwidth of 1 GHz. Note that, due to the scaling factor 1:10, a frequency of 100 GHz should be used for the simulation of X-band measurements. However, this is not supported by the EMSL facility and represents a limitation that we took into account during the analysis.

As shown in Figure 4.2, the plate was mounted on the target support which was situated 70 cm below the focal point of the chamber. The model was positioned decentralized on the plate so that the layover and shadow areas matched the ground plate for all the considered aspect angles (see Figure 4.3). The building model was measured at three polarizations (HH, HV and VV) with 30° incidence angle. The plate was sensed from 0° to 90° aspect angle in 0.1° steps. Then, the final images were obtained by processing 100 consecutive aspect measurements in an integration window of 10° centered on 1° aspect angle steps. For the processing, we used a 3-D time-domain back propagation SAR processor, which was specifically developed by the JRC for the EMSL [56]. This resulted in a series of 90 synthesized SAR images for each polarization, which have 17.2 cm azimuth and 30 cm range resolution, respectively. Without the processing step the azimuth resolution would not be useful for the aim of this study. The main drawback of the processing could be the inclusion of scattering effects that may vary over the angular range covered by the measurements.

Figure 4.4 shows two examples for typical power images. Only HH and VV polarizations are considered, as the HV measurements were always at the background noise level. This is an expected behavior as the main scattering mechanisms are single and double bounce surface scattering. The position of the building model and the ground plate are highlighted by the inner and outer rectangles, respectively. 0° aspect angle means that the

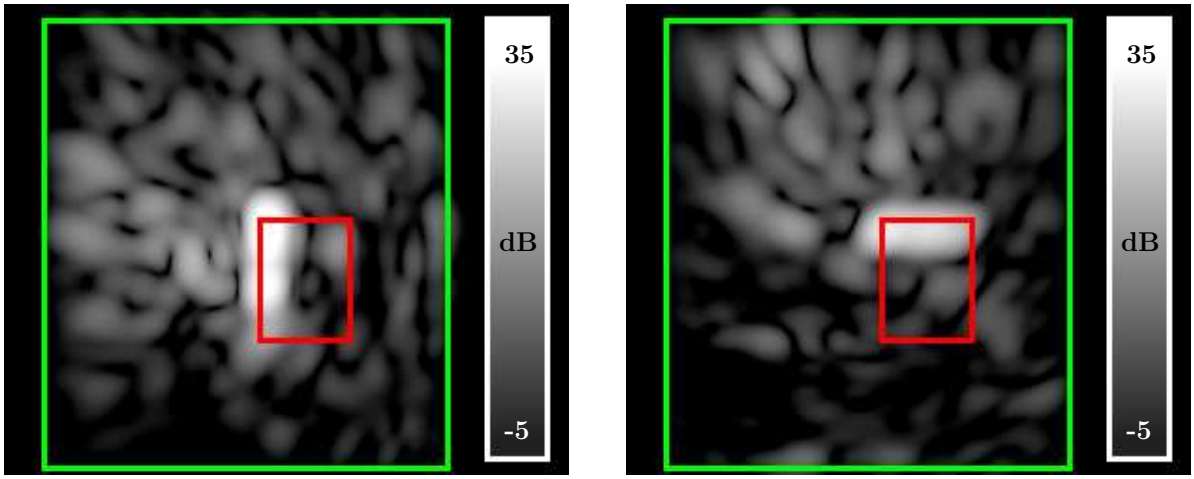

(a) (b)

Figure 4.4: Examples of dB-power images. Power values are between -5 dB (black) and 35 dB (white). The big frame indicates the ground plate area, while the small one identifies the model position. (a) 0° aspect angle - HH polarized. (b) 80° aspect angle VV-polarized.

longer building wall was parallel to the azimuth direction. In this case, the illumination was from left to right. On the contrary, 90° aspect angle means that the shorter building wall was oriented to the sensor, which means that the illumination was from the top. The scale is between -5 dB (black) and 35 dB (white).

4.3 Analysis of scaled building model measurements

In this section we investigate the relation between the double bounce effect and the aspect angle of the building model using the EMSL data in the power domain, the CCC, as well as the Pauli- and H/A/$\bar{\alpha}$ decompositions. Meaningful results were already achieved by analyzing the first half of the measurements so that we report here only the results between 0° and 45° aspect angle.

4.3.1 Power domain

The HH and VV power images generally show that the return from the ground plate is stronger in VV than in HH. This can be explained by the small perturbation model [22, pp. 922-1033], which leads to the higher VV backscattering for $\theta \leq 30°$, as the random surface roughness is expected to fulfill its conditions [22, pp. 962-966]. Focusing on the double bounce area, the images do not present a clear and uniform strong stripe along the complete wall of the model, but a main scattering point close to the corner of the model and several local power peaks. We expect that the non-uniform scattering stripe of the model wall were due to a specific scattering pattern related to the geometry and the physical characteristics of the model itself [57]. This "antenna behavior", which can be shown to be dependent on the illumination conditions, seems to become relevant in this scenario. The enhanced return from the model corner seems to be related to

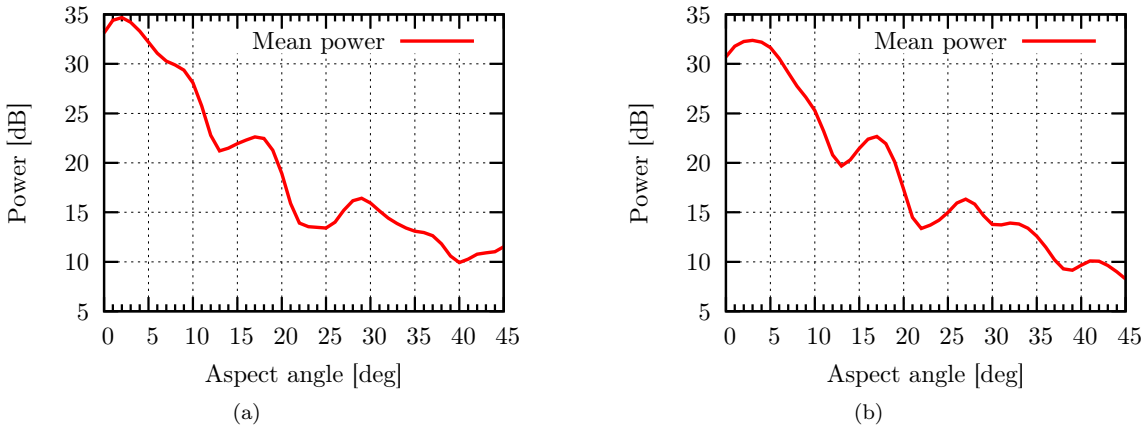

Figure 4.5: Mean power of the expected double bounce area. (a) HH. (b) VV.

diffraction effects that become relevant due to the absence of the correct scaling factor of the wavelength. This causes that the model dimensions are not very large with respect to the wavelength so that the diffraction effects are not negligible anymore [40].

In Figure 4.5 we plot the mean power of the expected double bounce stripe area as a function of the aspect angle for the HH (Figure 4.5a) and VV polarizations (Figure 4.5b). For low aspect angles, the mean power in the double bounce area drops consistently, with a significant difference of approximately 13 dB between 0° and 13° aspect angle. For larger aspect angles, the overall decreasing trend becomes shallower, while some local intermediate maxima occur giving the curve an oscillating behavior. In total the mean power drops by 24 dB from around 32 dB at 0° degree aspect angle to 8 dB at 45° aspect angle (VV channel).

4.3.2 Co-polarized correlation coefficient

The CCC modulus images were mainly characterized by values near 1. This means that the scattering mechanisms involved in the measurements were well defined and the degree of depolarization was low. The double bounce effect presents an average power value consistently higher than the remaining returns. By considering only pixels above a defined power threshold value, a “pure” double bounce scattering mechanism can be isolated and spurious effects coming from the plate are removed. Figure 4.6a shows the resulting CCC absolute phase image for the 10° aspect angle case. As expected, there is an area that is in correspondence with the building wall which shows high values (near 180°), meaning that this region is indeed characterized by double bounce scattering mechanisms. A statistical analysis of the CCC phase defined the CCC phase range, for which double bounce can be considered as the major scattering mechanism in the resolution cell, to be between 120° - 180°. The relationship between the number of pixels, whose major scattering mechanism is double bounce, and the aspect angle of the building model was derived by counting the pixels belonging to the double bounce phase range in the expected double bounce area (Figure 4.6b). This showed that there is a relation between the number of double bounce pixels and the mean power of the double bounce stripe itself. In fact, the curve derived

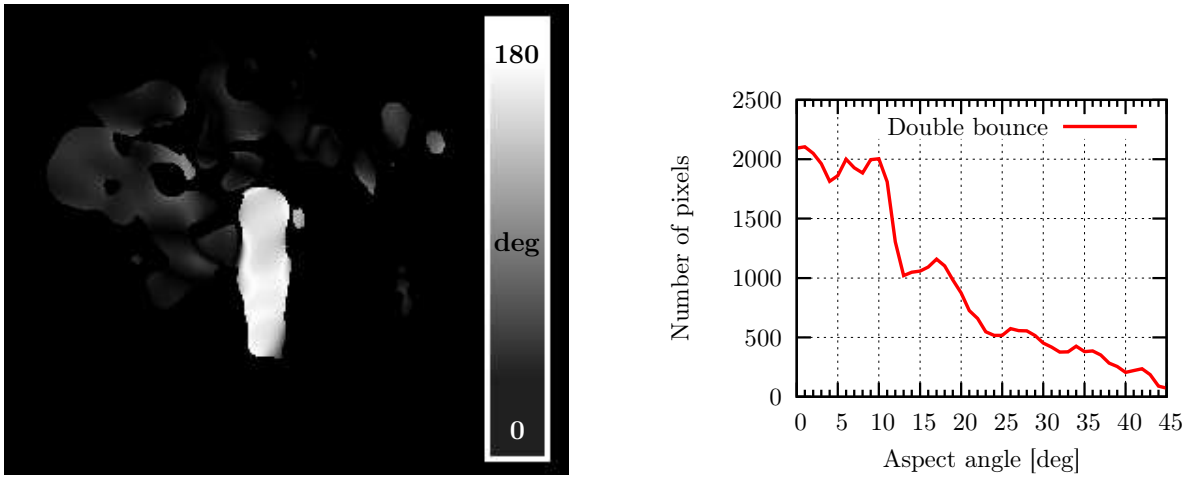

(a) (b)

Figure 4.6: (a) CCC absolute phase image for 10° aspect angle (9 dB power threshold; black=0, white=180°). (b) Double bounce pixels vs. aspect angle (9 dB power threshold).

from this analysis has a behavior that resembles the mean power graphs of Figure 4.5, with a significant drop in the low aspect angle range and a shallower decaying behavior for larger aspect angles.

4.3.3 Pauli decomposition

In order to obtain a power characterization of the double bounce effect, the Pauli decomposition was applied to the data. In Figure 4.7a and Figure 4.7b an example of the Pauli decomposition is presented. We considered only the α_p- (single bounce) and β_p-channels (double bounce) as the volume component of the decomposition was always at the background noise level due to the characteristics of the cross-polarized channels. In the α_p-channel the return from the ground plate, the layover area, and the remaining roof scattering are better distinguishable than in the β_p-channel. The latter is dominated by a double bounce stripe, which is in correspondence with the building wall. In Figure 4.7c the mean power values within the expected double bounce area in the β_p-channel are drawn as a function of the aspect angle. This plot resembles the general behavior of the one presented in Figure 4.6b, given that they were obtained measuring different parameters (mean power and number of double bounce pixels). Furthermore, Figure 4.7c confirms that the mean power values of the double bounce areas of Figure 4.5 result from the double bounce effect, and are not due to single bounce backscattering contributions or other spurious effects.

4.3.4 H/A/$\bar{\alpha}$ decomposition

After the analysis of the results of the coherent Pauli decomposition, we applied the incoherent H/A/$\bar{\alpha}$ decomposition to the EMSL data set to achieve an unsupervised classification of single and double bounce pixels. In particular, we studied the entropy and

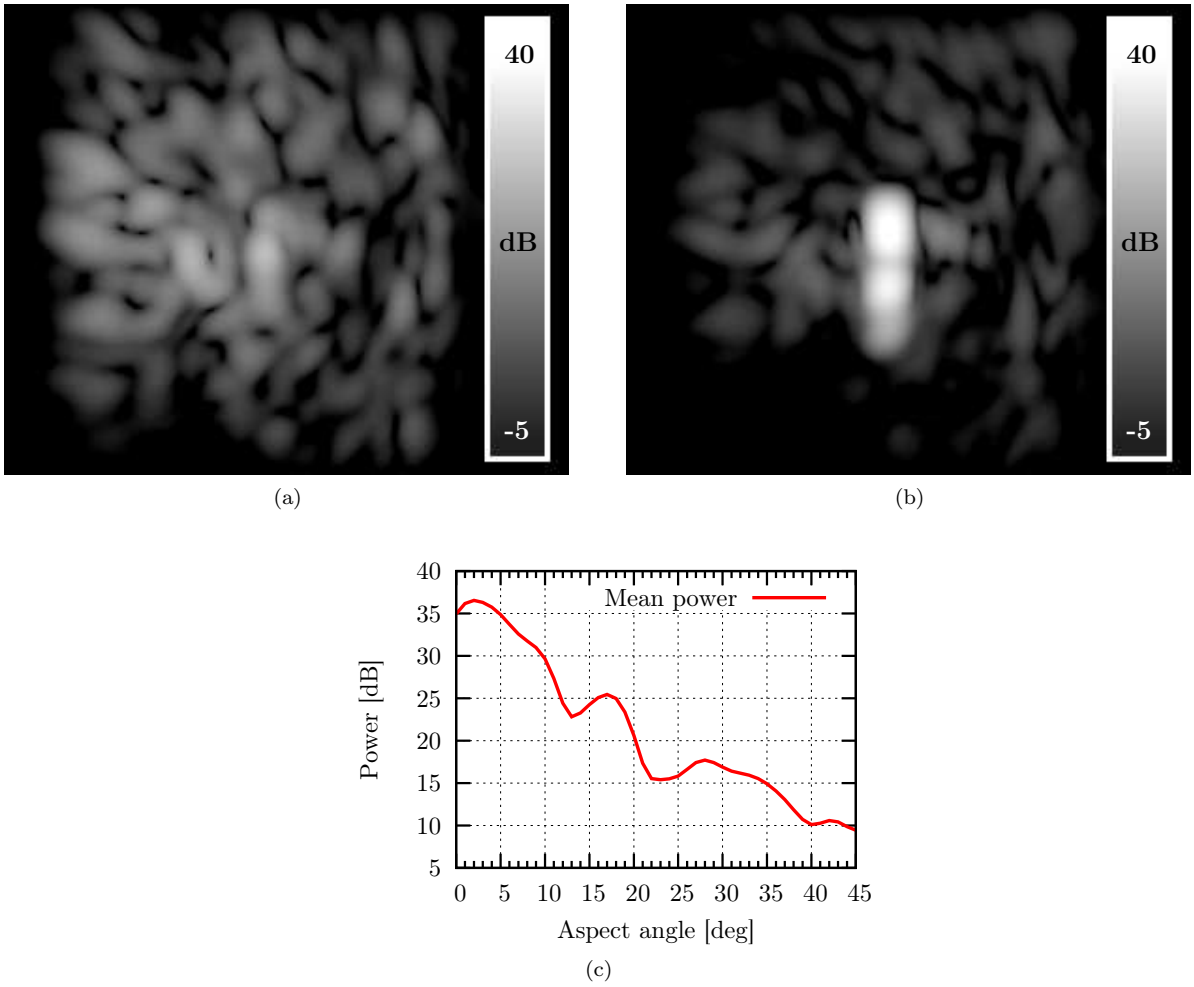

Figure 4.7: Example of the Pauli decomposition for the 0° aspect angle; (a) α_p-channel; (b) β_p-channel; (black=-5 dB, white=40 dB). (c) Mean double bounce power (for the expected double bounce area) vs. aspect angle.

the $\bar{\alpha}$ angle parameter, which show a relationship with the CCC modulus and phase. The higher the entropy is, the lower the CCC modulus and vice versa. On the contrary, the higher the $\bar{\alpha}$ angle is, the higher the CCC phase, given that the range of $\bar{\alpha}$ is exactly half of the CCC phase range. The H/$\bar{\alpha}$ planes were derived either for the whole image or limited to the pixels inside the double bounce region.

Figure 4.8a and Figure 4.8b show the obtained planes for the 0° aspect angle image. The prevailing surface scattering effect of the ground plate (bottom left part of the plane in Figure 4.8a) is evident. In the top-left part of the plane (best visible in Figure 4.8b) there is a double bounce pixel concentration, which corresponds mainly to the pixels located at the building model front wall. Following the classification scheme proposed in [29], we calculated the number of double bounce pixels for each aspect angle within the expected double bounce region, which is shown in Figure 4.8c. The shapes of the graphs are more irregular than in the previous studies. However, the overall trend is similar. It

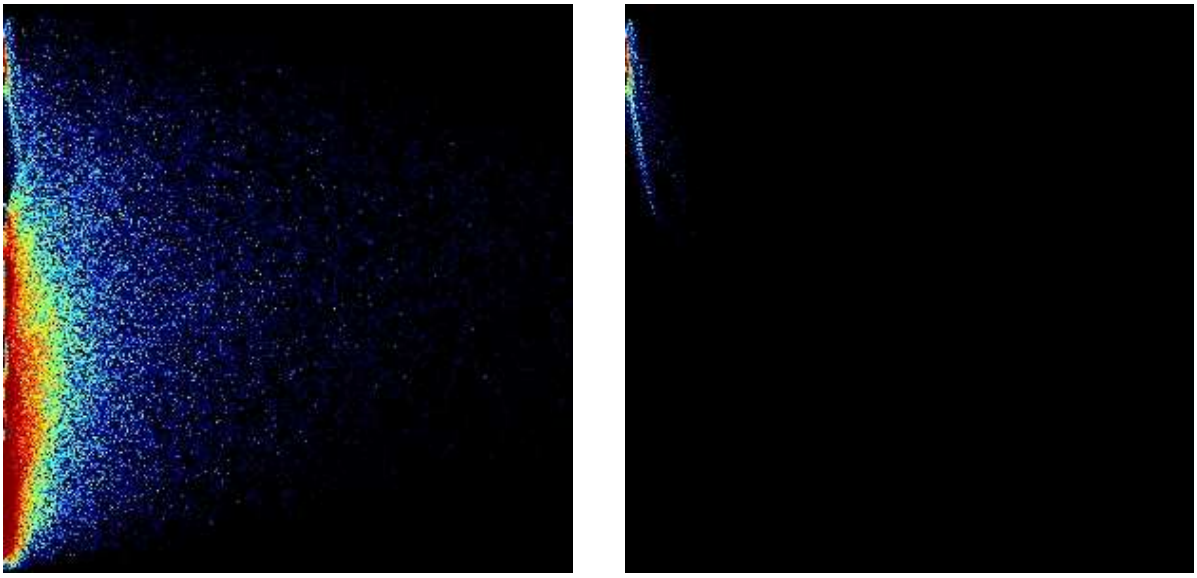

(a) (b)

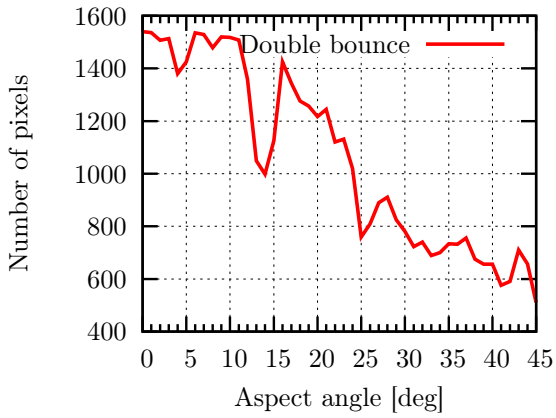

(c)

Figure 4.8: H/$\bar{\alpha}$ planes corresponding to 0° aspect angle image. Abscissa: H (values between 0 and 0.5), ordinate: $\bar{\alpha}$ (values between 0° and 90°). As preprocessing, a -10 dB power threshold was applied to suppress noisy pixels. (a) Decomposition applied to the whole image. (b) Decomposition applied only to the double bounce area. (c) Number of double bounce pixels vs. aspect angle using the H/$\bar{\alpha}$ classification for the double bounce area.

can be noted that this decomposition scheme classifies more pixels as double bounce than the classifier based on the CCC phase criterion adopted for Figure 4.6b. Interestingly, a classification in double bounce pixels using the CCC absolute phase criterion gave approximately the same results as the H/$\bar{\alpha}$ classifier if double bounce is considered for an absolute phase range between 100° and 180°.

4.4 Analysis of actual spaceborne VHR SAR data

To compare the findings from the previous section with actual data, we analyzed the ascending and descending TerraSAR-X pair, which will be described in detail in Section 6.4. As ground truth, we used optical images retrieved from Google Earth™ [58] and Microsoft Virtual Earth™ [59] virtual globe viewers. We also collected additional information regarding the meteorological precipitations and the temperature for the December 2007 and January 2008 in the area considered.

We selected a set of candidate buildings which presented smooth (or almost smooth) walls with asphalt or grass ground surfaces in the surroundings. The smoothness of a wall was verified using the birds eye view from Virtual Earth™, which can display a building from four different sides. We estimated their dimensions from the optical images, so that we predicted their scattering behavior by a geometric approach using 3-D models. These estimations were then confirmed measuring the return of the buildings on the SAR image. The expected scattering behavior of a building permitted to estimate the position of the double bounce stripe, the layover and shadow areas, and the eventual single bounce stripe due to the building roof.

The study set included 55 buildings suitable for a double bounce stripe analysis (e.g. the extraction of the mean RCS value of the expected double bounce area). We grouped them in three categories: residential buildings surrounded by asphalt terrain (*residential/asphalt*), industrial buildings surrounded by asphalt terrain (*industrial/asphalt*) and residential buildings surrounded by grass covered soil (*residential/grass*). The number of samples for each category is summarized in Table 4.1. We considered buildings with different aspect angles in the range between 0° and 42°. For larger aspect angles the double bounce areas of suitable buildings were not well distinguishable from the surroundings so that we did not consider these buildings in the study. Single bounce backscattering from the building roofs presents another difficulty for extracting the double bounce stripes, as in many cases this contribution is superimposed with the double bounce stripe itself. In our observations it occurs mainly when the roof is not facing the SAR sensor, which might be due to the roof tile coverage. The theoretical models presented in literature show a quadratic dependence of double bounce RCS on the building height [40], [43]. Hence, we normalized the measured RCS in order to derive a set of values relative to a fixed reference height (chosen to be 6.5 m, which is the mean height of the buildings in the data set). As the azimuth resolution is smaller than the building length, we did not consider the length in the normalization step [40]. The difference of the incidence angles between the two scenes is about 3°. Based on theoretical models, we confirmed that this variation only implies a marginal change of the RCS of the double bounce, which can be assumed to be less than the error introduced by the analysis process. Hence, we considered the buildings

Table 4.1: Number of building samples per category.

Building type	**Ground material**	
	Asphalt	*Grass*
Residential	17	19
Industrial	19	-

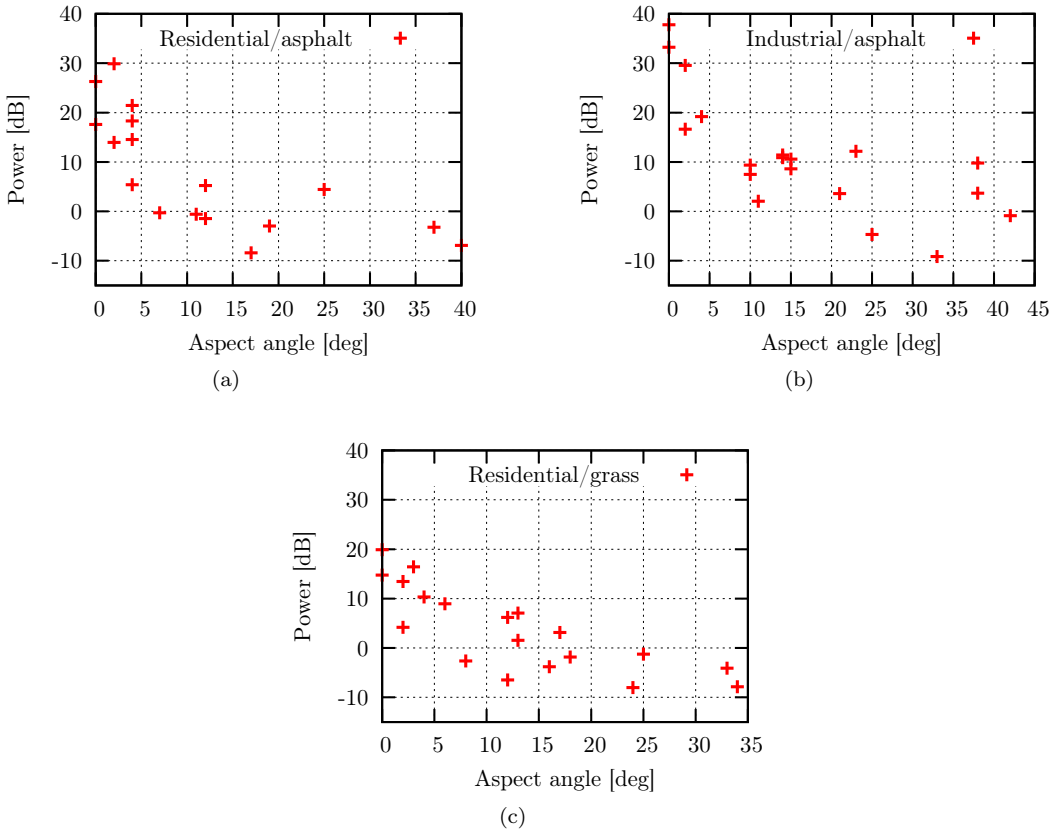

Figure 4.9: Relation between double bounce RCS and aspect angle. (a) *Residential/asphalt* category. (b) *Industrial/asphalt* category. (c) *Residential/grass* category.

in the two scenes as if they were contained in a single scene.

The results of the analysis are displayed in Figure 4.9, which shows the relation between the RCS of the corner reflector and the aspect angle per building set. The graphs show that buildings with similar aspect angles can have double bounce stripes that differ by several dBs. This behavior reflects the fact that in real SAR data many variables affect the scattering behavior of surfaces, which are mainly unknown, such as the soil moisture content or different wall materials. Therefore, our goal was to analyze the overall trend of the double bounce effect for each building category, rather than the double bounce stripe of individual buildings.

Figure 4.9a is related to the *residential/asphalt* case. The graph shows that the double bounce is significant in the first 10° aspect angle range, having values in the order of 30 dBs and then decreasing considerably. This is related to the strong coherent scattering coming from the double bounce. On the other hand, for larger aspect angles the relevance of incoherent scattering due to the surface roughness increases and the trend of the strength of the double bounce becomes shallower. The analysis of the *industrial/asphalt* category is reported in Figure 4.9b. The trend is similar to that for the *residential/asphalt* category, but with generally higher power values. The difference in RCS between these two classes is about 10 dBs. Moreover, the double bounce stripes of the buildings in

the *industrial/asphalt* category present a sparser distribution. These two effects can be explained by the variable and inhomogeneous materials used for industrial buildings, and by the presence of more metal parts that are not as common as for residential buildings. Finally, Figure 4.9c depicts the distribution of the double bounce RCS for the *residential/grass* category. Due to the impact of the roughness of the grass surrounding the buildings (which is expected to be more relevant than for asphalt grounds) the contrast between the double bounce peak at near 0° aspect angles and the remaining part of the graph is lower than for buildings which are surrounded by asphalt. The peak power is about 10 dBs lower compared to the *residential/asphalt* category, while the RCS decreases with increasing aspect angles in a smoother way, suggesting a pronounced relevance of incoherent scattering.

4.5 Discussion and conclusion

In this chapter we presented an empirical study of the double bounce scattering mechanism of buildings in VHR SAR. We focused on the analysis of the strength of the double bounce with respect to the aspect angle. The study first analyzed a series of images acquired under well-controlled conditions on a scaled building model measured in the EMSL laboratory. Then, these results were validated and refined by analyzing three categories of buildings in two TerraSAR-X images.

The results pointed out that the double bounce effect has a strong power signature for buildings which have the wall on the sensor close side almost parallel to the SAR azimuth direction. Furthermore, the strength of the double bounce decays rapidly in a narrow range of aspect angles, while it decays moderately for larger angles. The exact characteristic of the decay depends on the materials and surface parameters. For buildings which are surrounded by asphalt the strength of the double bounce decreases significantly from 0° to 10° aspect angle, while it decreases moderately for higher values of the aspect angle. Considering buildings which are surrounded by grass, the drop of the strength for low values of the aspect angle is less evident, but it is more constant on the full range of aspect angles. This result is especially important for the development of novel automatic robust building damage assessment methods based on double bounce stripe analysis, which need to take into account the non-linear relation between double bounce and aspect angle.

Chapter 5

Radar imaging simulation for buildings

With the recent advent of the VHR SAR sensors, the potential to use radar imaging simulators is increasing. They can be used to support the analysis of radar scattering effects, assist in scene interpretation, and for training and teaching. Moreover, they can be used for information extraction, by generating simulated images based on hypotheses and comparing them with measured images. In this chapter, we propose a radar imaging simulator that is relatively simple to implement and that focuses on the calculation of the geometrical effects of the scattering. The main goal of the proposed method is to obtain a precise simulation of the geometry of objects in SAR images rather than a detailed radiometric simulation. The simulator is based on an adapted ray tracing procedure to determine which surfaces of a generic object are visible. The backscatter contributions are calculated by means of a Lambertian-specular mixture model. The proposed simulator is employed successfully in methodologies for the information extraction from single detected VHR SAR imagery, as detailed in the two subsequent chapters of this thesis. Here, we show its results on two rather different structures, a rectangular gable roof building and an Egyptian pyramid.

5.1 Introduction to radar imaging simulation

In the era of VHR SAR imagery, radar imaging simulators [60] are becoming increasingly popular. They permit to investigate and understand the scattering effects of buildings under a variety of configurations (e.g. different viewing angles), in a relatively easy, inexpensive and fast manner. Furthermore, they have an important role in education, when for instance scene interpreters are trained to manually analyze VHR SAR imagery to extract specific information, or students are familiarized with SAR and its peculiarities [61].

Various simulators with different simulation techniques and backscattering models have been proposed in literature. Scattering based on PO and/or GO approximations were proposed in [62], [63], and [64], while [65] uses the FDTD method, and [66] IEM. These models take into account the roughness parameters (i.e. Root Mean Square (RMS) height

and correlation length) and dielectric properties of the surfaces in the scene to calculate the scattering. Instead, [67] and [68] use diffuse and specular reflection, similar to the Phong shading model [69]. For larger scenes in particular, these scattering models are often combined with ray tracing, where rays are transmitted from an antenna and traced through the scene until they return to the sensor (e.g. used in [67] and [62]). Ray tracing has the drawback that the rays are only reflected in specular direction, which is a valid assumption for very smooth (metallic) surfaces. This implies that the non-specular scattering contributions from rough surfaces are neglected. Ray casting, which is similar to ray tracing without the possibility that rays are reflected when they hit a surface, was used for the simulator described in [70]. Recently also a fast simulator based on rasterization, which is supported by state of the art Graphical Processing Units (GPUs), was presented [68].

In this thesis, we employ radar imaging simulators as part of information extraction methods by generating simulated images based on hypotheses and comparing them with measured data. In particular we use this concept in Chapter 6 for estimating building heights from single detected VHR SAR imagery, and in Chapter 7 for detecting buildings which were destroyed in a crisis event using VHR optical pre-event and VHR SAR post-event imagery. These application scenarios need a fast simulator and aim at the extraction of information from SAR scenes over areas for which surface roughness parameters and dielectric properties of the materials in the scene are generally not known a priori, so that GO, PO, IEM or FDTD cannot readily be adopted. Hence, simplified scattering models need to be used instead, which take into account the radar imaging mechanism. Rather than simulating absolute radiometric effects related to material properties and surface roughness parameters, for such models it suffices to accurately represent the geometry of the scene and to approximate the relative differences in backscatter.

In this chapter, we present in detail a simple to implement, yet effective radar imaging simulator (disregarding synthetic aperture effects) for urban structures that aims to precisely model the geometry of the objects in the SAR scene and to approximate the relative radiometric differences. The proposed approach offers two novel contributions: 1) we extend standard ray tracing so that the rays are reflected in various directions. Hence, also the non-specular scattering contributions from rough surfaces for instance of buildings are considered in the simulation; 2) we introduce an adjustable mixture of Lambertian and specular scattering as radiometric model to calculate the backscattering from the surfaces, focusing on modeling effects related to the surface roughness while neglecting the dielectric characteristics of the materials. The simulator includes multiple bounce scattering, and can therefore simulate multiple interactions between objects, such as neighboring buildings. The speckle effect is simulated using the Chi-Square distribution [71]. We demonstrate the efficiency of the proposed radar imaging simulator in two examples: 1) simulation of a rectangular gable roof building in Dorsten, Germany, in comparison to submeter airborne SAR data; 2) simulation of the complex structured Menkaure pyramid in Giza, Egypt, in comparison to meter resolution TerraSAR-X data.

The remainder of this chapter is organized as follows. Section 5.2 provides a detailed description of the concepts of the simulator. In Section 5.3 we present the simulation results. Finally, Section 5.4 draws some conclusions.

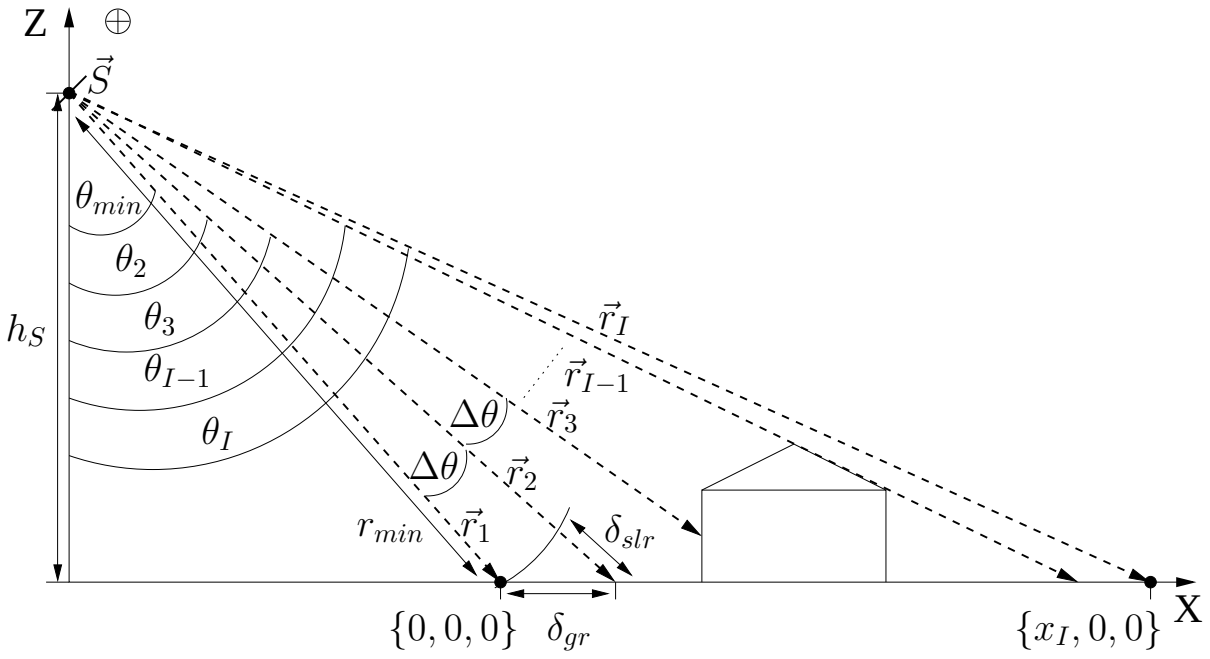

Figure 5.1: Geometry of the radar imaging simulator in range direction.

5.2 Proposed methodology

5.2.1 Enhanced ray tracing

Let us consider the geometry of the radar imaging simulator as depicted in Figure 5.1, with θ_{min} denoting the incidence angle at the near range of the scene. We fixed the scene for which the image shall be simulated (here it is a gable roof building) to start at the origin of a three dimensional Cartesian coordinate system $\{x, y, z\} = \{0, 0, 0\}$. The scene extends horizontally in positive **X** and **Y** direction and is elevated in positive **Z** direction. The azimuth direction of the sensor is in positive **Y** direction. Considering θ_{min} and h_S, the initial sensor position is given by $\vec{S} = \{-h_S \cdot \tan(\theta_{min}), 0, h_S\}$. The distance from the sensor to the first range bin is denoted as $r_{min} = |\vec{S}|$. The model does not include synthetic aperture generation, but instead directly assumes a radar beam limited in azimuth by δ_a. This contributes to the efficiency of the simulation, at the cost of disregarding specific synthetic aperture effects.

The simulator starts with the calculation of all contributions of the first azimuth resolution cell before the sensor is moved in positive **Y** direction by δ_a to calculate the next azimuth resolution cell. We model the radar illumination in range direction as composition of a series of small beams with a finite cone (narrow-beam approximation), the so called rays $\vec{r}_i, i = \{1, \ldots, I\}$. Two subsequent rays have a variation in the incidence angle by $\Delta\theta$, which is fixed by the slant range resolution at near range as:

$$\Delta\theta = \left[\arccos\left(\frac{h_S}{r_{min} + \delta_{slr}}\right) - \theta_{min}\right] / o \tag{5.1}$$

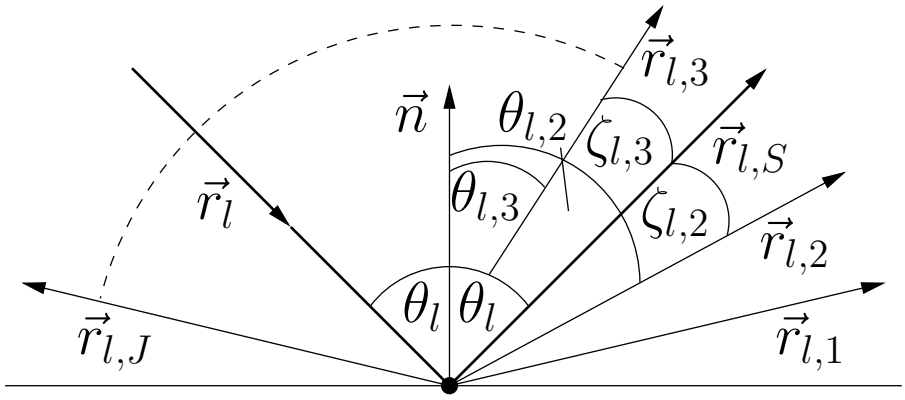

Figure 5.2: Reflection of ray at surface.

with $o > 1$ being a factor to increase the number of rays per resolution cell to avoid undersampling. Indeed, to choose $o = 2$ is enough, whereas higher values have only a marginal effect on the simulation results, while increasing the computing time. The corresponding incidence angles of the individual rays $\vec{r}_i$ are denoted by θ_i.

The number of initial rays I, which are released from the sensor per azimuth resolution cell, depends on the extent of the objects contained in the scene. It has to be high enough so that all scattering effects in range direction (such as shadowing effects) are captured by the rays, i.e. the range point x_I needs to be illuminated by ray $\vec{r}_I$. Hence, $I = (\theta_I - \theta_{min})/\Delta\theta$, with $\theta_I = \arctan\{[x_I + h_S \cdot \tan(\theta_{min})]/h_S\}$.

Each ray illuminates a small surface element, which we detail in the next subsection in Equation (5.5), giving rise to scattering from that element in all directions. Each scattered ray is in turn traced to check whether it scatters at another surface element. This is repeated, for a definable maximum number of bounces which shall be simulated. Tests on different models of simplified 3-D structures show that contributions from more than two bounces do not contribute significantly to the overall backscattering. All rays that travel back in the direction of the radar contribute to the final backscatter.

As detailed in Section 2.4.2, the scattering of microwaves from a surface is composed by a mix of specular and Lambertian scattering, depending on the surface roughness. In standard ray tracing, the rays are only reflected in specular direction, which limits the simulation to the specular contributions. However, to simulate also the non-specular scattering from a rough surface we adapt this scheme so that rays are reflected from the same surface element in all possible directions within the same azimuth resolution cell. This is illustrated in Figure 5.2, with $\vec{n}$ denoting the surface normal, $\vec{r}_l$ the incoming ray coming either directly from the sensor or previously reflected from a surface (multibounce contribution), θ_l the local incidence angle, $\vec{r}_{l,S}$ the ray reflected in specular direction, $\vec{r}_{l,j}, j = \{1, \cdots, J\}$, the rays reflected in other possible directions, and $\theta_{l,j}$ the reflection angle for ray $\vec{r}_{l,j}$. The angle $\zeta_{l,j}$ is the angle between the reflected ray $\vec{r}_{l,j}$ and the specular direction $\vec{r}_{l,S}$ given by:

$$\zeta_{l,j} = \arccos\left(\frac{\langle \vec{r}_{l,j}, \vec{r}_{l,S} \rangle}{|\vec{r}_{l,j}| \cdot |\vec{r}_{l,S}|}\right), \tag{5.2}$$

which we need in the following in order to calculate the amount of energy reflected in direction of $\vec{r}_{l,j}$. Only scattering in the **X**,**Z**-plane is considered: rays which are scattered outside the azimuth resolution cell are not considered anymore. By this, we disregard: 1) specular reflection that could be strong but only occurs for some elaborate geometries that are not considered here; and 2) diffuse scattering back into the **X**,**Z**-plane that will be at a very low level.

5.2.2 Radiometric model

At each intersection point between a ray and a surface (bounce), the amount of energy which is returned to the sensor, as well as the amount which is scattered in direction of a reflected ray, is calculated. The latter is the total amount of energy which is scattered at the next bounce (if any). We separate the RCS σ into the Normalized Radar Cross Section (NRCS) σ° and the effective area A_e according to the relationship:

$$\sigma = A_e \cdot \sigma^\circ \tag{5.3}$$

For the NRCS we define the following Lambertian-specular mixture model, which is based on the bistatic Lambertian model and a specular coefficient:

$$\sigma^\circ = \frac{\cos(\theta_l) \cdot \cos(\theta_{l,j}) \cdot \cos\left(\frac{\zeta_{l,j}}{2}\right)^q}{\int \cos(\theta_l) \cdot \cos(\theta_{l,j}) \cdot \cos\left(\frac{\zeta_{l,j}}{2}\right)^q d\theta_{l,j}} \cdot C \tag{5.4}$$

with C being a constant determining the absolute scattering level. Since we do not intend to calculate absolute radiometry, C can be disregarded. The parameter $q \geq 0$ denotes the specularity of the surface and thus incorporates surface roughness and radar wavelength. The smoother a surface is, the larger the value of q. In the extreme case of a perfectly smooth surface q has to be set to infinity; to simulate a Lambertian surface, q has to be set to 0. In Figure 5.3 we show the behavior of the NRCS with respect to the specularity of the surface and the reflection angles. Negative reflection angles correspond to scattering back into the quadrant of the radar, while a reflection angle of 0° shows the reflection in direction of the surface normal, and positive reflection angles correspond to scattering away from the radar. The graphs show for $q = 0$ a wide distribution with a maximum in the direction of the surface normal, whereas for smoother surfaces, the distribution becomes more peaked with a maximum in the direction of specular reflection. The value of q is determined empirically in the context of the simulations for which the model is used. Different values of q are tested, and the one that produces the best resemblance to the observed image is retained. In our simulations, we use either a single value for all surfaces or two values, i.e. one for the surrounding surface and one for the object.

The effective area is given by:

$$A_e = \frac{|\vec{r}| \cdot \cos(\theta_l)}{\left[\vec{n}_x \cdot \sin(\theta_i) + \vec{n}_z \cdot \cos(\theta_i)\right]^2} \cdot \Delta\theta \cdot \delta_a \tag{5.5}$$

with $\vec{n}_x$ and $\vec{n}_z$ denoting the x and z component of the surface normal, respectively. Note that the local incidence angle θ_l and the angle θ_i, which is the incidence angle for the

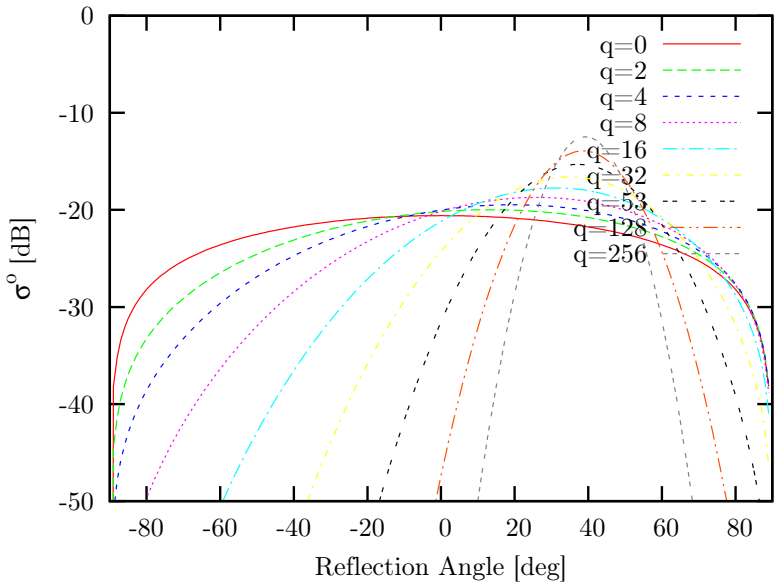

Figure 5.3: Normalized RCS of the Lambertian-specular mixture model (5.4) as a function of incidence angle. The negative reflection angles correspond to backward scattering, while the positive angles are forward scattering (40° incidence angle).

ray directly coming from the sensor (see Figure 5.1), are only the same for first bounce contributions which occur at flat (horizontal) terrains.

Although the model implementation can accommodate coherent ray tracing simulation, this is not used for the present application. The simulation of metallic structures, such as cars, would need a coherent approach, even allowing the exclusion of non-specular reflection. However, since we model urban surface structures we need to consider their roughness at X-band. In this setting a incoherent simulation (allowing for some specular reflection within the Lambertian-specular mixture model) is sufficient.

5.3 Experimental results

5.3.1 Simulation of a gable roof building

To demonstrate the results of our simulator, we choose as first example a mid sized rectangular apartment building with a gable roof structure, which is shown in Figure 5.4, in an airborne scene from the AeS-1 sensor from Intermap Technologies. The parameters of the acquisition and the parameters used for the simulation are given in Table 5.1. We preprocessed the airborne data by multilooking the image by four samples in azimuth and two samples in range direction, which resulted in an equivalent number of looks of 2.59 and an approximately quadratic pixel spacing (0.64 m in azimuth and 0.76 m in slant range). The building has the dimensions 15.9 m × 27.1 m × 12.0 m, a roof inclination angle of approximately 35°, and was measured with 42° local incidence angle and 35° aspect angle (ground truth: measured in-situ, Light Detection And Ranging (LIDAR) DSM, and VHR orthophoto).

(a) (b)

Figure 5.4: Rectangular gable roof building example. (a) Subset in orthophoto. (b) Photograph from the outside of the building. (Orthophoto: © Landesvermessungsamt NRW, Bonn, 2007.)

Table 5.1: Acquisition and simulation parameters of examples.

Parameters	Airborne / Building	TerraSAR-X / Pyramid
Acquisition date	2003-03-13	2007-07-02
Mode	-	HS
Azimuth resolution	0.16 m	1.4 m
Slant range resolution	0.38 m	1.1 m
Incidence angle	28° - 52°	53°
q for surrounding	12	10
q for building	20	10
o	2	2

In Figure 5.5 we show the building in the actual SAR image (Figure 5.5a) in comparison to the simulation results, once without speckle (Figure 5.5e) and once with speckle corresponding to 2.59 looks (Figure 5.5f). Figure 5.5b shows the 3-D model in the viewing configuration as the building was measured in the actual scene, which served as input for the simulation. Overall, the simulations have a good correspondence with the actual scene. The shadow area is accurately simulated, while the bright scattering features appear in the simulations at the correct location. Geometrically the simulated and the measured radar image coincide within 1.4 m. This discrepancy can be explained by inaccuracies in the in-situ measurements on which the simulation is based. From the single bounce contributions shown in Figure 5.5c it can be concluded that the major strong scattering feature results from direct backscattering from the inclined roof. Instead, the L-shaped stripes in the double bounce image (Figure 5.5d) result from the corner reflector composed by the walls facing the sensor and the ground surface. These stripes are not apparent in the final image, so that they are weak with respect to the single bounce contributions, which is explained by the 35° aspect angle of the building (see Chapter 4). The actual SAR image shows some bright spots close to the double bounce, which are not visible in our simulation. They can be attributed to scattering from structures at the facade, such as balconies or rain drains, which we disregarded in our simplified 3-D model. The simulation of the 62 x 49 pixel image took less than 6 seconds, with a memory consumption

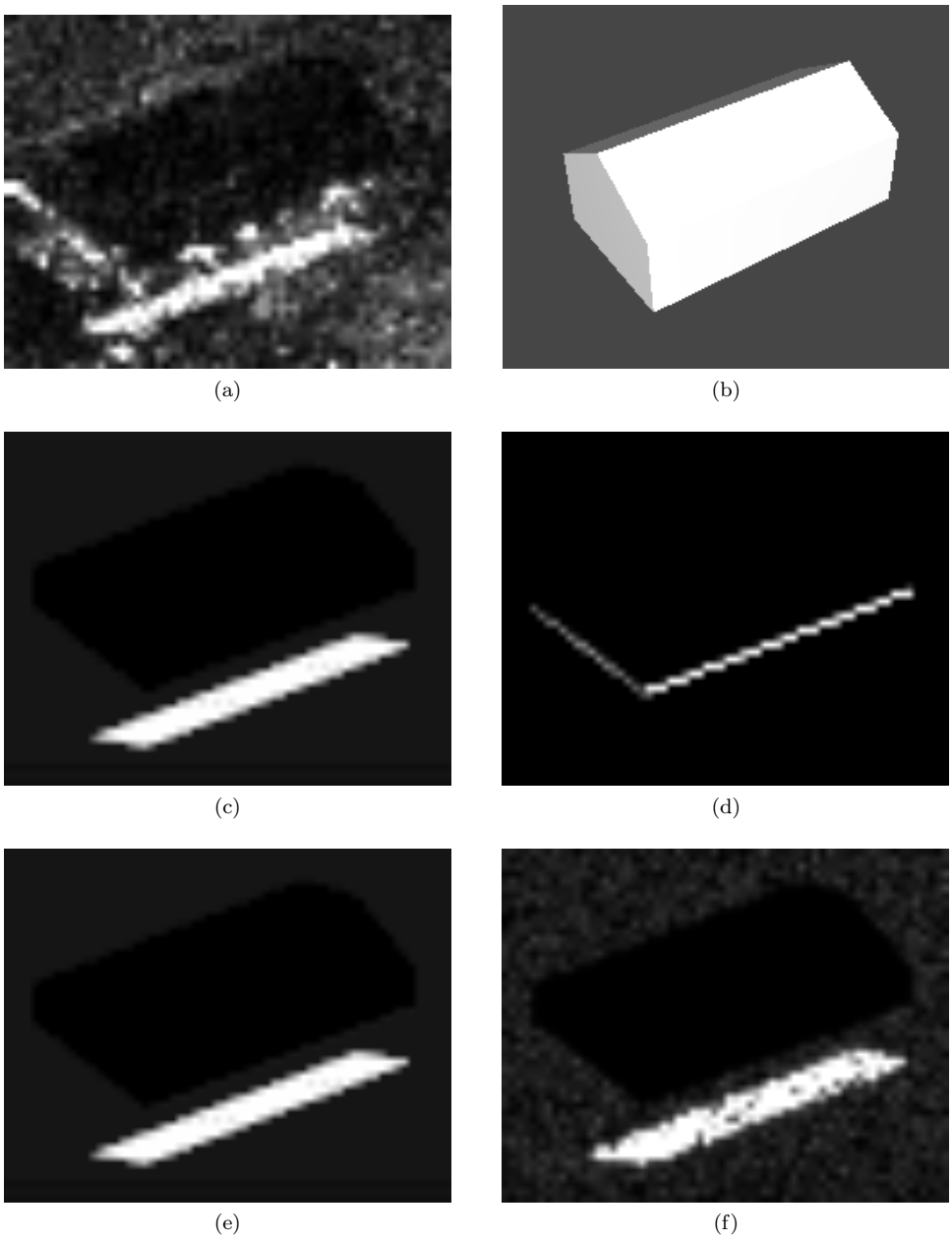

(a) (b) (c) (d) (e) (f)

Figure 5.5: Comparison of simulations of a rectangular gable roof building with actual airborne data. The viewing direction is from the bottom. (a) Airborne SAR image of the building. (b) 3-D model of the simulated building with viewing configuration aligned with airborne scene. (c) Single bounce contribution. (d) Double bounce contribution. (e) Final image without speckle. (f) Final image with 2.59 looks speckle. (SAR image: © Intermap Technologies GmbH, 2003.)

(a) (b)

Figure 5.6: Menkaure pyramid example. (a) Subset in QuickBird satellite image. (b) Photograph of a side of the Menkaure pyramid, highlighting its staircase like structure. (QuickBird image: © DigitalGlobe, 2007; Photo: Sandra Eckert, 2008.)

not exceeding 25 MB (Intel® Core™ 2 Duo Central Processing Unit (CPU) box with 2.53 GHz, 3 GB RAM and Ubuntu 9.04 32-bit operating system), highlighting the good performance of the simulator.

5.3.2 Simulation of a pyramid

As a second demonstration, we compare the simulation of the Menkaure pyramid (29° 58' 21" N, 31° 7' 42" E) in Giza, Egypt, to a recent TerraSAR-X image [72] (see Table 5.1 for the parameters of the acquisition and simulation). At present, the Menkaure pyramid (Figure 5.6a) is 61.0 m high (original height was 65.5 m), with a square base of 103.4 m and an inclination angle of about 51° [73]. The outside of the pyramid is constructed of large stone blocks that are stacked stepwise (see Figure 5.6b). The pyramid has a 5° aspect angle with respect to the azimuth direction of the TerraSAR-X image.

In Figure 5.7 we show the simulation results for the Menkaure pyramid in comparison to the pyramid shown in the actual SAR data (Figure 5.7a), once without speckle effect (Figure 5.7e), and once considering the speckle effect corresponding to 1.9 looks (Figure 5.7f). Figure 5.7b shows the 3-D model of the pyramid which is simulated, considering the viewing configuration as the pyramid was measured in the actual scene.

The pyramid is characterized in the SAR image by three bright sides and a dark one, plus a shadow of the apex on the ground extending behind the dark side of the pyramid. However, the sides do not regularly converge into one clearly defined apex, and the ribs that separate the four sides are well defined at the base of the pyramid but not anymore towards its top. The top of the pyramid has a rather more complex structure. In addition, there is a marked bright stripe at the foot of the radar-facing side.

Considering the single bounce contributions (Figure 5.7c), we can explain the bright stripe at the radar-facing foot of the pyramid by classical layover. The radar incidence angle at 53° is almost exactly the same as the pyramid's slope of 51°. All the backscatter from the front side is therefore imaged at one single range, namely at the base facing

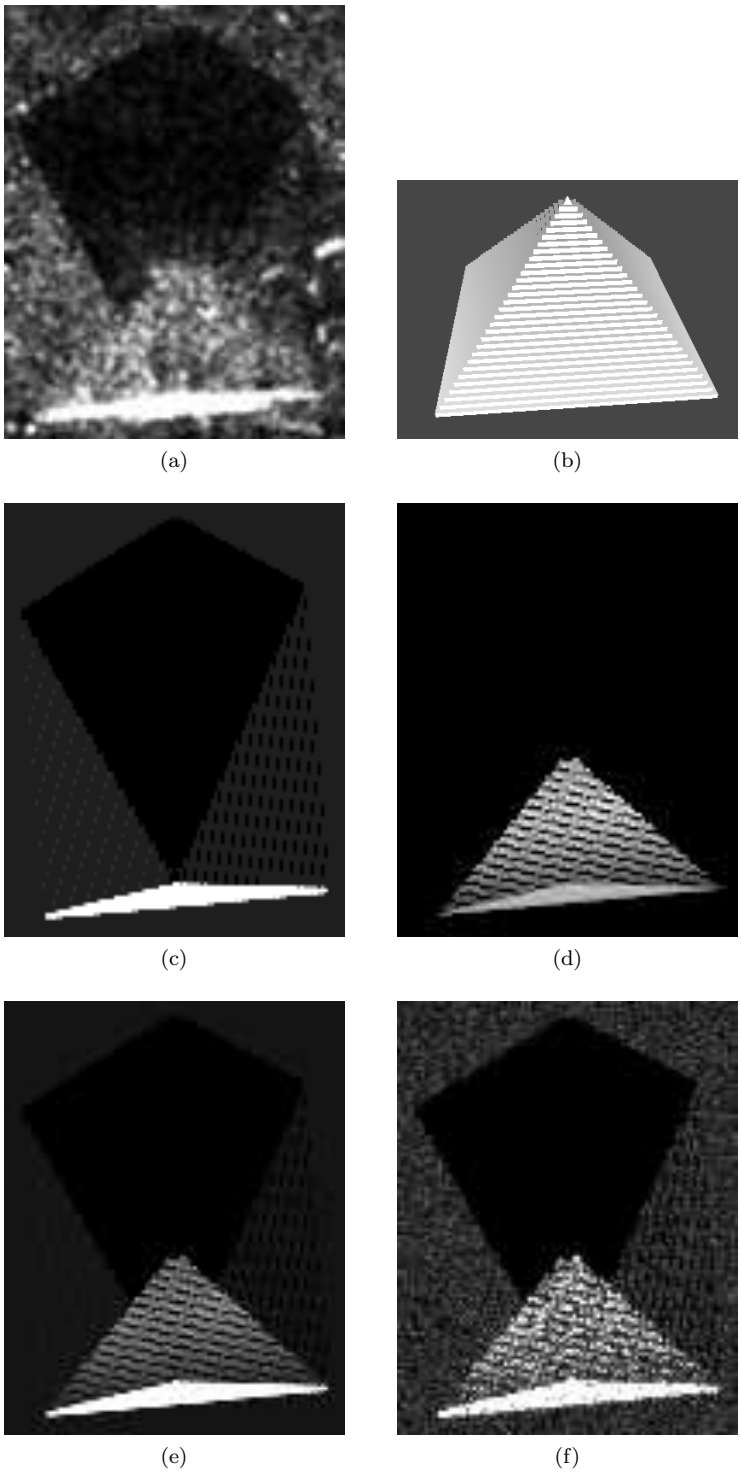

(a) (b) (c) (d) (e) (f)

Figure 5.7: Comparison of simulations of the Menkaure pyramid with actual TerraSAR-X data. The viewing direction is from the bottom. (a) TerraSAR-X image of the Menkaure pyramid. (b) 3-D model of the simulated pyramid. The viewing is adjusted as it would have been seen by the sensor. (c) Single bounce contribution. (d) Double bounce contribution. (e) Final image without speckle. (f) Final image with speckle (1.9 looks). (SAR image: © DLR, 2007.)

the radar. The explanation for the lack of a well-defined apex was first described in [72]. It can be found in double bounce reflections (Figure 5.7d) between the front face of the pyramid and the ground surface in front of the pyramid. The pyramid has a staircase like structure, and the vertical faces of its steps form dihedral reflecting structures with the ground. Each level gives a separate contribution at a different distance, longer for the higher levels. Disregarded in the 3-D pyramid model, the very top of the actual pyramid is smooth (not stepped) and therefore it does not show up as double bounce contribution in the actual SAR image.

A comparison between the pyramid in the actual SAR data and the simulated image shows that the simulator is able to reproduce the major scattering effects which are related to the side looking geometry realistically. As in the previous case the discrepancies (3 m) can be explained by inaccuracies in the in-situ data. The simulation of the 99 x 126 pixel image took less than 46 seconds, with a memory consumption < 116 Mb, confirming the efficiency of the simulator.

5.4 Discussion and conclusion

In this chapter, we proposed a relatively simple to implement, yet effective radar imaging simulator. It is based on an adapted ray tracing scheme and a Lambertian-specular mixture model, taking into account both specular and diffuse scattering. The method aims at simulating precisely the geometry of objects in SAR rather than absolute radiometric effects related to material properties and surface roughness parameters. For the later, the simulator would need to be extended with a more detailed scattering model (e.g. IEM, PO, GO, or FDTD) that takes into account these physical parameters. However, this would sacrifice the computational efficiency that is essential for using the model in the hypothesis-simulation-comparison loop. Moreover, due to the nature of problems analyzed with remote sensing, the values of the physical parameters are often not known.

To highlight the effectiveness of our approach, we showed simulation results for a gable roof building and the Menkaure pyramid in Giza, Egypt, in comparison to actual VHR SAR data. We demonstrated that the simulator based on this simplified radiometric model is sufficient to calculate effects which are related to the geometry, such as layover, shadow, and multibounce scattering effects. If this simulator is used in combination with techniques that compensate for the effects of an approximate radiometry it can be used for advanced methodologies in information extraction scenarios, where the material properties are generally not known (as we show in Chapter 6 and Chapter 7). Furthermore, the simulator can be deployed for instance for educational purposes or to investigate scattering effects of buildings.

Chapter 6

A novel technique for building height extraction from single detected VHR SAR data

In this chapter[1], we present a novel concept for the height estimation of buildings from single detected SAR data. The proposed approach is based on the definition of a hypothesis on the height of the building and on the simulation of a SAR image for testing that hypothesis. A matching procedure is applied to the estimated and the actual SAR images in order to test the height hypothesis. The process is iterated for different height assumptions until the matching function is optimized and thus the building height is estimated. In addition, we propose an extension of this concept in order to investigate the accuracy improvements on the height estimation which can be achieved by using an additional aspect as input data. We test the proposed methods on a set of 40 flat and gable roof buildings using two submeter VHR airborne and two 1 m resolution TerraSAR-X SAR scenes all acquired from the same residential area in Dorsten, Germany.

6.1 Introduction to building height estimation

Urban building detection provides an indirect measure for population density, which is an essential parameter in impact assessment that drives emergency response actions. Both, the spatial extent of urbanized areas and the spatial characterization of building volume

[1]Part of this chapter appears in:

[74] D. Brunner, G. Lemoine, L. Bruzzone, and H. Greidanus, "Building height retrieval from VHR SAR imagery based on an iterative simulation and matching technique," *IEEE Transactions on Geoscience and Remote Sensing*, in press, 2010.

[75] D. Brunner, G. Lemoine, and L. Bruzzone, "Extraction of building heights from VHR SAR imagery using an iterative simulation and match procedure," in *Proceedings of IEEE International Geoscience and Remote Sensing Symposium (IGARSS)*, vol. 4, Boston, MA, USA, July 2008, pp. 141-144.

[76] D. Brunner, G. Lemoine, and L. Bruzzone, "Building height retrieval from airborne VHR SAR imagery based on an iterative simulation and matching procedure," in *Proceedings of SPIE Conference on Remote Sensing for Environmental Monitoring, GIS Applications, and Geology VIII*, vol. 7110, Cardiff, Wales, UK, September 2008, pp. 71100F-1-71100F-12.

[77] D. Brunner, G. Lemoine, and L. Bruzzone, "Estimation of building heights from detected dual aspect VHR SAR imagery using an iterative simulation and matching procedure in combination with functional analysis," in *Proceedings of IEEE Radar Conference (RadarCon09)*, Pasadena, CA, USA, May 2009.

are crucial parameters to estimate affected population and infrastructural damage as well as to enumerate economic losses resulting from the emergency event. Building volume is the product of spatial extent of a built-up structure and its height. Furthermore, the height of a building is a structural indicator about the status of a building after the event, e.g. whether it is still structurally intact. Hence, height determination of buildings is a key issue in post-emergency event information retrieval in urban areas. Successful height characterization of buildings in VHR SAR data therefore, will add substantial value to operational remote sensing applications in emergency response.

Several building height retrieval techniques have already been proposed for VHR SAR imagery in the literature. Semi-automatic methods for the height estimation in detected VHR SAR imagery by means of shadow or layover analysis are proposed in [35], [78], and [79], while methods in [80], [81], and [82] make use of InSAR. The use of stereoscopic SAR (radargrammetry) is proposed in [83], and [84]. Recently, methods based on multiaspect SAR data, in which the same area is imaged from different flight paths, have been proposed in [47] and [85]. A method based on multiaspect InSAR data is presented in [42]. In [86] the use of multiaspect polarimetric InSAR data is investigated. First results with circular SAR are shown in [87]. The presented methods have in common that the achieved accuracy improves with the use of multidimensional data. However, the performance of a proposed methodology is typically presented for a small set of test data, usually comprising only few buildings, leaving a general applicability of the method in doubt.

The height extraction by radiometric analysis of the typical double bounce reflection of a building (see Chapter 3 for details) using an electromagnetic scattering model [40] based on the GO and PO approximations for a simplified rectangular flat roofed building is demonstrated in [41]. This method has the potential to extract the height of the building accurately from a single image, but needs extensive a priori knowledge of the material and surface roughness properties (i.e. dielectric constant, RMS height, correlation length) of the building and its surrounding, which may not always be available.

SAR simulators [60], [62], [63] are not only suitable for the analysis of scattering phenomena, but also as part of information extraction methodologies for actual SAR imagery. In [88], for instance, the polarimetric GrecoSAR simulator is deployed to detect vessel scattering hotspots, which are then used to classify ships in actual SAR imagery. As an extension, GrecoSAR was tested in [89] for the simulation of urban structures. In the case of building reconstruction from multiaspect InSAR data, [36] proposes an iterative procedure based on the predictions of height maps compared to the actual DEM.

In this chapter, we propose a novel automatic 3-D reconstruction concept for the extraction of the height of buildings from single detected SAR (power) imagery under the assumption that: 1) a map with the location of the building is available; and 2) the width, length, and roof type of the investigated building is known. The approach is based on a "hypothesis generation - rendering - matching" procedure. A series of hypotheses are generated and rendered by a radar imaging simulator taking into account the acquisition parameters of the actual VHR SAR data. The simulations are compared to the actual VHR SAR data; the estimated height corresponds to the hypothesis for which the simulated image best matches with the actual scene. The novelty of the presented concept consists in the use of single detected VHR SAR images instead of multidimensional data

(e.g. interferometric, polarimetric, multiaspect). It is worth noting that the use of a single detected VHR SAR image for height estimation can support a wide range of current applications including the use of the new spaceborne SAR sensors such as TerraSAR-X and COSMO-SkyMed. Furthermore, the potential use of single detected SAR data can provide significant economic efficiencies in emergency response (e.g. speed, cost).

The proposed height estimation process is applicable to different building shapes under the full range of aspect angles. One of the key characteristics of the proposed procedure is the simultaneous consideration of the major scattering characteristics of the building in SAR (i.e. layover and shadow areas, multibounce contributions) for estimating the height.

In addition, we present in this chapter a generalization of the method for estimating the height from single detected VHR SAR imagery to the application to dual aspect data sets[2]. Our aim is to investigate the accuracy improvements on the height estimation which can be achieved by using an additional aspect as input data. Furthermore, we analyze how the two aspects should be chosen so that the estimation procedure yields best possible results.

We demonstrate the performance and the properties of the proposed approaches analyzing a set of 40 flat and gable roof buildings in: 1) submeter dual aspect VHR airborne SAR data, which were acquired from approximately perpendicular flight paths; and 2) meter resolution ascending and descending TerraSAR-X scenes for a residential area in Dorsten, Germany.

The remainder of this chapter is structured as follows. In Section 6.2 we describe the proposed approach for estimating the height from single detected VHR SAR data in detail. Then, in Section 6.3, we present the extension for dual aspect data sets. We introduce the test data in Section 6.4, while Section 6.5 presents the results of the proposed method. We finish with the discussion and conclusions in Section 6.6.

6.2 Proposed methodology for height estimation from single images

Let h and h_{true} be an assumption of the height and the true height of the analyzed building, respectively. Let X_{true} denote the true SAR image and $\widehat{X}$ a simulated SAR image at building height h. In order to find the best estimate $\widehat{h}$ for the height of the building, we define a "hypothesis generation - rendering - matching" approach, which is illustrated in Figure 6.1. A building is simulated at different heights and compared to the actual scene, under the assumption that the simulated and actual scenes are coregistered. The simulation requires the knowledge of both a set of parameters related to the acquisition of the actual SAR image and a set of parameters related to the shape and size of the building. The last set also includes the hypothesis on the height of the building h. Thus a simulation is defined by $\vec{H} \equiv \{w, l, h, \alpha_r, \theta, \phi, \delta_a, \delta_{slr}\}$. The final estimated height of the object corresponds to the hypothesis which matches best with the actual scene and

[2]Here, only the case of dual aspect data sets is discussed. However, the proposed approach can handle multiaspect data in general.

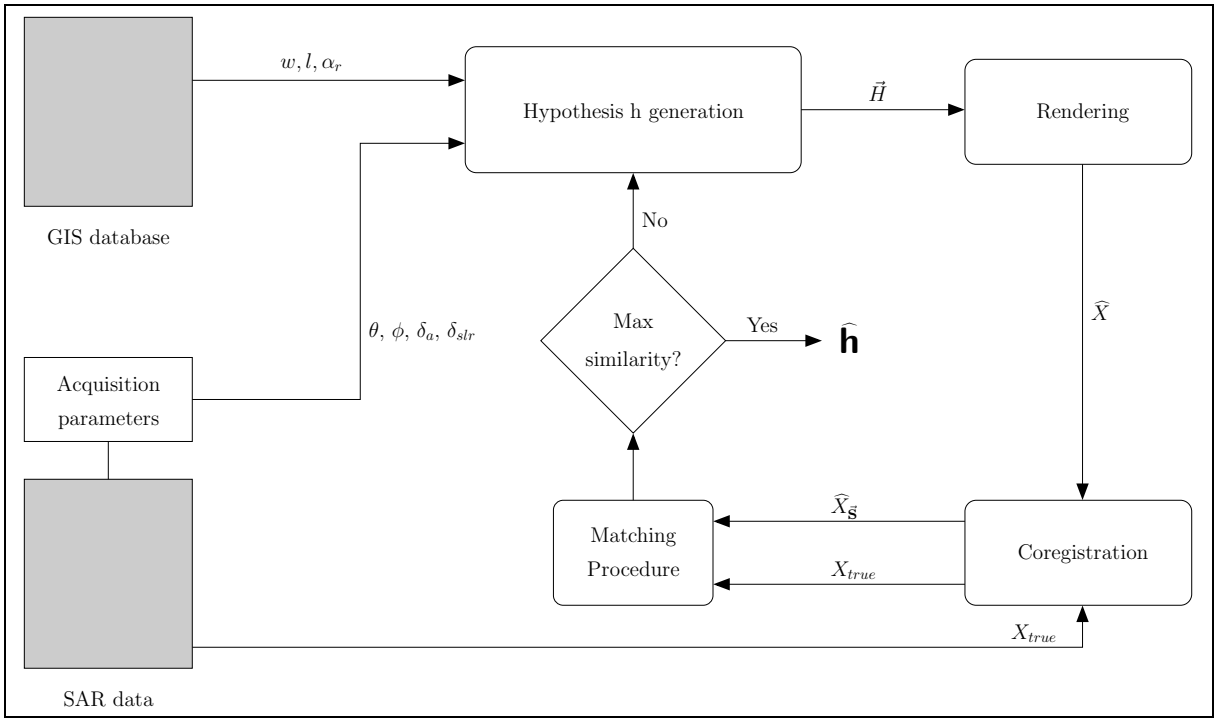

Figure 6.1: Block scheme of the proposed methodology for building height estimation from single detected VHR SAR data.

is given by:

$$\widehat{h} = \arg\max_{\mathrm{h}}\{f(h)\}, \tag{6.1}$$

and

$$f(h) = \digamma[\widehat{X}(\vec{H}), X_{true}], \tag{6.2}$$

with $\digamma$ denoting the similarity measure. The highest value of $\digamma$ corresponds to the best match between the hypothesis and the actual scene. To calculate the match between the simulation and the actual scene, both images need to be coregistered. In practice, coregistration and height estimation are similar tasks which can be executed at the same time in the matching procedure. The value of the measure $\digamma$ for which the best coregistration between a simulation and the actual scene is achieved, is also the final match value for this pair, expressing in a quantitative way how well the simulation fitted with the actual scene. Since the viewing configuration at which the object under investigation was sensed in the actual scene is modeled by the radar imaging simulator, only translations are considered as transformation. Hence, the similarity function in (6.2) becomes:

$$f(h) = \max_{\vec{s}}\{\digamma[\widehat{X}_{\vec{s}}(\vec{H}), X_{true}]\}, \tag{6.3}$$

where $\widehat{X}_{\vec{s}}$ denotes the translation of the image $\widehat{X}$ by the two dimensional vector $\vec{s} = \{\Delta x, \Delta y\}$ associated with the coregistration process.

To solve the maximization problem of (6.1) we use the multidimensional Nelder-Mead [90] (or downhill simplex) function optimization method. Alternatively, the use

of simulated annealing [91] could also be considered to limit the effects of local maxima, though this would increase computational costs. In order to avoid instability in the similarity measure, an averaging over the similarity values in a predefined height interval, for instance $[h - 0.4m; h + 0.4m]$ sampled in 0.2 m steps, can be performed. The three methodological steps, namely, hypothesis generation, rendering, and matching, are described next.

6.2.1 Hypotheses generation

For the height estimation process, only the height parameter is variable in $\vec{H}$, while the other parameters are constant throughout the estimation procedure. Planar dimensions w and l are derived from a Geographic Information System (GIS) database (e.g. cadastral maps, digitized maps from independent ancillary data, optical remote sensing images), which contains the footprint of the building. For flat roof buildings $\alpha_r = 0°$, while for gable roof buildings α_r is chosen according to the characteristic roof inclination angle for the investigated area, which is for the test region considered in this chapter 35°. The incidence angle and the SAR sensor parameters are defined by the acquisition conditions of the actual SAR scene from which the height of the building is extracted. ϕ is obtained by combining the information from the GIS database with the information on the flight track of the airplane in the case of an airborne acquisition, or with the information about the orbit of the satellite in the case that the actual scene was acquired by a spaceborne sensor. A number of hypotheses are generated for the same building during the maximization of (6.1). This can be achieved implicitly by the function optimization method which jointly maximizes for h and $\vec{s}$. For a better performance, an explicit hypothesis generation can be performed by iterating h in a predefined range of expected building heights with a given step size. Thus, the function optimizer has only the task to coregister a rendered hypothesis with the actual scene by varying $\vec{s}$.

6.2.2 Rendering

For evaluating which hypothesis matches best with the actual scene, a radar imaging simulator is employed, which renders the hypothesis into the geometry of a SAR image. First, a 3-D model is generated from the information in $\vec{H}$, taking into account the building parameters w, l, h, and α_r. Second, the 3-D model is triangulated so that in the third step its backscattering can be simulated considering the parameters θ, ϕ, δ_a, and δ_{slr} specified in $\vec{H}$.

Our application scenario aims at extracting building information from SAR scenes over areas where surface roughness parameters and the dielectric properties of the materials in the scene are generally unknown a priori. Thus electromagnetic models such as GO, PO, IEM or the FDTD method cannot be adopted to calculate the backscattering. Hence, we use the simulator proposed in Chapter 5 to calculate the dominant geometrical effects of surface and dihedral scattering of the building models. Note that for the proposed method any simulator which can calculate the effects related to the SAR geometry, can be employed, irrespective of its exact radiometric model.

The output of the simulator is a 2-D rectangular image, whose dimension is determined

such that it includes the scattering effects of the simulated object (i.e. single bounce contributions, shadow, layover, and double bounce) plus a border area, which contains backscattering from the ground. Note that the ratio ξ between the number of pixels belonging to the scattering effects from the object (foreground pixels) and the number of pixels belonging to the ground scattering of the surrounding (background pixels) varies for different buildings or for the same building measured with different viewing configurations. This can be observed for instance in Figure 3.4 for three simulations of the same building, which differ only in ϕ: ξ of Figure 3.4a is larger than ξ of Figure 3.4b, which is larger than ξ of Figure 3.4c. We will highlight the consequence of this effect and propose a solution to compensate for it in the next section.

6.2.3 Matching

In order to estimate the height of a building according to (6.1), we need to optimize the match between the simulated image and the actual scene with respect to h and $\vec{s}$. Image matching and registration are two operations which are closely linked to each other. A slave image which must be coregistered to a master image is translated so that the match between these two images reaches a maximum similarity based on a chosen similarity measure. Hence, the matching between two images is an integral part of a coregistration method, so that we can jointly optimize for h and $\vec{s}$.

For image matching, two types of methods exist: area based and feature based methods [92]. Area based methods calculate directly the correlation between all (or a subset of) samples in the two corresponding images. For instance, [93] proposes a method for pattern matching based on a profiling approach using morphological transforms. Feature based methods, instead, first extract structural information such as lines and edges from the images to be compared, and then in the second step match them in the feature space. Depending on the underlying data, various features are in use, such as tie points [94], gradients computed from grayscale intensity images [95], fractal features based on fractal theory [96], and higher level features such as the shape of objects derived from their edge information [97]. The use of the scale invariant feature transform method, which extracts features that are invariant to image scale and rotation, and which are robust with respect to affine distortions, change in 3-D viewpoint, addition of noise, and change in illumination, is proposed in [98]. This method shows good performance for optical images, while it has a decreased accuracy for SAR images, depending on the content of the SAR scene [99].

Our matching task is faced with two challenges: 1) comparing the actual SAR data with speckle to synthetic images without speckle, i.e. the geometry of the images are similar, but the local statistics in the comparison are different; 2) the radiometry of the simulated image does not match with that of the actual scene.

We proposed a feature based method in [100], which is based on the extraction of shadow areas and edges. As match criterion we used the normalized cross-correlation coefficient [101]. The drawback of feature based methods is the dependence of the effectiveness and stability of the feature extraction procedures on parameter settings, which is especially critical for SAR images. Therefore, we propose in this chapter an area based method based on Mutual Information (MI) for F in (6.3).

MI is a measure derived from information theory, which is suitable for multimodality image matching/registration tasks. It was independently proposed in [102] and [103] for the registration of multimodality medical images, and studied by Xie *et al.* [104] for its application in the SAR domain. The MI between $\widehat{X}$ and X_{true} is given by:

$$MI(\widehat{X}, X_{true}) = H(\widehat{X}) + H(X_{true}) - H(\widehat{X}, X_{true}), \tag{6.4}$$

where $H(\widehat{X})$ and $H(X_{true})$ are the entropies of $\widehat{X}$ and X_{true}, respectively, and $H(\widehat{X}, X_{true})$ is their joint entropy. Using x_{true} and $\widehat{x}$ to denote the pixel values in the measured and simulated image, respectively, the entropies can be computed by:

$$H(\widehat{X}) = -\sum_{\widehat{x}} p_{\widehat{X}}(\widehat{x}) \cdot \log p_{\widehat{X}}(\widehat{x}), \tag{6.5}$$

$$H(X) = -\sum_{x_{true}} p_{X_{true}}(x_{true}) \cdot \log p_{X_{true}}(x_{true}), \tag{6.6}$$

$$H(\widehat{X}, X_{true}) = -\sum_{\widehat{x}, x_{true}} p_{\widehat{X}, X_{true}}(\widehat{x}, x_{true}) \cdot \log p_{\widehat{X}, X_{true}}(\widehat{x}, x_{true}), \tag{6.7}$$

where $p_{\widehat{X}}(\widehat{x})$ and $p_{X_{true}}(x_{true})$ are the marginal probability mass functions, and $p_{\widehat{X}, X_{true}}(\widehat{x}, x_{true})$ is the joint probability mass function. They can be calculated by:

$$p_{\widehat{X}, X_{true}}(\widehat{x}, x_{true}) = hist(\widehat{x}, x_{true}) / \sum_{\widehat{x}, x_{true}} hist(\widehat{x}, x_{true}), \tag{6.8}$$

$$p_{\widehat{X}}(\widehat{x}) = \sum_{x_{true}} p_{\widehat{X}, X_{true}}(\widehat{x}, x_{true}), \tag{6.9}$$

$$p_{X}(x_{true}) = \sum_{\widehat{x}} p_{\widehat{X}, X_{true}}(\widehat{x}, x_{true}), \tag{6.10}$$

where *hist* denotes the joint histogram of the two images. The reason for the independence of this similarity measure to the absolute intensity values of the two images is that the MI is only sensitive to the occurrence of the same pairs of intensity values in $\widehat{X}$ and X_{true}.

Depending on the speckle filtering of the SAR images, the number of bins for the joint histogram is an uncritical parameter. It should be chosen so that the joint histogram has on average at least one entry per bin [104]. Since the lowering of the number of bins has a comparable effect to a low-pass filter, the number of bins should decrease the more the data are affected by speckle. The simulations are without speckle, so that we choose 256 bins for $\widehat{X}$. Since we apply a speckle filter in the preprocessing step to the actual SAR data (Section 6.4), we only decrease the number of bins for X_{true} to 128. A test with 64 bins did not yield an increased matching accuracy.

For the coregistration of $\widehat{X}$ and X_{true} we allow subpixel accuracy, which means that we allow shifts in x and y directions, which do not match the grid spacing of the image. Therefore, it is necessary to interpolate the values for the pixels that do not coincide with a grid point of the original raster. With respect to the coregistration of two images with MI, the Partial Volume (PV) interpolation method was proposed in [105], where instead

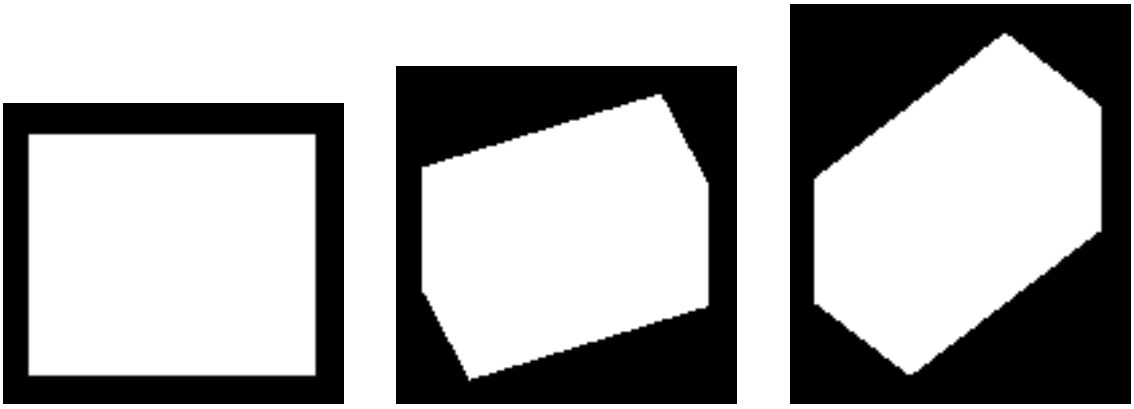

(a) (b) (c)

Figure 6.2: Object masks of the corresponding simulations in Figure 3.4. (a) $\phi = 0°$. (b) $\phi = 22.5°$. (c) $\phi = 45°$.

of interpolating new intensity values the joint histogram is updated directly. A series of empirical tests showed that PV outperforms in accuracy other methods such as bilinear interpolation.

In Section 6.2.2 we highlighted that the ratio ξ between foreground and background pixels is not constant for different buildings and viewing configurations. In the case of a building with $\phi = 0°$ (Figure 3.4a), ξ has a relative high value, which means that the matching (and hence the height estimation) is dominated by the scattering of the object itself. Instead, for $\phi = 45°$ (Figure 3.4c) the value of ξ is relatively low implying that the estimation procedure is influenced more significantly by the background than by the foreground pixels. Since an optimal height estimation accuracy is only achieved for a certain trade-off between fore- and background pixels, we have to ensure that the matching procedure always uses the same ξ. To fix ξ, we defined a binary object mask, where all foreground pixels have the value 1 and all background pixels the value 0. This object mask is generated by the simulator as a secondary result of the simulation run. Figure 6.2 shows the corresponding object masks for the simulations of Figure 3.4. By expanding the object masks using the morphological dilation operator [106] and by only considering, for the calculation of the MI value, those pixels which have the value 1 in the expanded object mask, ξ can be fixed for the matching procedure for different buildings and viewing configurations. As structuring element for the dilation operator, we use a disk, whose size is determined separately for each simulation to fulfill the desired ξ value. A series of tests showed that the best accuracy for the height estimation is achieved for $\xi = 1$, which means that the number of foreground pixels is equal to the number of the background pixels.

6.2.4 Constraint for obtaining reliable estimations

The proposed method estimates the height of an individual building by simulating the expected SAR signature of a simplified building model and evaluating the match with the actual scene. However, the simulation process does not consider the effects of other struc-

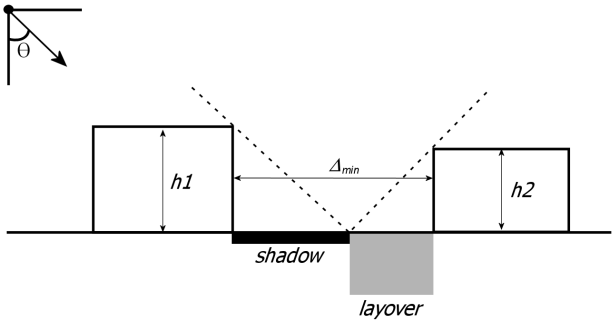

Figure 6.3: Minimum distance Δ_{min} which is required between two buildings so that their scattering effects do not interfere.

tures in the surrounding of a building under investigation, which might have an impact on its actual backscattering. The minimum distance Δ_{min} which is required between two buildings in order that their scattering effects do not interfere with each other is given by [36]:

$$\Delta_{min} = h_1 \cdot tan(\theta) + h_2 \cdot cot(\theta), \tag{6.11}$$

where h_1 is the height of the building at the sensor close side and h_2 denotes the height of the building, which is behind the first building (see Figure 6.3). Hence, optimal accuracy for the height estimation process for a building can only be achieved if the condition:

$$\Delta_{act} > \Delta_{min}, \tag{6.12}$$

is fulfilled, where Δ_{act} denotes the actual distance between the buildings.

6.3 Proposed methodology for height estimation from dual aspect data sets

In order to investigate the accuracy improvements which can be achieved by using dual aspect data sets, we extend the methodology for the height estimation from single detected VHR SAR imagery. The resulting procedure can be separated in two steps. Firstly, the height of a building is estimated from each of the two aspects separately using the height estimation procedure for single detected imagery, which results in two individual height estimates per building. Second, the quality of each of the two estimates is assessed by functional analysis. This information is used to either select one of the individual estimates as final height assumption, or to fuse the two individual estimates to derive a new height assumption which is based on the two aspects.

For simplicity let us consider one of the dual aspect data sets. Let $f_1(h)$ and $f_2(h)$ be the similarity functions (6.3) of a building in aspect 1 and 2 of a dual aspect data set, respectively. Let $\widehat{h}_1$, and $\widehat{h}_2$ be the estimated heights resulting from the maximization of $f_1(h)$ and $f_2(h)$, respectively. The final estimated height $\widehat{h}_{1,2}$ is obtained by merging the two individual estimates, taking into account their respective qualities. The quality of an individual height estimate reflects its plausibility to be a reliable estimate for the height

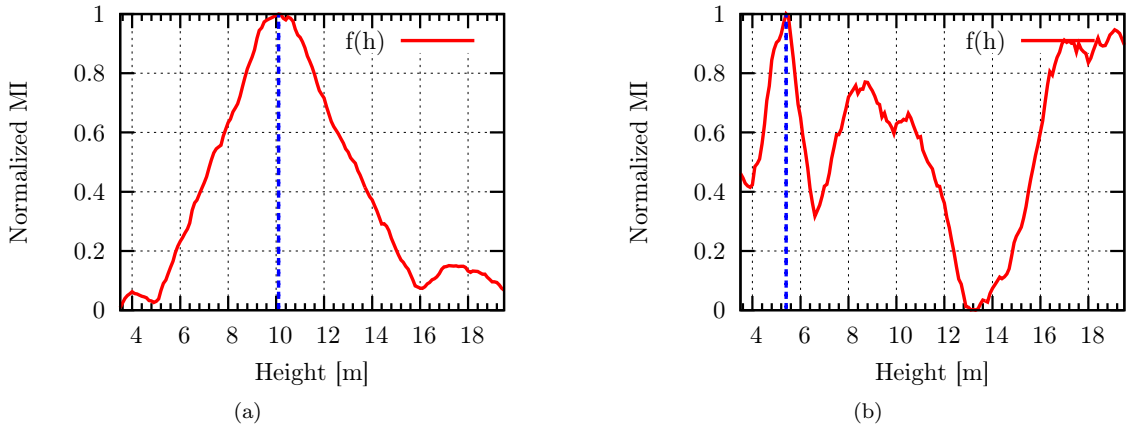

Figure 6.4: Examples of similarity functions. (a) High quality estimate with one distinct global maximum. (b) Low quality estimate without one distinct global maximum.

of the building, and is obtained by a functional analysis of the similarity function $f_n(h)$ where $n = \{1, 2\}$.

An example of a height estimate with high quality is shown in Figure 6.4a. It shows high values in the vicinity of the true height whereas the values decrease with increasing the offset between true and assumed height. Hence, a height estimate with high quality is characterized by a concave similarity function with a clear peak. Figure 6.4b instead shows an example for a low quality estimate. It has two local maxima, which have similar values, but at very different heights. Therefore, lower quality estimates are characterized by a similarity function with several local minima and maxima without one distinct global maximum. They are not smooth, which means that they change between convex and concave.

In practice $f_n(h)$ has several very small local extrema. In order to conduct the functional analysis, we first apply a 2-D thin plate spline [107], which smooths the function and limits the effects of the local extrema for the assessment of the quality:

$$s_n(h) = \text{spline}[f_n(h)]. \tag{6.13}$$

Note that $s_n(h)$ is only used for the assessment of the quality of the estimate, while the fusion and the derivation of $\widehat{h}_{1,2}$ is based on the original similarity function $f_n(h)$.

For the assessment of the quality of an estimate and the calculation of $\widehat{h}_{1,2}$, the first derivative $s'_n(h)$ and second derivate $s''_n(h)$ of $s_n(h)$ are analyzed. In particular, the number of local maxima of $s'_n(h)$ denoted by m_n, and the number of zero crossings of $s''_n(h)$ denoted by z_n, are considered. m_n is a measure of the number of ascending slopes of $s_n(h)$. An estimate for which $m_n = 1$ is characterized by one distinct maximum. z_n corresponds to the number of inflection points of $s_n(h)$, which is equivalent to the number of changes between convex and concave behavior of the function. Hence, it is a measure of the smoothness of the similarity function. An unstable function, which changes often its behavior between convex and concave, has a high value. An ideal concave similarity function has $z_n = 0$.

The quality assessment and fusion strategy gives first preference to similarity functions which have one distinct maximum. If both or none of the functions satisfy this, the quality is assessed based on the smoothness of the function. In particular, if only one of the estimates shows one distinct maximum ($m_1 = 1$ or $m_2 = 1$), the estimated height is based solely on this estimate. If this is true for both similarity functions ($m_1 = 1$ and $m_2 = 1$), z_n is investigated in order to determine which estimate is superior. The smoothness of the function is as quality measure less expressive, so that one similarity function is only considered superior to the other function if it has a significant lower number of inflection points. In this context, significant lower means that the difference between z_n must be bigger than two. The estimated height corresponds to the estimate which has the higher quality. If none of the estimates is superior, $\widehat{h}_{1,2}$ results from the maximization of the fusion (multiplication) of the two similarity functions. In case that both similarity functions have several local maxima ($m_1 > 1$ and $m_2 > 1$), the decision which function is superior is based again on the number of zero crossings (z_n) of the function.

The process can be formulated as follows:

1. if $f_1(h)$ and $f_2(h)$ have one local maxima, or if both functions have several local maxima, i.e. ($m_1 = 1$ and $m_2 = 1$) or ($m_1 > 1$ and $m_2 > 1$), then evaluate the smoothness of $f_1(h)$ and $f_2(h)$:

$$\widehat{h}_{1,2} = \begin{cases} \arg\max_{h}\{f_1(h) \cdot f_2(h)\} & \text{if} \quad |z_1 - z_2| \leq 2 \\ \widehat{h}_1 & \text{if} \quad |z_1 - z_2| > 2 \text{ and } z_1 < z_2 \\ \widehat{h}_2 & \text{if} \quad |z_1 - z_2| > 2 \text{ and } z_1 > z_2 \end{cases}$$

2. else if $m_1 = 1$ and $m_2 > 1$, then $\widehat{h}_{1,2} = \widehat{h}_1$;

3. otherwise, i.e. $m_2 = 1$ and $m_1 > 1$, $\widehat{h}_{1,2} = \widehat{h}_2$.

In the proposed strategy the range for which the qualities of the two similarity functions are considered as similar are quite restrictive. It follows that the method tends to select the final height estimate from one of the two individual estimates rather than to fuse the estimates by multiplying the individual similarity functions. The rules can be made less restrictive by choosing higher values than '1' for the comparison with m_n and '2' for the comparison with z_n. This would imply that also lower quality estimates are considered for the fusion. If both estimates show a low quality, the estimate for this building could be rejected. If, as in our scenario, a height estimate shall be derived anyway, the fusion of the estimates is preferable over the selection of an estimate, as it increases the probability to derive an estimate which has good accuracy. As alternative to fusing the estimates by multiplying the similarity functions, an averaging of h_1 and h_2 could be performed. The advantage of the multiplication over the averaging is because the complete information of each of the original similarity functions is used to derive the final height. This means that at the estimated height both $f_1(\widehat{h}_{1,2})$ and $f_2(\widehat{h}_{1,2})$ have high values, whereas the averaging could result in a height estimate whose function values $f_1(\widehat{h}_{1,2})$ and $f_2(\widehat{h}_{1,2})$ have both low values.

An alternative approach to the functional analysis would be to simultaneously match the rendered hypotheses for both of the dual aspect scenes and select the hypothesis for

which the joint similarity function is at the global maximum. However, according to our experience, this leads to more cases where the lower quality estimate influences the final height estimate significantly. Rather, functional analysis as proposed in the scheme above will lead to a qualitatively better final estimate in disparate matching quality cases.

6.4 Data set description

The test area chosen was a subset of the city of Dorsten (51°40'18" N, 6°59'34" E), Germany, for which we considered both dual aspect airborne and a pair of ascending and descending spaceborne VHR SAR data. Ancillary data, which was used to retrieve the building footprint parameters for initializing the simulator, was provided by an orthophoto acquired on June 09, 2006 with 0.3 m resolution. Furthermore, ground data was manually collected in combination with a LIDAR DSM with approximately 0.1 m vertical resolution. An overview of the composed data set is shown in Figure 6.5.

We consider two types of building structures for which we estimate the heights: flat roof buildings and gable roof buildings. All buildings are assumed to be individual buildings with rectangular footprints. To evaluate the performance of the method under a variety of conditions, we choose 40 individual industrial and apartment buildings with different shapes at various aspect and incidence angles, which we categorized in three groups. Category A contains flat roof buildings and category B contains gable roof buildings. Category C contains the buildings which do not fit the structural assumptions of our building models completely. This category includes buildings which have a non-rectangular footprint (such as buildings with a tower attached to it), or buildings which have non-uniform heights. The majority of the selected buildings are gable roof buildings, which is the prevailing type of structure for residential houses in this area. Only few flat roof buildings could be identified, some of which are apartment buildings (flats) and some are industrial or commercial structures (e.g. factories, stores). Six buildings belong to category A, 27 buildings to B, while seven buildings were classified as C. To distinguish between the different buildings in the various categories we use the naming scheme *<Category>-<Number of building in category>*, e.g. *A-3* denotes the third building in the category for flat roof buildings.

Figure 6.6 shows a subset of the orthophoto and the corresponding DSM with some example buildings for two of the three categories: buildings denoted by *A-1*, *A-2*, *A-3*, and *A-4* are flat roof buildings, while buildings *B-1* to *B-5*, and *B-18* to *B-23* belong to the class of gable roof buildings. An example of a building belonging to category C is given in Figure 6.11 in Section 6.5.1.

The two airborne SAR scenes taken by the AeS-1 sensor from Intermap Technologies [108], for which the corresponding subset of Figure 6.6 is displayed in Figure 6.7 (in slant range geometry), were acquired in X-band on March 13, 2003 with 16 cm azimuth and 38 cm slant range resolution in HH polarization. The incidence angle ranges over the swath from 28° (near range) to 52° (far range). The dual aspect data were measured in almost perpendicular flight paths with a right pointing antenna so that the flight path for the "horizontal" scene was approximately from west to east, while the "vertical" scene was measured from north to south. The overlapping area in the two scenes, where we

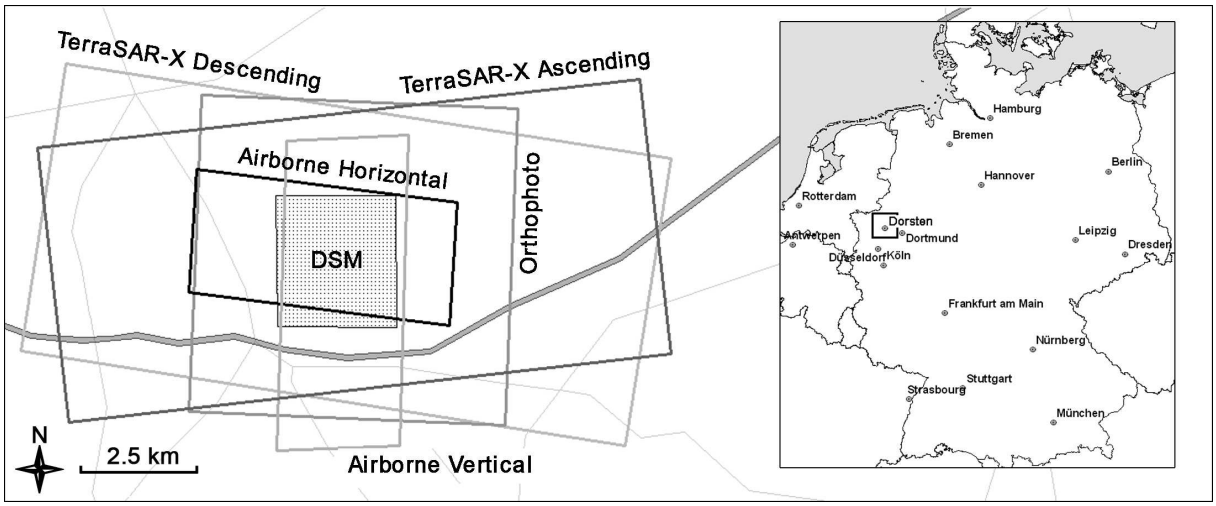

Figure 6.5: Overview of data set from Dorsten. Note that for the spaceborne data the azimuth dimension of the images is smaller than the range dimension, while for the airborne data the azimuth dimension is larger compared to the range dimension.

focus on in this study, is about 2.3 x 2.3 km^2 and includes a medium dense residential urban area, and several smaller industrial zones.

In order to use the MI as similarity measure for SAR image registration/matching, speckle reduction is essential [104]. Hence, we preprocessed the airborne data by multilooking the image by four samples in azimuth and two samples in range direction, which resulted in an equivalent number of looks of 2.59 and an approximately square pixel spacing (64 cm in azimuth and 76 cm in range). Furthermore, we speckle filtered the image with the Gamma Maximum A-Posteriori Probability (MAP) filter [109] and the mean shift filter proposed in [110], which acts mainly on shadow areas.

The TerraSAR-X spaceborne data, for which the corresponding subset of Figure 6.6 is shown in Figure 6.8, were acquired in HS mode with an azimuth and slant range resolution of 1.1 m and 1.2 m, respectively. The data were processed so that the azimuth and the slant range spacing is 0.9 m. The descending scene was acquired on December 13, 2007 with θ varying from 53.4° - 54.1° over the swath, while the ascending scene was taken on January 22, 2008 with θ in the range of 50.3° - 51.0°. Due to the lower resolution of the spaceborne data, we did not multilook the data before speckle reduction. Hence, the preprocessing of the data was limited to the application of the Gamma MAP and the mean shift filter.

6.5 Experimental results

The results of the height estimation process for our test data set are presented in this section. Section 6.5.1 lists and discusses the results of the three groups of buildings for the horizontal airborne scene in greater detail. In Section 6.5.2 we highlight the results for the vertical airborne scene, especially with respect to the differences to the results from the horizontal scene. To investigate the impact of the lower resolution of the TerraSAR-X data

(a)

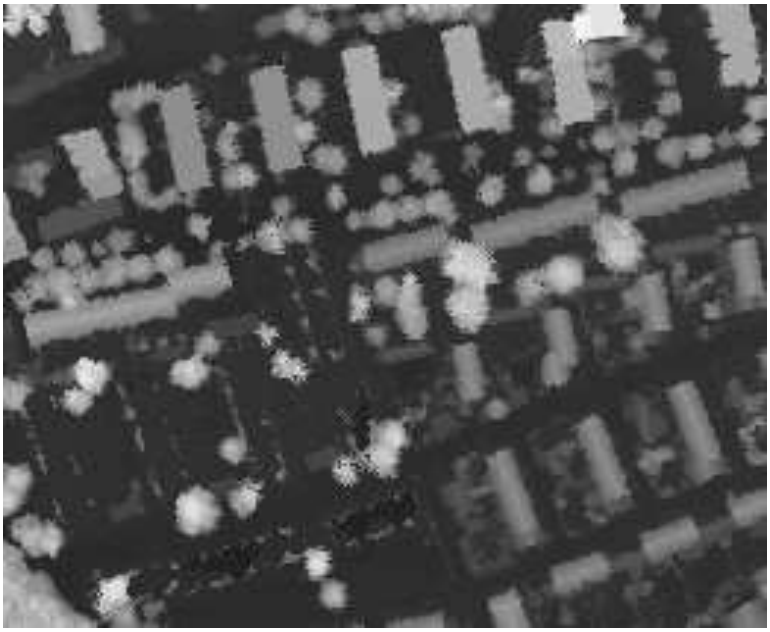

(b)

Figure 6.6: (a) Subset of the orthophoto (top corresponds to north), showing examples of buildings for two categories: Buildings *A-1*, *A-2*, *A-3*, and *A-4* belong to the category of flat roof buildings, while buildings *B-1* to *B-5* and *B-18* to *B-23* are classified as gable roof buildings. (b) Corresponding subset of the DSM. In the lower left corner it can be noted that due to some manual editing the height information of some buildings was removed (e.g. buildings *B-18* - *B-23*). For these buildings, manual height measurements were carried out using a laser device. (Orthophoto: © Landesvermessungsamt NRW, Bonn, 2007; DSM: © Fugro NPA, 2003.)

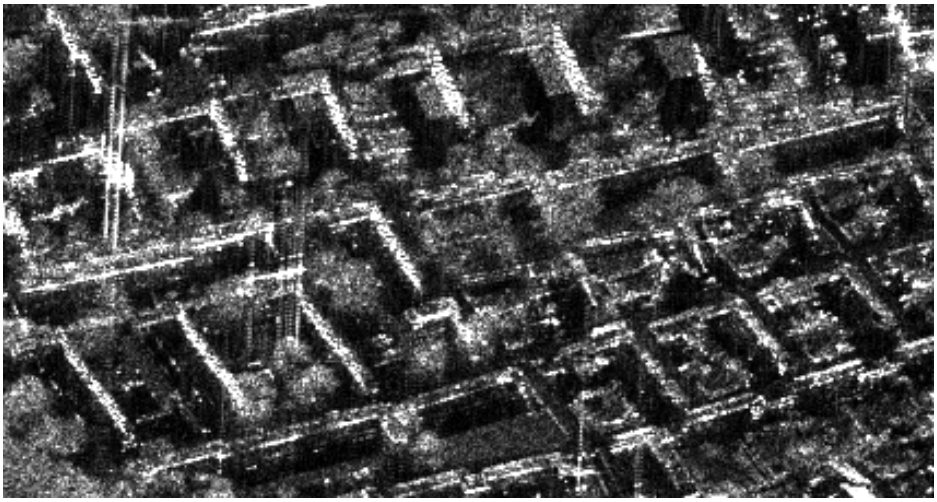

(a)

(b)

Figure 6.7: Subsets of the airborne SAR scenes in slant range geometry. (a) Horizontal scene (acquisition from west to east with right looking sensor) with viewing direction from the top. (b) Vertical scene (acquisition from north to south with right looking sensor) with viewing direction from the right side. (© Intermap Technologies GmbH, 2003.)

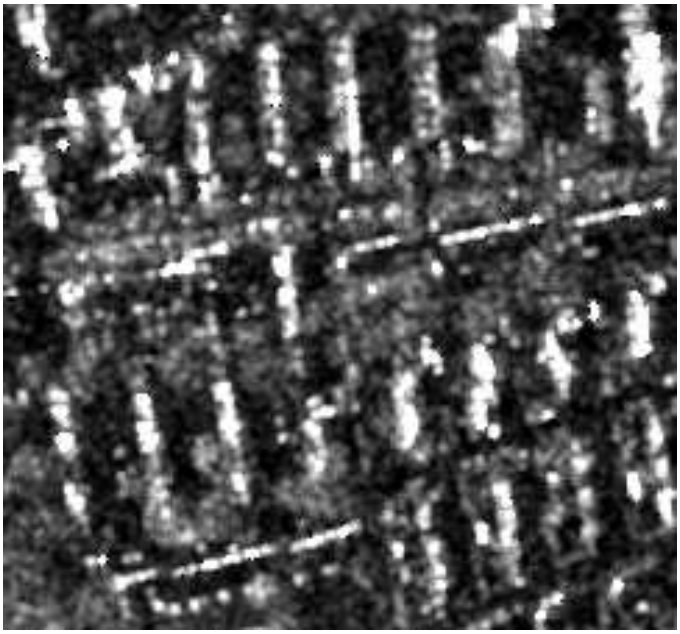

(a)

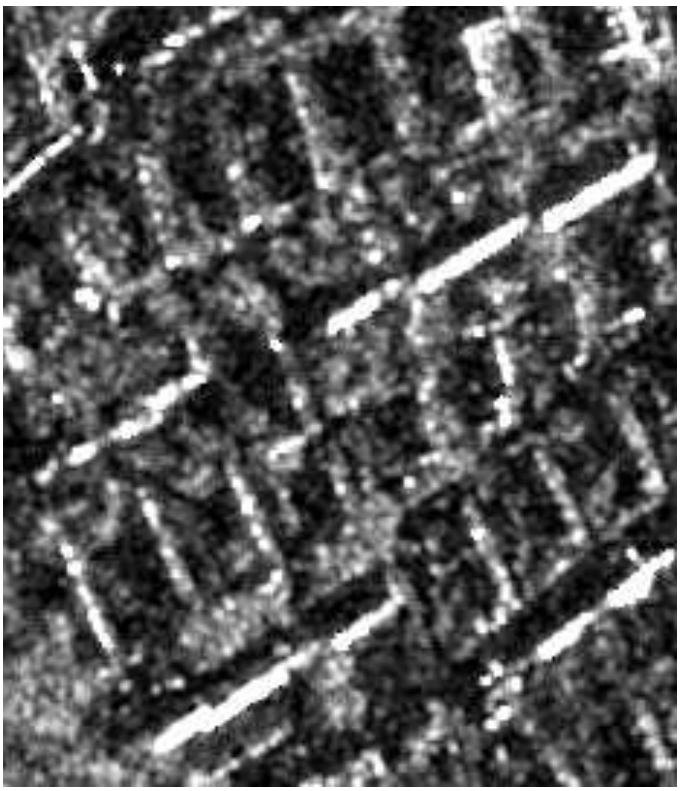

(b)

Figure 6.8: Subsets of TerraSAR-X scenes in slant range geometry, which corresponds to the subsets shown in Figure 6.6. (a) Ascending with viewing direction from the left. (b) Descending with viewing direction from the right. (© Infoterra GmbH/DLR, 2007-2008.)

Table 6.1: Results for flat roof buildings (category A) for horizontal airborne scene.

Building	Width	Length	ϕ	Local θ	Height	Estimate	Difference	Relative Difference
A-1	12.1 m	35.8 m	16.6°	45.4°	12.5 m	12.4 m	-0.1 m	-0.8%
A-2	12.4 m	35.9 m	16.3°	45.4°	12.5 m	12.0 m	-0.5 m	-4.0%
A-3	12.3 m	36.3 m	16.6°	45.6°	10.0 m	9.5 m	-0.5 m	-5.0%
A-4	12.4 m	36.0 m	15.5°	45.7°	10.0 m	14.4 m	4.4 m	44.0%
A-5	15.8 m	45.7 m	14.0°	43.0°	7.0 m	5.4 m	-1.6 m	-22.9%
A-6	13.1 m	37.8 m	30.4°	43.0°	5.1 m	5.1 m	0.0 m	0.0%
Mean							0.3 m	1.9%
Standard deviation							± 2.1 m	± 22.3%

with respect to the airborne data on the accuracy of the height estimation, we summarize in Section 6.5.3 the results for the ascending and descending TerraSAR-X scenes. In Section 6.5.4 we show the results of the height estimation from the dual aspect data sets, before we discuss in Section 6.5.5 some computational aspects of the method.

6.5.1 Horizontal airborne scene

Flat roof buildings (category *A*)

To highlight the results of our method in detail, we show in Figure 6.9 the output generated by the method for building *A-2*, which is also included in Figure 6.6. A photograph of the building is displayed in Figure 6.9c, and further details are listed in Table 6.1. The plot in Figure 6.9a shows MI values normalized between 0 and 1, for hypotheses with an height range from 3 m to 20 m using a 0.1 m step size. The graph shows a good match around the true height of the building (12.5 m), while it drops off with increasing difference between simulated and actual height. The global maximum is at 12.0 m which is 0.5 m lower than the true height. Figure 6.9b shows the simulation of the building at the estimated height in comparison to the actual SAR scene (Figure 6.9d), which is coregistered with the simulation. It is obvious that the Lambertian-specular mixture model used in the simulation does not reproduce the correct radiometry of the actual SAR scene. However, qualitative differences in scattering effects, and their characteristic image areas in the SAR geometry (i.e. double bounce, layover, and shadow), are reflected accurately in the simulation. Since we use MI as similarity measure, the difference in the radiometry between simulation and actual scene does not seem to degrade the accuracy of the height estimate.

A summary of the results of the proposed height estimation procedure for the buildings in category A is given in Table 6.1, together with the details (dimensions and the corresponding viewing configuration of the sensor) of the buildings. The overall mean difference is 0.3 m, which indicates that the method has no significant tendency for under- or overestimation. The corresponding standard deviation of 2.1 m demonstrates a good accuracy in the estimates for flat roof buildings.

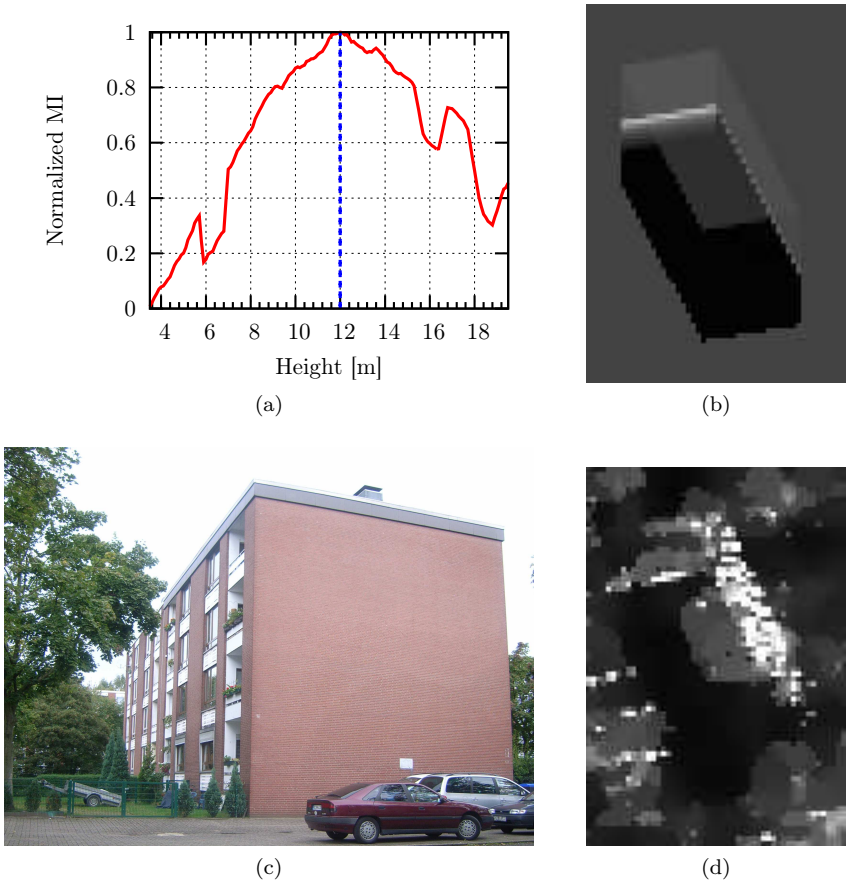

Figure 6.9: Results for building *A-2*. (a) Plot of the MI values normalized between 0 and 1, with a maximum at 12.0 m. (b) Simulation of the flat roof building model with height 12.0 m. (c) Photograph from the outside of the building. (d) Subset of airborne VHR SAR scene showing building *A-2*, which is coregistered to the simulation shown in (b). (SAR image: © Intermap Technologies GmbH, 2003.)

Gable roof buildings (category *B*)

The category of gable roof buildings contains the largest distinct set of buildings in the test data set. Figure 6.10 shows in detail the results for building *B-18*, which is also shown in Figure 6.6. A photograph of the building is displayed in Figure 6.10c, and further characteristics are listed in Table 6.2. The plot in Figure 6.10a shows the match values for the same height hypotheses as in Section 6.5.1. Similar to the plot in Figure 6.9a, the maximum value at 10.2 m is close to the true height of the actual building (9.5 m). Comparing the simulation in Figure 6.10b to the actual building shown in Figure 6.10d, it can be noticed again that the SAR image geometries of the two images match well, while there is a significant difference in the radiometries of the two images, which justifies the use of MI as measure for the matching procedure.

The results of the height estimation for the 27 gable roof buildings are summarized in Table 6.2. The mean difference is 0.9 m, which indicates that the method has a small tendency to overestimate heights. The standard deviation is 1.5 m, which is slightly better than what was achieved for the flat roof buildings.

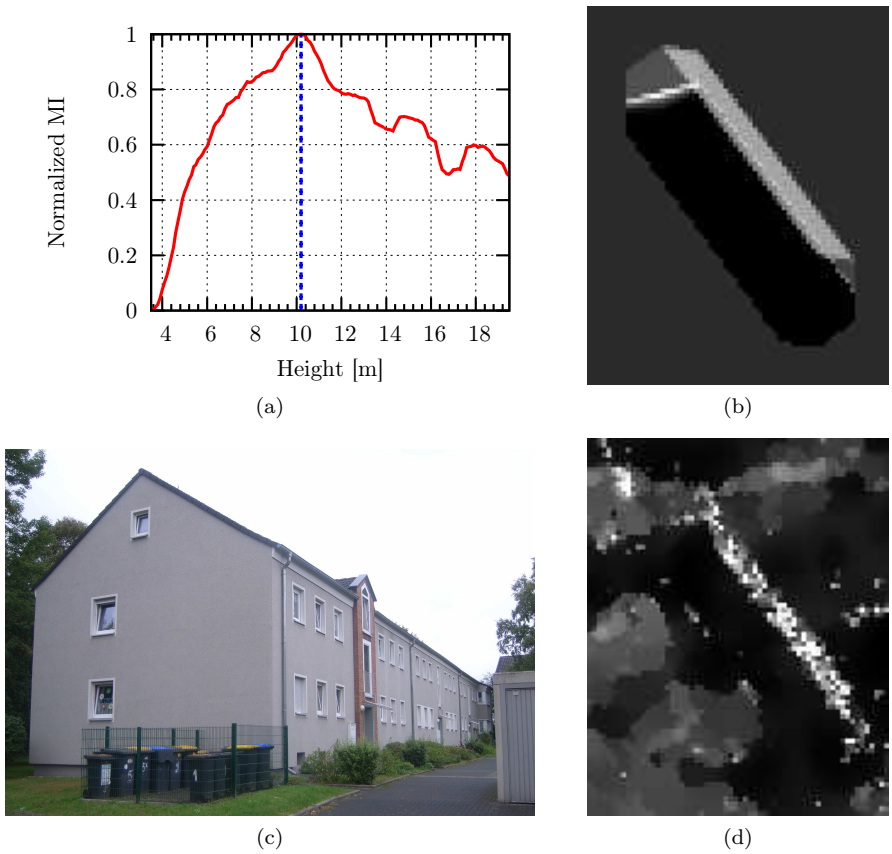

Figure 6.10: Results for building *B-18*. (a) Plot of the normalized MI values with a maximum at 10.2 m. (b) Simulation of the flat roof building model with height 10.2 m. (c) Photograph from the outside of the building. (d) Subset of airborne VHR SAR scene showing building *B-18*, which is coregistered to the simulation shown in (b). (SAR image: © Intermap Technologies GmbH, 2003.)

The method provides consistent results when matching buildings at different orientations. Let us consider for example buildings *B-1* and *B-4*, which are similar in size and structure. *B-1* is oriented approximately perpendicular to *B-4* (see Figure 6.6), while they were imaged with about the same incidence angle. The results for the height estimation, with an estimation difference of 1.5 m for *B-1* and 1.0 m for *B-4*, are good matches for both buildings, demonstrating the robustness of the method with respect to varying aspect angles.

Buildings for which the structural type does not fit the models (category *C*)

For the present study we assume that buildings have a rectangular footprint and have either a flat or a gable roof. However, these simplifying assumptions do not match all actual buildings. To investigate the performance of the proposed height estimation procedure for buildings that have a different structure than our assumptions, but are approximated in the simulation step by rectangular flat or gable roof buildings, we summarize in Table 6.3 the results for seven buildings.

Building *C-1* is a gable roof building, but with a very low roof inclination angle. It is

Table 6.2: Results for gable roof buildings (category B) for the horizontal airborne scene.

Building	Width	Length	ϕ	Local θ	Height	Estimate	Difference	Relative Difference
B-1	9.7 m	39.7 m	19.5°	46.1°	9.5 m	11.0 m	1.5 m	15.8%
B-2	10.5 m	30.3 m	21.2°	45.9°	9.5 m	13.7 m	4.2 m	44.2%
B-3	11.3 m	45.2 m	20.5°	45.8°	9.5 m	10.6 m	1.1 m	11.6%
B-4	10.8 m	45.2 m	24.8°	45.6°	9.5 m	10.5 m	1.0 m	10.5%
B-5	10.4 m	50.0 m	17.3°	46.2°	9.5 m	12.5 m	3.0 m	31.6%
B-6	9.8 m	16.9 m	44.5°	40.9°	9.5 m	10.3 m	0.8 m	8.4%
B-7	10.2 m	17.5 m	44.5°	41.1°	9.5 m	10.2 m	0.7 m	7.4%
B-8	9.9 m	17.5 m	44.5°	41.2°	9.5 m	10.6 m	1.1 m	11.6%
B-9	10.3 m	32.0 m	38.0°	40.2°	9.5 m	9.6 m	0.1 m	1.1%
B-10	12.7 m	24.6 m	37.9°	39.8°	10.5 m	10.5 m	0.0 m	0.0%
B-11	10.4 m	32.0 m	37.5°	40.5°	9.5 m	9.0 m	-0.5 m	-5.3%
B-12	10.3 m	32.0 m	37.6°	40.7°	9.5 m	9.6 m	0.1 m	1.1%
B-13	10.2 m	32.6 m	38.1°	40.9°	9.5 m	8.7 m	-0.8 m	-8.4%
B-14	11.3 m	27.6 m	40.1°	41.2°	9.5 m	9.5 m	0.0 m	0.0%
B-15	10.6 m	27.6 m	41.8°	41.8°	9.5 m	8.1 m	-1.4 m	-14.7%
B-16	15.9 m	27.1 m	35.5°	42.2°	12.0 m	12.3 m	0.3 m	2.5%
B-17	9.8 m	27.3 m	41.1°	42.0°	9.5 m	11.2 m	1.7 m	17.9%
B-18	10.0 m	48.1 m	23.8°	46.7°	9.5 m	10.2 m	0.7 m	7.4%
B-19	9.9 m	52.1 m	22.8°	46.6°	9.8 m	11.0 m	1.2 m	12.2%
B-20	10.0 m	48.3 m	23.6°	46.5°	9.8 m	8.5 m	-1.3 m	-13.3%
B-21	9.9 m	32.1 m	27.9°	46.7°	9.8 m	15.5 m	5.7 m	58.2%
B-22	10.6 m	46.9 m	23.5°	46.9°	9.5 m	10.1 m	0.6 m	6.3%
B-23	9.7 m	22.8 m	22.0°	46.5°	9.5 m	9.5 m	0.0 m	0.0%
B-24	10.9 m	38.4 m	11.1°	50.4°	9.5 m	8.8 m	-0.7 m	-7.4%
B-25	11.2 m	35.8 m	13.3°	50.5°	9.5 m	11.5 m	2.0 m	21.1%
B-26	10.0 m	47.6 m	8.1°	50.2°	9.5 m	11.0 m	1.5 m	15.8%
B-27	9.1 m	31.6 m	10.0°	50.5°	9.5 m	10.8 m	1.3 m	13.7%
Mean							0.9 m	9.2%
Standard deviation							± 1.5 m	± 16.2%

approximated by a flat roof building. In this case, the height is underestimated by 1.3 m, which is in the range of the standard deviations for flat or gable roof buildings.

Building *C-2* has a rectangular footprint, but with a tower attached to it, which is oriented towards the SAR sensor. Furthermore, the roof structure is not a classical gable roof structure, where two sides of the roof are inclined, but a hipped roof where all four sides of the roof are inclined. We approximate this structure with a gable roof building, neglecting the tower, which results in an underestimation of 1.6 m.

Building *C-3* (Figure 6.11a and Figure 6.11b) is a flat roof building, which has three different heights. The major part (middle part) of the building is 7.0 m high, while the left and right parts are approximately 3.2 m and 0.5 m lower than the main part. We approximate this building with a standard flat roof building, which is, given the complex signature in the actual scene, a significant simplification. This is reflected in the estimation result, which overestimates the height by 2.9 m.

The main part of *C-4* is an industrial rectangular flat roof building, which has several lower building parts attached to it. For the estimation of the height of the main part, we

Table 6.3: Results for buildings where the structural shape of the actual building does not match our rectangular flat or gable roof models (category C) for the horizontal airborne scene.

Building	Width	Length	ϕ	Local θ	Height	Estimate	Difference	Relative Difference
C-1	10.8 m	25.5 m	21.1°	44.0°	12.5 m	11.2 m	-1.3 m	-10.4%
C-2	12.0 m	38.8 m	31.4°	43.2°	14.5 m	12.9 m	-1.6 m	-11.0%
C-3	21.5 m	42.7 m	33.4°	45.7°	7.0 m	9.9 m	2.9 m	41.4%
C-4	13.1 m	36.1 m	38.4°	45.0°	12.6 m	10.5 m	-2.1 m	16.7%
C-5	12.0 m	60.9 m	27.4°	43.4°	12.5 m	11.1 m	-1.4 m	-11.2%
C-6	11.5 m	57.6 m	40.9°	41.3°	12.0 m	12.7 m	0.7 m	5.8%
C-7	11.1 m	56.5 m	27.3°	45.4°	12.9 m	8.2 m	-4.7 m	-36.4%
Mean							-1.1 m	-5.5%
Standard deviation							± 2.4 m	± 24.1%

neglected the structures in the surrounding and assumed the building to be a standalone rectangular flat roof building, which resulted in an underestimation of 2.1 m.

Each of the building groups *C-5*, *C-6*, and *C-7* consists of three row houses with similar dimensions, which are not arranged in a perfect row, but are slightly staggered. In these cases we did not estimate the height for each building in the group separately, but considered a group as one individual flat or gable roof building. This implies that we do not model the correct footprint of the building group for the simulations, but approximate it by one rectangle. In Figure 6.11c and Figure 6.11d we show the building group *C-6* consisting of three gable roof buildings in the orthophoto and SAR image, respectively. In this situation the estimated height is 0.7 m higher than the true height. The gable roof building group *C-7* has the buildings positioned significantly staggered to each other. Hence the approximation as single gable roof building is quite rough, which can be seen in the significant underestimation by 4.7 m.

The overall mean and standard deviation for this category is -1.0 m ± 2.4 m. This is somewhat less accurate than in the other two categories, but still demonstrates that the method is relatively robust with respect to the structural assumption of the buildings.

Quality of height estimation

In order to detect outliers and to derive a representative overall assessment of the accuracy of the height estimation procedure, we carry out a statistical analysis of the results for the 33 buildings of category A and B. Since category C only contains buildings which do not fit the considered models, we do not take them into account for the assessment of the overall accuracy.

Figure 6.12a shows a normal Quantile-Quantile-Plot (Q-Q-Plot) for the estimation differences for the 33 buildings of category A and B. It highlights that the differences are normal distributed, with some outliers above 4 m. Using the Chauvenet's criterion [111, pp.166-8] to detect statistical outliers from the set of observations, we identified the estimations for the buildings *A-4*, *B-2*, and *B-21* as outliers.

Building *A-4* and *B-2* were overestimated by 4.4 m and 4.2 m, respectively, since they are largely surrounded by tall trees. This leads to a SAR signature which is different

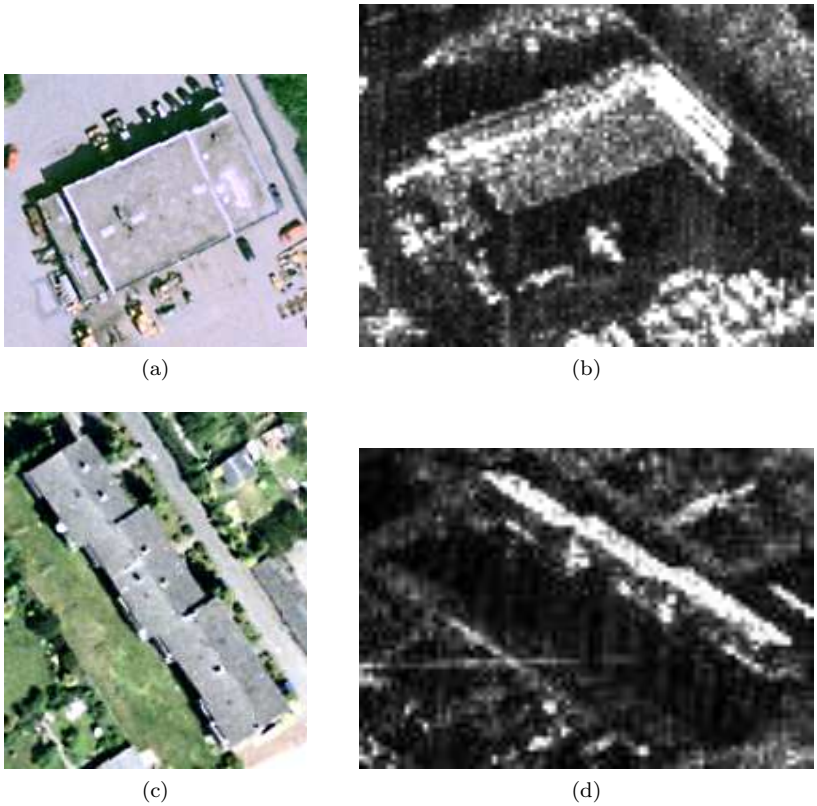

(a) (b)

(c) (d)

Figure 6.11: (a) Building *C-3* in orthophoto. (b) Building *C-3* in SAR image with viewing direction from the top. (c) Building *C-6* in orthophoto. (d) Building *C-6* in SAR image with viewing direction from the top. (Orthophoto: © Landesvermessungsamt NRW, Bonn, 2007; SAR image: © Intermap Technologies GmbH, 2003.)

from the signature of a building not affected by objects in the surrounding (which can be observed in Figure 6.7a by comparing the signature of *B-2* for example to the signature of building *B-4*). Since we do not model trees in the simulation procedure, they have an impact on the accuracy of the height estimation.

Building *B-21* was overestimated by 5.7 m since it is surrounded by a relatively smooth surface, giving it a low backscatter, similar to the shadow. Hence, the matching function does not capture well the edge of the shadow region of the building signature in the actual SAR image, leading to the overestimate in height. Hence, the shadow region of a building seems to be important for the method to estimate the correct height.

Figure 6.12b displays the Q-Q-Plot of the estimation differences where the three outliers were removed, which shows a good correspondence of the set with the normal distribution. The mean of the reduced set is 0.4 m, which demonstrates that the method has no significant preference for over- or undersegmentation, while the standard deviation of 1.0 m highlights the good estimation performance of the proposed approach.

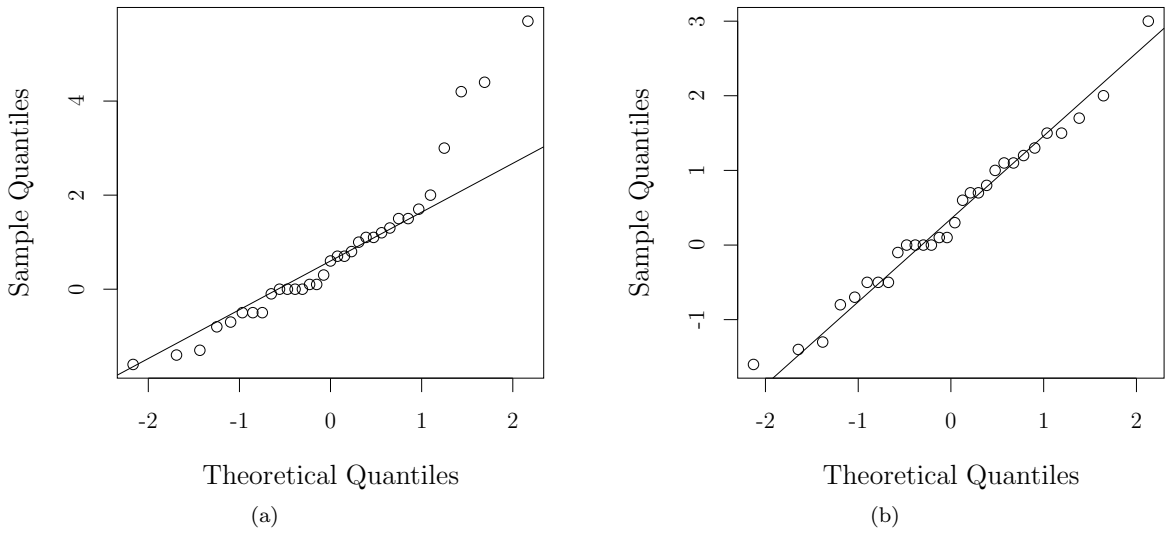

Figure 6.12: (a) Normal Q-Q-Plot for the 33 buildings of category *A* and *B*. (b) Normal Q-Q-Plot for the buildings of category *A* and *B* whereas three outliers were removed.

Effects of trees

Backscattering from trees positioned near a building tend to superimpose on the backscattering signature of the buildings, and, therefore, affect the accuracy of the height estimation. We analyze building *A-3* and *A-4*, which are very similar and have identical viewing configurations. The amount and the density of trees are similar for both buildings, whereas the relative locations of the trees are different (see Figure 6.6a and Figure 6.6b). Since the sensor images the buildings from the top of the image, the majority of trees which are in the immediate surrounding of building *A-3* are located in its layover area. For building *A-4*, instead, the majority of the trees which are close to the building are located behind the building, affecting its shadow area. The estimation errors of -0.5 m (*A-3*) and 4.4 m (*A-4*), confirm that the shadow area of the building plays an important role in the height estimation.

The density of trees surrounding the building weighs on the accuracy of the height estimation as well. Consider the buildings *B-2*, *B-4*, and *B-5*, which are three gable roof buildings with equal heights, located close to each other and with the same orientation towards the sensor. Building *B-4* has only some trees in the front, while building *B-5* has a higher density of trees in the front and some additional trees in the back, which are not as close and dense as for building *B-2*, which is completely surrounded by trees. The height estimation for *B-4* shows a difference to the actual height of 1.0 m, a difference of 3.0 m for building *B-5*, and 4.2 m for building *B-2*, demonstrating the limitation of the height estimation method in situations that are not conform with the model assumptions.

6.5.2 Vertical airborne scene

The vertical scene of the dual aspect data set was acquired such that the angle between the flight paths of the horizontal and vertical scenes is 84.5°. Hence, if the aspect angle of

Table 6.4: Actual and minimum distances between buildings *A-1* to *A-4* for the vertical airborne scene.

Buildings	Δ_{act}	Δ_{min}
A-1 ↔ *A-2*	22.7 m	26.6 m
A-2 ↔ *A-3*	19.8 m	23.0 m
A-3 ↔ *A-4*	19.7 m	21.2 m

a building was defined in the horizontal scene by the angle between the azimuth direction and the short wall of the building, it will be given in the vertical scene by the angle between the azimuth direction and the long wall of the building (see also Figure 3.3). The local incidence angle of a building might change significantly between the horizontal and vertical scenes depending on the location of the building. In the extreme case, the same building might be measured in one scene with 28° incidence angle, while it is measured in the other scene with 52°.

For category *A*, the height estimation procedure resulted in a mean error of 0.8 m with a large standard deviation of 5.4 m. The reasons for the low accuracy are buildings *A-1*, *A-2*, *A-3*, and *A-4*, which have estimation errors ranging from -7.5 m to 7.5 m. This is caused by the fact that these buildings are too close to each other, so that condition (6.12) is not fulfilled. A part of the shadow area of building *A-1* is superimposed by the layover area of building *A-2*. The actual and minimum distances between the buildings *A-1* to *A-4* are reported in Table 6.4.

The height estimation for the 27 buildings in category *B* resulted in a mean error of -0.4 m with a standard deviation of 1.9 m. These values are in the same order of magnitude as the ones from the horizontal scene.

For category *C*, the mean value of the error is 0.0 m with a standard deviation of 3.2 m. The reason for the higher standard deviations for categories *B* and *C* with respect to the horizontal scene is the incidence angle, which is for the horizontal scene on average 44.5° and for the vertical scene 37.8° (considering buildings in category *B* and *C*). The lower mean incidence angle for the vertical scene causes that the shadow areas are smaller with respect to the ones in the horizontal scene, confirming again the relative importance of the shadow feature for the height estimation.

6.5.3 TerraSAR-X scenes

The goal of the analysis of the TerraSAR-X scenes is mainly to investigate the effect of using a lower resolution spaceborne image compared to an airborne image. The ascending and descending scenes were acquired approximately from a north-south and south-north orbit, respectively, which are from an orientation point of view quite similar to the flight path from which the vertical airborne scene was measured (see Figure 6.5). In fact, the vertical airborne and the descending TerraSAR-X scenes were both acquired with a right looking sensor from a similar north-south path. The ascending TerraSAR-X scene was also acquired with a right looking sensor but from a south-north track, so that the buildings were measured from nearly the opposite side with respect to the descending TerraSAR-X and the vertical airborne scene. This implies that a building was measured with similar aspect angles throughout the ascending and descending TerraSAR-X and the

Table 6.5: Actual and minimum distances between buildings *A-1* to *A-4* for the ascending and descending TerraSAR-X scenes.

Buildings	Δ_{act}	Δ_{min} ascending	Δ_{min} descending
A-1 $\leftrightarrow$ *A-2*	22.7 m	25.5 m	26.2 m
A-2 $\leftrightarrow$ *A-3*	19.8 m	22.4 m	24.3 m
A-3 $\leftrightarrow$ *A-4*	19.7 m	20.3 m	20.9 m

vertical airborne scenes. The incidence angle varies within each of the TerraSAR-X scenes by only 1° over the swath, while there is a difference of 3° between the ascending and descending TerraSAR-X scenes (see Section 6.4).

In the ascending TerraSAR-X scene, the mean and standard deviation of the difference in height estimation for category *A* is -3.3 m and 5.8 m, respectively. The results for the descending TerraSAR-X scene show a similar mean of -3.4 m with a standard deviation of 4.3 m. The low accuracy for this category has the same reason as for the buildings in category *A* in the vertical airborne scene. The buildings *A1* to *A4* are located too close to each other so that the scattering effects of different buildings overlap with each other (see Section 6.5.2). In Table 6.5, we summarize the minimum distances required according to equation (6.12) and compare these to the actual values. Even though Δ_{min} between buildings *A-3* and *A-4* is quite similar to Δ_{act}, the height estimate of *A-4* is imprecise due to a high density of trees in the immediate surrounding of the two buildings.

The mean values for category *B* for the ascending and descending scenes are 1.9 m and -0.5 m, respectively. The standard deviations are 3.1 m and 3.4 m, respectively. The fact that they are very similar in both scenes points out a constant height estimation accuracy.

For the ascending scene, the estimation procedure for category *C* resulted in a mean value of -2.2 m and a standard deviation of 4.6 m. Those figures are -0.8 m and 1.3 m, respectively, for the descending scene. Since they are in the same order of magnitude as for categories A and B, the structural differences from the basic building assumptions are maybe less critical in lower resolution VHR spaceborne data.

The results for the TerraSAR-X data show that meter resolution VHR SAR data are not sufficient to get an accurate height estimate for the building dimensions that were investigated in this study. Nevertheless, if the height of a single floor of a building is approximately known, the method permits to estimate the number of floors of the building. This information can be of use for instance to distinguish between different types of buildings, such as residential housing, apartment buildings, industrial buildings or skyscrapers.

6.5.4 Dual aspect data sets

In this subsection we illustrate the results obtained by the joint usage of two aspects. First, we show the different intermediate results for the height estimation for one flat and one gable roof building from the airborne VHR SAR pair. On the basis of the three building categories we discuss then the summarized results.

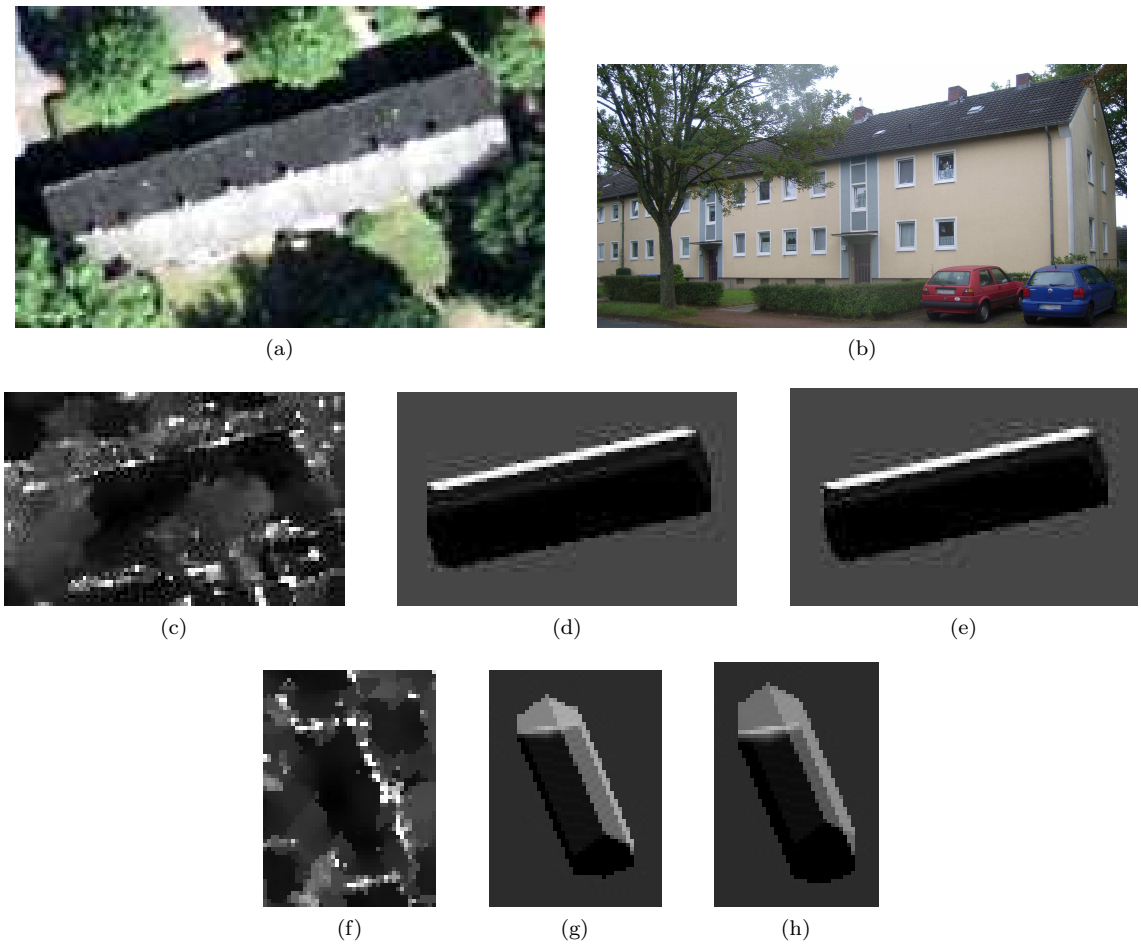

Figure 6.13: Gable roof building example *B-3*. (a) Building in orthophoto. (b) Photograph from the outside of the building. (c) Building in horizontal VHR SAR scene. (d) Simulation of building at height 10.6 m, which is the height estimated from the horizontal scene, with the viewing configuration of horizontal VHR SAR scene. (e) Simulation of building at height 9.6 m, which is the estimated height resulting from the fusion of the individual estimates, with viewing configuration of horizontal VHR SAR scene. (f) Building in vertical VHR SAR scene. (g) Simulation of building at height 6.9 m, which is the height estimated from the vertical scene, with viewing configuration of vertical VHR SAR scene. (h) Simulation of building at height 9.6 m, which is the estimated height resulting from the fusion of the individual estimates, with viewing configuration of vertical VHR SAR scene. The SAR scenes and simulations are with viewing direction from the top. (Orthophoto: © Landesvermessungsamt NRW, Bonn, 2007; SAR image: © Intermap Technologies GmbH, 2003.)

Detailed results for one flat and one gable roof building

To demonstrate the detailed results for an example for category *B*, we selected building *B-3*. Its dimensions and viewing configuration in the horizontal and vertical airborne scenes are summarized in Table 6.6. The building is shown in the orthophoto in Figure 6.13a and as photograph taken from the street passing in front of the building in Figure 6.13b. Figure 6.13c and Figure 6.13f show the building in the filtered horizontal- and vertical airborne VHR SAR scenes, respectively. The height estimation for the build-

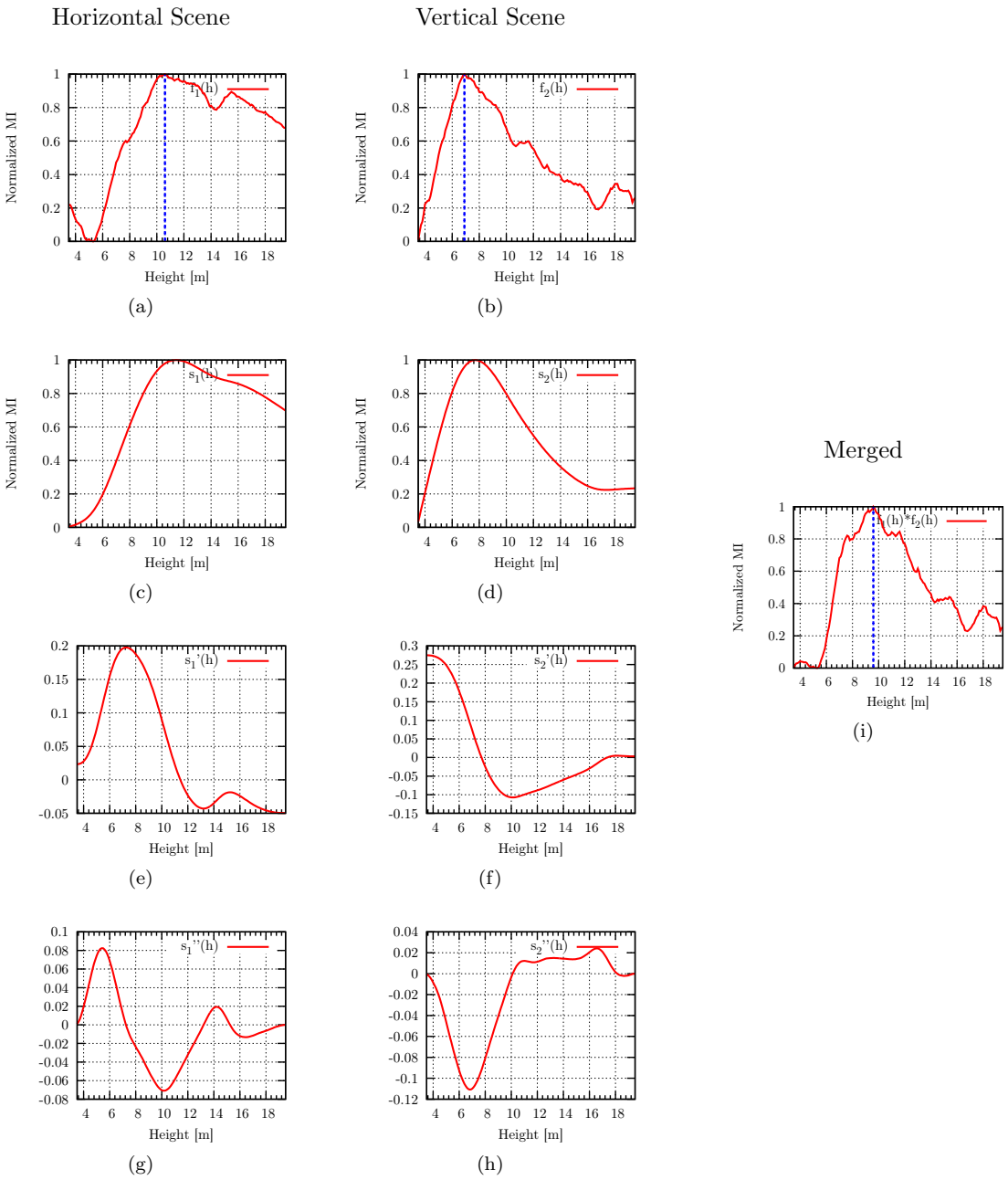

Figure 6.14: Intermediate results derived during the quality assessment and fusion procedure for building *B-3* in an interval from 3 m to 20 m. The left column shows the plots with respect to the horizontal scene, while the plots in the right column refer to the vertical scene. (a) and (b) Original similarity functions. (c) and (d) Splines of the similarity functions. (e) and (f) First derivatives of the splines. (g) and (h) Second derivatives of the splines. (i) Merged similarity function by multiplication.

ing from the horizontal scene results in the similarity function shown in Figure 6.14a having its maximum at 10.6 m, which is 1.1 m higher than h_{true}. The corresponding simulation of the building at height 10.6 m is shown in Figure 6.13d. The similarity

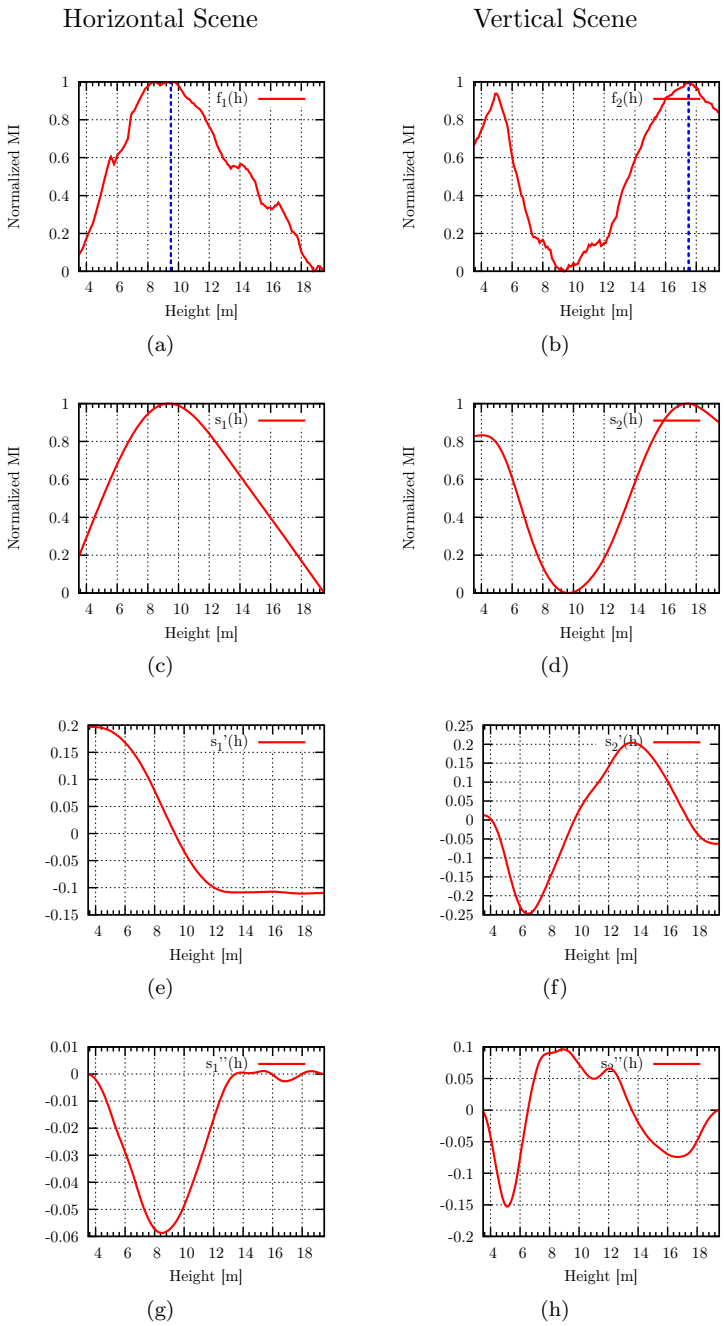

Figure 6.15: Intermediate results derived during the quality assessment and fusion procedure for building *A-3* in an interval from 3 m to 20 m. The left column shows the plots for the horizontal scene, while the plots in the right column refer to the vertical scene. (a) and (b) Original similarity functions. (c) and (d) Splines of the similarity functions. (e) and (f) First derivatives of the splines. (g) and (h) Second derivatives of the splines.

function in Figure 6.14b results from the height extraction for the building from the vertical scene. The graph has a maximum at 6.9 m, which is 2.6 m lower than h_{true}. The corresponding simulation at 6.9 m height is shown in Figure 6.13g. Both plots are charac-

Table 6.6: Detailed characteristics of two test buildings in the airborne VHR SAR scenes.

Building	Gable Roof (*B-3*)	Flat Roof (*A-3*)
Width	11.3 m	12.3 m
Length	45.2 m	36.3 m
Real Height	9.5 m	10.0 m
ϕ Horizontal Scene	20.5°	16.6°
θ Horizontal Scene	45.8°	45.6°
ϕ Vertical Scene	3.1°	1.4°
θ Vertical Scene	34.7°	35.6°

terized by smaller local minima and maxima, which are eliminated with a spline function. This results in the graphs shown in Figure 6.14c and Figure 6.14d, capturing the general behaviors of the similarity functions, which are analyzed during the functional analysis. Each of their respective first derivatives (Figure 6.14e and Figure 6.14f) has one local maxima. This indicates that $f_1(h)$ and $f_2(h)$ have relatively good estimation qualities. $s_1''(h)$ (Figure 6.14g) has three inflections points, while $s_2''(h)$ (Figure 6.14h) has two. It follows that neither of the two functions seems to be significantly better than the other, so that the final height estimate is based on the multiplication of $f_1(h)$ and $f_2(h)$, which is shown in Figure 6.14i. The maximization of $f_1(h) \cdot f_2(h)$ results in a final height estimate for the gable roof building of 9.6 m, which is 0.1 m higher than the true height. The corresponding simulations of the building are shown in Figure 6.13e and Figure 6.13h for the horizontal and vertical scenes, respectively. Instead of multiplying the two similarity functions, a simple averaging of h_1 and h_2 would result in a final estimate of 8.75 m, which is 0.75 m off the true height and hence 0.65 m less accurate than what is achieved with the fusion by multiplication.

As example for category A we selected building *A-3* (Table 6.6). Estimating the height for this building from the horizontal scene results in the similarity function shown in Figure 6.15a. It reaches its maximum at 9.5 m which is 0.5 m lower than h_{true} of the building. Instead, the similarity function resulting from the height estimation from the vertical scene (Figure 6.15b) has its maximum at 17.5 m, which is 7.5 m higher than the true height. Analyzing the splines of the two functions (Figure 6.15c and Figure 6.15d), we find that $s_1'(h)$ (Figure 6.15e) has one local maximum, while $s_2'(h)$ (Figure 6.15f) has two maxima. This means that $f_1(h)$ yields a significant better estimate of the height than $f_2(h)$. Hence, the final height estimate $\widehat{h}_{1,2}$ is the one from the horizontal scene. The second derivatives $s_1''(h)$ and $s_2''(h)$ (Figure 6.15g and Figure 6.15h) are not considered in this decision, since the first derivatives were sufficient to determine $f_1(h)$ as the estimate with higher quality, and are only shown for completeness.

Summary of height estimation results from dual aspect data sets for the test set of 40 buildings

In Table 6.7 we summarize the height estimation results for the full test set consisting of 40 buildings for the different scenes. The results for category B, the largest group of buildings, are consistent for the horizontal and vertical airborne scenes. The fusion invokes a slight increase in the estimation accuracy, between 0.1 m - 0.4 m compared to the single

Table 6.7: Summary of height estimation results from dual aspect data sets for the set of 40 buildings.

	Category A	Category B	Category C	$A + B$	$A + B + C$
Horiz.	0.3 m ± 2.1 m	0.9 m ± 1.5 m	-1.0 m ± 2.4 m	0.8 m ± 1.6 m	0.6 m ± 1.9 m
Vertic.	0.8 m ± 5.4 m	-0.4 m ± 1.9 m	0.0 m ± 3.2 m	-0.2 m ± 2.8 m	-0.2 m ± 2.8 m
Fused	0.7 m ± 1.9 m	0.5 m ± 1.5 m	0.4 m ± 2.0 m	0.6 m ± 1.5 m	0.6 m ± 1.6 m
Asc.	-3.3 m ± 5.8 m	1.9 m ± 3.1 m	-2.2 m ± 4.6 m	0.9 m ± 4.2 m	0.4 m ± 4.4 m
Desc.	-3.4 m ± 4.3 m	-0.5 m ± 3.4 m	-0.8 m ± 1.3 m	-1.0 m ± 3.7 m	-1.0 m ± 3.4 m
Fused	-2.9 m ± 5.2 m	1.7 m ± 3.0 m	-0.3 m ± 1.3 m	0.8 m ± 3.9 m	0.7 m ± 3.6 m

aspect horizontal and vertical scene results, respectively. The estimates for category C have less accuracy than the ones for category B, which is expected since the models which are simulated in category C do not fit the true situation. Here, the fusion of the estimates results in a more significant increase in accuracy which is between 0.4 m - 1 m. As already discussed in Section 6.5.2, the estimates for category A from the horizontal scene (standard deviation of 2.1 m) are significantly more accurate than the ones from the vertical scene (standard deviation of 5.4 m). The reason for this is that four out of the six buildings are positioned in such a way that they build a row. Since the azimuth direction of the horizontal scene is parallel to the row of buildings, it does not affect the estimates from the horizontal scene. However, for the vertical scene, the building row is approximately perpendicular to the azimuth direction. In this situation, the buildings are located too close to each other so that the scattering phenomena of two neighboring buildings interfere, which is not modeled in our approach. However, as highlighted in the discussion of the flat roof building, the proposed analysis of the similarity functions indicates that the estimates are not reliable and thus the quality assessment and fusion strategy eliminates the wrong estimates. This results in an accuracy, which is slightly better regarding the horizontal scene (0.1 m) and significantly better compared to the vertical scene (3.5 m). Considering the improvement for the categories $A + B$ for the airborne data, the average estimation accuracy was improved by 0.1 m and 1.3 m with respect to the horizontal and vertical scenes, respectively. The improvement for all three categories is 0.3 m for the horizontal scene and 1.0 m for the vertical scene.

Similarly to the airborne data, the fusion of the estimates from the TerraSAR-X data for category B results in a small improvement. The accuracy for category C for the ascending scene is significantly lower than for the descending one. Here, the fusion procedure could identify the good estimates so that the fused results for category C could be improved significantly with respect to the results from the ascending scene. The orientation for the azimuth directions for the ascending and descending scenes are very similar to the one from the vertical airborne scene. This implies that the row of buildings in category A is approximately perpendicular to the azimuth directions of the ascending and descending scenes, which explains the poor estimation quality for category A for the TerraSAR-X data (see also Section 6.5.3). In this situation, the fusion of the different estimates does not yield any increase in accuracy. Considering the results for categories $A + B$ and $A + B + C$ for the spaceborne case, no significant improvements could be achieved with respect to the estimation based only on single scenes.

In operational scenarios, the proposed quality assessment and fusion scheme can be

employed in a fully automatic way resulting in the final height estimate. Furthermore, the method is very well suited to be applied in a semi-automatic procedure, to integrate for instance additional expert knowledge in the height estimation process. We have achieved this by visualizing the functions and their derivatives for individual buildings (e.g in Google Earth™), which are then analyzed and fused in an interactive manner by a domain expert.

6.5.5 Computational aspects of method

The computational complexity of the proposed approach is still significant. A typical performance of the full height estimation is illustrated with the run-time results for building *A-2* estimate using the airborne horizontal scene. The platform used is a PC with two dual core 2.8 GHz Intel® Xeon™ CPUs and 3 GB RAM running the 32-bit Linux operating system (Ubuntu 8.04). Considering an explicit hypothesis generation from 3.0 m to 20.0 m in 0.1 m steps (171 hypotheses), the simulation process takes 67 minutes, while the matching procedure takes 16 minutes.

In order to avoid simulating a building at a certain viewing configuration more than once, we store all simulation results in a Database Management System (DBMS). If the combination of a building and viewing configuration is retrievable from the DBMS, then the simulation is simply loaded from the database. Otherwise, a new simulation is triggered and added to the database. In this way, a library of SAR building signatures is generated over time, decreasing, with increasing database size, the number of simulations needed per estimation cycle. An alternative solution to speed up the simulation process, which could be seamlessly combined with the DBMS, may use a very fast simulator based on the GPU, as proposed for instance in [68], achieving simulation run times in the order of milliseconds.

The matching procedure for a single building is a linear process (executed on a single CPU), in which the position ($\vec{s}$) for which the best coregistration for one hypothesis is found can be used as initialization for coregistering the subsequent hypothesis. However, additional building matches can be run in parallel. We use a clustered computing environment with 32 CPU cores. This leads to a gain in performance which is roughly proportional to the number of CPU cores available, apart from some minor overhead due to the task distribution in the cluster.

6.6 Discussion and conclusion

In this chapter we proposed a novel concept for building height estimation from single VHR SAR detected images and tested it on a representative set of residential area urban structures in Dorsten. The approach is based on a hypothesis generation - rendering - matching procedure, in which a series of building hypotheses with varying heights are rendered by a radar imaging simulator and the results are matched with the actual scene. The estimated height is given by the hypothesis whose simulation matches best with the actual scene. In such a scenario, the simulator needs to calculate effects related to the SAR geometry without modeling exact radiometry, since the use of detailed electromag-

Table 6.8: Overview of height estimation errors for the different building categories and analyzed scenes. A^* and B^* show the values for flat and gable roof buildings, respectively, where buildings which were identified as outliers and which do not fit the model assumptions are removed.

		A (6)	A^*	B (27)	B^*	C (7)
Width range		12.1 m - 15.8 m		9.7 m - 15.9 m		10.8 m - 21.5 m
Length range		35.8 m - 45.7 m		16.9 m - 52.1 m		25.5 m - 60.9 m
Height range		5.1 m - 12.5 m		9.5 m - 12.0 m		7.0 m - 14.5 m
Airborne	Horizontal	0.3 m ± 2.1 m	-0.5 m ± 0.6 m	0.9 m ± 1.5 m	0.6 m ± 1.1 m	-1.0 m ± 2.4 m
	Vertical	0.8 m ± 5.4 m	-	-0.4 m ± 1.9 m	-0.2 m ± 1.7 m	0.0 m ± 3.2m
TerraSAR-X	Ascending	-3.3 m ± 5.8 m	-	1.9 m ± 3.1 m	1.3 m ± 2.8 m	-2.2 m ± 4.6 m
	Descending	-3.4 m ± 4.3 m	-	-0.5 m ± 3.4 m	-0.8 m ± 2.4 m	-0.8 m ± 1.3 m

netic scattering models would imply the need for extensive a priori knowledge about the roughness parameters and dielectric constants of the surfaces in the scene. Such detailed parameters are generally not available in real world operational scenarios. The MI approach for matching model and observation is well suited in this context because it is sensitive to the spatial arrangement of features rather than to the absolute radiometry of the scattering effects.

We demonstrated the efficiency and generic nature of the proposed concept using dual aspect airborne and ascending and descending TerraSAR-X VHR SAR scenes, all covering the same test area. A test data set made up of 40 buildings, containing flat and gable roof buildings at different viewing configurations (i.e. various aspect and incidence angles) was used. To evaluate the robustness of the method with respect to the simplified assumptions on the building structure, we also included in the test data set buildings that only partially met our assumed rectangular flat or gable roof building models.

In Table 6.8 we list a summary of the accuracies for the three categories of buildings achieved in the different scenes. Considering the results for categories A^* and B^* (buildings which were categorized as flat or gable roof buildings excluding the buildings whose results were identified as outliers or which do not match the model assumptions) for the two submeter resolution airborne data, the standard deviation of the height estimation is 1.4 m, which means the method has a good overall estimation quality. The corresponding mean difference between estimation and actual height is 0.1 m indicating that the proposed method has no tendency to over- or underestimate the height. The overall standard deviation of the buildings in category B^* in the two TerraSAR-X scenes is 2.8 m. This shows that for meter resolution VHR SAR data the method can only provide rough height estimates, which can be used for instance to estimate the number of floors of the buildings. Such information is still of interest to characterize urban landscapes.

The detailed analysis of the category A and B highlighted that the method can handle

buildings with these two structural types. The results for the buildings which do not meet our assumptions (category C) show that the method is able to tolerate some degree of deviation from the assumptions, with the estimation results getting less accurate for higher degrees of simplification. This means that with a reliable information on the footprint and the type of building an accurate estimate of the height can be achieved, while in case of a limited availability of this information the method can still provide a rough estimate.

The approach is shown to be insensitive to the aspect angle of a building. This is an important characteristic because buildings in urban settings are typically not oriented in a systematic way. Airborne SAR has a higher flexibility to acquire imagery for multiple aspects, although this is usually costly. For spaceborne SAR, aspect angles in imagery are limited by the ascending and descending orbits of the satellite.

The analysis showed that the approach favors larger incidence angles. This is explained by the shadow areas, which become larger with increasing (shallower) incidence angles, suggesting an important role of the shadow area for an accurate estimate of the height. Furthermore, the results demonstrated that large trees, which backscattering interfere with the SAR shadow area of a building, decrease the accuracy of the method, which confirms the relatively important role of the shadow feature. One of the reasons for this is the approximation of the layover area by a homogeneous area. However, in reality, it is rather heterogeneous due to windows, balconies and other structures present at the front wall of a building having different materials and composing several smaller corner reflectors. Hence, the similarity between the simulated and the actual layover area is lower compared to the similarity between a simulated and actual shadow area. The importance of the shadow areas could be relaxed by modeling the building facade more accurately using facade grammar approaches [112]. The drawback of this would be the increased complexity of the building model and the need for additional a priori information on the building facades. Regarding the presence of trees or other disturbing objects in the neighborhood of a building, it would be relatively straightforward to log them at the footprint capturing stage, using VHR optical orthocorrected imagery. That information would then be useful to filter height estimation results.

The method assumes that buildings are isolated. The rendering procedure does not consider interferences between different buildings, which arise if they are positioned close enough so that for example their shadow and layover areas are not separated any more, but superimposed in a mixed area. This imposes the constraint that a building needs to have a minimum distance to a neighboring building (only if they are in the same azimuth position) so that no backscattering interferences from the different buildings occur. If this constraint is not fulfilled, the height estimation for the building is not accurate. The minimum distance between two buildings depends on the height of the neighboring buildings and on the local incidence angle: 1) the higher the buildings the larger the minimum distance; 2) the shallower the incidence angle, the larger the minimum distance and vice versa. Hence we suggest to acquire the VHR SAR imagery for rural and medium dense urban areas with a shallow incidence angle. In dense urban areas with low buildings instead, the data should be measured with a steep incidence angle, which relaxes the minimum distance constraint at the cost of a decreased estimation accuracy. The approach is not suitable for dense urban areas with high buildings.

In order to generate the hypotheses, we require information (i.e. footprint and type of building) derived from ancillary data. This information can either be provided as cadastral maps or can be directly extracted from the SAR image or other VHR optical data. With the growing global availability of VHR data from urban areas these requirements while demanding, appear to be realistic.

The results from the joint usage of dual aspect data sets showed that with a pair of airborne perpendicular scenes some improvements in the height estimation accuracy can be achieved. The usage of a TerraSAR-X scene pair acquired from ascending and descending orbits does not resolve complex scattering behavior, for instance, overlapping of backscattering signatures of adjacent buildings. Hence, no significant improvement in accuracy is evident in the TerraSAR-X pair. Given the current cost of acquiring and processing spaceborne VHR SAR data, the additional expenditure for a second scene is not justified. Instead, to achieve best accuracy with spaceborne data, the acquisition mode for the single scene should be selected such that complex scattering interferences between buildings are limited. For instance, the incidence angle should be selected in such a way that the actual distance between two buildings which are aligned as row perpendicular to the azimuth direction is larger than the sum of the shadow length of the building at the sensor close side and the layover length of the building at the sensor far side. The use of dual aspect airborne data acquired with perpendicular flight tracks has not only a positive effect on the estimation accuracy, but also increases the level of confidence in the final height estimate, since it is derived giving preference to individual estimates with high qualities. From our experience in analyzing the similarity functions we can state that the proposed functional analysis is a good indicator for the accuracy of the height estimate.

We want to stress that we addressed in this study an automatic information extraction scenario capable of dealing with different types of buildings at various viewing configurations. The proposed method was designed with a minimum number of constraints and minimal requirements on the data. Taking into account the ambitious objective of this study, and the fact that no a priori information on the height of buildings is used, we believe that the achieved quality of the estimation results is reasonable. Moreover, this study yielded first quantitative evidence of what can be expected from the new meter resolution spaceborne SAR sensors in terms of automatic information extraction in urban settings.

Chapter 7

A novel technique for earthquake damage assessment of buildings using VHR optical and SAR imagery

In this chapter[1], we present a novel method that detects buildings destroyed in an earthquake using pre-event VHR optical and post-event detected VHR SAR imagery. First, the 3-D parameters of a building are estimated from the pre-event optical imagery. Second, the building information and the acquisition parameters of the VHR SAR scene are used to predict the expected signature of the building in the post-event SAR scene assuming that it is not affected by the event. Third, the similarity between the predicted image and the actual SAR image is analyzed. If the similarity is high, the building is likely to be still intact, while a low similarity indicates that the building is destroyed. A similarity threshold is used to classify the individual buildings. We demonstrate the feasibility and the effectiveness of the proposed method for a subset of the town of Yingxiu, China, which was heavily damaged in the Sichuan earthquake of May 12, 2008. For the experiment we use QuickBird pre-event optical imagery, and TerraSAR-X and COSMO-SkyMed post-event SAR data. Post-event QuickBird and WorldView-1 imagery as well as ground photography is used as reference data.

7.1 Introduction to damage assessment based on SAR imagery

Information on the impact of a catastrophic event, e.g. an earthquake, can be derived from suitable satellite imagery by comparing data from a chosen reference before the event (pre-event) to imagery acquired shortly after the event (post-event). Optical VHR sensors have spatial resolutions finer than 1 m. Some of these sensors have existed for almost a decade and have already imaged large parts of the earth. The increased availability of this type of sensor and their growing image archives that are frequently updated, make VHR optical data well suited as the pre-event reference data source. If post-event VHR optical

[1] Part of this chapter appears in:
[113] D. Brunner, G. Lemoine, and L. Bruzzone, "Earthquake damage assessment of buildings using VHR optical and SAR imagery," *IEEE Transactions on Geoscience and Remote Sensing*, in press, 2010.

data are also available, general unsupervised change detection methods can be used to investigate the impact of the event [13], [14], [15], [114], [115]. Methods focused on the detection of damage to built-up structures are proposed in [116] and [117], but rely on a rapid supply of high quality optical VHR data, thus requiring nearly cloud free weather conditions and suitable solar illumination. Consequently, useful data of this type is not guaranteed shortly after an event.

The advantage of SAR imagery is its relative insensitivity to atmospheric conditions and independence from sun illumination. SAR data availability shortly after an event is thus, in principle only based on the SAR sensor's orbiting characteristics, i.e. the sensor's revisit capability. The COSMO-SkyMed sensor constellation currently has three satellites, allowing to revisit a target every 2-3 days, while TerraSAR-X has a revisit time of about 11 days. Unsupervised change detection methods using multitemporal SAR data have been proposed in [9], [16], and [118]. Methods utilizing the interferometric coherence to detect damages were proposed and demonstrated in [119] for the earthquake example in Kobe (Japan, 1995), in [120] for the Bam (Iran, 2003) earthquake and in [121] for the Izmir (Turkey, 1999) earthquake. Damage assessment methods for urban areas using medium and/or high resolution pre- and post-event SAR images based on changes in the backscatter coefficient and intensity correlation were proposed in [122] for the 2004 Indonesia earthquake, and in [123] and [124] for the Kobe earthquake. The latter approach is tested in [125] for the Bam and in [126] for the 2003 Algeria earthquakes. Methods for the generation of damage maps using pre- and post-event SAR and VHR optical imagery were proposed in [127] for the Bam earthquake. Hybrid methods using SAR in combination with GIS layers were proposed for the Bam earthquake in [10], for the Algeria and 2007 Peru earthquakes in [128], and with respect to the high seismicity of Tehran, Iran, in [129]. Terrain surface changes after the recent 2008 Sichuan, China, earthquake were investigated in [130] analyzing the difference image of multitemporal ALOS PALSAR data. A study about the appearance of damaged bridges in SAR was presented in [131].

A major improvement of the new VHR SAR sensors with spatial resolutions down to 1 m over coarser spatial resolution legacy spaceborne SAR sensors, such as Envisat or RADARSAT-1, is that VHR SAR can be used to analyze the structural integrity of individual urban structures, such as buildings and infrastructure elements. To derive this information, the spatial image patterns of the objects must be explored rather than the radiometric characteristics of individual pixels. Nevertheless, if change detection in a VHR SAR image pair is to be performed by means of a direct comparison at the pixel level, the image pair acquired must have the same acquisition parameters, and in particular the same viewing configuration. Any deviation will result in local image differences which are not necessarily related to changes on the ground. If such differences are not compensated for appropriately, they may lead to a high rate of false alarms. The spaceborne VHR SAR data archives are relatively recent and have limited pre-event imagery. In fact, since both COSMO-SkyMed and TerraSAR-X can operate in different resolution modes, archives are typically richer in coarser spatial resolution imagery (e.g. at 3 m - 10 m) than in 1 m resolution imagery. Consequently, VHR SAR is not yet a reliable source of pre-event reference data.

Considering the above mentioned practical difficulties, the best combination of imagery for rapid damage assessment is spaceborne VHR optical for the pre-event imagery and spaceborne VHR SAR for post-event imagery. However, it is difficult to compare them directly in a change detection approach because both types of data have entirely different radiometric and physical image formation characteristics. This challenge was addressed in [132], by statistically relating the two different observations in order to use a classical change detector, and was tested on a medium resolution SPOT-XS and ERS image pair. The information content in VHR imagery based on statistics is limited for building damage assessment because the spatial arrangement of pixels within an object provides the necessary information to perform this type of change detection.

In this chapter, we propose a novel method to assess the structural status of individual, rectangular buildings in an urban setting affected by a catastrophic event using pre-event VHR optical and post-event detected VHR SAR imagery. Given a set of buildings delineated from the pre-event image, the method determines from the post-event scene whether a building was destroyed or is still likely to be intact. The procedure is based on the concepts introduced in Chapter 6 for the estimation of building heights from single detected VHR SAR scenes. First, the 3-D measurements of a building are estimated from the pre-event imagery. The building information from step 1 and the acquisition parameters of the post-event VHR SAR scene are used to simulate the expected SAR signature of the building in the post-event SAR scene. Then, the similarity between the simulated and the actual SAR data is computed. Similarity suggests no change and that a building is likely to be intact, while dissimilarity suggests the opposite. The similarity decision is based on a Bayesian classifier which is applied in the final step of the procedure. We demonstrate the feasibility and analyze the performance of the proposed method on a subset of Yingxiu (31°03'40" N, 103°29'13" E), Wenchuan County, China, which was heavily damaged in the Sichuan earthquake on May 12, 2008. For the experiment, we use QuickBird pre-event optical imagery, and TerraSAR-X and COSMO-SkyMed post-event SAR data. Post-event QuickBird and WorldView-1 imagery as well as ground photography is used as the reference data.

The chapter is structured as follows: In Section 7.2 we review the microwave backscattering characteristics of damaged buildings defining the features of interest for our analysis. In Section 7.3 we describe the proposed similarity matching approach in detail. We introduce the test data set in Section 7.4 before we discuss the results of the method in Section 7.5. Finally, we draw the conclusions in Section 7.6.

7.2 Damaged building properties in VHR SAR

The backscattering characteristics of a damaged building in VHR SAR are strongly dependent on the type and the extent of destruction. Some damaged buildings generate SAR signatures similar and/or indistinguishable to those of undamaged buildings. Other damaged buildings are characterized by the absence of the expected building signature, and produce random scattering effects almost similar to speckle. In the following, we discuss three building examples in VHR SAR imagery with varying degrees and types of damage in comparison with optical satellite image samples and in-situ photographs.

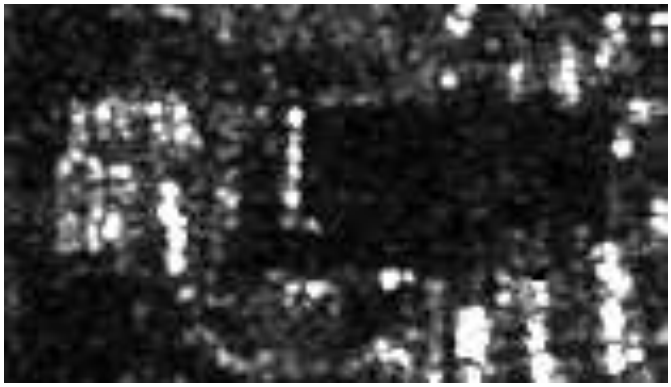

(a)

(b)

(c)

Figure 7.1: Example of a flat roof industrial building severely damaged, but still standing. (a) The same building in a TerraSAR-X image with 1 m resolution with viewing direction from the left. (b) The same building in a WorldView-1 image after the earthquake. (c) An in-situ photo of the building. (SAR image: © Infoterra GmbH/DLR, 2008; WorldView-1 image: © DigitalGlobe distributed by Eurimage S.p.A., 2008; Photo: © Eason Cheung, 2008.)

Corresponding image samples are taken from the study data set described in Section 7.4. The figures are discussed from the perspective of the SAR sensor. It follows that *before/in front of* refers in the image to something further to the left, while *after/behind* relates in the image to something further to the right. The corresponding buildings in the optical images are rotated with respect to the SAR data viewing configuration. The planar dimensions of the buildings given in the tables and throughout the text (width, length) are measured directly from the optical images and can be considered to be fairly accurate. Instead, building heights are derived by shadow analysis in the optical satellite imagery and only provide a rough estimate.

In Figure 7.1c we show an in-situ photo of a flat roof industrial building, with dimensions 25.6 m $\times$ 32.1 m $\times$ 16.8 m. The building is still standing but has obvious structural damage to the facade as evidenced by broken windows, missing plaster and cracks and holes in the walls. Figure 7.1b shows the building in a panchromatic WorldView-1 satellite image. Even though the building was imaged with a parallax showing the side wall, the damage as seen in Figure 7.1c is not evident due to the insufficient resolution. Fig-

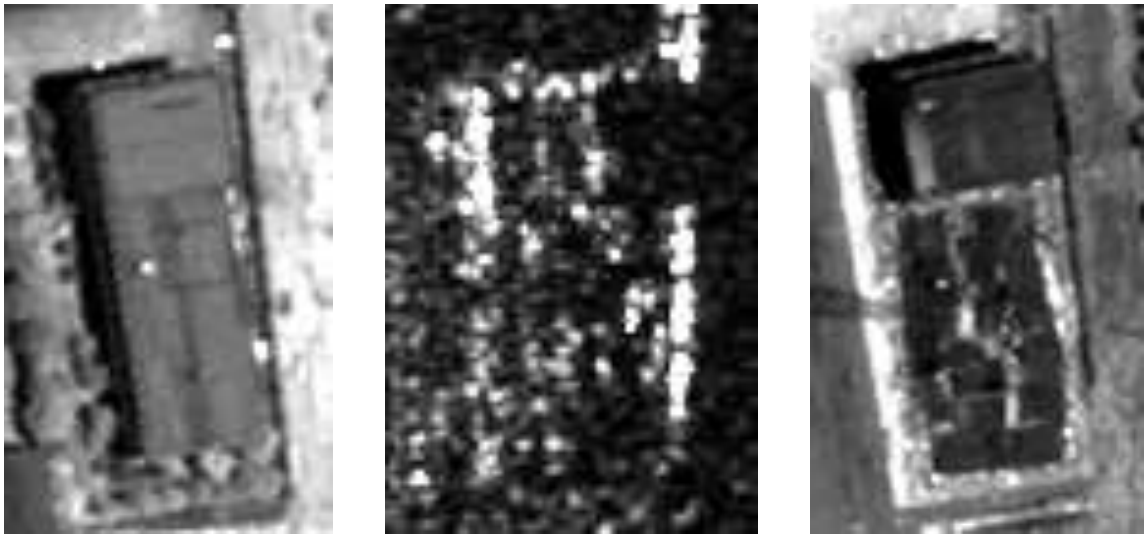

(a) (b) (c)

Figure 7.2: Example of a flat roof industrial building where 2/3 of the building are completely collapsed and 1/3 is still standing but damaged. (a) The same building in a QuickBird image (panchromatic channel) prior to the event. (b) The same building in a TerraSAR-X image with 1 m resolution with viewing direction from the left after the event. (c) The same building in a WorldView-1 image after the event. (QuickBird image: © DigitalGlobe distributed by Eurimage S.p.A.; SAR image: © Infoterra GmbH/DLR, 2008; WorldView-1 image: © DigitalGlobe distributed by Eurimage S.p.A., 2008.)

ure 7.1a shows the building in a TerraSAR-X scene with 1 m resolution, imaged with $\theta = 49.1°$ and $\phi = 3.0°$. The shadow is distinguishable from the surrounding scattering and has dimensions corresponding to the estimated height of the building derived from the shadow length in Figure 7.1b. However, the double bounce is not as pronounced as for the building in Figure 3.5, which may be due to the large openings caused by missing windows and holes in the wall facing the SAR sensor (see Figure 7.1c). Therefore, the single returns from the facade are pronounced leading to the bright backscattering spots visible in the layover area. Furthermore, due to the openings, part of the energy can follow multibounce paths in the inside of the building. These effects reduce the amount of energy which follows the standard double bounce path, resulting in a less bright double bounce stripe of the building. However, in the absence of a pre-event VHR SAR reference image, it is difficult to verify whether these effects are attributable to the structural damage of the building or not.

The flat roof industrial building shown in Figure 7.2a has dimensions 16.9 m × 50.4 m × 10.0 m and was imaged by QuickBird prior to the earthquake. The dark stripe behind the building is a metal fence. The same building is shown in Figure 7.2c after the event in a WorldView-1 panchromatic image. The lower two-thirds of the building completely collapsed leaving the rest damaged but still standing. A meter resolution TerraSAR-X image with $\theta = 49.1°$ and $\phi = 1.0°$ of the same building is shown in Figure 7.2b. The fence is very pronounced where the building collapsed because it acts as a metal corner reflector oriented parallel to the azimuth direction. The part of the building which is still standing produces the expected building signature with the double bounce, the roof scattering, and

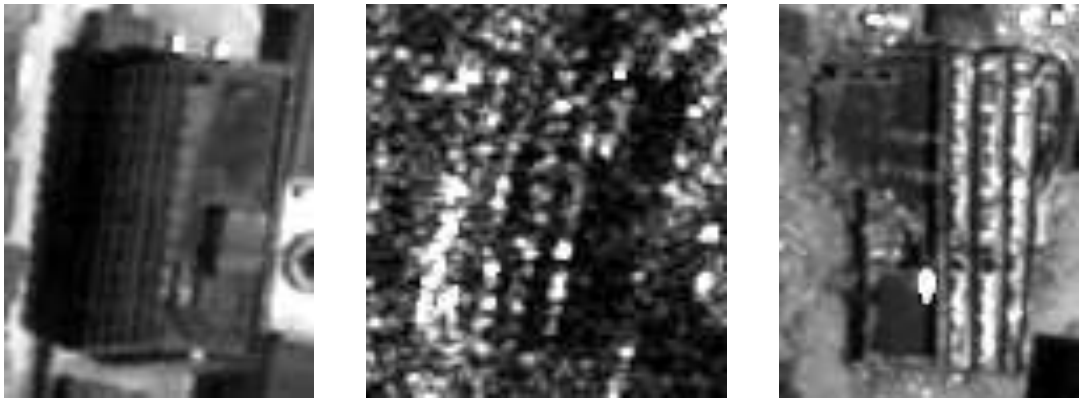

(a) (b) (c)

Figure 7.3: Example of a flat roof building, which is tilted to the side. (a) The same building in QuickBird image (panchromatic channel) prior to the event. (b) The same building in TerraSAR-X image with 1 m resolution with viewing direction from the left. (c) The same building in WorldView-1 image after the event. (QuickBird image: © DigitalGlobe distributed by Eurimage S.p.A., 2005; SAR image: © Infoterra GmbH/DLR, 2008; WorldView-1 image: © DigitalGlobe distributed by Eurimage S.p.A., 2008.)

the shadow areas being visible. The bright stripe of the fence is interrupted since part of it is occluded by the building and thus located in the shadow area. The collapsed part of the building lacks a clear backscattering signature. It has no double bounce, layover-, roof-, or shadow region and exhibits random scattering from the rubble of the collapsed building, similar to SAR speckle found in homogeneous regions.

The final example in Figure 7.3a shows a flat roof building with dimensions 15.1 m × 42.9 m × 26.1 m prior to the earthquake. The earthquake caused the whole building to tilt to the side as shown in the post event WorldView-1 imagery (Figure 7.3c). Figure 7.3b shows the same building in a TerraSAR-X scene with $\theta = 49.1°$ and $\phi = 10.4°$. At first glance, the scattering signature in the SAR image could be interpreted as the one from a building which is still standing. It shows a bright stripe similar to a double bounce, a distinct shadow region, and some brighter scattering area between the double bounce and the shadow that could be interpreted as roof scattering. The bright point scatterers in this area are likely related to metal structures on the roof. The absence of a visible layover region is not a damaged building indicator because it is not always visible even for undamaged buildings as shown in Section 3. However, given its original dimensions and the viewing configuration of the SAR acquisition, it can be observed that the signature does not correspond to the original building, i.e. the shadow area is too short, and the roof scattering region is too long.

The examples presented above demonstrate that not all types of building damage are readily discernible in meter resolution VHR SAR imagery as shown in Figure 7.1. The damage of buildings can only be observed where at least parts of the corpus or the roof have collapsed. Hence, we will focus in this chapter on the detection of completely destroyed buildings rather than on buildings which have suffered damage but are still standing. Furthermore, damaged buildings do not have a distinct scattering signature in VHR SAR, which is challenging for the development of automatic detection methods. Moreover, a

collapsed building may still produce a signature similar to undamaged structures, as shown in Figure 7.3. Consequently, information about the situation prior to the event are required to distinguish between damaged and undamaged buildings in the post-event VHR SAR scene. In the following we will show how we incorporate the information from the pre-event imagery in the damage detection approach.

7.3 Proposed methodology for damage assessment of buildings using VHR optical and SAR imagery

Let us consider the subset of a VHR optical image X_1 with a building and the corresponding subset of a VHR SAR scene X_2 acquired at different times t_1 (pre-event) and t_2 (post-event) with $t_1 < t_2$. Let $\Omega = \{\omega_u, \omega_d\}$ be the set of classes of undamaged and damaged buildings, respectively. As demonstrated in Section 7.2, damaged buildings in VHR SAR do not have an unique pattern with which they can be easily detected. Therefore, we model the problem of classifying a building into the classes ω_u and ω_d by evaluating in X_2 the presence or absence of the expected VHR SAR signature of the undamaged building. To do this, we extract the parameters of a building from the pre-event imagery, predict its VHR SAR signature in the post-event SAR scene (assuming that the building is undamaged), and compare the simulation with the actual scene. Similarity between simulation and actual scene indicates that a building is likely to be intact, whereas dissimilarity indicates that a building is likely to be destroyed. As shown in Figure 7.4, the proposed methodology consists of three main sections: 1) parameter extraction; 2) Rendering/Matching Analysis (RMA); and 3) classification of the RMA result into damaged and undamaged building. The method works on each building footprint separately and, thus is applied to each building tested for damage.

Figure 7.4 indicates that a direct pixel based coregistration between the optical pre-event and SAR post-event image (including the conversion of the SAR image from slant to ground range), which is a challenging topic [133], is not required. The extracted information on a building from the optical image (parameter extraction) is transformed by a simulator (rendering) into the slant range geometry of the actual SAR scene. In particular, a small image subset is rendered, containing only the scattering features belonging to the building under investigation. Since the pre- and post-event images are georeferenced, the approximate position of the investigated building in the actual SAR imagery is known. Therefore, only a local fine coregistration between simulation and actual SAR scene is required prior to the matching. This coregistration is implicit in the proposed matching procedure.

7.3.1 Building parameter extraction

As shown in Figure 7.4, two sets of parameters are extracted first: 1) the shape and size of the building extracted from X_1; and 2) acquisition parameters for X_2.

The width, length, height, and the roof inclination angle of the building are estimated from X_1. For 1 m resolution satellite data it is sufficient to distinguish between flat and gable roof buildings, because errors in the estimation of α_r are not significant at this

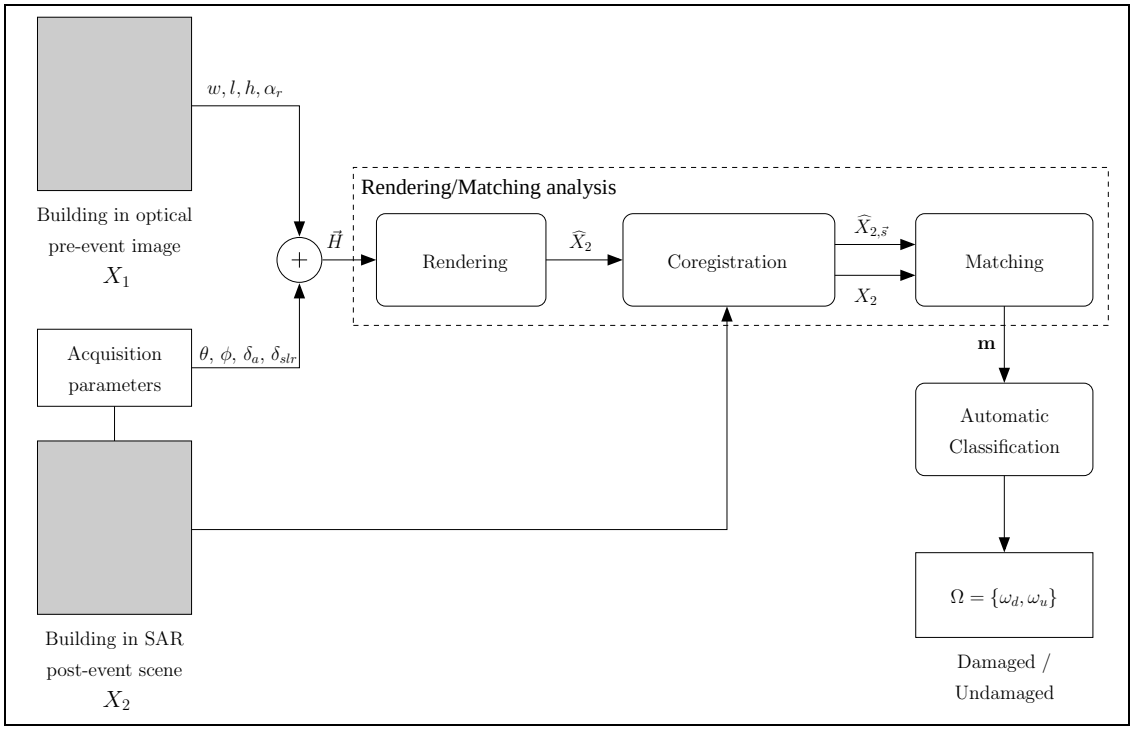

Figure 7.4: Block scheme of the proposed method for building damage detection from VHR optical and VHR SAR images. The procedure is applied to each building which shall be investigated for damage separately.

resolution. For flat roof buildings $\alpha_r = 0°$. For gable roof buildings the roof inclination angle can be set to a default angle, which is typical for the regional building style or class of buildings (e.g. industrial, residential), for instance $\alpha_r = 30°$. The building width and length are manually extracted from the building footprint, while the height is computed based on the length of the shadow cast by the building knowing the sun illumination at the time X_1 was acquired. While the width, length, and height were computed here manually, semi-automatic [134], [135], and fully automatic building detection and reconstruction methods [136], [137], are also available. Some of the required parameters could also be extracted from other data sources such as cadastral maps, LIDAR data [138], [139], or optical stereo pairs [140]. However, since the availability of these types of data is often limited, we use only a single spaceborne VHR optical scene as the source for the pre-event data. For a discussion on the effects of errors in the height estimation and how we compensate for in this case, the reader is referred to Section 7.3.4.

From the post-event VHR SAR data we extract the azimuth resolution, the slant range resolution, and the incidence angle. The aspect angle with which the building was imaged by the SAR sensor is calculated based on the azimuth direction of the SAR acquisition and the orientation of the building wall, which is facing the sensor, estimated from the optical image. The simulation is parameterized in the following manner:

$$\vec{H} \equiv \{w, l, h, \alpha_r, \theta, \phi, \delta_a, \delta_{slr}\}\,. \tag{7.1}$$

7.3.2 Rendering and matching analysis

A SAR imaging simulator is used to render $\vec{H}$ to produce $\widehat{X}_2$, i.e. the undamaged building SAR signature. As already discussed in Section 6.2.2, electromagnetic models cannot be adopted in our application scenario to calculate the backscattering, since we aim at extracting building information whereas roughness parameters and the dielectric properties of the materials in the scene are generally unknown a priori. Hence, we use the simulator proposed in Chapter 5, which approximates the relative differences in backscatter taking into account the dominant geometrical effects of surface and dihedral scattering, but does not calculate absolute radiometry based on material and surface roughness parameters.

For the evaluation of the match between $\widehat{X}_2$ and X_2, the two images are coregistered:

$$m = \max_{\vec{s}} \left\{ F[\widehat{X}_{2,\vec{s}}(\vec{H}), X_2] \right\}, \tag{7.2}$$

with F being the similarity measure and $\widehat{X}_{2,\vec{s}}$ the translation of the image $\widehat{X}_2$ by the two dimensional vector $\vec{s} = \{\Delta x, \Delta y\}$. The result of this maximization is also the final result of the evaluation of the matching between the simulated and the actual scene. Note that the orientation with which the building was imaged in the actual SAR scene, i.e. the aspect angle ϕ, is considered in the simulation (see (7.1)), which means that the simulated building is already oriented as it is in the actual VHR SAR scene. Hence, no rotation is required for accurate coregistration, but translation is enough. Indeed, in order to locate the considered building from the optical pre-event image also in the post-event SAR scene, a high accuracy (in the order of few meters) of the geolocation of the two scenes is assumed. This requires especially in mountainous areas geocoding with the use of an accurate digital terrain model. In case the overall geocoding is not precise enough, manual tie points may be selected to locally register the pre- and post-event SAR data.

For the coregistration and matching we compare the actual SAR data with speckle to the synthetic images without speckle, i.e. the geometry of the images are similar but the local statistics in the comparison are different. Furthermore, the radiometry of the simulated image differs with that of the actual scene. Therefore, we used in (6.3) MI as the similarity measure because of its suitability to multimodal image matching/registration tasks. However, MI depends on the overlap/size of the two images that are compared [141]. Since we evaluate the absolute value of the matching analysis to distinguish between damaged and undamaged buildings it needs to be invariant to the size of the overlap. Thus, we use here the Normalized Mutual Information (NMI) [142] for F in (7.2). Various NMI measures were proposed in the literature so far. We consider here three different versions, which we compare in the results section according to their performance for the damage detection task:

- The *symmetric uncertainty coefficient* proposed by Saerndal [143]:

$$SAE(\widehat{X}_2, X_2) = \frac{MI(\widehat{X}_2, X_2)}{\frac{1}{2}[H(\widehat{X}_2) + H(X_2)]}. \tag{7.3}$$

- The NMI proposed by Joe [144]:

$$JOE(\widehat{X}_2, X_2) = \frac{MI(\widehat{X}_2, X_2)}{\min[H(\widehat{X}_2), H(X_2)]}. \tag{7.4}$$

- The NMI proposed by Studholme [141]:

$$STU(\widehat{X}_2, X_2) = \frac{H(\widehat{X}_2) + H(X)}{H(\widehat{X}_2, X_2)}. \tag{7.5}$$

The values of SAE and JOE range between $[0, 1]$. Note that SAE has not necessarily the value 1 if there is a perfect dependence between $\widehat{X}_2$ and X_2 while this is guaranteed for JOE [142]. In fact, STU is not a strict normalization of MI but rather a version that is less sensitive to changes in the size of the overlap [145] and does not have a predefined range of values ($STU > 0$).

For the rectangular simulation results, the ratio between the number of pixels belonging to the scattering effects from the object (foreground pixels) and the number of pixels belonging to the ground scattering of the surrounding (background pixels) varies for different buildings and viewing configurations. To ensure that the classification of the buildings in the data set is neither guided by the foreground nor by the background, we only consider for the similarity calculation those pixels that are part of an expanded object mask, as explained in detail in Section 6.2.3.

7.3.3 Identifying damaged and undamaged buildings

After the RMA analysis, we classify the building into $\Omega = \{\omega_u, \omega_d\}$ by thresholding the value of m. Assuming that both class distributions are Gaussian, we can perform this in a supervised or an unsupervised way. Both methods are based on the Bayes rule:

$$\text{Decide } \omega_u \text{ if } p(Y(i)|\omega_u) \cdot P(\omega_u) > p(Y(i)|\omega_d) \cdot P(\omega_d);\ \text{otherwise decide } \omega_d, \tag{7.6}$$

where $P(\omega_u)$ and $P(\omega_d)$ are the prior probabilities of the classes ω_u and ω_d, respectively. The conditional probability density functions are denoted by $p(Y|\omega_u)$ and $p(Y|\omega_d)$, whereas Y is the random variable representing the m values of the I observations in the set $Y_{RMA} = \{Y(i), 1 \leq i \leq I\}$. Using (7.6) as criterion is equivalent to applying a threshold T_0 calculated by solving the likelihood ratio with respect to Y [146]:

$$\frac{P(\omega_d)}{P(\omega_u)} = \frac{p(Y|\omega_u)}{p(Y|\omega_d)}. \tag{7.7}$$

In the Gaussian case, this is equivalent to solving the quadratic equation:

$$(\sigma_u^2 - \sigma_d^2) \cdot T_0^2 + 2 \cdot (\mu_u \cdot \sigma_d^2 - \mu_d \cdot \sigma_u^2) \cdot T_0 + \mu_d^2 \cdot \sigma_u^2 - \mu_u^2 \cdot \sigma_d^2 - 2 \cdot \sigma_u^2 \cdot \sigma_d^2 \cdot ln \left[\frac{\sigma_d \cdot P(\omega_u)}{\sigma_u \cdot P(\omega_d)}\right] = 0, \tag{7.8}$$

with μ_u and μ_d denoting the mean values, and σ_u and σ_d the standard deviations of the classes ω_u and ω_d, respectively. The resulting decision criterion is given by:

$$\text{Decide } \omega_u \text{ if } Y(i) > T_0;\ \text{otherwise decide } \omega_d. \tag{7.9}$$

For the supervised procedure, the parameters for (7.8) are calculated from a training set. For the unsupervised procedure, T_0 is calculated automatically [146] by deriving the statistical parameters and the prior probabilities of the two classes using the Expectation Maximization (EM) algorithm [147], [148]. In particular, the probability density function $p(Y)$ of Y is modeled as a mixture density distribution composed by two density components:

$$p(Y) = p(Y|\omega_u) \cdot P(\omega_u) + p(Y|\omega_d) \cdot P(\omega_d). \tag{7.10}$$

Since we model $p(Y|\omega_u)$ and $p(Y|\omega_d)$ as Gaussian distributions, the statistical parameters and the prior probabilities for the classes ω_k, $k = \{u, d\}$, can be derived iteratively with the EM algorithm by the following equations [149]:

$$P^{t+1}(\omega_k) = \frac{\sum\limits_{Y(i)\in Y_{RMA}} \frac{P^t(\omega_k)\cdot p^t(Y(i)|\omega_k)}{p^t(Y(i))}}{I}, \tag{7.11}$$

$$\mu_k^{t+1} = \frac{\sum\limits_{Y(i)\in Y_{RMA}} \frac{P^t(\omega_k)\cdot p^t(Y(i)|\omega_k)}{p^t(Y(i))} \cdot Y(i)}{\sum\limits_{Y(i)\in Y_{RMA}} \frac{P^t(\omega_k)\cdot p^t(Y(i)|\omega_k)}{p^t(Y(i))}}, \tag{7.12}$$

$$(\sigma_k^2)^{t+1} = \frac{\sum\limits_{Y(i)\in Y_{RMA}} \frac{P^t(\omega_k)\cdot p^t(Y(i)|\omega_k)}{p^t(Y(i))} \cdot [Y(i) - \mu_k^t]^2}{\sum\limits_{Y(i)\in Y_{RMA}} \frac{P^t(\omega_k)\cdot p^t(Y(i)|\omega_k)}{p^t(Y(i))}}, \tag{7.13}$$

where the superscripts t and $t+1$ refer to the current and next iterations, respectively.

7.3.4 Height estimation error compensation

The accuracy with which the width and length of a building can be estimated from the VHR pre-event imagery is directly related to the spatial resolution of the pre-event image. An acceptable precision for simulating a submeter resolution VHR SAR building signature can be achieved using submeter X_1 data. However, the height of the building must be derived from the 2-D pre-event image by:

$$h = l_s \cdot \tan(\theta_s), \tag{7.14}$$

with l_s being the length of the shadow and θ_s the sun elevation angle. Considering for instance the relatively fine spatial resolution of the panchromatic channel of the QuickBird sensor (0.6 m) and a sun elevation angle of 75°, the height resolution assuming a 1 pixel planar measurement error is $\delta_h = 2.2$ m. For tall buildings, this height accuracy can be slightly improved by oversampling the original 11-bit integer image and interpolate a line along the strong shadow edge features giving a more precise measurement of the shadow length. Nevertheless, the δ_h estimate given above is a practical compromise. It follows that the height estimate can only be considered as a rough estimate $\widetilde{h}$ of the building height.

In Chapter 6 we demonstrated that the maximum similarity between the synthetic image and actual scene is achieved for simulations of buildings which use the true building height. In other words, the matching values are lower if the difference between the

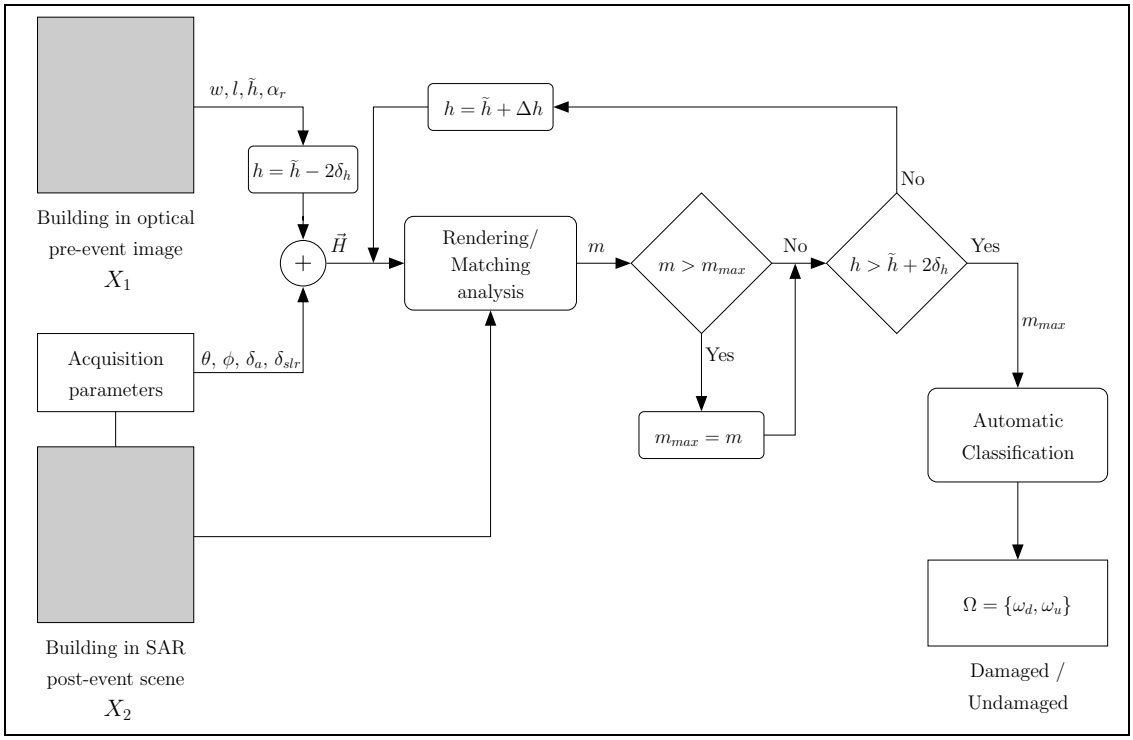

Figure 7.5: Block scheme of the proposed method for building damage detection from VHR optical and VHR SAR imagery including an error compensation step for building height estimation inaccuracies.

simulated and the true building height increases. By performing the RMA iteratively for a range of building heights and classifying the best match value m_{max} which occurred during the RMA iterations, inaccuracies in the height estimation process can be compensated for. This procedure only affects undamaged buildings because they do not show any characteristic building signature in the SAR post-event imagery anyway. The height range used for the RMA is defined by $h \in [\widetilde{h} - 2\delta_h, \widetilde{h} + 2\delta_h]$ and thus (7.2) can be extended to:

$$m_{max} = \max_{\vec{s}, h \in [\widetilde{h} - 2\delta_h, \widetilde{h} + 2\delta_h]} \left\{ F\left[\widehat{X}_{2,\vec{s}}(\vec{H}), X_2\right] \right\}. \tag{7.15}$$

The resulting matching process is illustrated in Figure 7.5 and is an extension of Figure 7.4. We maximize (7.15) with respect to the two variables jointly, but in two different ways. For the maximization with respect to $\vec{s}$ we use the multidimensional Nelder-Mead [90] (or downhill simplex) function optimization method. For maximizing with respect to h we perform a brute force search in the given interval with the height sampling frequency Δh. The smaller Δh is, the more accurate the result, but the more computationally expensive the process is. A value of $0.10\delta_h$ was chosen as a good trade off between accuracy and computation time. Alternatively, the Nelder-Mead or other function maximization methods such as simulated annealing could be directly used to jointly maximize for $\vec{s}$ and h. In the first case, the number of simulations and the simulation heights are fixed by Δh, while in the second case they are variable and determined at runtime influenced by the initialization parameters of the function maximization method.

Table 7.1: Parameters of VHR optical data.

Sensor	QuickBird	QuickBird	WorldView-1
Label	pre-QB	post-QB	post-WV
Date of acquisition	2005-06-26	2008-06-03	2008-06-27
Resolution (Panchromatic)	0.6 m	0.6 m	0.5 m
Resolution (Multi-spectral)	2.4 m	2.4 m	-

Indeed, just using the function optimizer to optimize with respect to both variables might lead to a lower number of simulations with respect to the brute force solution. However, the drawback is that function maximization is an intrinsically linear process, which means that it is executed sequentially on a single processor. In order to decrease significantly the computational time, we distribute the function optimization of (7.15) in a grid framework in such a way that each CPU in the grid performs a simulation for a certain height together with the maximization with respect to $\vec{s}$. Another advantage of the brute force solution is that an averaging over the NMI values in a height interval centered at h, for instance $[h-0.4m; h+0.4m]$, can be performed efficiently, which avoids instability in the similarity measure.

To distinguish between the different NMI versions with which m_{max} can be calculated we define $m_{max,SAE}$, $m_{max,JOE}$, and $m_{max,STU}$ as being m_{max} calculated using $SAE(\widehat{X}_2, X_2)$, $JOE(\widehat{X}_2, X_2)$, and $STU(\widehat{X}_2, X_2)$, respectively.

7.3.5 Building location constraint

The RMA can handle different building types at various dimensions that were imaged by the SAR sensor at different viewing configurations (i.e. changing θ and ϕ). However, the simulation does not take into account interferences from other objects in the vicinity of the buildings. Therefore, reliability of the method increases with building isolation, which is given if the condition (6.12) (see Section 6.2.4) is fulfilled. If Δ_{min} (6.11) is larger than the actual distance between the buildings, the shadow region of the first building interferes with the layover region of the second building which is not considered in the simulation process. Other objects in the immediate surrounding, e.g. trees, are also not taken into account in the simulation.

In practice, the RMA of a building whose backscattering signature overlaps with those of other objects in the vicinity will have a lower match value than the RMA of a building with no structures in the local surrounding. Consequently, the classification error will be influenced depending on the number and type of objects in the surrounding area. Commission errors, whereby undamaged buildings are classified as damaged, lead to an overestimation of class ω_d. Note that buildings with numerous objects in the surrounding can already be flagged when building outlines are delineated earlier in the process.

7.4 Data set description

Sichuan province, China, experienced an earthquake with a magnitude of 8.0 on the Richter scale on May 12, 2008. The earthquake's epicenter was located in Wenchuan

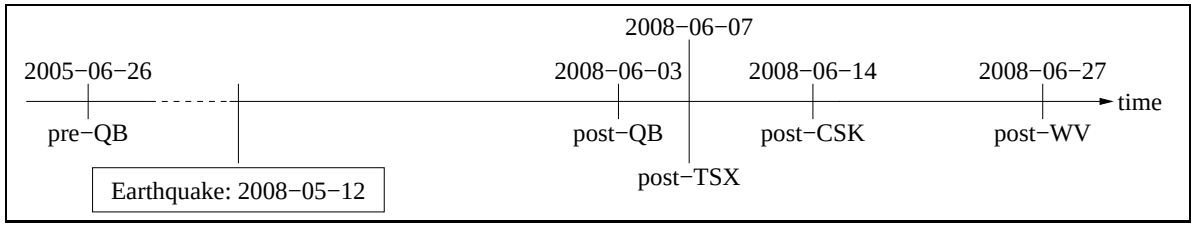

Figure 7.6: Overview of available scenes showing their temporal sequence.

County, Sichuan province and left 70,000 people killed, 375,000 people injured, and 4.8 million people homeless [150]. The above method is tested on the town of Yingxiu (centered at 31°03'40" N, 103°29'13" E), which had about 7000 inhabitants prior to the event [151]. It is located near the epicenter of the earthquake and was, with about 80% destruction, one of the most affected areas. Weather conditions were cloudy in the period after the event, and therefore the acquisition of cloud-free VHR optical data for assessing the damage was difficult. The first satellite images after the event were acquired by COSMO-SkyMed and TerraSAR-X on May 13, 2008 and May 14, 2008, respectively, but in lower resolution mode (SM, 3 m spatial resolution). The earthquake occurred one year after the launch of the first COSMO-SkyMed and TerraSAR-X VHR SAR sensors and was the first important natural disaster for which meter resolution spaceborne VHR SAR post-event data were available. No pre-event VHR SAR data exist for this region, however.

The only available pre-event VHR optical imagery was an archived QuickBird scene (pre-QB) acquired on June 26, 2005, which we used to establish the reference situation X_1. For the post-event reference data there are two VHR optical scenes: one QuickBird (post-QB), and one WorldView-1 (post-WV) (see Table 7.1 for a reference data summary). The pre-QB image was acquired three years prior to the event. Comparing the pre- and post-event optical images land cover changes were identified in some parts of the area. Consequently, we have excluded areas with extensive pre-event change from the damage assessment.

Two VHR SAR scenes were acquired (Table 7.2), which we used as post event data X_2. The TerraSAR-X scene (post-TSX) was taken in ascending mode while the COSMO-SkyMed scene (post-CSK) was taken in descending orbit. Given that both scenes were acquired with a right looking antenna, they show the same area from opposite viewing

Table 7.2: Parameters of SAR post-event acquisitions.

Sensor	TerraSAR-X	COSMO-SkyMed
Label	post-TSX	post-CSK
Date of acquisition	2008-06-07	2008-06-14
Mode	HS	Enhanced SL
Resolution ($\delta_a \times \delta_{slr}$)	1.1 m ×1.0 m	0.7 m × 0.7 m
Original pixel spacing	0.5 m × 0.5 m	0.7 m × 0.5 m
Resampled pixel spacing	0.75 m × 0.75 m	0.75 m × 0.75 m
Incidence Angle	49.5°	50.5°
Look direction	Right	Right
Orbit direction	Ascending	Descending

(a)

(b)

(c)

Figure 7.7: Image subsets of the optical scenes in the data set showing the same area in Yingxiu. (a) Pre-QB image. (b) Post-QB image. (c) Post-WV image. (QuickBird images: © DigitalGlobe distributed by Eurimage S.p.A., 2005 and 2008; WorldView-1 image: © DigitalGlobe distributed by Eurimage S.p.A., 2008.)

directions. Both scenes were resampled, using the pixel aggregate function in ENVI, to 0.75 m pixel spacing and speckle filtered with the Gamma MAP filter. Note that only one scene is required to carry out the damage assessment. In case of the supervised classification, both scenes are used in order to train the Bayesian classifier on one scene and test it on the other one. Relative acquisition times of the available images are illustrated in Figure 7.6. Note that the post-CSK and post-TSX postings do not illustrate the expected

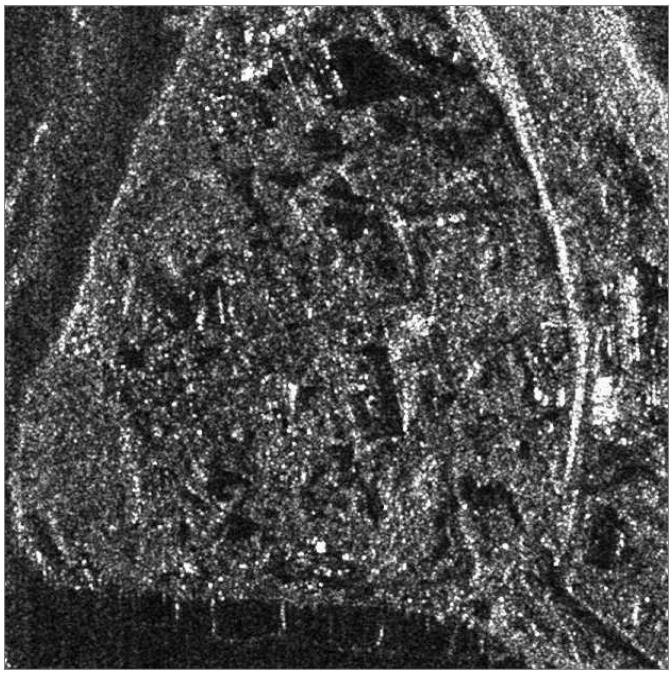

(a)

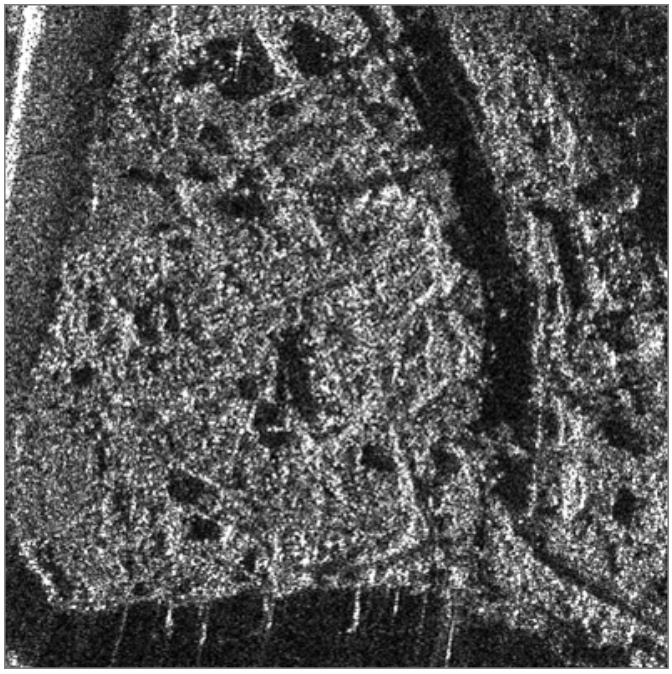

(b)

Figure 7.8: Image subsets of the SAR scenes in the data set showing the same area in Yingxiu as in Figure 7.7. (a) Post-TSX image, with viewing direction from left to right. (b) Post-CSK image with viewing direction from right to left. (TerraSAR-X image: © Infoterra GmbH/DLR, 2008; COSMO-SkyMed image: © Italian Space Agency (ASI) distributed by eGeos S.p.A., 2008.)

response time of post-event VHR SAR that is crucial in a damage assessment scenario. This is due to saturation of the programming requests for both platforms at the time, most of which were for lower resolution modes, and with higher priority. In the meantime, two additional COSMO-SkyMed sensors have been launched providing greater acquisition flexibility. Image subsets of all available scenes of the same area of Yingxiu are shown in Figure 7.7 and Figure 7.8.

7.5 Results

After analyzing the optical pre- and post-event imagery, we selected for each class in Ω a set of 15 individual candidate buildings. All are flat roof buildings, because this is the prevailing building type in the area under investigation. The selection of candidate buildings is driven by the need to test the methodology in an accurate way and was mainly limited by the following issues:

1. The town is not very large, thus the number of candidate buildings is limited;
2. The pre-event image was acquired about three years prior to the event, thus, in our analysis we had to exclude those areas of the town for the analysis which could be identified as already changed prior to the event (e.g. newly developed areas, changes in road outlay);
3. The earthquake itself was very destructive so that few undamaged buildings could be found;
4. According to the present assumptions of the proposed method, buildings should be isolated; thus structures in the dense part of the town were not considered;
5. After a destructive earthquake, the affected area typically experiences many significant changes in a short period. For instance, buildings that are structurally damaged but still standing may be quickly demolished. Temporary housings may also be build to house the displaced population or to support humanitarian relief. The post-QB and post-WV imagery straddle the acquisition period of the post-TSX and post-CSK scenes (see Figure 7.6) and only buildings that appear in both the post-QB and the post-WV data in the same state (either both damaged or both undamaged) were chosen for this analysis. This excludes, for instance, three buildings which were apparently undamaged in the post-QB image, but appeared to be demolished in the post-WV scene. Hence, the true status of these buildings in the post-TSX and post-CSK scenes is unknown. We visually interpreted the post-TSX and post-CSK scenes to assess the status of these three buildings and found that one building appeared damaged in the post-TSX scene, meaning that it must have been demolished in the period from 2008-06-03 to 2008-06-07 and is considered belonging to ω_d. The other two buildings were found to be still standing in the post-CSK scene so that they must have been demolished between 2008-06-14 and 2008-06-27. We classified these building as ω_u. Note that we do not consider the three buildings for the quantitative evaluation of the performance of the proposed method. Instead, they are the topic of the discussion at the end of this section.

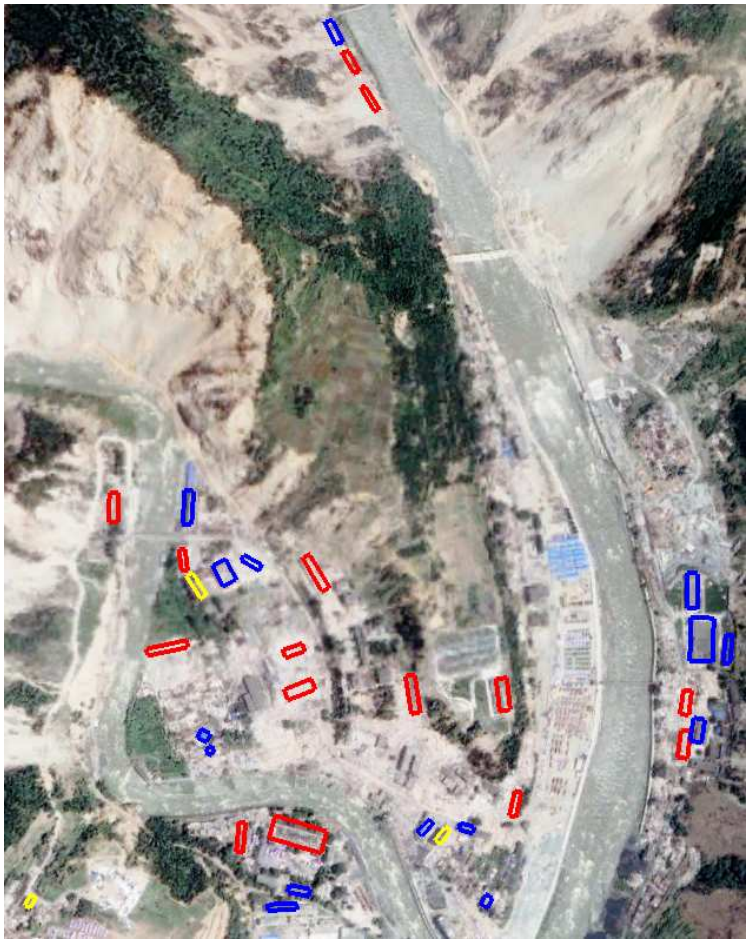

Figure 7.9: Footprints of selected buildings overlaid to the post-QB image, giving an overview of the distribution of the candidates in the test set. Buildings of class ω_d are marked with red polygons, while blue polygons correspond to the class ω_u. The yellow polygons show the three buildings where the true status in the post-TSX and post-CSK is unknown. (QuickBird image: © DigitalGlobe distributed by Eurimage S.p.A, 2005.)

In Figure 7.9 we show the geographic distribution of the buildings in the test set overlaid with the post-QB image. The buildings of class ω_u and ω_d are distributed uniformly over the investigated area, as the entire city was stricken equally by the earthquake.

The parameters of the undamaged buildings in ω_u are listed in Table 7.3 with each building denoted as $\omega_u^{[i]}$, where i is a building identifier. The kinds of buildings found in this class are quite diverse. Their widths range from 9.7 m - 34.4 m, their lengths from 11.4 m - 68.5 m, and their heights from 7.1 m - 16.1 m. Since the two VHR SAR scenes were acquired by spaceborne sensors, there is little variation in the local incidence angles within each scene. Furthermore, the difference between the incidence angles of the post-TSX and post-CSK scenes is only about 1°. The aspect angles with which the buildings were imaged vary in the post-TSX scene between 4.2° - 40.2°, and for the post-CSK scene between 0.8° to 36.6°. The two buildings that were visually assessed in the post-CSK and post-TSX images are $\omega_u^{[16]}$ and $\omega_u^{[17]}$.

Table 7.3: Undamaged building parameters.

Name	w	l	h	post-TSX		post-CSK	
				θ	ϕ	θ	ϕ
$\omega_u^{[1]}$	15.3 m	55.2 m	10.1 m	49.1°	8.2°	50.3°	9.3°
$\omega_u^{[2]}$	34.4 m	68.5 m	11.2 m	49.1°	5.8°	50.3°	7.6°
$\omega_u^{[3]}$	10.1 m	44.7 m	16.5 m	49.1°	9.0°	50.3°	4.5°
$\omega_u^{[4]}$	17.7 m	36.7 m	10.1 m	49.1°	14.3°	50.3°	0.8°
$\omega_u^{[5]}$	12.9 m	37.9 m	9.3 m	49.1°	20.3°	50.4°	35.9°
$\omega_u^{[6]}$	13.9 m	52.2 m	11.2 m	49.1°	7.9°	50.4°	4.4°
$\omega_u^{[7]}$	23.2 m	36.6 m	14.9 m	49.1°	21.1°	50.4°	36.1°
$\omega_u^{[8]}$	9.7 m	44.5 m	12.3 m	49.1°	4.2°	50.4°	11.6°
$\omega_u^{[9]}$	12.8 m	18.0 m	13.5 m	49.1°	34.8°	50.4°	21.2°
$\omega_u^{[10]}$	10.9 m	22.6 m	8.9 m	49.1°	21.4°	50.4°	7.9°
$\omega_u^{[11]}$	10.4 m	26.9 m	10.8 m	49.1°	40.2°	50.4°	36.6°
$\omega_u^{[12]}$	15.0 m	16.2 m	7.8 m	49.1°	35.6°	50.4°	20.7°
$\omega_u^{[13]}$	9.9 m	11.4 m	7.1 m	49.1°	33.9°	50.4°	20.4°
$\omega_u^{[14]}$	10.0 m	31.7 m	7.1 m	49.1°	35.8°	50.4°	20.5°
$\omega_u^{[15]}$	11.6 m	33.3 m	11.9 m	49.1°	17.2°	50.4°	2.8°
$\omega_u^{[16]}$	10.9 m	26.4 m	11.2 m	49.1°	40.8°	50.4°	33.5°
$\omega_u^{[17]}$	9.5 m	17.7 m	10.1 m	49.1°	37.4°	50.4°	19.8°

Table 7.4: Damaged building parameters.

Name	w	l	h	post-TSX		post-CSK	
				θ	ϕ	θ	ϕ
$\omega_d^{[1]}$	11.2 m	35.1 m	9.7 m	49.1°	25.6°	50.4°	39.2°
$\omega_d^{[2]}$	7.9 m	42.0 m	10.5 m	49.1°	25.2°	50.4°	40.9°
$\omega_d^{[3]}$	13.5 m	38.0 m	14.9 m	49.1°	12.8°	50.3°	1.4°
$\omega_d^{[4]}$	15.1 m	42.9 m	24.3 m	49.1°	10.4°	50.3°	2.3°
$\omega_d^{[5]}$	16.9 m	50.4 m	11.2 m	49.1°	0.8°	50.4°	15.5°
$\omega_d^{[6]}$	14.2 m	45.0 m	3.7 m	49.1°	5.7°	50.4°	8.7°
$\omega_d^{[7]}$	13.2 m	32.7 m	14.9 m	49.1°	12.8°	50.4°	25.1°
$\omega_d^{[8]}$	9.4 m	34.1 m	14.9 m	49.1°	0.9°	50.4°	15.7°
$\omega_d^{[9]}$	11.1 m	39.9 m	18.3 m	49.1°	21.5°	50.4°	6.2°
$\omega_d^{[10]}$	14.5 m	59.9 m	13.1 m	49.1°	3.3°	50.4°	17.7°
$\omega_d^{[11]}$	12.7 m	60.5 m	11.2 m	49.1°	24.2°	50.4°	39.9°
$\omega_d^{[12]}$	35.7 m	85.3 m	11.2 m	49.1°	22.3°	50.4°	7.7°
$\omega_d^{[13]}$	17.5 m	46.5 m	13.1 m	49.1°	14.4°	50.4°	28.6°
$\omega_d^{[14]}$	10.6 m	46.1 m	7.5 m	49.1°	11.2°	50.4°	9.1°
$\omega_d^{[15]}$	10.8 m	63.9 m	16.1 m	49.1°	5.1°	50.4°	21.0°
$\omega_d^{[16]}$	11.0 m	41.4 m	13.1 m	49.1°	26.7°	50.4°	41.4°

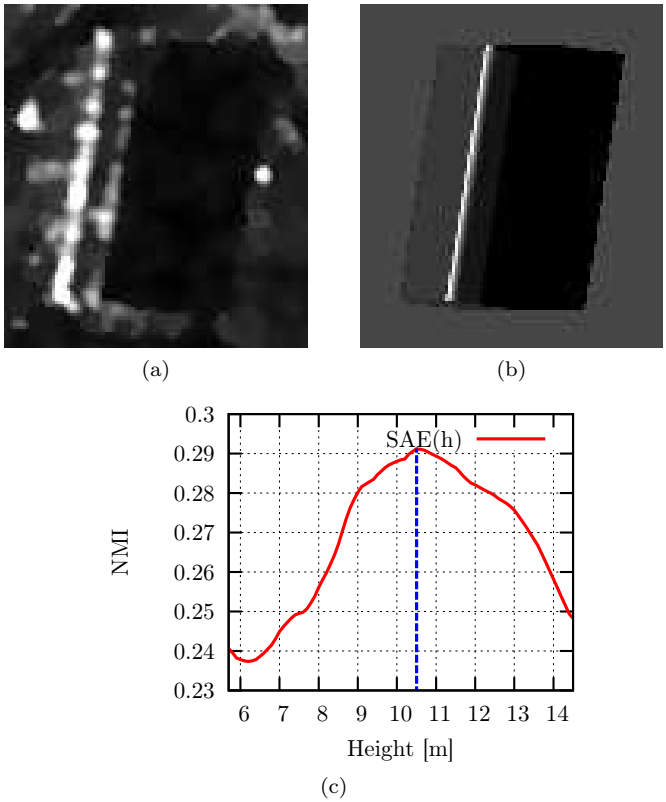

Figure 7.10: RMA example for the undamaged building shown in Figure 3.5 using SAE (7.3) as the similarity measure. (a) Image subset of building in filtered post-TSX scene. Simulation and actual scene are coregistered. (b) Simulated building at height where the similarity is highest ($h = 10.5$ m). (c) Plot of similarity as a function of height. (SAR image: © Infoterra GmbH/DLR, 2008.)

The building characteristics of ω_d are provided in Table 7.4 and distinguished by the identifier i in $\omega_d^{[i]}$. The set of buildings in class ω_d is as diverse as those in ω_u. The widths vary between 7.9 m - 35.7 m, the lengths between 32.7 m - 63.9 m and the heights from 3.7 m - 24.3 m. The aspect angle varies in the post-TSX scene from 0.8° - 25.6° and in the post-CSK scene from 1.4° - 40.9°. $\omega_d^{[16]}$ is the building which appeared undamaged in the post-QB scene and damaged in the post-WV scene. The diversity of the buildings in both classes is relevant to the testing of the robustness of the classification results and to demonstrate that the proposed method can handle buildings having a wide range of characteristics.

7.5.1 Results of RMA for damaged and undamaged buildings

Detailed results for an undamaged building example

In Figure 7.10 we show the detailed results of the proposed method for building $\omega_u^{[1]}$. This is the same building found in the post-WV image in Figure 3.5a. The corresponding filtered image of the unfiltered subset (Figure 3.5b) is presented in Figure 7.10a. Based on the pre-QB images we estimated the building height to be 10.1 m. With $\delta_h = 2.2$ m

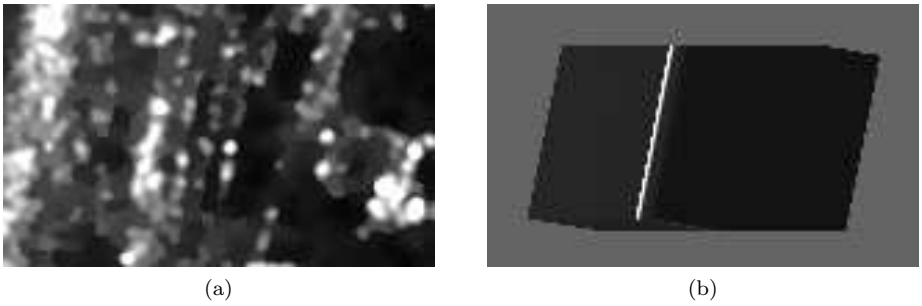

(a) (b)

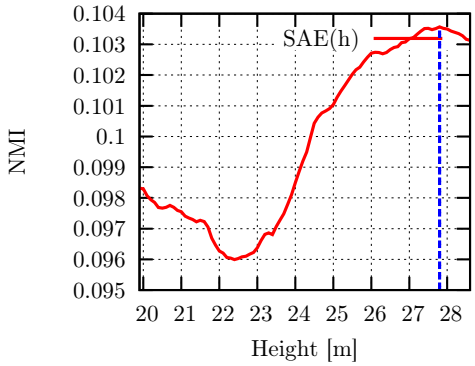

(c)

Figure 7.11: RMA example for the damaged building shown in Figure 7.3 using *SAE* (7.3) as the similarity measure. Viewing direction is from the left. (a) Image subset of building in filtered post-TSX scene. (b) Simulated building at height where the similarity is highest ($h = 27.8$ m). (c) Plot of similarity as a function of height. (SAR image: © Infoterra GmbH/DLR, 2008.)

(see Section 7.3.4), the RMA is applied to simulations with varying heights in the range of [5.7 m, 14.5 m]. This result is plotted in Figure 7.10c. The greatest similarity (m_{max}) is achieved with a value of $h = 10.5$ m. All points of the plot are greater than 0.23. Such high similarity values indicate that the simulations are similar to the actual scene and that the building in the post-TSX image is undamaged. Indeed, comparing visually the actual scene (Figure 7.10a) with the simulation at $h = 10.5$ m (Figure 7.10b), we find significant similarity between the two images.

Detailed results for a damaged building example

Detailed results for the damaged building $\omega_d^{[4]}$ are provided in Figure 7.11. The corresponding subsets of the post-WV and the original post-TSX scenes are found in Figure 7.3. The computed similarity vs. height plot (Figure 7.11c) is characterized by dissimilarity because the values are lower than 0.11 for heights ranging between [19.9 m,28.7 m]. Consequently, the building is most likely damaged. In fact, a visual comparison between the simulation at $h = 27.8$ m (Figure 7.11b) and the actual scene (Figure 7.11a) shows that the predicted signature of the building does match the actual scene at all.

Table 7.5: Match values of undamaged buildings.

Name	post-TSX						post-CSK					
	SAE		*JOE*		*STU*		*SAE*		*JOE*		*STU*	
	m_{max}	h_{est}	m_{max}	h_{est}	m_{max}	h_{est}	m_{max}	h_{est}	m_{max}	h_{est}	m_{max}	h_{est}
$\omega_u^{[1]}$	0.291	10.5 m	0.499	10.6 m	1.170	10.5 m	0.238	10.1 m	0.382	10.5 m	1.135	10.1 m
$\omega_u^{[2]}$	0.144	10.2 m	0.236	10.2 m	1.077	10.2 m	0.130	6.8 m	0.211	6.8 m	1.070	6.8 m
$\omega_u^{[3]}$	0.179	14.2 m	0.343	14.2 m	1.098	14.2 m	0.231	11.8 m	0.377	11.8 m	1.131	11.8 m
$\omega_u^{[4]}$	0.200	6.1 m	0.342	5.7 m	1.111	6.1 m	0.208	8.5 m	0.346	8.5 m	1.116	8.5 m
$\omega_u^{[5]}$	-	-	-	-	-	-	0.207	6.9 m	0.368	6.2 m	1.115	7.0 m
$\omega_u^{[6]}$	0.252	9.9 m	0.473	10.5 m	1.144	9.9 m	0.227	6.8 m	0.366	6.8 m	1.128	6.8 m
$\omega_u^{[7]}$	0.226	14.1 m	0.398	14.1 m	1.128	14.1 m	0.184	10.5 m	0.305	10.5 m	1.101	10.5 m
$\omega_u^{[8]}$	0.208	7.9 m	0.373	7.9 m	1.116	7.9 m	0.218	7.9 m	0.380	7.9 m	1.122	7.9 m
$\omega_u^{[9]}$	0.300	10.1 m	0.515	10.3 m	1.176	10.1 m	0.278	9.0 m	0.456	9.1 m	1.161	9.0 m
$\omega_u^{[10]}$	0.246	4.6 m	0.422	4.6 m	1.140	4.6 m	0.264	5.5 m	0.439	5.0 m	1.152	5.5 m
$\omega_u^{[11]}$	0.279	10.3 m	0.513	10.3 m	1.162	10.3 m	0.292	8.5 m	0.505	8.5 m	1.171	8.5 m
$\omega_u^{[12]}$	0.264	8.8 m	0.432	8.6 m	1.152	8.8 m	0.263	7.2 m	0.447	3.4 m	1.152	6.8 m
$\omega_u^{[13]}$	0.331	6.1 m	0.512	6.0 m	1.198	6.1 m	0.327	6.7 m	0.564	6.7 m	1.195	6.7 m
$\omega_u^{[14]}$	0.195	3.1 m	0.364	3.0 m	1.108	3.1 m	0.195	8.9 m	0.319	6.8 m	1.107	9.1 m
$\omega_u^{[15]}$	0.199	11.9 m	0.329	11.5 m	1.110	11.9 m	0.243	9.3 m	0.436	9.5 m	1.138	9.3 m
$\omega_u^{[16]}$	0.224	6.8 m	0.417	6.8 m	1.126	6.8 m	0.209	6.8 m	0.389	6.8 m	1.117	6.8 m
$\omega_u^{[17]}$	0.265	9.5 m	0.447	9.5 m	1.153	9.5 m	0.267	5.7 m	0.450	5.7 m	1.154	5.7 m
μ_u	0.237		0.411		1.135		0.234		0.393		1.133	
σ_u	0.053		0.085		0.034		0.048		0.086		0.031	

Table 7.6: Match values of damaged buildings.

Name	post-TSX			post-CSK		
	$m_{max,SAE}$	$m_{max,JOE}$	$m_{max,STU}$	$m_{max,SAE}$	$m_{max,JOE}$	$m_{max,STU}$
$\omega_d^{[1]}$	-	-	-	0.163	0.296	1.089
$\omega_d^{[2]}$	-	-	-	0.155	0.305	1.083
$\omega_d^{[3]}$	0.119	0.228	1.063	0.154	0.290	1.085
$\omega_d^{[4]}$	0.104	0.200	1.055	0.124	0.227	1.066
$\omega_d^{[5]}$	0.196	0.309	1.108	0.163	0.293	1.089
$\omega_d^{[6]}$	0.185	0.291	1.102	0.185	0.293	1.102
$\omega_d^{[7]}$	0.137	0.255	1.074	0.167	0.296	1.090
$\omega_d^{[8]}$	0.179	0.312	1.099	0.145	0.273	1.078
$\omega_d^{[9]}$	0.162	0.284	1.088	0.125	0.228	1.067
$\omega_d^{[10]}$	0.167	0.303	1.091	0.137	0.241	1.073
$\omega_d^{[11]}$	0.180	0.334	1.099	0.168	0.303	1.091
$\omega_d^{[12]}$	0.078	0.142	1.041	0.080	0.160	1.042
$\omega_d^{[13]}$	0.137	0.248	1.074	0.142	0.256	1.077
$\omega_d^{[14]}$	0.165	0.326	1.090	0.171	0.315	1.093
$\omega_d^{[15]}$	0.149	0.265	1.080	0.122	0.214	1.065
$\omega_d^{[16]}$	0.142	0.248	1.077	0.145	0.250	1.078
μ_d	0.151	0.269	1.082	0.147	0.266	1.079
σ_d	0.035	0.055	0.020	0.026	0.086	0.015

Summarized results of all buildings in data set

In Table 7.5 and Table 7.6 we list the results of the RMA for the post-TSX and post-CSK scenes, respectively. The buildings $\omega_u^{[5]}$, $\omega_d^{[1]}$, and $\omega_d^{[2]}$ were excluded from the analysis of the post-TSX scene because they were in the shadow region produced by a mountain. The mean matching values of ω_d (μ_d) are smaller than for ω_u (μ_u). The main difference between the NMI versions is the value of μ_u and μ_d. The corresponding mean values of SAE are smaller than the ones of JOE, which are smaller than the ones of STU. The corresponding μ_d and μ_u values between the post-TSX and post-CSK scenes are remarkably similar even though the buildings are viewed from opposite directions from the ascending (post-TSX) and descending (post-CSK) orbits of the SAR sensors. This demonstrates that the RMA effectively incorporates the effects in the SAR backscatter signature that arise from different SAR geometries. The standard deviations (σ_d and σ_u) are relatively small so that the difference in the mean values between the Ω classes can be considered significant. For instance, considering $m_{max,SAE}$ for the post-TSX scenes, ω_u has $\mu_u = 0.237$ and ω_d has $\mu_d = 0.151$ which is a significant difference taking into account that $\sigma_u = 0.053$ and $\sigma_d = 0.035$, respectively. Applying Welch's t test [152] to the six sets produces p-values less than $1.42 \cdot 10^{-9}$, whereas class differences are considered significant for p-values less than 0.05.

The h_{est} values in Table 7.5 are the height values for which the highest NMI values were computed. Assuming that the manual extracted heights reported in Table 7.3 and

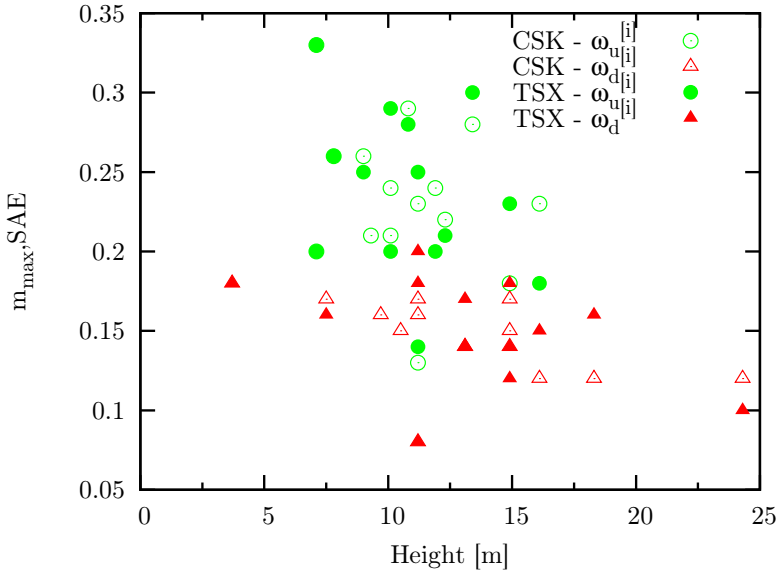

Figure 7.12: *SAE* values for ω_d and ω_u as a function of the height for post-TSX and post-CSK scenes.

Table 7.4 were not consistently overestimated, the heights calculated by the RMA are overall too low, with results from *JOE* being the lowest. The heights of buildings $\omega_u^{[2]}$, $\omega_u^{[3]}$, and $\omega_u^{[8]}$ are significantly underestimated (bound by the lower bound of the evaluation range) because the neighboring buildings are too close and therefore condition (6.12) is not fulfilled (see discussion in Section 7.5.4). Applying NMI as the similarity measure is not the best choice for estimating building heights and, instead, MI should be used as proposed in Chapter 6.

In Figure 7.12, the *SAE* values are plotted against the estimated building height for ω_d and ω_u computed in the post-TSX and post-CSK scenes. Visually, the two classes can be reasonably separated. A clear outlier at 11.2 m can also be observed where an undamaged building produced a low match value (the discussion in Section 7.5.4). It is worth noting that the average pre-event heights of the buildings in ω_d are slightly higher than those found in ω_u suggesting that the taller buildings may have been more vulnerable to the earthquake.

7.5.2 Supervised classification results

We analyze the impact of the NMI version on the damage detection problem by training separate classifiers with each of the NMI versions. To test the robustness of the proposed approach, we perform the training with the post-TSX data and the testing with the post-CSK data and vice versa. In this manner, we define a total of six classifiers that were named according to the following scheme: $C_{\text{[NMI Version],[Training Scene]}}$ with [NMI Version] $\in$ {SAE, JOE, STU} and [Training Scene] $\in$ {post-TSX, post-CSK}. For instance the classifier $C_{SAE,post-CSK}$ was trained using the $m_{max,SAE}$ values from the post-CSK scene and tested with the $m_{max,SAE}$ values from the post-TSX scene. In Table 7.7 we list the parameters for the distributions per class and the corresponding T_0 values

Table 7.7: Parameters for conditional probability density functions $p(Y|\omega_u)$ and $p(Y|\omega_d)$ and corresponding threshold values T_0 of supervised classifiers.

	μ_d	σ_d	$P(\omega_d)$	μ_u	σ_u	$P(\omega_u)$	T_0
$C_{SAE,post-TSX}$	0.151	0.035	0.481	0.237	0.053	0.519	0.192
$C_{JOE,post-TSX}$	0.269	0.055	0.481	0.411	0.085	0.519	0.336
$C_{STU,post-TSX}$	1.082	0.020	0.481	1.135	0.034	0.519	1.107
$C_{SAE,post-CSK}$	0.147	0.026	0.50	0.234	0.048	0.50	0.186
$C_{JOE,post-CSK}$	0.266	0.086	0.50	0.393	0.086	0.50	0.327
$C_{STU,post-CSK}$	1.079	0.015	0.50	1.133	0.031	0.50	1.103

Table 7.8: Confusion matrices for the classification results for the six supervised classifiers. *(a)* $C_{SAE,post-TSX}$. *(b)* $C_{SAE,post-CSK}$. *(c)* $C_{JOE,post-TSX}$. *(d)* $C_{JOE,post-CSK}$. *(e)* $C_{STU,post-TSX}$. *(f)* $C_{STU,post-CSK}$.

post-TSX

SAE

		True class ω_d	True class ω_u
Estimated class	ω_d	15	2
	ω_u	0	13
Omissions		0.0%	13.3%
Commissions		13.3%	0.0%
Accuracy		93.4%	

(a)

post-CSK

		True class ω_d	True class ω_u
Estimated class	ω_d	12	2
	ω_u	1	12
Omissions		7.7%	14.3%
Commissions		15.4%	7.1%
Accuracy		88.9%	

(b)

JOE

		True class ω_d	True class ω_u
Estimated class	ω_d	15	3
	ω_u	0	12
Omissions		0.0%	20.0%
Commissions		20.0%	0.0%
Accuracy		90.0%	

(c)

		True class ω_d	True class ω_u
Estimated class	ω_d	12	1
	ω_u	1	13
Omissions		7.7%	7.1%
Commissions		7.7%	7.1%
Accuracy		92.6%	

(d)

STU

		True class ω_d	True class ω_u
Estimated class	ω_d	15	2
	ω_u	0	13
Omissions		0.0%	13.3%
Commissions		13.3%	0.0%
Accuracy		93.4%	

(e)

		True class ω_d	True class ω_u
Estimated class	ω_d	12	2
	ω_u	1	12
Omissions		7.7%	14.3%
Commissions		15.4%	7.1%
Accuracy		88.9%	

(f)

of the six classifiers. Indeed, given the similarity between the threshold values for the same NMI version, there is no significant difference in training the classifier either with the post-TSX or the post-CSK scenes. Note that the mean and standard deviations in this table are the same than in Table 7.5 and Table 7.6, and are only listed again to provide a good overview and to support a better comparison with the results from the unsupervised classification.

In Table 7.8, the confusion matrices from testing the six classifiers are provided. The omission errors for ω_d vary between 0% - 7.7%, and can be interpreted as almost all dam-

Table 7.9: Estimated parameters for conditional probability density functions $p(Y|\omega_u)$ and $p(Y|\omega_d)$ and corresponding threshold values T_0 for unsupervised classifiers.

	μ_d	σ_d	$P(\omega_d)$	μ_u	σ_u	$P(\omega_u)$	T_0
$C_{SAE,post-TSX}$	0.165	0.036	0.731	0.278	0.029	0.269	0.235
$C_{JOE,post-TSX}$	0.296	0.036	0.749	0.482	0.036	0.251	0.421
$C_{STU,post-TSX}$	1.090	0.021	0.728	1.162	0.020	0.272	1.132
$C_{SAE,post-CSK}$	0.149	0.027	0.581	0.247	0.036	0.419	0.197
$C_{JOE,post-CSK}$	0.271	0.046	0.619	0.425	0.063	0.381	0.350
$C_{STU,post-CSK}$	1.081	0.016	0.584	1.142	0.024	0.416	1.109

aged buildings are detected correctly. Their respective commission errors range between 7.7% - 20.0% indicating that the method tends to moderately overestimate the damage. The accuracies vary in a narrow range between 88.9% - 93.4% with an overall mean accuracy of 91.2%. On the one hand this demonstrates that the proposed method is well suited for damage assessments using VHR optical pre-event and VHR SAR post-event data. On the other hand, it also indicates that the NMI version does not affect the overall performance of the method.

The classification of the buildings $\omega_u^{[16]}$, $\omega_u^{[17]}$, and $\omega_d^{[16]}$ with the six classifiers attributed the buildings correctly. Considering that a VHR SAR post-event time series is available, the proposed method can be used to monitor the cleaning and reconstruction process after the disaster.

7.5.3 Unsupervised classification results

For the unsupervised classification we use a similar naming scheme than for the supervised classification: $C_{\text{[NMI Version],[Classification Scene]}}$ with [NMI Version] $\in$ {SAE, JOE, STU} and [Classification Scene] $\in$ {post-TSX, post-CSK}. In Table 7.9 we list the parameters (mean, standard deviation, and prior probabilities) for the conditional probability density functions $p(Y|\omega_u)$ and $p(Y|\omega_d)$ derived by the EM algorithm together with the corresponding T_0 values of the classifiers. Comparing the estimated values with the actual ones from the supervised classification (Table 7.7) it can be seen that the mean values are estimated with a good accuracy. Furthermore, the estimated standard deviations are very small, so that the difference between μ_d and μ_u can be considered as significant. The prior probabilities estimated from the post-CSK scene show a good correspondence with the actual values. Hence, the T_0 values derived in an unsupervised manner from the post-CSK scene match with a good accuracy the ones derived in a supervised way. However, comparing the prior probabilities estimated from the post-TSX scene with the actual numbers, it can be noticed that they have a significant error in such that the estimated $P(\omega_d)$ are higher than the true values. Therefore, T_0 numbers estimated from the post-TSX scene show a remarkable offset to the actual T_0 values. In fact, the thresholds derived in an unsupervised manner from the post-TSX scene are significantly higher than the thresholds from the supervised classification.

The impact on the classification results can be seen in the confusion matrices listed in Table 7.10. The classification results of the buildings in the post-CSK scene (right column of table) show that class ω_d has no omission errors, and only slightly higher

Table 7.10: Confusion matrices for the classification results for the six unsupervised classifiers. *(a)* $C_{SAE,post-TSX}$. *(b)* $C_{SAE,post-CSK}$. *(c)* $C_{JOE,post-TSX}$. *(d)* $C_{JOE,post-CSK}$. *(e)* $C_{STU,post-TSX}$. *(f)* $C_{STU,post-CSK}$.

post-TSX

			True class	
			ω_d	ω_u
SAE	Estimated class	ω_d	14	7
		ω_u	0	6
	Omissions		0.0%	53.8%
	Commissions		50.0%	0.0%
	Accuracy		74.1%	

(a)

post-CSK

			True class	
			ω_d	ω_u
SAE	Estimated class	ω_d	15	3
		ω_u	0	12
	Omissions		0.0%	20.0%
	Commissions		20.0%	0.0%
	Accuracy		90.0%	

(b)

			True class	
			ω_d	ω_u
JOE	Estimated class	ω_d	14	7
		ω_u	0	6
	Omissions		0.0%	53.8%
	Commissions		50.0%	0.0%
	Accuracy		74.1%	

(c)

			True class	
			ω_d	ω_u
JOE	Estimated class	ω_d	15	4
		ω_u	0	11
	Omissions		0.0%	26.7%
	Commissions		26.7%	0.0%
	Accuracy		86.7%	

(d)

			True class	
			ω_d	ω_u
STU	Estimated class	ω_d	14	7
		ω_u	0	6
	Omissions		0.0%	53.8%
	Commissions		50.0%	0.0%
	Accuracy		74.1%	

(e)

			True class	
			ω_d	ω_u
STU	Estimated class	ω_d	15	3
		ω_u	0	12
	Omissions		0.0%	20.0%
	Commissions		20.0%	0.0%
	Accuracy		90.0%	

(f)

commission errors (20.0% - 26.7%) compared to the supervised classification. This means that no damaged buildings are classified as undamaged buildings, while some undamaged buildings are assigned to the class of damaged buildings. The results from the post-TSX scene (left column of table) show that class ω_d has no omission errors, but 50% commission errors. Hence, many undamaged buildings are classified as ω_d, while there are no damaged buildings which are classified as ω_u. This is explained by (7.9) showing that a higher threshold value causes the preferential classification of the buildings in class ω_d. The overall accuracies of the unsupervised classification of the post-CSK scene are still about 90% and only marginal lower than the results from the supervised classification. Instead, the accuracies of the post-TSX scenes are 74%, which is about 15% lower than the ones achieved in a supervised way. The overall mean accuracy of the six unsupervised classifiers is 81.5%.

To analyze the reasons for the diverse unsupervised classification results, we plot in Figure 7.13a and Figure 7.13b the supervised and unsupervised $C_{SAE,post-CSK}$ classifiers in terms of their posterior probabilities. The actual m_{max} values of the buildings, are plotted as "+" and "×" below the probability functions. Due to the low number of samples a statistical test to verify whether the two classes actually follow the assumed Gaussian distribution (e.g. using the Kolmogorov-Smirnov test), cannot be performed.

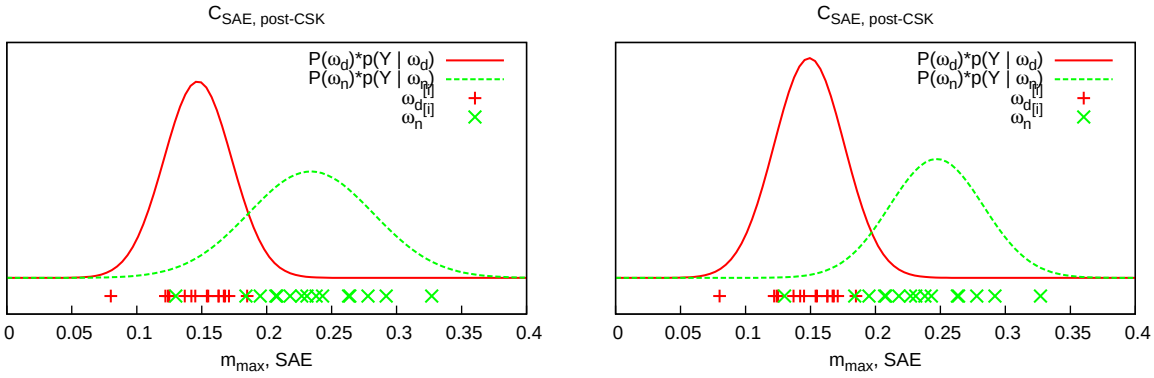

(a) (b)

Figure 7.13: Comparison between supervised and unsupervised $C_{SAE,post-CSK}$ classifiers. In this example the EM algorithm estimated the parameters for the unsupervised classifier with a good accuracy. The symbols "+" and "×" denote the actual m_{max} values of the buildings in class ω_d and ω_u, respectively. (a) Supervised classifier. (b) Unsupervised classifier.

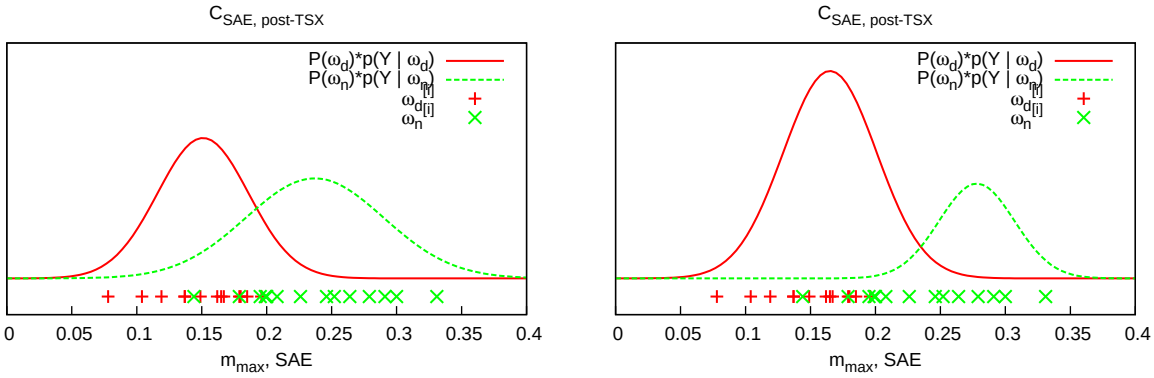

(a) (b)

Figure 7.14: Comparison between supervised and unsupervised $C_{SAE,post-TSX}$ classifiers. In this example the EM algorithm estimated the parameters for the unsupervised classifier inaccurately. The symbols "+" and "×" denote the actual m_{max} values of the buildings in class ω_d and ω_u, respectively. (a) Supervised classifier. (b) Unsupervised classifier.

Looking at the distribution of the actual m_{max} values of the buildings per class, which should show the majority of the samples centered at the mean value, this seems to be verified for class ω_d, but not necessarily for ω_u. In this case, the EM algorithm is able to find the actual priors, mean values, and standard deviations, with a good accuracy. As second example, we plot in Figure 7.14a and Figure 7.14b the supervised and unsupervised $C_{SAE,post-TSX}$ classifiers, respectively. For both classes it is not obvious that they verify the Gaussian assumption. In this example the EM algorithm cannot determine the actual parameters of the two classes with a good accuracy anymore. As a matter of fact, during the definition of the supervised classifiers, prior information is used. Hence, the potential non-Gaussianity of the Ω classes can be compensated for effectively. However, the EM

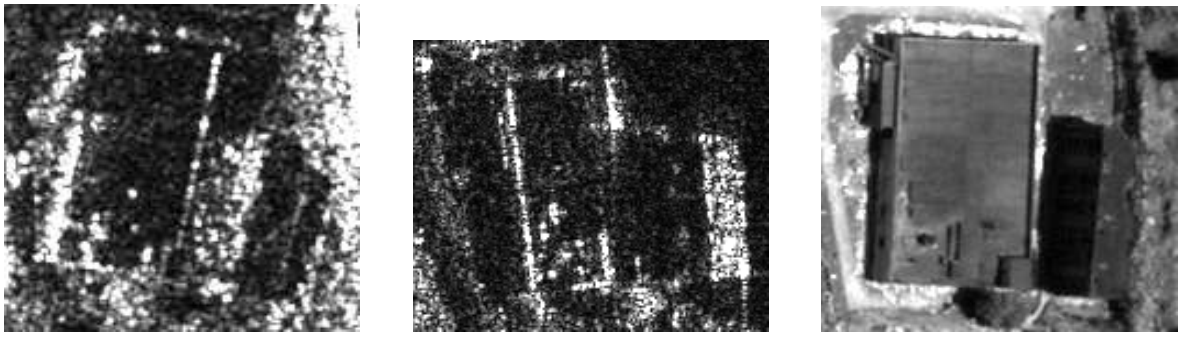

(a) (b) (c)

Figure 7.15: Interference of backscattering from buildings $\omega_u^{[2]}$ and $\omega_u^{[3]}$ ($\omega_u^{[2]}$ is left from $\omega_u^{[3]}$). (a) Subset of post-TSX scene with viewing direction from left. (b) Subset of post-CSK scene with viewing direction from right. (c) Subset of post-WV scene. (WorldView-1 image: © DigitalGlobe distributed by Eurimage S.p.A, 2008; TerraSAR-X image: © Infoterra GmbH/DLR, 2008; COSMO-SkyMed image: © ASI distributed by eGeos S.p.A., 2008.)

algorithm, which assumes a Gaussian model, does not use any prior information but relies only on the m_{max} values of the buildings. This information is not enough to offset the deviations between the model and the actual data, highlighting the sensitivity of the EM algorithm to the Gaussian model.

7.5.4 Impact of building location constraint

To investigate the impact of the building location constraint, we investigate the supervised classification results in detail. $\omega_u^{[2]}$ is the only building consistently misclassified by all six classifiers. Indeed, $\omega_u^{[2]}$ and $\omega_u^{[3]}$ are next to each other, aligned in a row in the range direction (see Figure 7.15) and the Δ_{act} between these two buildings is about 10.0 m. In the post-TSX scene, $\omega_u^{[2]}$ is at the sensor facing side so that given (6.11) $\Delta_{min} = 26.7$ m. However, in the post-CSK scene, $\omega_u^{[3]}$ is at the sensor facing side and $\Delta_{min} = 29.6$ m. For both scenes, condition (6.12) is not fulfilled and the shadow region of the first building overlaps with the layover region of the second. Building $\omega_u^{[2]}$ in fact is relatively short, so that its theoretical shadow- and layover areas are not large. It follows that the interference with the neighboring building can result in an almost complete absence of these areas. Hence, the predicted image signature of the undamaged building $\omega_u^{[2]}$ does not correspond to the signature in the actual scene, generating a low match and classifying the building as ω_d. This also occurs for the building $\omega_u^{[3]}$ that is misclassified by two out of the six (supervised and unsupervised) classifiers. Since building $\omega_u^{[3]}$ is higher than $\omega_u^{[2]}$, the interference with the lower building only results in a moderate shortening of its respective layover and shadow regions. Thus, most classifiers still make the correct decision. Building $\omega_u^{[8]}$, which is attached to its neighbor, was correctly classified by all six classifiers demonstrating that the violation of constraint (6.12) does not necessarily lead to a misclassification.

7.6 Discussion and conclusion

In this chapter we presented a novel damage assessment method for single (isolated) rectangular buildings using pre-event VHR optical and post-event VHR SAR images. The method is tuned to work at the individual building level and determines whether a building is completely destroyed (collapsed) after a catastrophic event or whether it is still standing. First, a reference pre-event VHR optical image is used to extract the 3-D parameters of a building which is tested for damage. This information is combined with the acquisition parameters of the actual post-event SAR data to simulate the VHR SAR signature of the undamaged building. The predicted signature is compared quantitatively to the actual VHR SAR scene. Based on the Bayes rule, the resulting comparison determines whether the building is destroyed or still standing. Similarity between the simulated and the actual scene indicates an undamaged building, while dissimilarity results in classifying the building into the damaged building class.

We demonstrate the effectiveness and the properties of the proposed approach using spaceborne pre-event VHR optical and post-event VHR SAR data from Yingxiu, China, which was heavily damaged in the Sichuan earthquake in May 2008. The results show that the method is able to distinguish between damaged and undamaged buildings with high overall accuracy of about 90% using the supervised classification procedure, and about 80% accuracy for the unsupervised classification based on the EM algorithm. The analysis was based on a set of 30 buildings of various sizes and heights. Furthermore, we tested the method using both ascending and descending scenes from two different spaceborne SAR sensors (TerraSAR-X and COSMO-SkyMed) demonstrating the robustness of the proposed method. Overall, the method misclassifies more undamaged buildings as damaged buildings than vice versa providing an upper limit for building damage. This misclassification is related to the fact that individual buildings in the image with complete and undisturbed SAR backscattering signatures provide the best results.

At present, we do not model building configurations for which backscattering signatures overlap. Furthermore, other objects which are located in the immediate surrounding of a building, such as trees or cars, are currently disregarded in the method. This effect can be partly anticipated with knowledge on tree positions, relevant to the building orientation in the SAR scene, taken from the pre-event optical scene. However, the effect of moving objects, such as cars, and the resulting interference with the backscattering signature of the building cannot be taken into account, as no prior knowledge on exact location is available. The overall effects of objects in the scene that are not taken into account in the simulation will lead to misclassification of undamaged buildings, i.e. confirming that ω_d provides an upper bound for the estimation of building damage.

Change detection and damage assessment methods, which directly compare pixels or pixel regions in pre- and post-event acquisitions, are often developed to be used with low/medium resolution SAR imagery. Their performance strongly depends on the accurate coregistration of the two scenes. These methods suffer when registration noise is high, which leads to an increase in the false alarm rate. This fact becomes more important if those methods are applied to VHR SAR imagery. In this case, coregistration methods specifically developed for VHR SAR imagery, such as proposed in [47], might limit this effect. The method proposed in this chapter does not rely on an accurate pixel based

coregistration of the pre- and post-event scenes. Instead, the matching procedure uses a local coregistration procedure between simulated and actual VHR SAR scene, which offsets the coregistration accuracy requirements.

The presented scenario used pre-event VHR optical data to visually detect and manually measure building dimensions. However, automatic building detection and reconstruction methodologies [136], [153] have significantly improved over the last years and we believe that this step can be automated. Moreover, pre-event data from other geospatial registries (e.g. cadastral maps) can be used to estimate the 3-D building parameters [154]. If available, even VHR SAR could be used for this purpose [47], [42]. The advantage here is the independence between the pre- and post-event data, i.e. orbit and incidence angle can change between the two acquisitions.

Chapter 8

Distributed geospatial data processing functionality to support collaborative and rapid emergency response

This chapter[1] presents a novel approach to integrate the latest generation VHR earth observation imagery into the operational workflow of geospatial information support for emergency response actions. The core concept behind this approach is the implementation of an image pyramid structure that allows each image tile to be addressed separately. We propose a novel way to collate geospatial feature data from distributed sources and integrate them in visualization and image processing. The system components enable rapid collaborative mapping, support for in-situ data collection, customized on-demand image processing, geospatial data queries and near instantaneous map visualization. We adapt functional software modules that are available in the public and open source domain. The approach is demonstrated with a test case in a rapid damage assessment scenario using VHR optical satellite QuickBird and IKONOS imagery over Southern Lebanon from 2006. Furthermore, we test the system for the 2008 Sichuan earthquake to highlight the integration of the method introduced in the previous chapter and consequently to demonstrate the use of the system in the context of VHR SAR.

8.1 Introduction to collaborative and rapid emergency response

Recent advances in software development have significantly expanded the role of remote sensing imagery and geospatial features data as important and up-to-date information sources. This is primarily driven by the uptake of web mapping applications, virtual

[1] Part of this chapter appears in:
[155] D. Brunner, G. Lemoine, F.-X. Thoorens, and L. Bruzzone, "Distributed geospatial data processing functionality to support collaborative and rapid emergency response," *IEEE Journal of Selected Topics in Applied Earth Observation and Remote Sensing*, vol. 2, no. 1, pp. 33–46, March 2009.
Figure 8.9 was selected as cover for the Vol. 2, No. 1, of the IEEE Journal of Selected Topics in Applied Earth Observation and Remote Sensing.

globe viewers, the pervasive use of Global Positioning System (GPS) based tracking and routing devices, and novel collaborative geotagging applications. Much of the relevant functionality is available as free or open source software modules or as web-hosted applications, which has led to the expansion of geospatial processing capabilities well beyond the traditional community of remote sensing and GIS experts. Furthermore, new public and commercial data supply models are evolving for high quality remote sensing data which will challenge the traditional supply mechanisms, in particular for near real time supply of post-event satellite data in emergency or conflict situations.

The characteristics of earth observation imagery and geospatial data integration in emergency response are distinctly different from those in typical environmental thematic use. Emergency response actions tend to be localized (e.g. at local or regional, rather than national or continental scales), thematically specific (e.g. classification of individual urban structures, rather than generic land use classes), and have stringent timing requirements for the delivery of the relevant derived data layers. A typical sequence of geospatial support activities responding to a call to support an emergency response is as follows:

1. In the pre-alert stage, early warning indicators may trigger the search for suitable archive earth observation data that could be used to establish the pre-event reference situation. This stage is relevant only for events of a probabilistic nature for which adequate early warning mechanisms are in place (e.g. tropical cyclones [6], forest fire risk [156] and flood forecasts [157]);

2. Either at a predetermined high alert level or directly after the event there is an immediate need to provide access to digital repositories of appropriate earth observation imagery and geospatial feature data at the required scale and accuracy to establish the reference situation. Data layers derived from these data sets need to be specific to the thematic needs of the response effort (i.e. populated area delineation, infrastructure mapping, vicinity analysis). At this stage, the ability to distribute the analysis workload amongst domain experts and image analysts and assemble the contributions from a large number of contributors is paramount;

3. Directly after the event, high resolution (airborne or satellite) imagery is tasked to be acquired over the event site. The primary use of this data is for the assessment of the post-event situation compared to the reference situation. Automatic classification and change detection algorithms [13], [14], [15], [16], are particularly relevant in this context, because they assist in the visual inspection and feature capturing stage to quantify the impact of the event. At this stage, early post-event collateral information may become available, e.g. the exact impact area, logistics of the relief effort, and media reports, that will help guide the geospatial analysis effort;

4. After the initial geospatial analysis results are disseminated to emergency response actors, new queries may be formulated that require the data layers to be revisited or the geospatial analysis to be fine-tuned. Depending on the nature of the event, several situation updates may be necessary (e.g. forest fires, extended conflicts).

In reality, due to the absence of a common collaborative rapid mapping platform, the individual steps in this workflow are only met in a non-standardized, ad hoc manner.

Different tasks are assigned to the team members, which typically conduct the analysis locally at their workstations with tools they are most familiar with. This implies that the various results produced throughout the analysis are often not compatible and immediately accessible by other team members. Therefore, additional efforts are necessary to synchronize the produced data within the team as well as to harmonize and compose the derived information to one product so that it is actually beneficial for the decision makers. Furthermore, the individual processing of the different tasks challenges the efficient organization and the overall monitoring of the progress of the geospatial support activity. Note that both points are crucial to meet the stringent timing requirements for delivering the relevant information. The outlined difficulties become even more profound if the team is spread across institutional boundaries.

In this chapter, we propose common steps for using geospatial data in general, and in particular earth observation imagery, to support emergency response actions using a common collaborative rapid mapping platform. This effort aims at increasing the efficiency of analyzing the data and hence the overall effectiveness of using geospatial data to support the relief effort. In particular, we propose a system integration effort that leverages the functionalities of publicly available and open source components to enable collaborative and rapid processing of distributed geospatial data, including large high resolution image coverages. We introduce a novel concept for the integration of privately held very large VHR images both in customized visualization environments and accessible to extensible image processing capacities via a web service mechanism. The system enables distributed access to geospatial feature sets that can be collected as digitized feature sets from a community of contributors and exposed through web services. Geospatial feature data can be integrated into the distributed image processing capacity, which is optionally backed up by a grid computing architecture to enhance processing speed. We demonstrate the use of the system in the emergency response context using both VHR optical and VHR SAR imagery.

The remainder of the chapter is organized as follows: Section 8.2 introduces the system architecture. In Section 8.3 we discuss how we integrate very large image data sets providing the algorithm implementation details and illustrating the procedure with an example (Section 8.3.6). In Section 8.3.7 we describe how we can trigger image processing requests on the image data sets. We then highlight the feature capturing (Section 8.4) and visualization (Section 8.5) capabilities of the system. In Section 8.6 we describe the integration of the automatic damage assessment method from Chapter 7 into the system architecture. In Section 8.7 and Section 8.8 we demonstrate the system for rapid damage assessments during the Southern Lebanon armed conflict in 2006 and after the Sichuan earthquake in 2008, respectively. The conclusions are presented in Section 8.9 with a summary of the key aspects of our system.

8.2 System architecture

The requirements to share data between teams suggests the need for a common distributed software platform based on a client-server model [158]. This architectural model allows communication between several distributed clients with one or more servers using network

connections. The client initiates server requests and waits for and receives server replies. It is typically a graphical user interface through which the user can interact with the data sets and the server. The server responds to client requests by performing a triggered processing task and providing the result. The use of the client-server model is generic to many current web applications. Its use in web mapping applications is an alternative to desktop or locally networked GIS applications because it functions across the boundaries between diverse organizations, stimulates the use of standard formats and exchange protocols, and permits the distribution of geospatial functionalities to relevant user communities in a tailored fashion. Drawbacks of the client-server model are the need for increased efforts supporting transactional management, including authentication, and possibly limitations in client functionality. A full discussion on the pros and cons of web mapping platforms is given in [159].

The overall system architecture is illustrated in Figure 8.1 using the Unified Modeling Language (UML) notation [160]. To manage the functional and computational complexity of geospatial data processing on the server, we use a three-tier architecture [158] following the so-called Model-View-Controller design pattern for distributed systems [161]. The first tier is the client (the View) which captures user data and composes client requests, forwards these to the application server and visualizes the application server's response to the user. The second tier is the application server (the Controller), which handles all the business logic required to process a client request (e.g. selection, processing actions, response compilation). The third tier (the Model) communicates with the data stores.

8.2.1 View

The View, which is the interface running on the client side, distinguishes three functional roles: 1) the geospatial analyst; 2) the project manager; and 3) the decision maker. The geospatial analyst inspects the satellite imagery and manually extracts features using the client interface. The analyst can either be a local expert familiar with the area under investigation, a domain expert specialized in urban areas, or an user who has been introduced to geospatial feature capturing using the client (see Section 8.4).

In our scenario, we use the Google Earth™ virtual globe viewer as the client platform for this role. Google Earth™ can be downloaded for free and runs on the Windows, Mac and Linux operating systems and has a very large user base. Furthermore, Google Earth™ provides ready access to a global archive of high and VHR imagery stored on the Google Earth™ server which is regularly updated, providing a background for reference situation mapping. In Section 8.3, we demonstrate how the Google Earth™ background imagery can be complemented with access to full resolution image products held in private archives.

The project manager is responsible for managing, controlling and supporting the overall collaborative analysis effort. Initially, she prepares the system by creating the project structure, uploading relevant archive data for the Region Of Interest (ROI), and processing the satellite images for display in Google Earth™. Based on requests and instructions received from the emergency response coordinator, the project manager distributes the work effort amongst collaborators, for instance, by assigning analysis tasks by theme or subregion of interest. At this stage, the use of ancillary and collateral information to

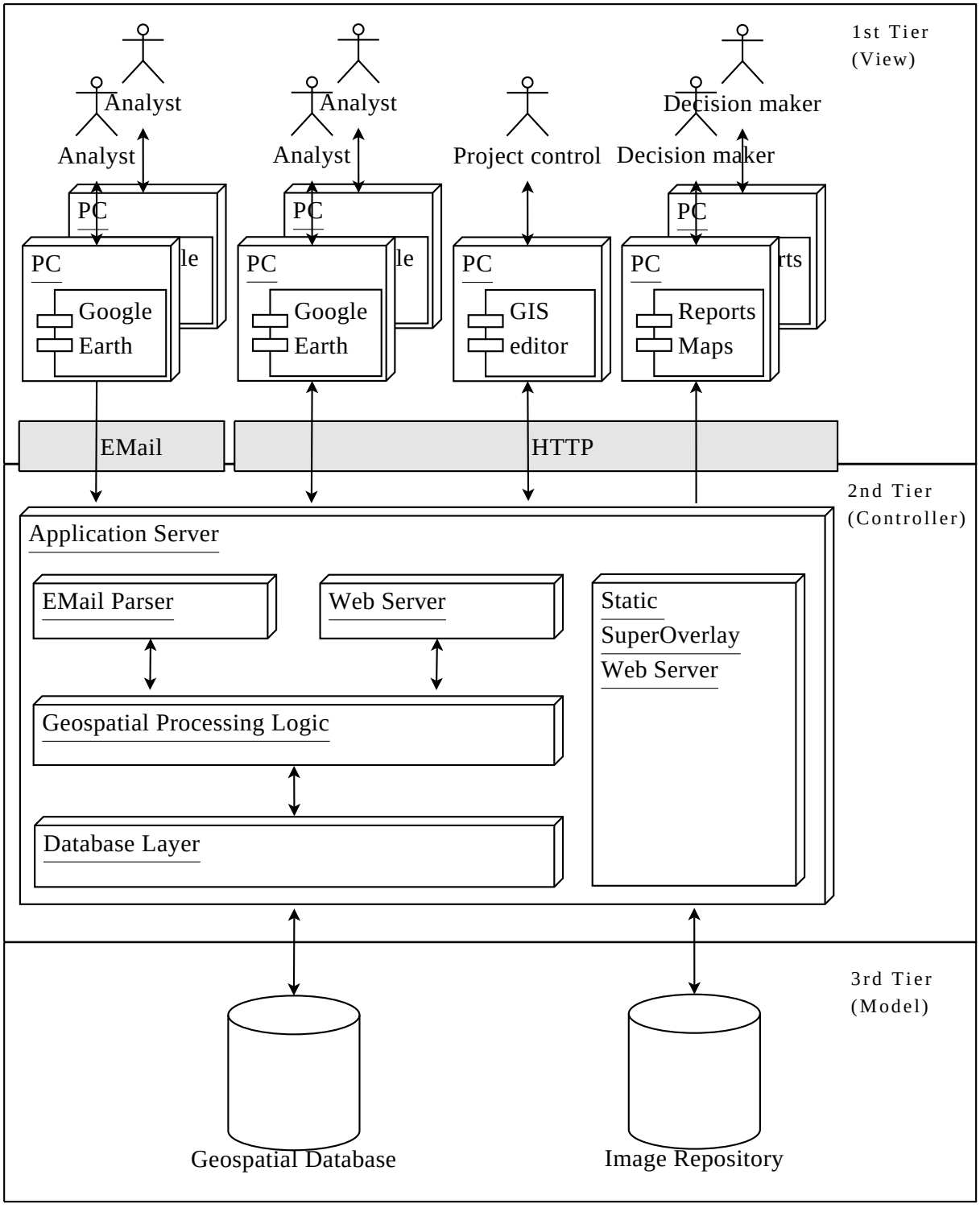

Figure 8.1: UML overview of a multi-tier client-server architecture for collaborative feature capturing and visualization.

stratify the ROI into priority zones is very important. The project manager is the main contact point for technical problems and collection of feedback on the use of the system. She uses the Google Earth™ client or other specialized GIS clients for data editing, quality control and management. In practice the project manager, or her technical team, will also have direct access to the various components of the server infrastructure to intervene when appropriate.

The decision maker roles are taken up by the emergency response coordinators who incorporate the geospatial analysis outputs and steer the intervention effort. They access the system in read-only mode receiving customized reports and maps that are compiled in real time from the available data via the web server interface of the system.

We have implemented a simple role-based authentication mechanism to ensure that the user of the system is only able to accomplish the actions in the system that his role prescribes. The analyst is allowed to create new vector data and update or delete data he has previously created. The project controller is the system administrator and is able to create, change, and delete globally any kind of data (i.e. raster and vector data). The decision maker is only granted read access to generate customized situation reports and map products. All data submissions are tagged with the user identifier and timestamped allowing changes to be tracked by user over time.

The client-server communication is synchronized via the Hypertext Transfer Protocol (HTTP). The refresh mechanism in Google Earth™ ensures that any data submitted by an analyst is distributed to other users who are connected to the system. In cases where there is no reliable Internet connection, which may be the case in developing countries or areas that are affected by a catastrophic event, client data can alternatively be forwarded by email to a functional mailbox. Google Earth™ can also work with locally stored feature data sets in offline mode.

Note that the choice of using Google Earth™ as the client places a number of constraints on data formats and standards. Imagery integrated into Google Earth™ must be reprojected to Plate-Carrée (or geographic) projection using the WGS 84 ellipsoid. The mandatory geospatial feature data format for Google Earth™ is the Keyhole Markup Language (KML) [162]. The Geospatial Data Abstraction Library (GDAL) [163] is particularly useful for converting other feature data formats (e.g. ESRI shape files) to KML and reprojecting imagery as required.

8.2.2 Controller

The second tier consists of the application server which is made up of five components: a web server, an email parser, the geospatial processing logic, a database abstraction layer, and a static `SuperOverlay` (see Section 8.3) web server. The web server is an Apache TOMCAT instance and receives the HTTP requests from the clients. The requests are either for data access or requests for data submission. An email parser makes asynchronous uploading to the system possible via a functional mailbox. The web server and the email parser delegate the requests to the geospatial processing logic component, which provides functionality for querying and manipulating geospatial data (create, read, update and delete). This component communicates indirectly via the database abstraction layer with the geospatial feature database. The static `SuperOverlay` web server serves static im-

agery as `SuperOverlay`s accessing the image repository directly and thus does not need to use the database abstraction layer. Our application server is implemented in Java and runs on a Linux platform. However, given the inherent platform independence of Java, the server can be deployed on any system for which a Java run-time environment is available.

8.2.3 Model

The geospatial database manages geographical feature data and their attributes. For organizing the geospatial information the object-relational PostgreSQL DBMS, with the PostGIS extension is used. It is available for Windows and Linux platforms. PostGIS allows storage of geographical objects and includes support for spatial indexing and functionality for the analysis and processing of geographical objects. The database layer in the controller, however, abstracts the implementation specific details of the geospatial database so that it is possible to change the DBMS quite easily.

The proposed separation between the geospatial feature data server and image data server is not obligatory. In fact, one web server would be enough to handle both feature and image data requests from the clients. Our setup does not include direct interaction between the two server parts. Such interaction is logically separated in the controller, which enhances portability and scaling of individual server components. This also makes it easier to integrate other data access protocols (e.g. the File Transfer Protocol) to serve specific purposes.

8.3 Integration of very large image data sets

The distribution of large image coverages among project collaborators, either for image processing or for the visualization of the processed data is a well known issue. This is particularly evident in operational scenarios such as emergency response, when large areas are analyzed at large scales for impact assessment, usually within stringent temporal constraints. The OpenGIS Consortium (OGC) [164] proposes the use of the Web Coverage Service [165] and the Web Map Service (WMS) [166] image serving protocols respectively, for image subselection and recomposition. Both services can provide reprojection functionality. These services however, tend to be computationally expensive and unable to handle a large user base in real time, i.e. the typical scenario in collaborative rapid mapping.

For the rapid visualization of large terrain data sets, [167] proposes the use of image pyramids (also known as MIP maps), i.e. a multiresolution stacked representation of the image. Each level of the pyramid is usually a 2 by 2 up-sampled version of the underlying, higher resolution level. The intrinsic relation between level of detail, tiling coordinates and the relative address in the stored image file allows for very fast access to the raw data. Image pyramids may either be stored inside a (propriety) binary image format (e.g. GeoTIFF, ENVI, ERDAS) or stored as individual files in a physical tile structure on disk. The latter is used in combination with an unique fixed tile coding convention by virtual globe server software such as Google Earth™, Microsoft Virtual Earth™ and NASA's World Wind [168] in order to efficiently visualize their global remote sensing archives.

8.3.1 SuperOverlay generation

To display privately owned static image pyramids within the Google Earth™ virtual globe viewer, the `SuperOverlay` [169] element was introduced in version 2.1 of KML. KML has recently become an OGC implementation standard (the current version is 2.2). A `SuperOverlay` is a hierarchical tree-like structure of `NetworkLink`s of regionalized `GroundOverlay`s, which is the standard KML element to display small georeferenced image tiles within Google Earth™. At the top of the tree, a `Region` element defines the geographical extents of the image composing the `SuperOverlay`. This `Region` loads the top level (i.e. lowest resolution) up-sampled image as a `GroundOverlay`. The top level KML file contains four `NetworkLink`s to the four quad-regions of the next tiling level. The "level of detail" (`minLodPixels`, `maxLodPixels` KML elements) controls the visibility of each tile level in such a way that the higher resolution levels become visible when the user zooms in closer. This mechanism ensures that only those tiles are loaded that are needed to fill the zoom window of the viewer. Google Earth™ suggests the use of tiles of 256 by 256 for optimum performance, but the user is free to decide the actual tile size. A key difference between static `SuperOverlay`s and standard MIP maps is that each image tile is individually addressable and loadable as a single file. In other words, it can be accessed at the static web server via an Uniform Resource Locator (URL) address. An added advantage of static `SuperOverlay`s is that they can be provided on separate media for offline integration into Google Earth™. For mobile platforms having limited disk space, caching parts of a `SuperOverlay`, e.g. to support in-situ data collection, requires a simple synchronization operation.

Several software implementations for generating a `SuperOverlay` are available (e.g. as part of the GDAL toolkit). We have implemented a Java application for batch generation of `SuperOverlay`s. Their creation can be broken down in the following processing steps [170]:

1: Reproject the image to Plate-Carrée projection and extend row and column dimensions to a quad-multiple of 256;
2: Tile the extended image into tiles of 256 by 256;
3: Create up-sampled tiles for each of the lower resolution pyramid level;
4: Create the `SuperOverlay` KML tree structure.

The actual processing steps are described in the following subsections.

8.3.2 Image reprojection and extension

Typically, images used in a project or local scope are in a local projection system (e.g. Universal Transverse Mercator (UTM)) and retain the original spatial and spectral resolution of the sensor. Visualization in Google Earth™ requires the data to be reprojected to Plate-Carrée projection and spectrally resampled to 8-bit. The spatial resolution can normally be retained, but some resampling is performed in the reprojection process.

Reprojection often results in imagery that is rotated with respect to the north-south orientation, with zero filled boundary areas. In order to avoid complex resampling at the lower resolution pyramid levels, it is useful to extend the reprojected image to an image size that is a quad-multiple of 256 (i.e. 2, 4, 8, 16, ... times 256 in both the row and

column dimensions). For instance, an image with a width and height of 800 by 800 pixels is extended to 1024 by 1024 pixels, corresponding to quad-level 2, resulting in 4 by 4 tiles. Our implementation centers the original image inside the extended image frame.

8.3.3 Image tiling

The tiling operation is only performed for tiles that are not completely in the background, i.e. either in the zero filled boundary area of the projected image or the zero filled quad-multiple extension. Before writing each tile to disk, all zero filled pixels are made transparent so that they do not hide the background imagery when visualized in Google Earth™. Tiles are written as Portable Network Graphics formatted files (*.png) that provide lossless compression and retain the transparency properties of the image tiles.

8.3.4 Creation of up-sampled image pyramid layers

The quad-level sizing of the reprojected image is particularly useful at this step, because it guarantees a 1 to 4 (2 by 2) relationship between tiles at each higher quad-level[2]. That is, each up-sampled tile is the result of a 2 by 2 resampling of exactly 4 higher resolution tiles. If a higher resolution tile does not exist, e.g. because it lies in the zero filled background, the relevant quadrant in the up-sampled tile remains zero filled, which is made transparent before the tile is written. A side effect of this operation is that all zero valued pixels become transparent.

We iterate the process until we reach the top quad-level, which results in a single 256 by 256 tile. In the previous example, the 1024 by 1024 pixels large extended original image has 3 quad-levels 2, 1 and 0 with 16, 4, 1 tiles respectively.

8.3.5 Creation of the SuperOverlay KML tree structure

Each tile at each of the quad-levels is a georeferenced image in Plate-Carrée projection. The `SuperOverlay` KML tree structure persists both the geolocation of each tile and the hierarchical pyramid tile structure in KML constructs. For each of the lowest quad-level (highest resolution) tiles, the KML document defines the geographical `Region` covered by the tile defined in a `GroundOverlay` element. Since these tiles are the leaf nodes of the tree, they do not link to others. Leaf node tile KML files are only created for tiles that are already on disk, i.e. created in the previous steps.

For each of the higher quad-levels, the KML document is similar to the one for the leaf node tiles, except that each has in addition up to four `NetworkLink`s giving the `Region` definition and link to the underlying tile KML descriptors.

8.3.6 A SuperOverlay example

To illustrate the process with a practical example, we show the typical output for a VHR (2.4 m pixel size) multispectral QuickBird image. The image is orthorectified to the

[2]The quad-levels are numbered according to their hierarchy in the image pyramid. The "top of the pyramid" corresponds to quad-level 0 and has 1 tile. Each lower pyramid level has an increasing quad-level index q_l, each with 2^{2q_l} tiles.

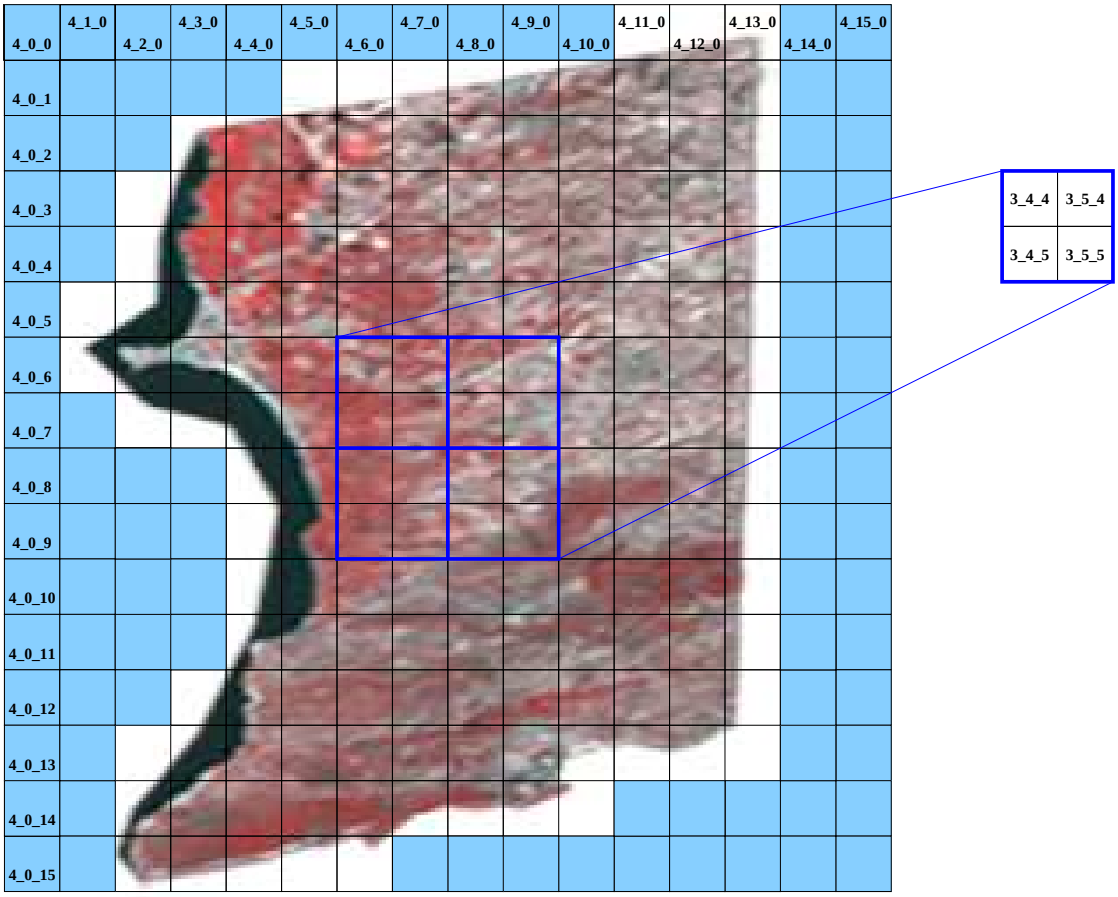

Figure 8.2: Schematic overview of the tiling process for the sample image. The input image in Plate-Carrée projection is first extended to a grid at quad-level 4, centered on the image. The grid is then tiled into 16 by 16 tiles. Tiles exclusively in the zero filled background values (light blue in the figure) are not saved to disk. Tiling at each of the higher quad-levels 3, 2, 1 and 0 results from composing each subsequent level from the up-sampled 4 tiles at the preceding level. (Satellite image: © DigitalGlobe distributed by Eurimage S.p.A., 2006.)

relevant UTM projection, masked to remove a significant section that covers the sea, and reprojected to Plate-Carrée projection resulting in an image of 3378 by 3875 pixels.

In the first step of the algorithm, the image is extended to 4096 by 4096 pixels (quad-level 4) and then tiled into 16 by 16 tiles of 256 by 256 pixels. This process is illustrated in Figure 8.2. The tile naming format is QQQ_NNN_MMM, where QQQ is the quad-level, NNN is the column index and MMM is the row index in the tiled grid. Three digits are used in this naming scheme so that a maximum tile index of 512 (i.e. quad-level 9) is possible. This maximum tile index corresponds to a grid size of 131072 by 131072, equivalent to an upper limit of 48 GB for the input image. This limitation can be relaxed by using more than three digits for the tile index. An alternative for processing images which are larger than 48 GB is to split up the image into blocks of not more than 48 GB and `SuperOverlay` each block separately. The results can then be linked

using KMLs `NetworkLink`s. However, the handling of files larger than 12 GB becomes difficult in practical terms because it exceeds the single-band 4 GB limits of the widely used GeoTIFF image format, which corresponds to an upper quad-level of 256 or a grid size of 65536 by 65536. Most single-scene satellite image data sets are well below the 12 GB limit. For very large data sets (e.g. image mosaics), raw or proprietary input file formats, which do not have a size limitation, may be used. For performance reasons `SuperOverlay`s are currently pregenerated from the imagery and stored with their full structure in the image repository.

A screenshot of the integration of the large QuickBird test image into Google Earth™ using `SuperOverlay`s is shown in Figure 8.3. Using the Google Earth™ navigation widgets, we are able to zoom into each of the subsequent quad-levels seamlessly, visualize the data in the 3-D landscape mode and overlay geographical features from other KML sources. Of special interest is the transparency slider that is associated with the `SuperOverlay`. We can control the transparency of the added `SuperOverlay` from fully opaque to fully transparent. If more than one `SuperOverlay` is loaded, we can use this control to look at each visualization separately. This is very useful in manual change detection scenarios, e.g. comparing "before" and "after" states in multitemporal series, which we can then capture with KML annotations.

`SuperOverlay`s are also suitable for the visualization of multitemporal imagery. The KML standard provides the `TimeStamp` element to allow rendering of the KML `GroundOverlay` at specific time intervals. Animation of time series can be controlled via Google Earth™'s time navigation widget.

8.3.7 SuperOverlays for image processing

The above example refers to using the `SuperOverlay` in a visualization environment, such as the Google Earth™ client. However, `SuperOverlay`s can also be used to support image processing tasks. Image processing algorithms that run on byte-formatted input, can integrate the `SuperOverlay` directly. If radiometric resolution requires the image to be kept in a different number format (i.e float or 16-bit integer format) the `SuperOverlay` algorithms can be adapted to produce image tiles in the TIFF format.

`SuperOverlay`s are especially suited to dedicated and CPU-intensive image processing tasks (e.g. image segmentation and/or classification) to be performed on a predetermined ROI. The pyramid tile structure can be used directly for multiscale image analysis and with feature extraction algorithms. This structure is also suitable for integrating image processing and pattern recognition algorithms specially designed for managing large images in split-based approaches [9]. In such cases, the tile structure can be automatically associated with the image split necessary for multilevel processing. The `SuperOverlay` also implicitly supports the use of multisource and multitemporal data sets since all are georeferenced to the same projection. Outputs generated by the image processing tasks, whether applied to the entire image pyramid or specific layers or tiles, can be made available as `SuperOverlay` structures for integration into the project data collection.

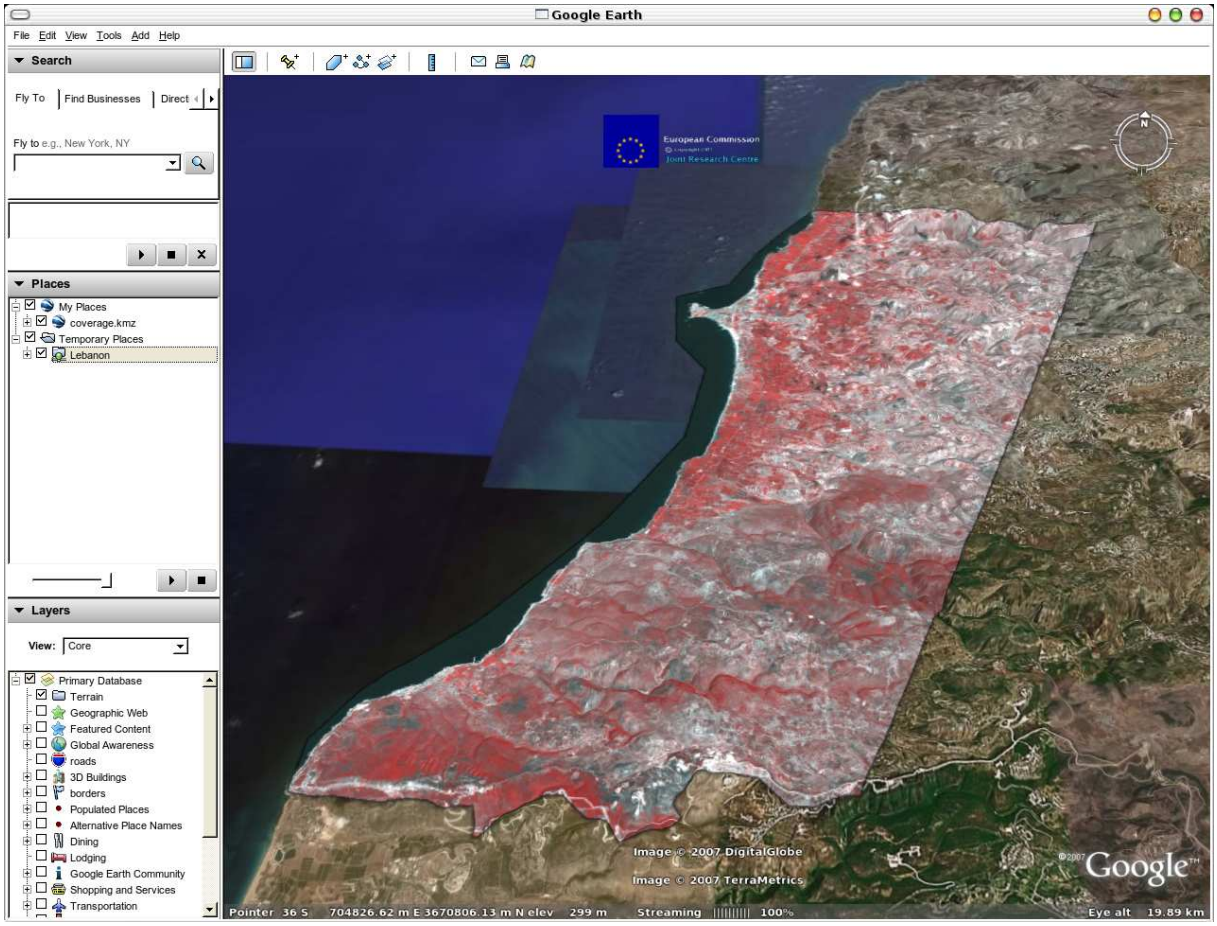

Figure 8.3: A screenshot of the Google Earth™ viewer after opening the `SuperOverlay`'s top level KML file. (Satellite image: © DigitalGlobe distributed by Eurimage S.p.A., 2006.)

Integrating image processing functionality

Our distributed system is able to provide dedicated image processing services that can be incorporated as third party web services. The relevant `SuperOverlay` URL and ROI feature (typically a polygon) can be forwarded, together with relevant processing parameters, to the published web service address. The public web service interface is separate from the privately hosted implementation of the image processing functionality. This is an especially attractive feature for specialized processing algorithms that are not available in off-the-shelf image processing software packages, for experimental routines, or where code protection is essential.

The workflow for integrating image processing into our system is shown in Figure 8.4. The process is divided into two systems: a public system that contains the data to be processed as a `SuperOverlay` and a private system that encapsulates the image processing routines. The project controller or expert analyst selects in a first step the ROI, which might be a predefined area or the result of a geospatial query (e.g. the automatic detection of built-up areas in optical VHR imagery within a 1 km buffer area around a river flood

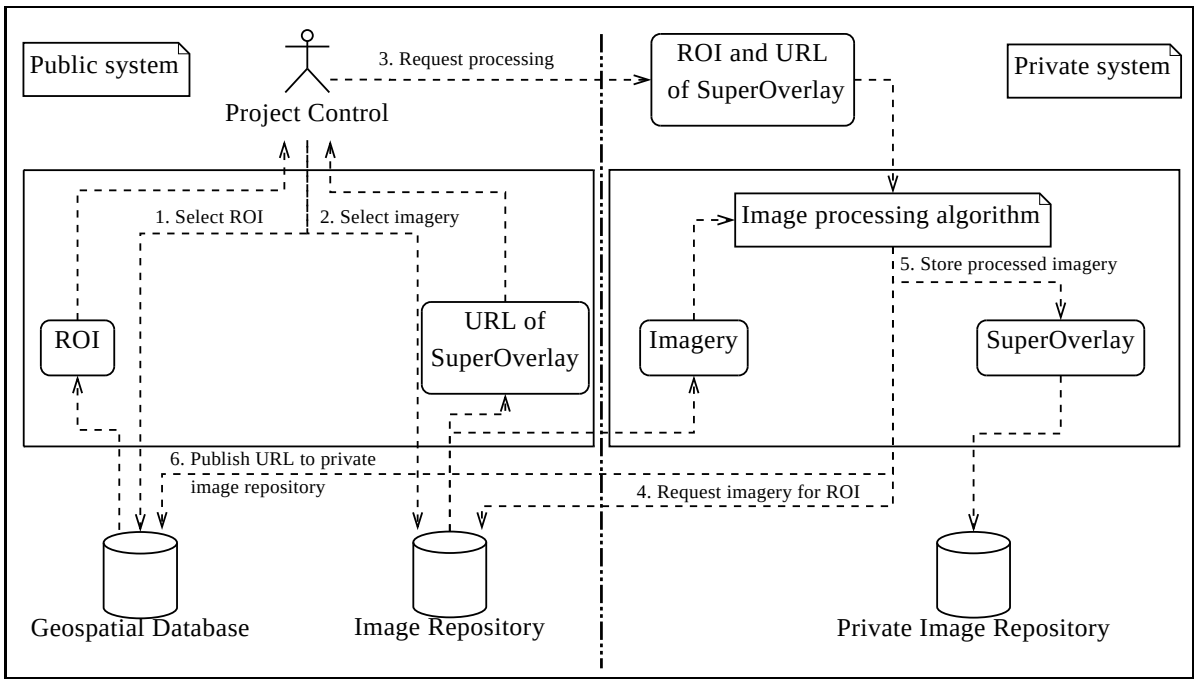

Figure 8.4: A schematic overview of the integration of image processing into the system. This process is divided into a public and a private system. The data to be processed are stored as `SuperOverlay` in the public image repository. The image processing routine is triggered by specifying the `SuperOverlay` and the ROI to be processed by an algorithm that is provided by a partner on their private system. The results are stored in the private image repository which is accessible by the public system.

plain). In a second step, the imagery is selected, which is addressed by the URL of the `SuperOverlay`. In a third step, the image processing request is triggered by forwarding the URL and the ROI to the public interface of the web service hosting the private algorithm implementation. Depending on the algorithm and its implementation, it may be necessary to compose the tiles of the `SuperOverlay` in a fourth step to a single or several larger images before the algorithm can be applied. In such cases, the resulting imagery has to be tiled back in a fifth step to the `SuperOverlay` structure so that it can be made accessible to the project partners through the Google Earth™ client via a `NetworkLink` posted to the server (sixth step).

Combining image processing and grid computing

In order to decrease the processing time of the image processing server, the algorithm designer may incorporate grid computing facilities as shown in [171]. Grid computing [172] is a hardware and software infrastructure that provides high-performance computational capabilities by combining the processing capacities of distributed CPUs to handle large processing tasks. The individually addressable tiles in the `SuperOverlay` structure are uniquely qualified to be processed in a grid environment, especially when image processing tasks can be easily parallelized as tile operations. Figure 8.5 illustrates the combination of `SuperOverlay`s and grid-enabled image processing. This figure is an extension of the

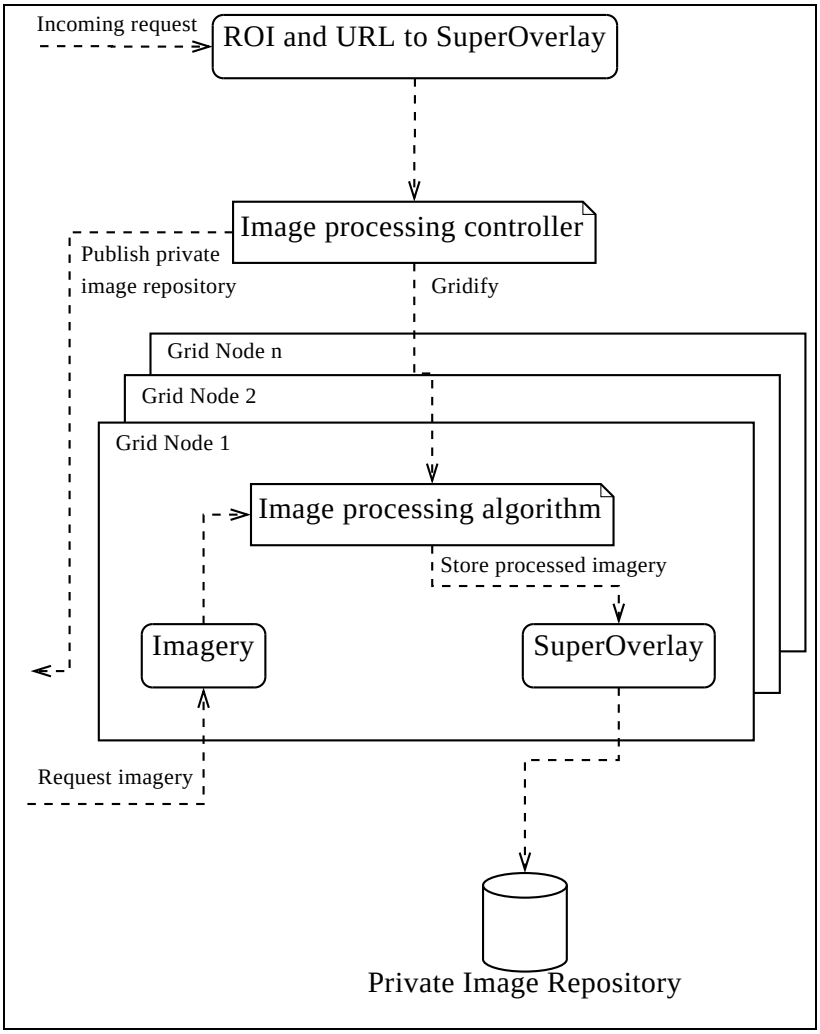

Figure 8.5: The `SuperOverlay` integrated into a grid-enabled image processing task.

right hand side of Figure 8.4. The key difference is that the image processing server, which receives the processing requests, acts as a task broker to subdivide the workload between available grid computing nodes based on the analysis of the ROI and `SuperOverlay` descriptors received in the request. Each grid node acts in the same way as a stand-alone instance processing the tile subset identified by the broker and storing the output in the private repository. The task broker monitors the processing nodes and publishes the address of the repository upon completion in exactly the same manner as the stand-alone process described in Figure 8.4. Note that the `SuperOverlay` integration enables the distribution of image tile identifiers, rather than image tiles themselves, leading to a significant reduction in intra-node communication. Each of the processing nodes only loads the relevant tile(s) for the identifiers passed to it by the broker. This mechanism allows for sophisticated processing load balancing, leading to a significant increase in image processing throughput.

8.4 Collaborative feature capturing

Our concept of "collaborative feature capturing" is some form of organized collation of geospatial feature data sets to support a given mapping task. The collaborative part assumes that more than a single person contributes to the collection, more or less simultaneous, but at different (machine) locations. The feature sets to be captured may be existing KML layers, those converted from other formats, or freshly digitized features in Google Earth™.

In our system, we exploit the forwarding mechanism found in Google Earth™ to collect the captured feature sets via the application server, into the spatial data repository. Capturing tasks can be organized either by geographical area, outlined as a polygon defining the ROI, by thematic layer (e.g. roads, buildings, etc.), or by a combination of both. Instructions to individual contributors can, in fact, be communicated using the system setup. We have implemented a basic authentication mechanism for contributors, based on preregistered login and password credentials, which are linked to a project identifier. Credentials are propagated and checked each time new features are submitted. Other checks can be incorporated in the application server logic, e.g. to limit contributions to the predefined ROI or thematic layer for that contributor.

In order to be able to collect captured data in a systematic way, we use predefined class hierarchies. A hierarchy includes a tree-like class definition and sub class definition up to the third level. For instance, a captured highway may be stored in the Road/Paved/Highway node of the hierarchy tree. In Google Earth™ the class hierarchy takes the form of a set of folders and subfolders, much like a directory structure in a file manager. The class hierarchy is stored for each of the submitted features. The possibility to link a project to a predefined class hierarchy allows for a flexible mechanism to address specific capturing tasks that need to conform to a user-defined map legend (e.g. topographic maps). Furthermore, the persisted class hierarchy or parts thereof can be transformed into hierarchies that are used in other mapping domains (e.g. tactical maps).

The feature capturing task supports feature updating and deletion. The spatial data repository uses feature versioning to keep track of changes to individual features. Versioning is an important mechanism in the support of feature updating, rollbacks, replays and release tagging. It protects the process from malfunctioning or from human error that could lead to unwanted data removal.

A feature can include a number of attributes that describe relevant properties (e.g. the road surface type and width). The system also allows the inclusion of additional multimedia information such as photographs, videos, or audio files. This is particularly interesting for integration of ground observations. Links to data held on other systems can be forwarded as `NetworkLink`s that relate to a geographic feature. The latter is a simple way of publishing the availability of a new image `SuperOverlay` to the project team.

8.5 Data visualization

All geospatial feature data are held in the spatial repository. A separate system component provides controlled access to the data stored in the system. The open source module GeoServer, which is an OGC compliant web map server, is used for visualization. GeoServer supports both the WMS and Web Feature Service [173] protocol standards that are relevant in our context. GeoServer exposes geospatial features from the spatial repository in a number of standard formats for integration into map clients, including KML. Feature querying and conditional styling capabilities [174] that are part of the OGC standards can present the GeoServer outputs in predefined class hierarchies and in map presentations that can be tailored to the required end-use. Data access and customization is based on predefined users and roles specified in the data repository.

Using the built-in refresh mechanisms in the Google Earth™ client, the user is able to display an instantaneous view of the data holdings even while the feature capturing process is ongoing. Since all submitted feature data is timestamped, the Google Earth™ time animation functionality can be deployed to display the collaborative effort chronologically. This is particularly useful for project managers, who must monitor work progress, identify processing bottlenecks and provide progress reports and intermediate map outputs to help inform the emergency response decision makers.

The use of the PostgreSQL database extended with PostGIS permits data access to geospatial clients that can perform enhanced processing beyond the feature capturing and visualization capabilities of Google Earth™. This may include data integrity checking, topology creation, spatial querying, and data conversion tasks that are performed by a limited number of project actors. This functionally extended Google Earth™ client interface is particularly useful because of its widespread exposure to the community of potential contributors.

8.6 Integration of VHR SAR damage assessment method

In Section 8.3.7 we explained how `SuperOverlay`s can be used for image processing. The image processing algorithm takes a `SuperOverlaid` raster image as input, performs the processing on the tiles of the previously selected ROI, and stores the result again in raster format as `SuperOverlay`. However, the damage assessment method from Chapter 7 requires additional input parameters and can store the results directly in the geospatial database, which is in this situation more efficient than storing the result as `SuperOverlay`. To integrate the damage assessment method into the system, we change the proposed scheme for performing image processing.

The damage assessment method, which is based on the usage of VHR optical pre-event and VHR SAR post-event data, determines on the level of individual buildings if it was destroyed by a catastrophic event or if it is still intact. For each building under investigation, a number of parameters are required, as described by (7.1). These parameters can be calculated from the building footprint, the shadow length of the building, and the acquisition parameters from the pre-event (e.g. sun incidence angle) and post-event imagery (e.g. azimuth direction, incidence angle). The footprint and the shadow length are

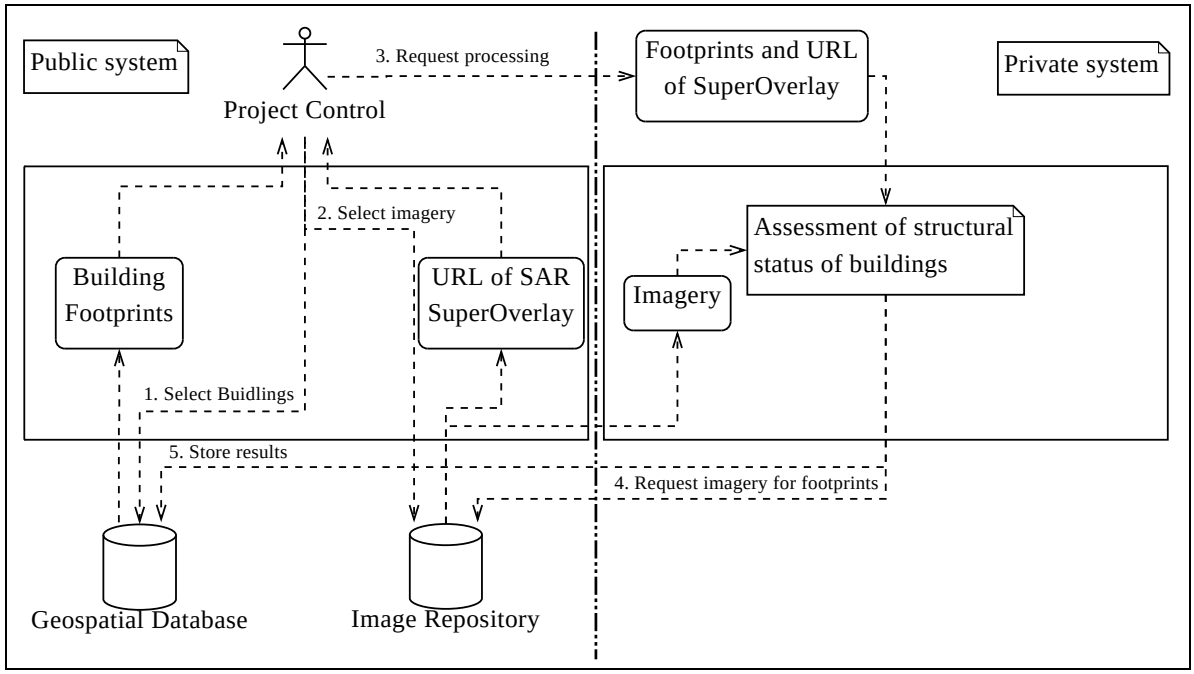

Figure 8.6: A schematic overview of the integration of the damage assessment method into the system.

derived manually from the VHR optical pre-event imagery, while the image parameters are given by the data providers in the header files. With this information, the automatic assessment of the structural status of a building can be triggered. The result is the classification into damaged or undamaged building. We store this information as feature data into the geospatial database. However, it is straight forward to save the results also in raster format as `SuperOverlay`.

The adaption of the workflow from Figure 8.4 for the integration of the damage assessment method is shown in Figure 8.6. In a first step, the project controller or expert analyst selects the buildings from the database which shall be analyzed according to their structural status. Then, the post-event SAR `SuperOverlay` is selected. In the third step, the damage assessment method is triggered via the public interface of a web service hosting the private implementation of the algorithm, passing the footprints and the URL to the SAR post-event `SuperOverlay`. Then the algorithm requests the individual tiles for evaluating the structural status of the buildings. Note that the algorithm operates in slant range geometry while the `SuperOverlay` tiles are geocoded. Hence, the tiles need to be transformed (scaling and rotation) into the original acquisition geometry prior to processing. Alternatively, if available, the slant range SAR image can be uploaded to the image repository so that the algorithm accesses the image directly without the `SuperOverlay` mechanism. In the fifth and final step, the results of the processing (classification into damaged or undamaged building) are stored in the geospatial database. For the proposed integration of the damage assessment method we assume that the classification is either performed using the unsupervised procedure, or, in case the supervised procedure is used, that the classifiers are already trained.

8.7 Test case 1: Lebanon armed conflict

8.7.1 Test case description

The system presented in the previous sections is generic and can be deployed within several application contexts that require collaborative and rapid geospatial analysis integration. It was specifically applied to a damage assessment scenario during the Lebanon crisis which was an international armed conflict between Lebanese and Israeli forces in July 2006. Geospatial data were collected to assess the situation in the conflict areas in order to estimate European Union (EU) support for funding of reconstruction and humanitarian aid in South Lebanon after the conflict. The scenario is particularly demanding for four reasons: 1) strict time constraints were imposed because the situation assessment had to be produced within 2 weeks; 2) very large data volumes had to be processed because the damage assessment analysis required VHR imagery for the entire Southern Lebanon area; 3) the accuracy of the orthorectified imagery had to be high for the comparative analysis; and 4) the distribution of the workload between two geographically dispersed image analyst teams.

Several mosaicked IKONOS scenes from 2005 covering the entire South Lebanon area (covering approximately 30 km north-south and 40 km east-west centered around 33°11'24" N, 35°21'36" E), with 4 m spatial resolution in four multispectral channels and 1 m resolution in the panchromatic channel were used as pre-event base data. The preprocessing of the image, with dimensions of 56260 x 41417 pixels and a size of 7.1 GB, comprised of pan-sharpening [175], orthorectification [176] and radiometric scaling to 8 bits. The preprocessed image was `SuperOverlaid` using the algorithm outlined in Section 8.3 resulting in 30016 tiles with a total size of 2.3 GB. The total processing time to produce the `SuperOverlay` on a standard workstation (two dual core Intel® Xeon™ 2.8 GHz CPUs, 3 GB RAM, Ubuntu 8.04) was slightly more than 2 hours (125 minutes and 45 seconds).

The post-event image was made up of a mosaicked QuickBird scene, which was acquired after the conflict ended in August 2006. This image mosaic has a panchromatic spatial resolution of 0.6 m and a spatial resolution of 2.4 m for the three multispectral channels. Preprocessing was the same as for the pre-event IKONOS mosaic. Applying the `SuperOverlay` algorithm on this 10.6 GB image whose dimensions were 73136 x 51821 pixels resulted in 49188 tiles and 4 GB in size. Total processing time was 176 minutes and 44 seconds.

Both pre- and post-event `SuperOverlay`s were uploaded to the web server by the project manager. The geospatial feature database was initialized with ancillary data that were made available through the Lebanese Council for Development and Reconstruction. Data sets included cadastral limits at 1:200,000 map scale, major populated places, roads and airports at 1:100,000 map scale, and rivers at 1:50,000 scale, which were converted and reprojected from ESRI shape files in UTM 33 N to Plate-Carrée projection.

As control data, we had a large set of point features that were digitized during a standard photointerpretation exercise by the EU Satellite Center immediately after the crisis, at which time our system was not yet available. Point features outlined partially or fully damaged structures based on the visual interpretation of pre- and post-event

imagery. Furthermore, field missions to the area in the aftermath of the crisis had yielded a large set of GPS-tagged photos that were very useful in assessing the quality of the visual interpretation.

8.7.2 Results and discussion

The collaborative effort is triggered when the pre-event imagery and ancillary feature data sets are available in the system. First, the analyst familiarizes himself with the area under investigation and checks whether the uploaded vector data are correctly geolocated based on the reference VHR image coverage. This is important because the data with which the system is initialized usually has its origins from different sources with varying spatial resolution, projection, and quality. If the precision of the initial data is not sufficient, it can be post-processed within the system. For instance, a western offset was found in the 1:100,000 scale road data set with respect to the georeferenced IKONOS pre-event mosaic. The analysts digitized a set of ground control points across the ROI to assess the overall shift and submitted these corrections to the system. This permitted the project manager to calculate the mean shift of 82.3 m $\pm$ 0.8 m and apply a translation to the road data set correcting for the shift. After a refresh request of the road layer, all users have access to the corrected road set.

The primary task of the project manager, at this stage, is to divide the ROI into manageable areas for eventual visual inspection and digitization. Since the damage assessment focuses on populated areas (humanitarian situation assessment) and infrastructure (logistics, damage value estimates) the priority is focussed on locating potentially affected settlements. The ancillary feature data on populated places was too coarse to be useful beyond queuing. A web service processing algorithm for the calculation of a built-up presence index [177] on the tiles of the pre-event `SuperOverlay` was used instead. The algorithm is based on the fuzzy rule based composition of anisotropic textural measures derived from the gray level co-occurrence matrix of the byte-scaled panchromatic image channel and highlights built-up areas. The results of this image processing algorithm is accessible as a `SuperOverlay` (see Figure 8.7) to the analysts, who can then outline the populated areas to be analyzed at the damage assessment stage. Groups of outlined areas were assigned to individual analysts to avoid duplication of digitization efforts (assignment is stored as an attribute to each polygon outline). Note that at this point media reports related to the conflict can be used to further focus on the areas most impacted by the conflict and store these as flagging features in the project data store.

For logistical support of the reconstruction effort road networks and specifically crossroads and bridges, are strategically important targets, which had a higher priority during the early assessment stage. One analyst team was tasked to digitize the road network, completing, as much as possible, the 1:100,000 scale feature set that includes only a non-exhaustive set of highways and primary roads. Another team digitized water ways, which were mostly irrigation channels and dry riverbeds in the South Lebanon scene (only the Litani river was available in the ancillary feature set). Note that automatic or semi-automatic algorithms for feature extraction can be applied at this stage to derive relevant layers in support of the digitization tasks.

The project manager can trigger spatial queries on the road and river network data sets

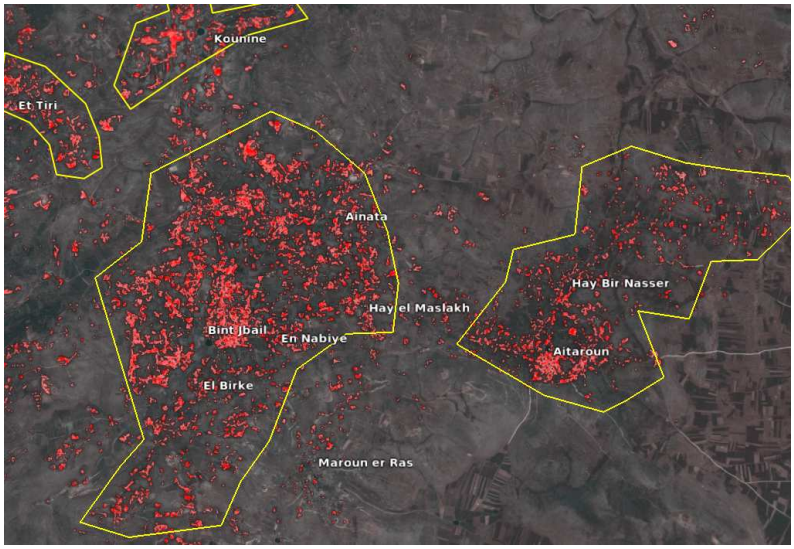

Figure 8.7: Example of the output of the built-up presence index algorithm applied to the pre-event IKONOS `SuperOverlay`. The pre-event image in the background is overlaid with the output, which depicts in the red channel the density of the built-up structure. Non-built-up areas are made transparent so that they do not obscure the background. Settlements are outlined as yellow polygons, using the built-up presence index as reference. (Satellite image: © Space Imaging International Ltd. distributed by European Space Imaging GmbH, 2005.)

to locate the relevant crossings and store these as point features, as shown in Figure 8.8. Each point feature is assessed by the analysts at the damage assessment stage. Furthermore, the point features may be used as seed points for a change detection algorithm which automatically assesses whether the region around those points has changed.

The actual damage assessment phase started as soon as the post-event QuickBird mosaic image was integrated as a `SuperOverlay`. The digitization proceeded according to a predefined class hierarchy as discussed in Section 8.4. Figure 8.9 shows the result of the digitization of a portion of the Bent Jbail settlement (33°7'8.40" N, 35°26'6.00" E) which was in a heavily damaged area of the conflict zone. Digitized paved and unpaved roads are shown with red and brown lines, respectively. Moderately damaged buildings are outlined with light blue polygons, while completely destroyed buildings are highlighted with dark blue polygons. Impact craters causing damage to the terrain rather than infrastructure are indicated by yellow polygons. In the "Places" section in the left part of Figure 8.9, the class hierarchy is shown. The class hierarchy was decided in a rather ad hoc manner, as classification standards for damage assessment are not yet available. Future application of our system in similar damage assessment efforts would benefit from standardization efforts at both the data capturing and map styling stages.

Ground truth data collected during the assessment phase can be uploaded to the system. In particular, GPS-referenced reports and field photography are very useful to the analysts. For example, damaged buildings may be annotated with the corresponding images taken in the field with a digital camera. The Google Earth™ client pops up the relevant photo once the building polygon is selected, as shown in Figure 8.9. In an

Figure 8.8: An example of automatic derived road-water crossings. The geospatial intersection function was applied to the road (red) and river (blue) networks resulting in the highlighted crossings. (Satellite image: © Space Imaging International Ltd. distributed by European Space Imaging GmbH, 2005.)

armed conflict, ground truth collection is a hazardous task and Internet connectivity is erratic at best. Our ground data was collected after the conflict and was uploaded in an offline fashion. Various community sites on the Internet provided detailed geolocated photographs that were taken during and immediately after the conflict. We were able to correlate these photographs with visible damage in the QuickBird scenes, demonstrating the potential of this methodology, especially in less challenging emergency scenarios. It is also possible to deploy our system to identify objects or areas of interest for in-situ inspections and communicate these to local field teams.

All activities related to the creation, modification, and deletion of data in the system were timestamped and associated with a user. This allowed us to monitor the system and retrieve information on the progress of digitization tasks. This was not only important for the identification of bottlenecks during the digitization phase, but also for post-analysis of the rapid mapping project to draw pertinent conclusions in order to improve collaborative feature capturing for the next crisis response.

8.8 Test case 2: Sichuan earthquake

In this section we demonstrate the proposed system applied in a damage assessment scenario with VHR SAR imagery. As practical example we illustrate the automatic detection of destroyed buildings after the Sichuan earthquake in 2008 for the town of Yingxiu using the method proposed in Chapter 7. The data set is described in Section 7.4 in detail. In particular, we use the pre-QB image to extract information about the buildings from the reference situation, while the assessment of the structural status is performed with the post-CSK scene.

Directly after the earthquake the image archives from the satellite providers were searched for suitable pre-event scenes. Once the pre-QB scene arrived, the project manager uploaded the data as `SuperOverlay`s to the system. First, she scaled the radiometry

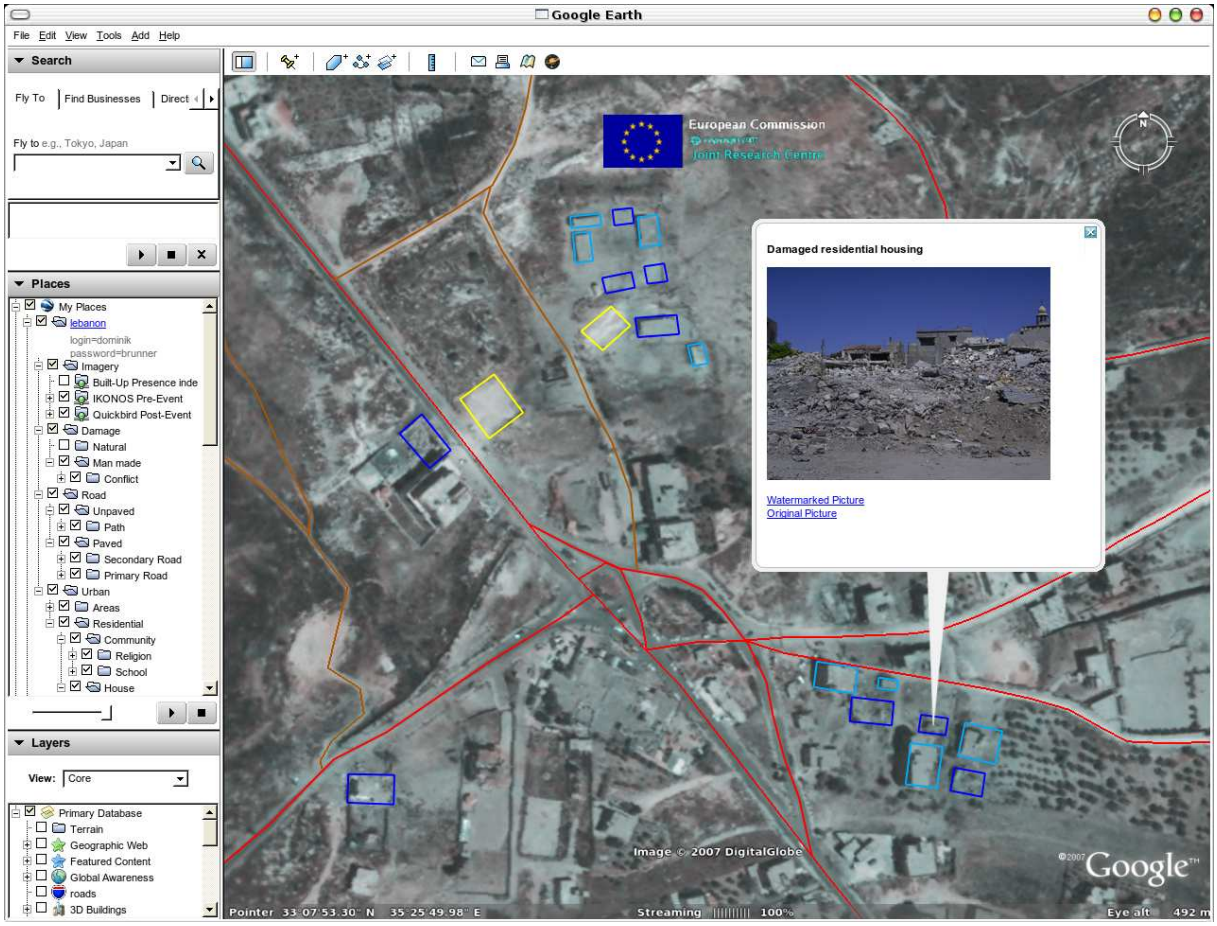

Figure 8.9: A screenshot of the Google Earth™ client interface showing the result of the feature capturing for an area in Bent Jbail, South Lebanon. Paved roads are marked red, unpaved streets are shown in brown. Moderately damaged buildings are outlined with light blue and destroyed buildings with dark blue polygons. The yellow polygons mark impact craters in non-built-up terrain. The pop-up shows the image of a destroyed building which is associated with the corresponding blue polygon. (Satellite image: © DigitalGlobe distributed by Eurimage S.p.A., 2006.)

of each channel to 8 bits and reprojected the image from UTM 48 N to the Plate-Carrée reference system. Then she extracted the Red-Green-Blue (RGB) channels from the scene and converted the 3368 x 4488 pixels image (43.3 Mb) in 38 seconds to a `SuperOverlay` with 301 tiles (34 Mb). The transformation of the panchromatic channel, which has 13472 x 17952 pixels (244.0 Mb), to a `SuperOverlay` took 10 minutes and 43 seconds and resulted in 4025 tiles with 245 MB total size.

When the pre-event data are uploaded to the system, the collaborative analysis effort starts. The ROI is defined, split in subregions, and assigned to the analysts in the team. Then, the building footprints which fulfill the model requirements of the automatic damage assessment method (e.g. rectangular footprint, building isolation), are digitized by the analysts. Furthermore, the shadow length of the buildings are measured. For this both (RGB and panchromatic) pre-event `SuperOverlays` can be used. The multispectral

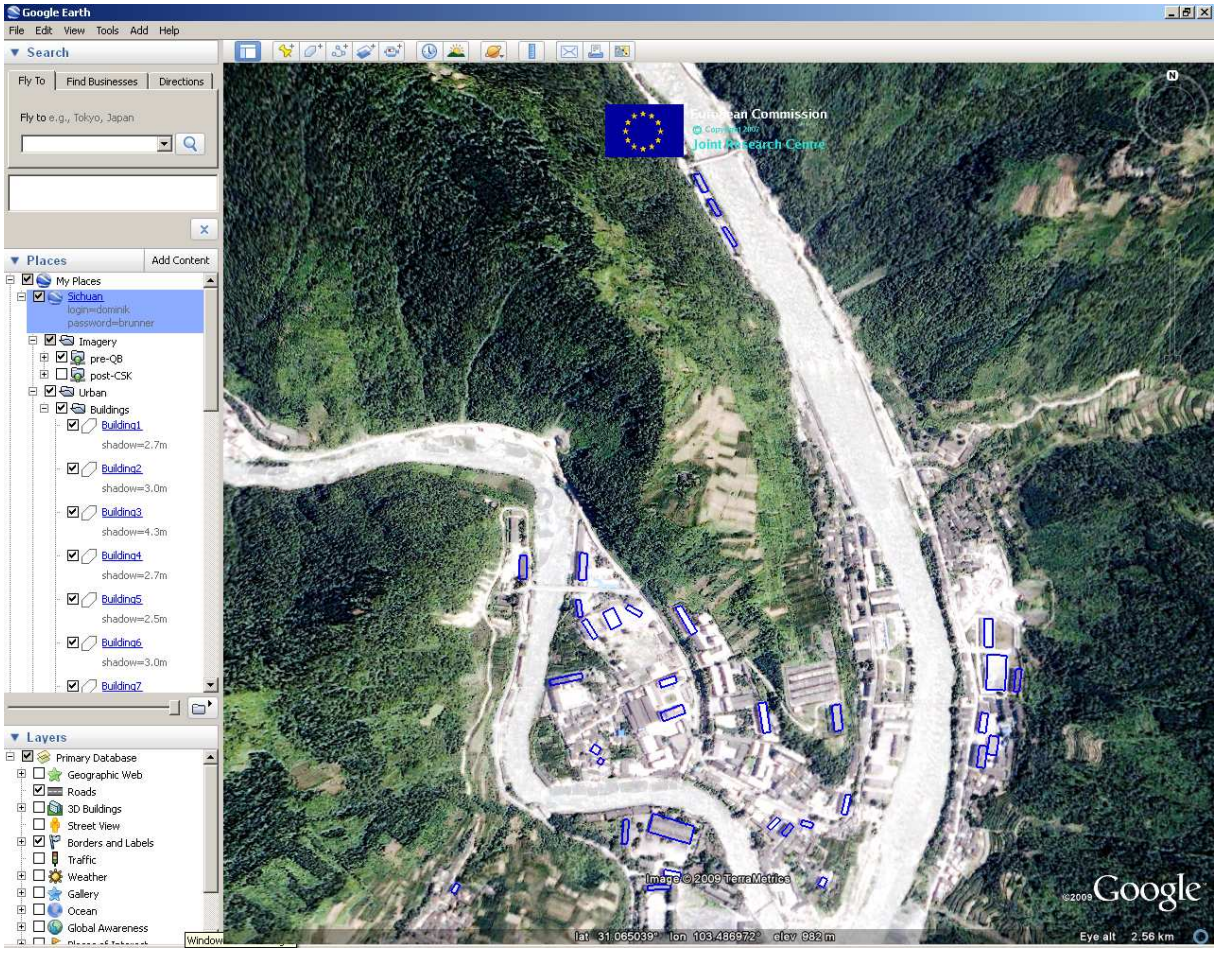

Figure 8.10: A screenshot of the Google Earth™ client interface showing the pre-QB scene and the outlined footprints (in blue) of the buildings which shall be analyzed according to their structural status. (QuickBird image: © DigitalGlobe distributed by Eurimage S.p.A., 2005.)

`SuperOverlay` allows for a better scene understanding, while the higher resolution of the panchromatic `SuperOverlay` supports a more accurate measurement of the shadow length. The result is shown as Google Earth™ screenshot in Figure 8.10, where the blue polygons mark the footprints of the buildings which shall be investigated according to damage. The shadow length is stored as attribute of the building footprint, as shown in the left column of the Google Earth™ client. Not all buildings fulfill the model requirements so that only a subset can be chosen for the automatic damage assessment procedure. To get a realistic overview of the situation in the city after the event and to analyze whether there is a spatial dependence between damaged and undamaged buildings, the candidate buildings should be spread out equally over the investigated area, as it is the case in Figure 8.10.

The post-CSK scene was received in single look complex format, so that the project manager transformed it first to 8 bit amplitude. Then she converted it to ground range and coregistered it via manual tie point selection to the pre-QB scene. The resulting

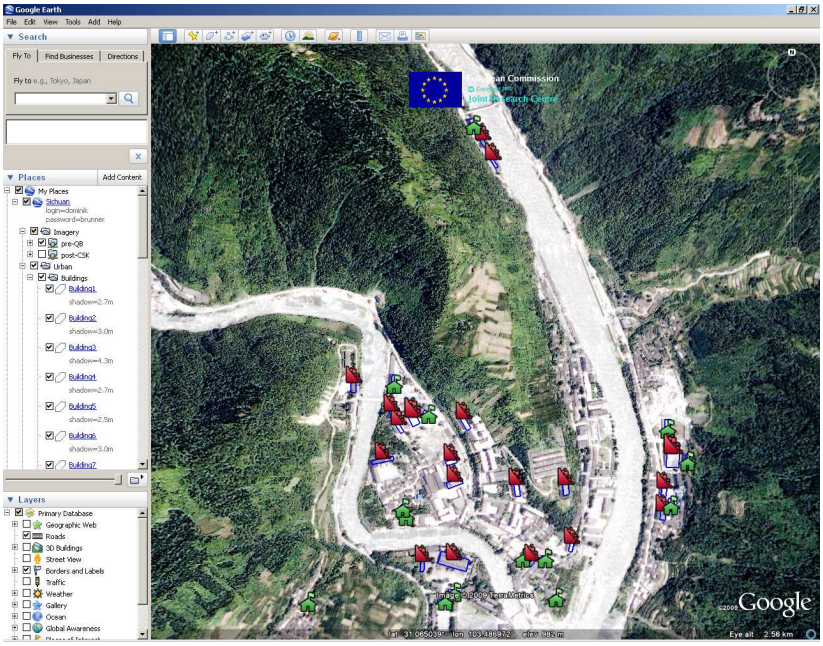

(a)

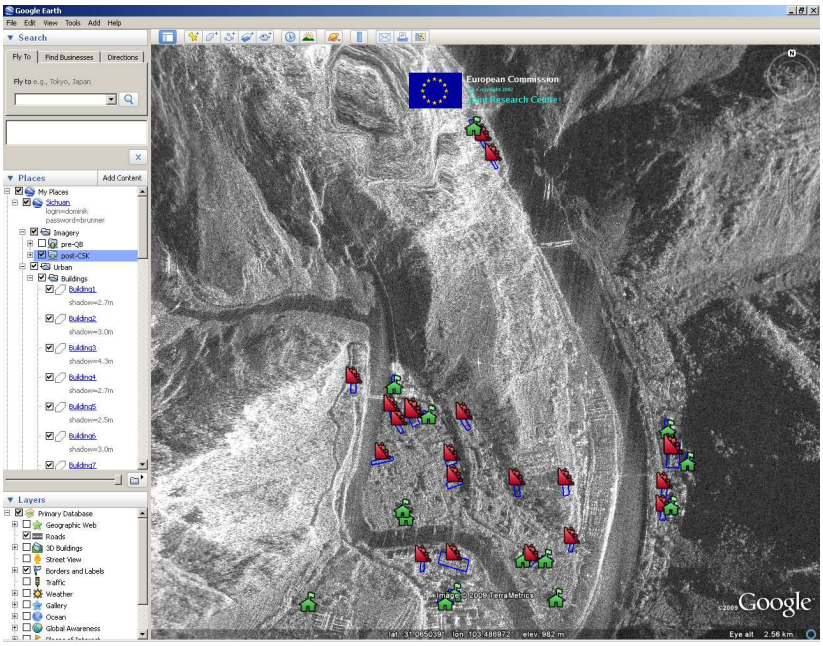

(b)

Figure 8.11: A screenshot of the Google Earth™ client interface showing the result of the automatic assessment of the structural status of the buildings. Green symbols refer to undamaged buildings, while the red symbols show damaged buildings. (a) Result overlaid to pre-QB scene. (b) Result overlaid to post-CSK scene. (QuickBird image: © DigitalGlobe distributed by Eurimage S.p.A., 2005; COSMO-SkyMed image: © ASI distributed by eGeos S.p.A., 2008.)

image, which has 13525 x 10861 pixels image (140.3 MB) was `SuperOverlaid`, which took 5 minutes and 1 second, resulting in 2408 tiles (177.0 MB). Note that for the automatic damage assessment method it would be in theory enough to upload the original data to the image repository. But since Yingxiu is located in a mountainous area it is likely that the two scenes are not accurately geolocated. Hence, the manual coregistration of the two scenes ensures that the damage assessment method investigates, starting from the building footprints which were derived from the optical pre-QB scene, the correct subset in the post-CSK scene.

When the post-CSK scene is uploaded to the system, the damage assessment algorithm is triggered by the project controller or expert analyst. Note that the manual interpretation of the pre-QB scene does not need to be finished at this point. Since individual buildings are selected for the automatic assessment, it is possible to execute the algorithm only for buildings which were added to the geospatial database after the last assessment run, without the need to reassess already processed buildings. Via the automatic refresh mechanism of the GoogleEarth™ client, all users have access to the results of the automatic damage assessment procedure. In Figure 8.11a we show the typical output of the method overlaid to the pre-QB scene. The green house symbols indicate that the building was not damaged, while the red symbols show damaged buildings. Since also the post-CSK scene was made available as `SuperOverlay`, the results can also be displayed overlaid to the SAR scene, as shown in Figure 8.11b. This can be beneficial if the results shall be validated by a SAR specialist. From the visualization of the results in the GoogleEarth™ client we see that the damaged and undamaged buildings are spread in a relatively homogeneous way over the investigated area. Hence, there is no spatial dependence between the two classes of buildings so that the earthquake affected the investigated area in an equal manner.

It is worth pointing out that much of the time consuming manual work can be done as soon as the pre-event image from the archive is available. Once the post-event scene is uploaded to the system, the evaluation of the structural status is performed automatically. The required time only depends on the available computational infrastructure. In this context state of the art grid or general purpose GPU computing solutions can help to handle the computational complexity [178].

8.9 Discussion and conclusion

In this chapter, three fundamental issues were addressed that, in our opinion, hinder the wide spread take up of earth observation information in operational applications. Firstly, we showed how very large image coverages can be made accessible to a geographically distributed audience by implementing the `SuperOverlay` mechanism available within Google Earth™. Secondly, it was shown how the use of `SuperOverlay`s can be extended to accommodate novel mechanisms for integrating dedicated image processing tasks. The image processing tasks can optionally be supported by grid computing resources. Finally, we demonstrated that access to distributed geospatial feature data in typical workflows that require an integrated analysis of image and feature information in support to decision making can be implemented.

We have demonstrated the proposed system use in the context of emergency response scenarios following the armed conflict in South Lebanon in 2006 and after the recent Sichuan earthquake (China, May 2008). The system was also used during the Georgia armed conflict (August 2008) in support of damage assessment. Note that for the Sichuan earthquake, VHR satellite pre- and post-event imagery was also provided for public access, as `SuperOverlay`s, directly by the satellite image providers [179]. More recently, NOAA has demonstrated a similar approach for the analysis of airborne orthophotos supporting relief efforts after the September 2008 Hurricane Ike [180].

The system functionality is sufficiently generic to be used in other contexts. We believe it is particularly useful in applications that require near real time access to event information for which in-situ or domain expert knowledge is essential in automated and manual image interpretation.

Our system is composed of free software and open source components, but the system structure is sufficiently generic to accommodate other proprietary or free software modules that implement the same functionality. The choice of the Google Earth™ client is optional and may be replaced with other client software that implements the `SuperOverlay` construct. We are currently evaluating the Java release of the open source World Wind client as an alternative. We believe that open source and public software components better address our long term goal to distribute geospatial processing capabilities to relevant end users and contributers within the emergency response domain, without the need for significant and recurring investment. This belief is in line with the mission of the United Nations SPIDER program whose goal is to "ensure that all countries have access to and develop the capacity to use all types of space-based information to support the full disaster management cycle" [181].

Chapter 9

Conclusions

This chapter concludes this dissertation by summarizing and discussing the results obtained in the development of the different research topics. Finally, it gives an outlook for future work.

9.1 Summary and discussion

This thesis investigated the use of remote sensing data for damage assessment in urban areas as part of the emergency response cycle. In this context, we proposed novel (semi-) automatic methods to extract information on the level of individual buildings from single detected spaceborne VHR SAR (e.g. TerraSAR-X and COSMO-SkyMed) data. First, we investigated the potential of the double bounce of a building to be exploited in automatic damage assessment techniques by analyzing empirically the relation between the double bounce effect and the aspect angle of a building for different ground materials. Then, we proposed a radar imaging simulator for urban structures based on an adapted ray tracing procedure and a Lambertian-specular mixture model. Furthermore, we developed a method to estimate building heights from single detected VHR SAR imagery, which can be used as indicator to analyze the structural integrity of buildings. Moreover, we defined an approach that detects destroyed buildings after a crisis event (e.g. earthquake) using VHR optical pre-event and VHR SAR post-event data. Finally, addressing the practical challenges of integrating remote sensing imagery into the operational workflow of geospatial information support for emergency response actions, we proposed an IT system infrastructure which is based on publicly available and open source software modules.

The empirical analysis of the behavior of the double bounce stripe of a building with respect to changes in the aspect angle of a building was conducted in two phases. First, we analyzed a set of polarimetric images which we measured on a scaled building model in the EMSL under controlled conditions and varying viewing configurations. These measurements are subject to a number of simplifying assumptions. For instance, the same factor which is used to scale the building model should be used to scale the wavelength for the measurements. However, in our case, the resulting frequency was not supported by the laboratory so that we selected a lower frequency. Hence, the scaled building model measurements should be used to find general trends of an effect, rather than to investigate

its exact behavior. In order to validate and further refine the results from the EMSL experiment, we analyzed in the second phase a set of residential and industrial buildings surrounded by two different ground materials in actual spaceborne VHR SAR data. The analysis pointed out that the double bounce effect gives a strong power signature to buildings with walls almost parallel to the SAR azimuth direction. It drops rapidly in the low aspect angle range, while it decreases moderately for larger angles. The exact characteristic of the decay depends on the materials and surface parameters. For smoother surfaces (e.g. asphalt) the strength of the double bounce decreases more significantly in a smaller range of aspect angles, while for rougher surfaces (e.g. grass) it decreases less steep but more constant over the full range of aspect angles.

The proposed radar imaging simulator for urban structures offers two novel contributions. First, it extends standard ray tracing so that the rays are reflected in various directions. Hence, also the Lambertian scattering contributions from rough surfaces for instance of buildings are considered in the simulation. Second, it introduces an adjustable mixture of Lambertian and specular scattering as radiometric model to calculate the backscattering from the surfaces, focusing on calculating geometrical effects of the scattering rather than absolute radiometry. We tested the proposed simulator for a rectangular gable roof building in submeter airborne SAR data and a complex structured pyramid in meter resolution TerraSAR-X data. The results showed that the spatial pattern of the scattering of the structures is simulated with an accuracy in the order of few pixels. This demonstrates that the simulator is effective to calculate effects which are related to the geometry, such as layover-, shadow-, and multibounce scattering.

The proposed method for estimating the height of a generic building from single detected VHR SAR imagery is based on the simulation of the building at different heights and the comparison of the predicted signatures with the building signature in the actual scene. The estimated height is given by the simulation which has the highest similarity with the signature in the actual scene. We tested the approach on a set of 40 flat and gable roof buildings using two submeter VHR airborne and two 1 m resolution TerraSAR-X SAR scenes. The results show that, in the absence of disturbing effects (e.g. trees or other buildings in the immediate surrounding), the method is able to estimate the height of flat and gable roof buildings in the submeter data to the order of 1 m, while the accuracy for the meter resolution spaceborne data is lower but still sufficient to estimate the number of floors of a building. The approach is shown to be insensitive to the aspect angle of a building, while it favors larger incidence angles. A generalization of the proposed method to the application to dual aspect data sets demonstrated that with a pair which was acquired with perpendicular flight paths some improvements in the height estimation accuracy can be achieved, while a pair of ascending and descending scenes does not yield any significant improvement.

The novel approach for detecting destroyed buildings (e.g. after an earthquake) using pre-event VHR optical and post-event detected VHR SAR imagery evaluates the similarity between the predicted building SAR signature and the corresponding subset in the actual post-event SAR scene. If this similarity is high, the building is likely to be intact, whereas a low similarity indicates that the building is partially or completely destroyed. A Bayesian technique is used to classify the individual buildings. We tested the proposed method

for a subset of the town of Yingxiu, China, which was heavily damaged in the Sichuan earthquake in 2008, using QuickBird pre-event and TerraSAR-X and COSMO-SkyMed post-event imagery. The results showed that the method distinguishes between damaged and undamaged buildings with a high overall accuracy of about 90% using a supervised classification procedure and about 80% using an unsupervised technique. It misclassifies more undamaged buildings as damaged buildings than vice versa providing an upper bound for building damage. This misclassification is explained by the fact that we do not model scatter interferences from neighboring objects in the building signature prediction step. Consequently, undamaged buildings which are affected by scattering from other objects in its surrounding (e.g. from trees, other buildings, or cars) can be misclassified as damaged building and hence raising the false alarm rate.

The proposed IT system infrastructure, which we designed to efficiently integrate remote sensing data in the workflow of geospatial data based emergency response, enables rapid collaborative mapping, support for in-situ data collection, customized on-demand image processing, geospatial data queries, and near instantaneous map visualization. The approach was demonstrated with a test case in a rapid damage assessment scenario using VHR spaceborne optical imagery over Southern Lebanon from 2006. Furthermore, we integrated our method for detecting destroyed buildings to highlight the suitability of the system for VHR SAR based damage assessment, using the 2008 Sichuan earthquake as test case. The core of the system is the implementation of the `SuperOverlay` mechanism available within Google Earth™. It makes privately owned very large image coverages accessible to a geographically distributed audience. Furthermore, the use of `SuperOverlay`s can be extended to accommodate novel mechanisms for integrating dedicated image processing tasks, optionally supported by grid computing. Most importantly, the system allows the integrated analysis of distributed image and feature information to support efficient decision making. It is worth noting that the proposed IT system infrastructure does not rely on the Google Earth™ client. It can be replaced with other software clients which support the `SuperOverlay` standard.

9.2 Concluding remarks and future work

One of our concerns regarding the usage of VHR SAR imagery was to analyze the effects of the aspect angle on the SAR signature of the building. Indeed, the proposed methods for building height estimation and damage assessment were designed to handle buildings at various viewing configurations, i.e. different aspect and incidence angles. However, the main limitation of the proposed methods is the assumption of building isolation. In particular, the scattering effects from objects (e.g. trees and other buildings) in the close surrounding of a building are not modeled. In fact, we analyzed the impact of a violation of this assumption and demonstrated empirically that the proposed methods can handle some deviations from this assumption, but tend to fail if significant objects are located in the surrounding of the building under investigation. In order to use VHR SAR to analyze dense urban areas (e.g. inner parts of cities), future work should focus on the analysis and the modeling of the effects of neighboring objects on the SAR signature of buildings leading to the definition of more generic building detection and reconstruction methods.

In the proposed damage assessment method the decision whether a building is damaged or undamaged is made either in a supervised or unsupervised way. Indeed, considering the supervised classification, it is not always necessary to train manually the classifier on a training set. For spaceborne VHR SAR, the classifiers reported in this thesis give reliable classification results as we tested them on both, meter resolution TerraSAR-X and COSMO-SkyMed data. In order to increase the practical relevance of the presented approach especially with regard to the availability of submeter data, we tested the use of an unsupervised classifier based on the Gaussian assumption. In order to improve the classification accuracy, future work should focus on using a more general distribution, e.g. the generalized Gaussian distribution, which parameters can also be derived using an EM algorithm as proposed in [182].

The proposed damage assessment method operates sequentially in such that it extracts first information from the VHR multispectral pre-event data before they are used after a conversion procedure in the VHR SAR post-event scene. Hence, also the use of advanced data fusion techniques, which consider simultaneously the VHR multispectral and SAR images, should be investigated.

With the completion of the COSMO-SkyMed constellation and the longer availability of VHR SAR sensors, the archives of spaceborne VHR SAR pre-event data will become richer. Hence, future work should focus on the integration of VHR SAR as pre-event data source in the proposed damage assessment method. In this context, the advantage of the rendering and matching analysis is the independence between the pre- and post-event data, i.e. orbit and incidence angle can change between the two acquisitions, which is especially beneficial if the available data set is composed by acquisitions from different sensors. If the pre- and post-event SAR data are acquired from the same viewing configuration, the use and effectiveness of interferometric methods for the VHR X-band data should be investigated.

The launch of the TanDEM-X sensor is scheduled for late 2009 - early 2010. It will orbit as constellation with TerraSAR-X and permit to acquire single pass InSAR data. Hence it offsets the need to revisit the same location after several days in order to complete the InSAR acquisition, making it a candidate as source for post-event SAR imagery. Here, future work should focus on integrating the proposed building height extraction method into a damage assessment procedure. In particular, building reference heights derived from single pre-event SAR scenes can be compared to the heights resulting from the post-event InSAR DSM in order to estimate the structural status of buildings. Again, the major advantage is the independence of the viewing configuration between the pre- and post-event SAR data.

Bibliography

[1] B. McGuire, I. Mason, and C. Killburn, *Natural Hazards and Environmental Change (Key Issues in Environmental Change)*. London, UK: Arnold, 2002.

[2] P. Hoyois, J.-M. Scheuren, R. Below, and D. Guha-Sapir, "Annual disaster statistical review: Numbers and trends 2006," CRED: Brussels, Tech. Rep., 2007.

[3] J. Thielen, J. Bartholmes, M.-H. Ramos, and A. de Roo, "The European flood alert system - Part 1: Concept and development," *Hydrology and Earth System Sciences*, vol. 13, no. 2, pp. 125–140, 2009.

[4] A. Rudloff, J. Lauterjung, U. Muench, D. J. Acksel, and GITEWS project team, "The German contribution to the Indian Ocean tsunami early warning system (GITEWS) - Status quo," in *Geophysical Research Abstracts*, vol. 10, 13-18 April, Vienna, Austria, 2008.

[5] R. M. Allen, *Earthquake Early Warning Systems*. Springer Berlin Heidelberg, 2007, ch. The ElarmS Earthquake Early Warning Methodology and Application across California, pp. 21–44.

[6] T. D. Groeve, L. Vernaccini, and A. Annunziato, "Global disaster alert and coordination system," in *Proceedings of 3rd International Conference for Information Systems for Crisis Response and Management (ISCRAM)*, Newark, NJ, USA, May 2006, pp. 1–10.

[7] D. Eriksson, "Modelling projections of international response to suddent-onset disasters," Ph.D. dissertation, Coventry University, 2006.

[8] S. Voigt, T. Kemper, T. Riedlinger, R. Kiefl, K. Scholte, and H. Mehl, "Satellite image analysis for disaster and crises-management support," *IEEE Transactions on Geoscience and Remote Sensing*, vol. 45, no. 6, pp. 1520–1528, June 2007.

[9] F. Bovolo and L. Bruzzone, "A split-based approach to unsupervised change detection in large-size multitemporal images: Application to tsunami-damage assessment," *IEEE Transactions on Geoscience and Remote Sensing*, vol. 45, no. 6, pp. 1658–1670, June 2007.

[10] P. Gamba, F. Dell'Acqua, and G. Trianni, "Rapid damage detection in the Bam area using multitemporal SAR and exploiting ancillary data," *IEEE Transactions on Geoscience and Remote Sensing*, vol. 45, no. 6, pp. 1582–1589, June 2007.

[11] F. Yamazaki and M. Matsuoka, "Remote sensing technologies in post-disaster damage assessment," *Journal of Earthquake and Tsunami*, vol. 1, no. 3, pp. 193–210, September 2007.

[12] S. Stramondo, C. Bignami, M. Chini, N. Pierdicca, and A. Tertulliani, "Satellite radar and optical remote sensing for earthquake damage detection: Results from different case studies," *International Journal of Remote Sensing*, vol. 27, no. 20, pp. 4433–4447, October 2006.

[13] L. Bruzzone and D. F. Prieto, "An adaptive parcel-based technique for unsupervised change detection," *International Journal of Remote Sensing*, vol. 21, no. 4, pp. 817–822, March 2000.

[14] L. Bruzzone and D. F. Prieto, "Automatic analysis of the difference image for unsupervised change detection," *IEEE Transactions on Geoscience and Remote Sensing*, vol. 38, no. 3, pp. 1171–1182, May 2000.

[15] L. Bruzzone and D. F. Prieto, "A minimum-cost thresholding technique for unsupervised change detection," *International Journal of Remote Sensing*, vol. 21, no. 18, pp. 3539–3544, December 2000.

[16] F. Bovolo and L. Bruzzone, "A detail-preserving scale-driven approach to unsupervised change detection in multitemporal SAR images," *IEEE Transactions on Geoscience and Remote Sensing*, vol. 43, no. 12, pp. 2963–2972, December 2005.

[17] F. Chaabane, A. Avallone, F. Tupin, P. Briole, and H. Maître, "A multitemporal method for correction of toposheric effects in differential SAR interferometry: Application to the Gulf of corinth earthquake," *IEEE Transactions on Geoscience and Remote Sensing*, vol. 45, no. 6, pp. 1605–1615, June 2007.

[18] S. Buckreuss, R. Werninghaus, and W. Pitz, "The German satellite mission TerraSAR-X," in *Proceedings of IEEE Radar Conference (RadarCon)*, Rome, Italy, May 2008, pp. 1–5.

[19] G. F. De Luca, G. Marano, M. Piemontese, B. Versini, F. Caltagirone, G. Casonato, A. Coletta, and M. De Carlo, "Interoperability, expandability and multi mission-sensor COSMO-SkyMed capabilities," in *Proceedings of IEEE International Geoscience and Remote Sensing Symposium (IGARSS)*, Barcelona, Spain, July 2007.

[20] A. R. Brenner and L. Roessing, "Radar imaging of urban areas by means of very high-resolution SAR and interferometric SAR," *IEEE Transactions on Geoscience and Remote Sensing*, vol. 46, no. 10, pp. 2971–2982, October 2008.

[21] A. Sieber, "The European microwave signature laboratory," in *Proceedings of IEEE International Geoscience and Remote Sensing Symposium (IGARSS)*, Houston, TX, USA, May 1992.

[22] F. T. Ulaby, R. K. Moore, and A. K. Fung, *Microwave Remote Sensing: Active and Passive*. Artech House, 1982, vol. 2.

[23] K. Yee, "Numerical solution of inital boundary value problems involving Maxwell's equations in isotropic media," *IEEE Transactions on Antennas and Propagation*, vol. 14, no. 3, pp. 302–307, May 1966.

[24] A. K. Fung, *Microwave Scattering and Emission Models and Their Applications*. Boston, MA, USA: Artech House, 1994.

[25] F. T. Ulaby, R. K. Moore, and A. K. Fung, *Microwave Remote Sensing: Active and Passive*. Addison-Wesley, 1981, vol. 1.

[26] J.-S. Lee, "Speckle suppression and analysis for synthetic aperture radar images." *Optical Engineering*, vol. 25, no. 5, pp. 636–643, May 1986.

[27] J.-S. Lee and E. Pottier, *Polarimetric Radar Imaging: From Basics to Applications*. CRC Press, 2009.

[28] S. R. Cloude, "The characterization of polarimetric effects in EM scattering," Ph.D. dissertation, University of Birmingham, 1986.

[29] S. Cloude and E. Pottier, "An entropy based classification scheme for land applications of polarimetric SAR," *IEEE Transactions on Geoscience and Remote Sensing*, vol. 35, no. 1, pp. 68–78, January 1997.

[30] D. Belcher and C. Baker, "Hybrid strip-map/spotlight SAR," in *IEE Colloquium on Radar and Microwave Imaging*, vol. 2, November 1994, pp. 1–7.

[31] A. Moreira, G. Krieger, I. Hajnsek, D. Hounam, M. Werner, S. Riegger, and E. Settelmeyer, "TanDEM-X: A TerraSAR-X add-on satellite for single-pass SAR interferometry," in *Proceedings of IEEE International Geoscience and Remote Sensing Symposium (IGARSS)*, Anchorage, AK, USA, September 2004, pp. 1000–1003.

[32] M. Zink, G. Krieger, H. Fiedler, and A. Moreira, "The TanDEM-X mission: Overview and status," in *Proeceedings of IEEE International Geoscience and Remote Sensing Symposium (IGARSS)*, Barcelona, Spain, July 2007, pp. 3944–3947.

[33] A. Roth, "TerraSAR-X: a new perspective for scientific use of high resolution spaceborne SAR data," in *Proceedings of 2nd GRSS/ISPRS Joint Workshop on Remote Sensing and Data Fusion over Urban Areas*, Berlin, Germany, May 2003, pp. 4–7.

[34] F. Covello, F. Battazza, A. Coletta, E. Lopinto, L. Pietranera, G. Valentini, and S. Zoffoli, "COSMO-SkyMed mission status," in *Proceedings of SPIE Conference on Image and Signal Processing for Remote Sensing XIV*, vol. 7109, Cardiff, Wales, UK, September 2008, pp. 710 918–710 918–15.

[35] A. J. Bennett and D. Blacknell, "Infrastructure analysis from high resolution SAR and InSAR imagery," in *Proceedigns of the 2nd GRSS/ISPRS Joint Workshop on Remote Sensing and Data Fusion over Urban Areas*, Berlin, Germany, May 2003, pp. 230– 235.

[36] U. Soergel, U. Thoennessen, and U. Stilla, "Iterative building reconstruction from multi-aspect InSAR data," in *Proceedings of the ISPRS working group III/3 workshop "3-D reconstruction from airborne laserscanner and InSAR data"*, vol. XXXIV, Part 3/W13, Dresden, Germany, October 2003, pp. 186–192.

[37] G. R. Burkhart, Z. Bergen, and R. Carande, "Elevation correction and building extraction from interferometric SAR imagery," in *Proceedings of IEEE International Geoscience and Remote Sensing Symposium (IGARSS)*, Lincoln, NE, USA, May 1996.

[38] F. Cellier and E. Colin, "Building height estimation using fine analysis of altimetric mixtures in layover areas on polarimetric interferometric X-band SAR images," in *Proceedings of IEEE International Geoscience and Remote Sensing Symposium (IGARSS)*, Denver, CO, USA, July 2006, pp. 4004–4007.

[39] A. Thiele, E. Cadario, K. Schulz, and U. Thoennessen, "Feature extraction of gable-roofed buildings from multi-aspect high-resolution InSAR data," in *Proceedings of IEEE International Geoscience and Remote Sensing Symposium (IGARSS)*, Barcelona, Spain, July 2007, pp. 262–265.

[40] G. Franceschetti, A. Iodice, and D. Riccio, "A canonical problem in electromagnetic backscattering from buildings," *IEEE Transactions on Geoscience and Remote Sensing*, vol. 40, no. 8, pp. 1787–1801, August 2002.

[41] G. Franceschetti, R. Guida, A. Iodice, D. Riccio, and G. Ruello, "Building feature extraction via a deterministic approach: Application to real high resolution SAR images," in *Proceedings of IEEE International Geoscience and Remote Sensing Symposium (IGARSS)*, Barcelona, Spain, July 2007, pp. 2681–2684.

[42] A. Thiele, E. Cadario, K. Schulz, U. Thoennessen, and U. Soergel, "Building recognition from multi-aspect high-resolution InSAR data in urban areas," *IEEE Transactions on Geoscience and Remote Sensing*, vol. 45, no. 11, pp. 3583–3593, November 2007.

[43] Y. Dong, B. Forster, and C. Ticehurst, "Radar backscatter analysis for urban environments," *International Journal of Remote Sensing*, vol. 18, no. 6, pp. 1351–1364, April 1997.

[44] D. Brunner, G. Lemoine, J. Fortuny, and L. Bruzzone, "Building characterisation in VHR SAR data acquired under controlled EMSL conditions," in *Proceedings of IEEE International Geoscience and Remote Sensing Symposium (IGARSS)*, Barcelona, Spain, July 2007, pp. 2694–2697.

[45] D. Brunner, L. Bruzzone, A. Ferro, J. Fortuny, and G. Lemoine, "Analysis of the double bounce scattering mechanism of buildings in VHR SAR data," in *Proceedings of SPIE Conference on Image and Signal Processing for Remote Sensing XIV*, vol. 7109, Cardiff, Wales, UK, September 2008, pp. 71 090Q–1–71 090Q–12.

[46] D. Brunner, L. Bruzzone, A. Ferro, and G. Lemoine, "Analysis of the reliability of the double bounce scattering mechanism for detecting buildings in VHR SAR images," in *Proceedings of IEEE Radar Conference (RadarCon09)*, Pasadena, CA, USA, May 2009.

[47] F. Xu and Y.-Q. Jin, "Automatic reconstruction of building objects from multi-aspect meter-resolution SAR images," *IEEE Transaction on Geoscience and Remote Sensing*, vol. 45, no. 7, pp. 2336–2353, July 2007.

[48] E. J. Jaselskis, J. Grigas, and A. Brilingas, "Dielectric properties of asphalt pavement," *Journal of Materials in Civil Engineering*, vol. 15, no. 5, pp. 427–434, September/October 2003.

[49] E. Li and K. Sarabandi, "Low grazing incidence millimeter-wave scattering models and measurements for various road surfaces," *IEEE Transactions on Antennas and Propagation*, vol. 47, no. 5, pp. 851–861, May 1999.

[50] H. Al-Mattarneh, D. Ghodgaonkar, and W. Majid, "Microwave sensing of moisture content in concrete using open-ended rectangular waveguide," *Subsurface Sensing Technologies and Applications*, vol. 2, pp. 377–390, October 2001.

[51] Y. Wang, E. S. Kasischke, J. M. Melack, F. W. Davis, and N. L. Christensen, "The effects of changes in loblolly pine biomass and soil moisture on ERS-1 SAR backscatter," *Remote Sensing of Environment*, vol. 49, no. 1, pp. 25–31, 1994.

[52] T. Jackson, H. McNairn, M. Weltz, B. Brisco, and R. Brown, "First order surface roughness correction of active microwave observations for estimating soil moisture," *IEEE Transactions on Geoscience and Remote Sensing*, vol. 35, no. 4, pp. 1065–1069, July 1997.

[53] T. Kempf, M. Peichl, S. Dill, and H. Süß, "Microwave radar signature acquisition of urban structures," in *Proceedings of ITG WFMN07 - Wave Propagation in Communication, Microwave Systems and Navigation*, Chemnitz, Germany, July 2007, pp. 68–73.

[54] Y. A. Hussin, "Effect of polarization and incidence angle on radar return from urban features using L-band aircraft radar data," in *Proceedings of IEEE International Geoscience and Remote Sensing Symposium (IGARSS)*, Florence, Italy, July 1995, pp. 178–180.

[55] J. M. Lopez-Sanchez, "Analysis and estimation of biophysical parameters of vegetation by radar polarimetry," Ph.D. dissertation, Universidad Politecnica de Valencia, 1999.

[56] J. Fortuny, "An efficient 3-D near-field ISAR algorithm," *IEEE Transactions on Aerospace and Electronic Systems*, vol. 34, no. 4, pp. 1261–1270, October 1998.

[57] J. M. Lopez-Sanchez, H. Esteban-Gonzalez, M. Baquero-Escudero, and J. Fortuny-Guasch, "An electromagnetic scattering model for multiple tree trunks above a

tilted rough ground plane," *IEEE Transactions on Geoscience and Remote Sensing*, vol. 37, no. 2, pp. 659–667, March 1999.

[58] GoogleEarth. [Online]. Available: http://earth.google.com

[59] VirtualEarth. [Online]. Available: http://maps.live.com

[60] H. Hammer, T. Balz, E. Cadario, U. Soergel, U. Thoennessen, and U. Stilla, "Comparison of SAR simulation concepts for the analysis of high resolution SAR data," in *7th European Conference on Synthetic Aperture Radar*, Friedrichshafen, Germany, June 2008, pp. 213–216.

[61] T. Balz and D. Fritsch, "High-performance SAR simulation on retail video gaming consoles for education and training purposes," in *Proceedings of XXIth ISPRS Congress*, vol. XXXVII, no. B6a, Beijing, China, July 2008, pp. 213–220.

[62] H.-J. Mametsa, F. Rouas, A. Berges, and J. Latger, "Imaging radar simulation in realistic environment using shooting and bouncing rays technique," in *Proceedings of SPIE: 4543. SAR Image Analysis, Modeling, and Techniques IV*, Toulouse, France, September 2001, pp. 34–40.

[63] G. Franceschetti, A. Iodice, D. Riccio, and G. Ruello, "SAR raw signal simulation for urban structures," *IEEE Transactions on Geoscience and Remote Sensing*, vol. 41, no. 9, pp. 1986–1995, September 2003.

[64] J. Meyer-Hilberg, "PIRDIS: A new versatile tool for SAR/MTI systems simulation," in *Proceedings of 6th European Conference on Synthetic Aperture Radar (EUSAR)*, Dresden, Germany, May 2006.

[65] J. Delliere, H. Maître, and A. Maruani, "SAR measurement simulation on urban structures using a FDTD technique," in *Proceedings of Urban Remote Sensing Joint Event*, Paris, France, April 2007.

[66] F. Xu and Y.-Q. Jin, "Imaging simulation of polarimetric SAR for a comprehensive terrain scene using the mapping and projection algorithm," *IEEE Transations on Geoscience and Remote Sensing*, vol. 44, no. 11, pp. 3219–3234, November 2006.

[67] S. Auer, S. Hernhardt, S. Hinz, N. Adam, and R. Bamler, "Simulation of radar reflection at man-made objects and its benefits for persistent scatterer interferometry," in *Proceedings of 7th European Conference on Synthetic Aperture Radar*, Friedrichshafen, Germany, June 2008.

[68] T. Balz and U. Stilla, "Hybrid GPU based single- and double-bounce SAR simulation," *IEEE Transactions on Geoscience and Remote Sensing*, vol. 47, no. 10, pp. 3519–3529, October 2009.

[69] B. T. Phong, "Illumination for computer generated pictures," *Communication of the ACM*, vol. 18, no. 6, pp. 311–317, June 1975.

[70] R. Bolter, "Reconstruction of man-made objects from high resolution SAR images," in *Proceedings of IEEE Aerospace Conference*, Big Sky, MT, USA, March 2000, pp. 287–292.

[71] R. Bolter, M. Gelautz, and F. Leberl, "SAR speckle simulation," *International Archives of Photogrammetry and Remote Sensing*, vol. 21, pp. 20–25, 1996.

[72] R. Bamler and M. Eineder, "The pyramids of Gizeh seen by TerraSAR-X - a prime example for unexpected scattering mechanisms in SAR," *IEEE Geoscience and Remote Sensing Letters*, vol. 5, no. 3, pp. 468–470, July 2008.

[73] Wikipedia, the free encyclopedia: Menkaure's Pyramid, 2008. [Online]. Available: http://en.wikipedia.org/wiki/Pyramid_of_Menkaure

[74] D. Brunner, G. Lemoine, L. Bruzzone, and H. Greidanus, "Building height retrieval from VHR SAR imagery based on an iterative simulation and matching technique," *IEEE Transactions on Geoscience and Remote Sensing*, in press, 2010.

[75] D. Brunner, G. Lemoine, and L. Bruzzone, "Extraction of building heights from VHR SAR imagery using an iterative simulation and match procedure," in *Proceedings of IEEE International Geoscience and Remote Sensing Symposium (IGARSS)*, vol. 4, Boston, MA, USA, July 2008, pp. 141–144.

[76] D. Brunner, G. Lemoine, and L. Bruzzone, "Building height retrieval from airborne VHR SAR imagery based on an iterative simulation and matching procedure," in *Proceedings of SPIE Conference on Remote Sensing for Environmental Monitoring, GIS Applications, and Geology VIII*, vol. 7110, Cardiff, Wales, UK, September 2008, pp. 71 100F–1–71 100F–12.

[77] D. Brunner, G. Lemoine, and L. Bruzzone, "Estimation of building heights from detected dual-aspect VHR SAR imagery using an iterative simulation and matching procedure in combination with functional analysis," in *Proceedings of IEEE Radar Conference (RadarCon09)*, Pasadena, CA, USA, May 2009.

[78] T. Balz and N. Haala, "SAR-based 3D reconstruction of complex urban environments," in *International Archives of Photogrammetry and Remote Sensing (IAPRS)*, vol. 34, Part 3/W13, 2003, pp. 181–185.

[79] F. Tupin, "Extraction of 3D information using overlay detection on SAR images," in *Proceedigns of 2nd GRSS/ISPRS Joint Workshop on Remote Sensing and Data Fusion over Urban Areas*, Berlin, Germany, May 2003, pp. 72–76.

[80] P. Gamba, B. Houshmand, and M. Saccani, "Detection and extraction of buildings from interferometric SAR data," *IEEE Transactions on Geoscience and Remote Sensing*, vol. 38, no. 1, pp. 611–618, July 2000.

[81] P. Gamba and B. Houshmand, "Digital surface models and building extraction: A comparison of IFSAR and LIDAR data," *IEEE Transactions on Geoscience and Remote Sensing*, vol. 38, no. 4, pp. 1959–1968, July 2000.

[82] C. Tison, F. Tupin, and H. Maître, "A fusion scheme for joint retrieval of urban height map classification from high-resolution interferometric SAR images," *IEEE Transactions on Geoscience and Remote Sensing*, vol. 45, no. 2, pp. 496–505, February 2007.

[83] E. Simonetto, H. Oriot, and R. Garello, "Rectangular building extraction from stereoscopic airborne radar images," *IEEE Transactions on Geoscience and Remote Sensing*, vol. 43, no. 10, pp. 2386–2395, October 2005.

[84] U. Soergel, E. Michaelsen, A. Thiele, E. Cadario, and U. Thoennessen, "Stereo analysis of high-resolution SAR images for building height estimation in cases of orthogonal aspect directions," *ISPRS Journal of Photogrammetry and Remote Sensing*, vol. 64, no. 5, pp. 490–500, September 2009.

[85] R. Hill, C. Moate, and D. Blacknell, "Estimating building dimensions from synthetic aperture radar image sequences," *IET Radar, Sonar and Navigation*, vol. 2, no. 3, pp. 189–199, June 2008.

[86] S. Sauer, L. Ferro-Famil, A. Reigber, and E. Pottier, "Multi-aspect POL-InSAR 3D urban scene reconstruction at L-band," in *Proceedings of 7th European Conference on Synthetic Aperture Radar (EUSAR)*, Friedrichshafen, Germany, June 2008.

[87] H. Oriot and H. Cantalloube, "Circular SAR imagery for urban remote sensing," in *Proceedings of 7th European Conference on Synthetic Aperture Radar (EUSAR)*, Friedrichshafen, Germany, June 2008.

[88] G. Margarit, J. J. Mallorqui, J. M. Rius, and J. Sanz-Marcos, "On the usage of GRECOSAR, an orbital polarimetric SAR simulator of complex targets, to vessel classification studies," *IEEE Transactions on Geoscience and Remote Sensing*, vol. 44, no. 12, pp. 3517–3526, December 2006.

[89] G. Margarit, J. J. Mallorqui, and C. Lopez-Martinez, "GRECOSAR, a SAR simulator for complex targets: Application to urban environments," in *Proceedings of IEEE International Geoscience and Remote Sensing Symposium (IGARSS)*, Barcelona, Spain, July 2007, pp. 4160–4163.

[90] J. A. Nelder and R. Mead, "A simplex method for function minimization," *The Computer Journal*, vol. 7, no. 4, pp. 308–313, January 1965.

[91] S. Kirkpatrick, C. D. Gelatt, and M. P. Vecchi, "Optimization by simulated annealing," *Science*, vol. 220, no. 4598, pp. 671–680, May 1983.

[92] G. Oller, P. Marthon, and L. Rognant, "Correlation and similarity measures for SAR image matching," in *Proceedings of the Conference on SAR Image Analysis, Modelling and Techniques VIII*, Barcelona, Spain, September 2003.

[93] C. Barat, C. Ducottet, and M. Jourlin, "Pattern matching using morphological probing," in *Proceedings of 10th International Conference on Image Processing*, vol. 1, Barcelona, Spain, September 2003, pp. 369–372.

[94] J. S. De Bonet and A. Chao, "Structure-driven SAR image registration," in *Proceedings of SPIE*, vol. 3370, September 1998, pp. 109–119.

[95] W. G. Eppler, S. M., L. M. J. Petersen, and D. W. Paglieroni, "Fast normalized cross-correlation of complex gradients for autoregistration of multi-source imagery," in *Proceedings of American Society for Photogrammetry and Remote Sensing Annual Meeting*, Washington D.C., USA, May 2000.

[96] J. Zheng, X. Bai, and X. Zhao, "SAR image matching based on fractal theory," in *Proceedings of 7th International Conference on Signal Processing*, Beijing, China, August 2004, pp. 1965–1968.

[97] F. Chen, H. Zhang, and C. Wang, "A novel feature matching method in airborne SAR image registration," in *Proceedings of IEEE International Geoscience and Remote Sensing Symposium (IGARSS)*, Seoul, South Korea, July 2005, pp. 4722–4724.

[98] D. G. Lowe, "Distinctive image features from scale-invariant keypoints," *International Journal of Computer Vision*, vol. 60, no. 2, pp. 91–110, November 2004.

[99] B. Wessel, M. Huber, and A. Roth, "Registration of near real-time SAR images by image-to-image matching," in *Proceedings of Photogrammetric Image Analysis*, vol. 36, Part 3/ W49B, Munich, Germany, September 2007, pp. 179–184.

[100] D. Brunner, G. Lemoine, and L. Bruzzone, "Height estimation of man made structures using hybrid VHR optical and SAR imagery," in *Proceedings of EARSeL Joint Workshop: Remote Sensing - New Challenges of High Resolution*, Bochum, Germany, March 2008, pp. 186–193.

[101] J. Lewis, "Fast normalized cross-correlation," in *Proceedings of Vision Interface*, Quebec, Canada, May 1995, pp. 120–123.

[102] A. Collignon, F. Maes, D. Delaere, D. Vandermeulen, P. Suetens, and G. Marchal, "Automated multi-modality image registration based on information theory," in *Proceedings of 14th International Conference on Information Processing in Medical Imaging*, Ile de Berder, France, June 1995, pp. 263–274.

[103] P. Viola and W. Wells, "Alignment by maximization of mutual information," *International Journal of Computer Vision*, vol. 24, no. 2, pp. 137–154, September 1997.

[104] H. Xie, L. E. Pierce, and F. T. Ulaby, "Mutual information based registration of SAR images," in *Proceedings of IEEE International Geoscience and Remote Sensing Symposium (IGARSS)*, Toulouse, France, July 2003, pp. 4028–4031.

[105] F. Maes, A. Collignon, D. Vandeermeulen, G. Marchal, and P. Suetens, "Multimodality image registration by maximization of mutual information," *IEEE Transactions in Medical Imaging*, vol. 16, no. 2, pp. 187–198, April 1997.

[106] P. Soille, *Morphological Image Analysis: Principles and Applications*, 2nd ed. Springer, 2003.

[107] J. Duchon, "Splines minimizing rotation-invariant semi-norms in sobolev spaces," in *Proceedings of Conference on Constructive Theory of Functions of Several Variables*, vol. 571, Oberwolfach, Germany, April 1977, pp. 85–100.

[108] M. Schwaebisch and J. Moreira, "The high resolution airborne interferometric SAR AeS-1," in *Proceedings of 4th International Airborne Remote Sensing Conference and Exhibition*, Ottawa, Canada, June 1999, pp. 540–547.

[109] A. Lopes, E. Nezry, R. Touzi, and H. Laur, "Structure detection and statistical adaptive speckle filtering in SAR images," *International Journal of Remote Sensing*, vol. 14, no. 9, pp. 1735–1758, June 1993.

[110] F. Cellier, H. Oriot, and J.-M. Nicolas, "Introduction of the mean shift algorithm in SAR imagery: Application to shadow extraction for building reconstruction," in *Proceedings of EARSeL Workshop 3D-Remote Sensing*, Porto, Portugal, June 2005.

[111] J. R. Taylor, *An Introduction to Error Analysis.*, 2nd ed. University Science Books, 1997.

[112] N. Ripperda and C. Brenner, "Data driven rule proposal for grammar based facade reconstruction," in *Proceedings of Photogrammetric Image Analysis*, vol. 36, Part 3/W49A, Munich, Germany, September 2007.

[113] D. Brunner, G. Lemoine, and L. Bruzzone, "Earthquake damage assessment of buildings using VHR optical and SAR imagery," *IEEE Transactions on Geoscience and Remote Sensing*, in press, 2010.

[114] M. Dalla Mura, J. A. Benediktsson, F. Bovolo, and L. Bruzzone, "An unsupervised technique based on morphological filters for change detection in very high resolution images," *IEEE Geoscience and Remote Sensing Letters*, vol. 5, no. 3, pp. 433–437, July 2008.

[115] F. Bovolo, L. Bruzzone, and S. Marchesi, "Analysis and adaptive estimation of the registration noise distribution in multitemporal VHR images,," *IEEE Transactions on Geoscience and Remote Sensing*, vol. 47, no. 8, pp. 2658–2671, August 2009.

[116] M. Pesaresi, A. Gerhardinger, and F. Haag, "Rapid damage assessment of built-up structures using VHR satellite data in tsunami-affected areas," *International Jounal of Remote Sensing*, vol. 28, no. 13-14, pp. 3013–3036, June 2007.

[117] M. Turker and B. T. San, "Detection of collapsed buildings caused by the 1999 Izmit, Turkey earthquake through digital analysis of post-event aerial photographs," *International Journal of Remote Sensing*, vol. 25, no. 21, pp. 4701–4714, November 2004.

[118] Y. Bazi, L. Bruzzone, and F. Melgani, "An unsupervised approach based on the generalized Gaussian model to automatic change detection in multitemporal SAR images," *IEEE Transactions on Geoscience and Remote Sensing*, vol. 43, no. 4, pp. 874–887, April 2005.

[119] Y. Ito, M. Hosokawa, H. Lee, and J. G. Liu, "Extraction of damaged regions using SAR data and neural networks," in *Proceedings of 19th ISPRS Congress*, vol. 33, Amsterdam, The Netherlands, July 2000, pp. 156–163.

[120] J. Hoffmann, "Mapping damage during the Bam (Iran) earthquake using interferometric coherence," *International Journal of Remote Sensing*, vol. 28, no. 6, pp. 1199–1216, March 2007.

[121] M. Matsuoka and F. Yamazaki, "Use of interferometric satellite SAR for earthquake damage detection," in *Proceedings of 6th International Conference on Seismic Zonation*, Palm Springs, CA, USA, November 2000.

[122] M. Chini, C. Bignami, S. Stramondo, and N. Pierdicca, "Uplift and subsidence due to the 26 December 2004 Indonesian earthquake detected by SAR data," *International Journal of Remote Sensing*, vol. 29, no. 13, pp. 3891–3910, July 2008.

[123] C. Yonezawa and S. Takeuchi, "Decorrelation of SAR data by urban damages caused by the 1995 Hyogoken-nanbu earthquake," *International Journal of Remote Sensing*, vol. 22, no. 8, pp. 1585–1600, May 2001.

[124] M. Matsuoka and F. Yamazaki, "Use of satellite SAR intensity imagery for detecting building areas damaged due to earthquakes," *Earthquake Spectra*, vol. 20, no. 3, pp. 975–994, August 2004.

[125] M. Matsuoka and F. Yamazaki, "Building damage mapping of the 2003 Bam, Iran, earthquake using Envisat/ASAR intensity imagery," *Earthquake Spectra*, vol. 21, no. S1, pp. S285–S294, December 2005.

[126] M. Matsuoka and F. Yamazaki, "Damage detection for the 2003 Algeria earthquake using SAR intensity images," in *Proceedings of 1st Asia Conference on Earthquake Engineering*, Manila, Philippines, March 2004.

[127] M. Chini, N. Pierdicca, and W. Emery, "Exploiting SAR and VHR optical images to quantify damage caused by the 2003 Bam earthquake," *IEEE Transactions on Geoscience and Remote Sensing*, vol. 47, no. 1, pp. 145–152, January 2009.

[128] G. Trianni and P. Gamba, "Damage detection from SAR imagery: Application to the 2003 Algeria and 2007 Peru earthquakes," *International Journal of Navigation and Observation*, vol. 2008, 2008.

[129] B. Mansouri, M. Shinozuka, and R. Nourjou, "SAR remote sensing for urban damage assessment for Tehran," in *Proceedings of 5th International Workshop on Remote Sensing Applications to Natural Hazards*, Washington DC, USA, September 2007.

[130] Y.-Q. Jin and D. Wang, "Automatic detection of terrain surface changes after Wenchuan earthquake, May 2008, from ALOS SAR images using 2EM-MRF method," *IEEE Geoscience and Remote Sensing Letters*, vol. 6, no. 2, pp. 344–348, April 2009.

[131] M. Shinozuka and K. Loh, "Remote sensing with the synthetic aperture radar (SAR) for urban damage detection," in *Proceedings of 9th Biennial ASCE Aerospace Division International Conference on Engineering, Construction, and Operations in Challenging Environments*, vol. 153, no. 40722, League City/Houston, TX, USA, March 2004, pp. 223–230.

[132] G. Mercier, G. Moser, and S. Serpico, "Conditional copulas for change detection in heterogeneous remote sensing images," *IEEE Transactions on Geoscience and Remote Sensing*, vol. 46, no. 5, pp. 1428–1441, May 2008.

[133] J. Inglada and A. Giros, "On the possibility of automatic multisensor image registration," *IEEE Transactions on Geoscience and Remote Sensing*, vol. 42, no. 10, pp. 2104–2120, October 2004.

[134] T. Kim, T. Javzandulam, and T.-Y. Lee, "Semiautomatic reconstruction of building height and footprints from single satellite images," in *Proceedings of IEEE International Geoscience and Remote Sensing Symposium (IGARSS)*, Barcelona, Spain, July 2007, pp. 4737–4740.

[135] S. Mayunga, Y. Zhang, and D. Coleman, "Semi-automatic building extraction utilizing Quickbird imagery," in *International Archives of Photogrammetry and Remote Sensing*, vol. XXXVI, Part 3/W24, no. 131-136, Vienna, Austria, August 2005.

[136] X. Jin and C. H. Davis, "Automated building extraction from high-resolution satellite imagery in urban areas using structural, contextual, and spectral information," *Journal on Applied Signal Processing*, vol. 2005, no. 14, pp. 2196–2206, 2005.

[137] A. Shackelford, C. Davis, and X. Wang, "Automated 2-D building footprint extraction from high-resolution satellite multispectral imagery," in *Proceedings of IEEE International Geoscience and Remote Sensing Symposium (IGARSS)*, vol. 3, Anchorage, AK, USA, September 2004, pp. 1996–1999.

[138] Q.-Y. Zhou and U. Neumann, "Fast and extensible building modeling from airborne LIDAR data," in *Proceedings of 16th International Conference on Advances in Geographic Information Systems*, Irvine, CA, USA, November 2008, pp. 1–8.

[139] G. Forlani, C. Nardinocchi, M. Scaioni, and P. Zingaretti, "Complete classification of raw LIDAR data and 3D reconstruction of buildings," *Pattern Analysis and Applications*, vol. 8, no. 4, pp. 357–374, February 2006.

[140] D. K. San and M. Turker, "Automatic building extraction from high resolution stereo satellite images," in *Proceedings of Conference on Information Extraction from SAR and Optical Data with Emphasize on Developing Countries*, Istanbul, Turkey, May 2007.

[141] C. Studholme, D. L. G. Hill, and D. J. Hawkes, "An overlap invariant entropy measure of 3D medical image alignment," *Pattern Recognition*, vol. 32, no. 1, pp. 71–86, January 1999.

[142] I. Kojadinovic, "On the use of mutual information in data analysis: An overview," in *Proceedings of International Symposium on Applied Stochastic Models and Data Analysis*, Brest, France, May 2005.

[143] C. Saerndal, "A comparative study of association measures," *Psychometrika*, vol. 39, no. 2, pp. 165–187, June 1974.

[144] H. Joe, "Relative entropy measures of multivariate dependence," *Journal of the American Statistical Association*, vol. 84, no. 405, pp. 157–164, March 1989.

[145] J. P. W. Pluim, J. B. A. Maintz, and M. A. Viergever, "Mutual information based registration of medical images: A survey," *IEEE Transactions on Medical Imaging*, vol. 22, no. 8, pp. 986–1004, August 2003.

[146] L. Bruzzone and D. F. Prieto, "Automatic analysis of the difference image for unsupervised change detection," *IEEE Transactions on Geoscience and Remote Sensing*, vol. 38, no. 3, pp. 1171–1182, May 2000.

[147] A. P. Dempster, N. M. Laird, and D. B. Rubin, "Maximum likelihood from incomplete data via the EM algorithm," *Journal of the Royal Statistical Society*, vol. 39, no. 1, pp. 1–38, 1977.

[148] T. Moon, "The expectation-maximization algorithm," *IEEE Signal Processing Magazine*, vol. 13, no. 6, pp. 47–60, November 1996.

[149] R. Redner and H. Walker, "Mixture densities, maximum likelihood and the EM algorithm," *SIAM Review*, vol. 26, no. 2, pp. 195–239, April 1984.

[150] 2008 Sichuan earthquake. [Online]. Available: http://en.wikipedia.org/wiki/2008_Sichuan_earthquake

[151] Yingxiu, Wenchuan County. [Online]. Available: http://en.wikipedia.org/wiki/Yingxiu,_Wenchuan_County

[152] B. L. Welch, "The generalization of "Student's" problem when several different population variances are involved," *Biometrika*, vol. 34, no. 1-2, pp. 28–35, January 1947.

[153] A. Katartzis and H. Sahli, "A stochastic framework for the identification of building rooftops using a single remote sensing image," *IEEE Transactions on Geoscience and Remote Sensing*, vol. 46, no. 1, pp. 259–271, January 2008.

[154] F. Taillandier, "Automatic building reconstruction from cadastral maps and aerial images," in *International Archives of Photogrammetry and Remote Sensing*, vol. XXXVI, Part 3/W24, Vienna, Austria, August 2005, pp. 105–110.

[155] D. Brunner, G. Lemoine, F.-X. Thoorens, and L. Bruzzone, "Distributed geospatial data processing functionality to support collaborative and rapid emergency response," *IEEE Journal of Selected Topics in Applied Earth Observation and Remote Sensing*, vol. 2, no. 1, pp. 33–46, March 2009.

[156] P. Barbosa, J. Kucera, P. Strobl, A. Camia, G. Amatulli, and J. San-Miguel, "European forest fire information system (EFFIS) rapid damage assessment: Appraisal of burnt area maps in southern Europe using Modis data (2003 to 2005)," in *Proceedings of 5th International Conference on Forest Fire Research*, Figueira da Foz, Portugal, November 2006.

[157] A. De Roo, C. Wesseling, and W. Van Deurzen, "Physically based river basin modelling within a GIS: the LISFLOOD model," *Hydrological Processes*, vol. 14, no. 11-12, pp. 1981–1992, August 2000.

[158] A. Berson, *Client/server architecture*. New York, NY, USA: McGraw-Hill, Inc., 1992.

[159] T. Mitchell, *Web Mapping Illustrated*. Sebastopol, CA, USA: O'Reilly Media, Inc., June 2005.

[160] I. Sommerville, *Software engineering*, 8th ed. Harlow, UK: Addison-Wesley, 2007.

[161] E. Gamma, R. Helm, R. Johnson, and J. Vlissides, *Design patterns: Elements of reusable object-oriented software*. Addison-Wesley Professional, 1995.

[162] KML 2.1 Reference. [Online]. Available: http://code.google.com/apis/kml/documentation/kmlreference.html

[163] Geospatial Data Abstraction Library (GDAL). [Online]. Available: http://www.gdal.org/

[164] Open Geospatial Consortium. [Online]. Available: http://www.opengeospatial.org

[165] Open Geospatial Consortium, OpenGIS Web Coverage Service 1.1.2 (WCS), 2007. [Online]. Available: http://www.opengeospatial.org/standards/wcs

[166] Open Geospatial Consortium, OpenGIS Web Map Service 1.3.0 (WMS), 2004. [Online]. Available: http://www.opengeospatial.org/standards/wms

[167] D. F. Stanfill, "Using image pyramids for the visualization of large terrain data sets," *International Journal of Imaging Systems and Technology*, vol. 3, no. 2, pp. 157–166, 1991.

[168] NASA World Wind. [Online]. Available: http://worldwind.arc.nasa.gov

[169] KML 2.1 Tutorial. [Online]. Available: http://code.google.com/apis/kml/documentation/kml_21tutorial.html#superoverlays

[170] G. Lemoine and D. Brunner, "Integration of full resolution image coverages using superoverlays," in *Proceedings of Conference on Freie und Open Source Software fuer Geoinformationssysteme (FossGIS)*, Berlin, Germany, March 2007.

[171] G. Lemoine, D. Brunner, and F.-X. Thoorens, "Superoverlay deployment in grid-enabled image processing," in *Proceedings of IEEE International Geoscience and Remote Sensing Symposium (IGARSS)*, Boston, MA, USA, July 2008.

[172] I. Foster and C. Kesselman, Eds., *The grid: Blueprint for a new computing infrastructure*. San Francisco, CA, USA: Morgan Kaufmann Publishers Inc., November 1998.

[173] Open Geospatial Consortium, OpenGIS Web Feature Service 1.1.0 (WFS), 2006. [Online]. Available: http://www.opengeospatial.org/standards/wfs

[174] Open Geospatial Consortium, OpenGIS Styled Layer Descriptor 1.1.0 (SLD), 2007. [Online]. Available: http://www.opengeospatial.org/standards/sld

[175] R. Welch and M. Ehlers, "Merging multiresolution SPOT HRV and Landsat TM data," *Photogrammetric Engineering and Remote Sensing*, vol. 53, no. 3, pp. 301–303, 1987.

[176] J. Grodecki and G. Dial, "Block adjustment of high-resolution satellite images described by rational functions," *Photogrammetric Engineering and Remote Sensing*, vol. 69, no. 1, pp. 59–70, January 2003.

[177] M. Pesaresi, "Texture analysis for urban pattern recognition using fine-resolution panchromatic satellite imagery," *Geographical and Environmental Modelling*, vol. 4, no. 1, pp. 43–63, May 2000.

[178] C. Bielski, G. Lemoine, and J. Syryczynski, "Accessible high performance computing solutions for near real-time image processing for time critical applications," in *Proceedings of SPIE Conference on Image and Signal Processing for Remote Sensing XIV*, Berlin, Germany, August 2009.

[179] Google Lat Long Blog - Imagery for Sichuan, China Earthquake, 2008. [Online]. Available: http://google-latlong.blogspot.com/2008/05/imagery-for-sichuan-china-earthquake.html

[180] National Oceanic and Atmospheric Administration's National Geodetic Survey (NOAA) - Hurrican Ike, 2008. [Online]. Available: http://ngs.woc.noaa.gov/ike/

[181] United Nations Platform for Space-based Information for Disaster Management and Emergency Response (SPIDER), 2007. [Online]. Available: http://www.unoosa.org/oosa/unspider/index.html

[182] Y. Bazi, L. Bruzzone, and F. Melgani, "Image thresholding based on the EM algorithm and the generalized Gaussian distribution," *Pattern Recognition*, vol. 40, no. 2, pp. 619–634, February 2007.